Deuterated Clathrate Hydrates as novel Moderator Material for a Source of Very Cold Neutrons

Valentin Czamler

THÈSE

Pour obtenir le grade de

DOCTEUR DE L'UNIVERSITÉ GRENOBLE ALPES

École doctorale : PHYS - Physique
Spécialité : Physique Subatomique et Astroparticules
Unité de recherche : Institut LAUE LANGEVIN

Les clathrate hydrates deutérés comme nouveau matériau modérateur d'une source de neutrons très froids

Deuterated Clathrate Hydrates as novel Moderator Material for a Source of Very Cold Neutrons

Présentée par :

Valentin CZAMLER

Direction de thèse :

Oliver ZIMMER Senior Scientist, Institut Laue Langevin	Directeur de thèse
Richard WAGNER Physicien, Institut Laue-Langevin	Co-encadrant de thèse

Rapporteurs :

MARTIN FALLY
ASSOCIATE PROFESSOR, UNIVERSITÄT WIEN
FREDERIC OTT
DIRECTEUR DE RECHERCHE, CEA CENTRE DE PARIS-SACLAY

Thèse soutenue publiquement le **20 novembre 2024**, devant le jury composé de :

LIVIA BOVE, DIRECTRICE DE RECHERCHE, CNRS DELEGATION PARIS CENTRE	Présidente
MARTIN FALLY, ASSOCIATE PROFESSOR, UNIVERSITÄT WIEN	Rapporteur
FREDERIC OTT, DIRECTEUR DE RECHERCHE, CEA CENTRE DE PARIS-SACLAY	Rapporteur
STEPHANIE ROCCIA, MAITRESSE DE CONFERENCES HDR, UNIVERSITE GRENOBLE ALPES	Examinatrice

Abstract

The objective of this thesis is the detailed analysis of the neutron scattering properties, characterization of important neutron cross sections, and the investigation of neutron transport in deuterated clathrate hydrates as necessary scientific prerequisites for their application as a novel moderator material for Very Cold Neutrons (VCN). VCN cover a wide spectral range within the long-wavelength tail of typical sources for cold neutrons, from energies below 1 meV down to the domain of ultracold neutrons (UCN) at a few hundreds of neV. Dedicated high-intensity VCN sources have the ability to enhance various neutron scattering techniques, with applications in condensed matter physics. VCN could improve spatial resolution in methods like small-angle neutron scattering (SANS) and refine energy resolution in techniques such as time-of-flight and neutron spin-echo spectroscopy. In particle physics, higher VCN intensities could increase the sensitivity of experiments employing beams of slow neutrons, such as the search for neutron-antineutron oscillations and in-beam searches for a static neutron electric dipole moment.

The efficacy of clathrate hydrates in neutron moderation is linked to the localized low-energy, so-called Einstein modes, of entrapped guest molecules. These facilitate slowdown of neutrons to very low temperatures. Besides the nuclear scattering of any guest molecule, the special case of dioxygen (O_2) offers an additional neutron slowdown mechanism through its zero-field splitting of its magnetic triplet ground state. The absence of a dispersion relation in this excitation allows for a 'cooling cascade', a process in which neutrons are progressively slowed down by increments of the field-splitting energy of 0.4 meV.

To quantify the neutronic properties of these compounds, a comprehensive neutron scattering campaign was conducted in the framework of this thesis. This investigation examined the hydrate's structure through neutron diffraction, its dynamics through inelastic neutron scattering, and its total neutron cross section using transmission experiments on fundamental physics beamlines. This experimental effort was complemented by contributions to collaborative works on the development of thermal scattering libraries (TSL) for clathrate hydrates based on ab-initio molecular dynamics simulations and density functional theory, as well as a magnetic scattering model for O_2. All these works were part of the European project HighNESS.

The experimental study presented here focuses on two specific hydrates: one hosting deuterated tetrahydrofuran (THF-d) and the other, a binary hydrate, hosting both THF-d and O_2. A manufacturing technique for the latter, developed during this study, was found to yield a high-purity hydrate with high O_2 cage occupancy. Experiments performed with neutron spectrometers measured the dynamic structure factor $S(q, \omega)$ over a large phase space in absolute units. The down-scattering of confined dioxygen at 0.4 meV was measured for the first time in a binary clathrate hydrate. Additionally, it was found that the THF-d molecule exhibits excitations, which allow bypassing of the magnetic "cooling cascade", leading to faster thermalization of neutrons in a moderator. Transmission experiments confirmed Bragg scattering up to a cut-off around 20 Å and revealed a significant increase in the cross section at higher wavelengths, attributed to SANS.

The manufacturing technique, experimental data, and theoretical models established over the course of this thesis provide a foundation for quantitatively assessing the potential of clathrate hydrates as moderator material for VCN production; enabling neutronic design studies in various moderator-reflector configurations at the ESS and other emerging neutron sources worldwide.

Résumé

L'objectif de cette thèse est l'analyse détaillée des propriétés de diffusion des neutrons, la caractérisation des sections efficaces importantes, et l'étude du transport neutronique dans les hydrates de clathrate deutérés, en tant que prérequis scientifiques nécessaires à leur application comme nouveau matériau modérateur pour les Neutrons Très Froids (VCN). Les VCN couvrent une large gamme spectrale dans la queue des longueurs d'onde typiques des sources de neutrons froids, depuis des énergies inférieures à 1 meV jusqu'au domaine des neutrons ultra-froids (UCN) à quelques centaines de neV. Des sources VCN à haute intensité dédiées pourraient améliorer diverses techniques de diffusion des neutrons, avec des applications en physique de la matière condensée. Elles pourraient améliorer la résolution spatiale dans des méthodes comme la diffusion des neutrons aux petits angles (SANS) et affiner la résolution énergétique dans des techniques telles que les spectromètres à temps de vol et à spin-écho. En physique des particules, des intensités plus élevées de VCN pourraient accroître la sensibilité des expériences utilisant des faisceaux de neutrons lents, telles que la recherche d'oscillations neutron-antineutron et de moments dipolaires électriques statiques.

L'efficacité des hydrates de clathrate dans la modération des neutrons repose sur les modes d'Einstein de basse énergie des molécules invitées piégées. Ceux-ci facilitent le ralentissement des neutrons à très basse température. Outre la diffusion nucléaire des molécules invitées, le cas particulier du dioxygène (O_2) présente un mécanisme supplémentaire de ralentissement des neutrons par le dédoublement de l'état fondamental magnétique. L'absence de relation de dispersion dans cette excitation crée une « cascade de refroidissement », où les neutrons sont ralentis par des incréments d'énergie de 0.4 meV.

Pour quantifier les propriétés neutroniques de ces composés, une vaste campagne de diffusion de neutrons a été menée dans le cadre de cette thèse. Cette étude a examiné la structure des hydrates par diffraction de neutrons, leur dynamique par diffusion inélastique et leur section efficace totale via des expériences de transmission sur des lignes de faisceaux de physique fondamentale. Cet effort a été complété par le développement de bibliothèques de diffusion thermique (TSL) pour les hydrates de clathrate, basées sur des simulations ab-initio et un modèle de diffusion magnétique pour O_2, dans le cadre du projet européen HighNESS.

L'étude expérimentale présentée ici se concentre sur deux hydrates spécifiques : l'un contenant du tétrahydrofurane deutéré (THF-d) et l'autre contenant à la fois du THF-d et du O_2. Une méthode développée pour produire des hydrates binaires de haute pureté, contenant à la fois du THF-d et du O_2, a permis de mesurer pour la première fois la diffusion du dioxygène confiné à 0.4 meV dans un hydrate binaire. Il a également été observé que le THF-d présente des excitations qui permettent de contourner la « cascade de refroidissement » magnétique, conduisant à une thermalisation plus rapide des neutrons dans un modérateur. Les expériences de transmission ont confirmé la diffusion de Bragg jusqu'à une coupure d'environ 20 Å et ont révélé une augmentation significative de la section efficace à des longueurs d'onde plus élevées, attribuée à une contribution SANS.

La technique de fabrication, les données expérimentales et les modèles théoriques établis au cours de cette thèse fournissent une base pour l'évaluation quantitative du potentiel des hydrates de clathrate en tant que matériau modérateur pour la production des VCN, permettant des études de conception neutronique dans diverses configurations modérateur-réflecteur.

Contents

1. Introduction

Neutrons have wide-ranging scientific applications, from probing the atomic structure of materials to fundamental particle-physics experiments. Traditionally, neutrons emerging from nuclear reactions with high initial energies are moderated into the thermal and cold energy ranges through interactions with hydrogenous materials. The growing need for even lower energy neutrons has prompted new approaches to extend neutron moderation into the Very Cold Neutron (VCN) regime. Achieving this could significantly enhance the capabilities of neutron scattering techniques and open new possibilities in particle-physics experiments employing slow neutron beams.

For a material to effectively moderate neutrons into the VCN regime, it must exhibit low neutron absorption and possess excitable low-energy modes that allow for an efficient energy reduction of the neutron. *Clathrate hydrates*, which are water-based inclusion compounds similar to ice, are a promising candidate. Their unique structure and low-energy dynamics suggest that they could meet the requirements for effective moderation in the VCN regime.

This work presents the first experimental investigation of the neutron scattering properties and cross sections of clathrate hydrates for their potential use as a novel moderator material for VCN. The results provide key insights into the feasibility and performance of these materials in moderating neutrons to very low energies, enhancing our understanding of these compounds and laying the groundwork for possible future neutron source developments. Before exploring the potential of VCN and the role clathrate hydrates may play in their production, it is worthwhile to review the discovery of the neutron and its fundamental properties.

1.1. The Neutron and its Basic Properties

Already more than a decade before the neutron's discovery in 1932 by J. Chadwick [1, 2], E. Rutherford speculated in his *Bakerian Lecture* about an "atom" with very similar properties:

> "In the other case, it involves the idea of the possible existence of an atom of mass 1 which has zero nucleus charge. [...], it may be possible for an electron to combine much more closely with the H nucleus, forming a kind of neutral doublet. Such an atom would have very novel properties. Its external field would be practically zero, except very close to the nucleus, and in consequence it should be able to move freely through matter." [3]

What Rutherford referred to as "a kind of neutral doublet" was later characterized in E. Fermi's theory of the β-decay [4, 5] and finally included in the standard model of particles as the neutron. Rutherford also alludes to the mass of the neutron, its eponymous electrical neutrality, and its resulting high penetrating power, without mentioning the neutron's ability to interact with thermal vibrations in the matter it passes through.

Today, it is well established that, as hadrons (i.e. particles composed of quarks), neutrons interact with all known fundamental forces: gravity, electromagnetism, weak, and strong interaction. Furthermore, it is plausible to hypothesize that neutrons could also participate in a potential "fifth" force, possibly originating from dark matter, which permeates the universe [6].

Combined with its absence of electrical charge[1], this makes it a very suitable probe for particle physics experiments. The absence of the long-range Coulomb interaction allows for more nuanced effects to become prominent [6]. This opens the possibility of exploring physics beyond the Standard Model in the low-energy regime.

Table 1.1.: Certain properties of the free neutron, based on [9]. The magnetic moment is given with respect to the nuclear magneton μ_N.

Property	**Value**
Mass	$m = (1.008\,664\,915 \pm 0.000\,000\,095)\,\mathrm{u}$
	$= (939.565\,420 \pm 0.000\,052)\,\mathrm{MeV/c^2}$
Spin	$s = \hbar/2$
Charge	$q = (-0.2 \pm 0.8) \times 10^{-21}\,\mathrm{e}$
Magnetic Moment	$\mu = (-1.913\,042 \pm 0.000\,073)\,\mu_\mathrm{N}$
Lifetime	$\tau = (878.0 \pm 0.4)\,\mathrm{s}$
Mean-square Charge Radius	$R = (-0.11 \pm 0.55)\,\mathrm{fm^2}$

The electrical neutrality of the neutron is also advantageous for condensed matter research. The kinetic energies of both thermal and cold neutrons coincide with the typical energy scales of thermal excitations in materials. Neutrons have a mass that results in de Broglie wavelengths in the Ångstrom range when moving at thermal velocities, which, by a fortunate coincidence, matches the typical interatomic distances in solids. This allows neutrons to provide structural information through elastic scattering, as in diffraction experiments, and dynamic information through inelastic scattering, such as in spectroscopy experiments.

Neutrons are typically bound within atomic nuclei. Free neutrons have a relatively short lifetime of about 15 minutes. They must be produced through nuclear reactions, such as fission[2] or spallation, which typically involve energies in the MeV range. However, the high-energy neutrons generated by these processes are not particularly useful for neutron scattering or low-energy particle physics experiments. To reduce their energy to the desired range, processes called *moderation* or *conversion* are employed, as is detailed in Section 2.2 and Section 2.4.

The classification around neutron energies is not always concise in the literature. Figure 1.1 shows the terminology used in the context of this work. The neutron can be assigned a de Broglie wavelength, λ, which depends on its energy:

$$|\mathbf{p}| = \frac{h}{\lambda} = \hbar k\,, \tag{1.1}$$

by using the non-relativistic relation between a particle's kinetic energy E and its momentum $\mathbf{p}$:

$$E = \frac{p^2}{2m_n} = \frac{\hbar^2 k^2}{2m_n}\,, \tag{1.2}$$

where $k = 2\pi/\lambda$ is the wavenumber. When considering a field of neutrons in thermal equilibrium, the average energy can be associated with a temperature using the relation:

$$\overline{E} = k_\mathrm{B} T\,, \tag{1.3}$$

where $\overline{E}$ is the average energy, k_B is the Boltzmann constant, and T is the temperature. A thermal neutron field is associated with a moderator at room temperature (approximately

[1] According to measurements of the neutron charge [7] it needs to be smaller than $(-0.2 \pm 0.8) \times 10^{-21}\,\mathrm{e}$ (see Table 1.1). Recently proposed experiments aim to improve this limit [8].

[2] At reactor sources, moderation is not only required to serve the instrumentation, nuclear reactors also require moderation to sustain the chain reaction due to the energy dependence of the neutron capture cross section.

$T \approx 300\,\mathrm{K}$). Using Equation 1.2, the average kinetic energy of the neutrons is found to be $4.1 \times 10^{-21}\,\mathrm{J} \sim 26\,\mathrm{meV}$. This energy corresponds to a de Broglie wavelength of $\lambda = 1.8\,\text{Å}$. With $p = m_n v$, this gives a neutron speed of approximately $v \sim 2200\,\mathrm{m/s}$. These values demonstrate the physical correspondence that enables thermal neutrons to effectively probe both atomic-scale structures and dynamics of condensed matter.

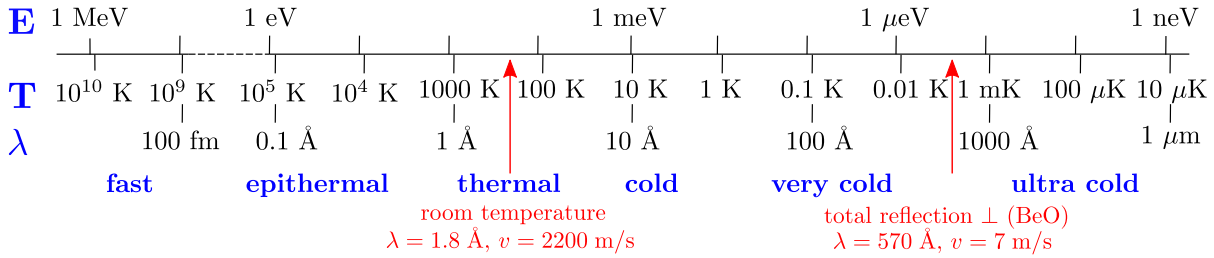

Figure 1.1.: A spectrum of neutron temperatures T, wavelengths λ and energies E and their common terminology. An explanation on how the neutron temperature is calculated is given in the text.

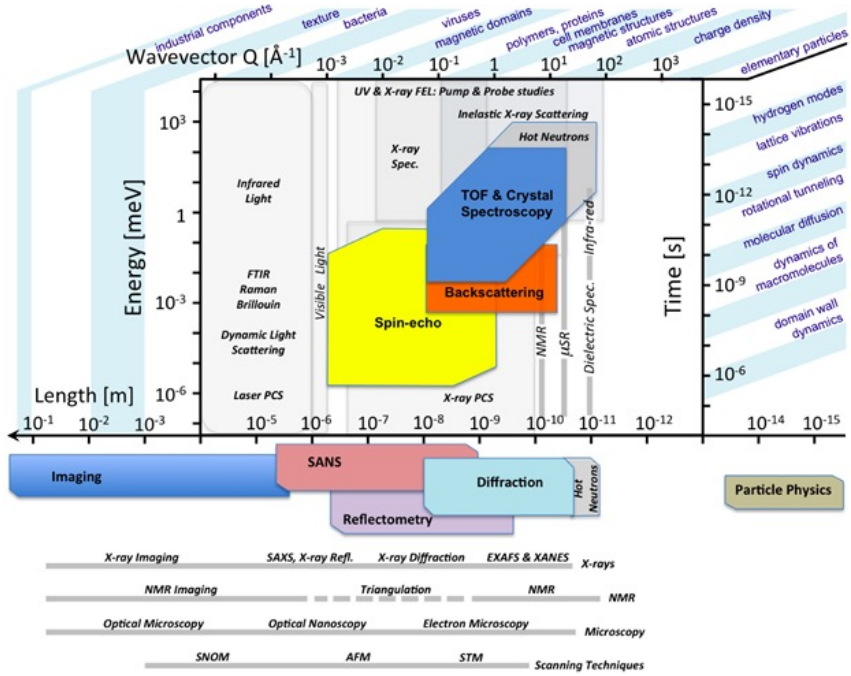

Figure 1.2.: Areas of wavevector q and energy E accessible through neutron scattering, qualitatively compared with other experimental probes. For comparison, the associated length and time scales are provided on the bottom and right axes, respectively. Neutron scattering techniques encompass the utilization of epithermal, thermal and cold wavelengths. Expanding the parameter space to larger structures and/or lower energies would require even slower, i.e. very cold neutrons. The blue annotations around the main figure delineate domains of scientific and technological relevance. The figure is taken from [10].

As a result, neutron scattering techniques can be applied across a wide range of length and time scales. Figure 1.2 illustrates this broad applicability, showing the associated regions of wavevector (q) and energy (E) where these techniques are used, alongside complementary experimental probes. These techniques are associated with the wide spectral ranges from hot neutrons with typical energies of 125 meV, through thermal neutrons of 25 meV, down to cold

neutrons with energies around 2 meV. One can see that the larger structures and smaller energy transfers require neutrons with small wavevectors (high wavelengths) and low energy, i.e. cold neutrons. However, the application of neutron scattering techniques to even larger structures or samples with smaller energy transfers, as found in biology or other large scale structures, necessitates intense sources of Very Cold Neutrons (VCN).

1.2. Scientific Motivation for Sources of Very Cold Neutrons

VCN cover a wide spectral range within the long-wavelength tail of cold neutron sources[3], with energies ranging from below 1 meV (9 Å) to few hundreds of neV (> several 100 Å), the domain of ultracold neutrons (UCN). In condensed matter physics, they could serve as a sensitive probe and could improve multiple neutron scattering techniques in terms of spatial resolution as e.g. for small angle neutron scattering (SANS), or energy resolution as e.g. in time of flight (TOF) or neutron spin echo (NSE) spectrometers [11]. Their main advantage in fundamental physics experiments is their very low energies. This causes them to exhibit long interaction times within the experimental apparatus. At the same time, unlike UCN, they can still be extracted as beams, making beam optics and related methods applicable. These experiments and neutron scattering applications will be discussed in the following section, a similar review is given by the author in [12].

1.2.1. Fundamental Physics Experiments

Following this line of reasoning, VCN allow an increase in the sensitivity of most fundamental physics experiments that employ beams of slow neutrons or that exploit the wave-optical properties of these beams. Moreover, they enhance the production of ultra-cold neutrons (UCN) in superfluid-helium converters.

Beam Experiments

Recently suggested particle physics experiments using beams of slow neutrons include:[4]

1. In-beam searches for a static neutron electric dipole moment (nEDM) [8, 13] [14, Section 5.3.1], and searches for new fundamental forces [15]. These kind of experiments profit linearly from the interaction time t of the neutron in the apparatus. Therefore, their figure of merit (FOM) can be considered proportional to λ.
2. Measuring the neutron lifetime τ_n by means of the *beam method*. Typically, these experiments contain a trapping region of some length L that intercepts a neutron beam. The neutron decay is observed by detecting decay protons within the volume of this region. In an experiment similar to [16], the mean number of neutrons in the decay region in cylindrical coordinates at any time is given by

$$N_n = \int_0^L \int_0^R \int_0^{2\pi} \int \frac{1}{v} r I(v, r, \theta, \ell) \, \mathrm{d}v \, \mathrm{d}\theta \, \mathrm{d}r \, \mathrm{d}\ell \, , \tag{1.4}$$

   with $I(v, r, \theta, \ell)$ being the velocity-dependent differential fluence rate[5] [16]. For a perfectly collimated beam and no attenuation within the length of the trap volume $L\, I(v, r, \theta, \ell)$

[3] The standard cold moderator materials for both spallation and fission sources are liquid or solid deuterium (LD_2, SD_2), liquid hydrogen (LH_2) and liquid or solid hydrocarbons, e.g. methane (CH_4).
[4] Note that this list is not exhaustive.
[5] The fluence rate is usually defined as the number of particles passing through a unit area per unit time.

would only be dependent on the neutron velocity and would reduce to $I(v)$, hence:

$$N_n = LA \int \frac{1}{v} I(v) \mathrm{d}v \ , \tag{1.5}$$

for a cylindrical decay region with the length L and a cross sectional area of $A = \pi R^2$. By increasing the VCN flux through such an experiment, the neutron density and hence the observed neutron decay rate increases, which in turn improves the statistical accuracy of the result. Similar to the nEDM experiments, there is an expected FOM$\propto\lambda$. It should be noted that these experiments still suffer from systematic uncertainty, associated with the determination of the absolute neutron flux. Further progress towards the reduction of this uncertainty, as pointed out in [17], could increase the precision of VCN beam lifetime experiments significantly and shed light on the neutron lifetime puzzle [18].

3. Experiments attempting to find neutron-antineutron oscillations [19, 20]. Here, it is not the interaction time, but the quasi-free flight time of VCN that allow to significantly increase the sensitivity of the experiment. Under these conditions, the probability for a transition can be expressed by:

$$P_{n\to\bar{n}} = \left(\frac{t}{\tau_{n\to\bar{n}}} \right)^2 \ , \tag{1.6}$$

with the free oscillation time $\tau_{n\to\bar{n}}$ [19]. This results in a FOM = $N_n t^2$, with N_n being the total number of neutrons observed. Due to the proportionality of the (FOM) to λ^2, VCN exhibit specific potential for neutron oscillation experiments.

One should note that in most experiments, under the assumption of equivalent phase-space density, the longer interaction or free flight times of VCN are in competition with their lower flux. It is therefore crucial, in order to truly increase the sensitivity of the experiments described above, to increase the phase space density of VCN in the source [14, 21].

Wave-Optical Experiments

Another class of experiments potentially benefiting from VCN exploit the wave-optical properties of the neutron, specifically in diffraction and interferometry. The potential of large wavelength neutrons for wave optics experiments was already suggested in the 1980s and early 1990s in the works of A.G. Klein, A. Zeilinger et. al. [22]. An extensive list of fundamental physics experiments exploiting means of neutron interferometry is given in [23]. Some of them profit from lower energy neutrons. Although certain proposed experiments have become less relevant because of advancements in other fields, wave-optical experiments involving VCN continue to be an exciting avenue for fundamental physics research.
A dedicated VCN source could, for example:

1. Contribute to the further investigation of gravitationally induced quantum interference as measured in the COW[6] experiment [24]. While this effect was already measured with VCN [25], the experiment could be significantly improved with higher fluxes, brightness and modern VCN optics.[7] With regard to the latter, the field of holographic gratings, as described in [26], has made especially significant progress over the past decade.
2. Improve the current limit on the neutron charge [7] with a Talbot-Lau interferometer [8].
3. Allow measurement of the gravitational constant G by means of an active gravitational mass other than the Earth itself, in a *Cavendish experiment*, as described in [27].

[6] Acronym for R. Colella, A. W. Overhauser, and S. A. Werner.
[7] It should be noted that VCN might not be competitive with the accuracy of atom interferometers, as pointed out in [23, p. 263f.].

Superfluid Helium Converters

As highlighted in [28], superfluid ^{4}He can be utilized as a converter in the production of UCN through a superthermal cooling process of CN or VCN. This is made possible by the crossing dispersion relations between superfluid ^{4}He and the free neutron, allowing neutrons with wavelengths of approximately 8.9 Å (equivalent to a kinetic energy of 1.0 meV) to be scattered down to the ultracold regime emitting a single phonon. An enhancement of the flux of neutrons with wavelengths around 8.9 Å would be a valuable asset for in-beam UCN sources exploiting this mechanism. This includes variants with in-situ UCN production and detection approaches, as proposed in [29].

1.2.2. Neutron Scattering Applications

The sensitivity of VCN as a probe for condensed matter research is determined by their accessible small momentum and energy transfers during scattering. This could make them highly effective for maximizing resolution in scattering techniques that study not only the structure but also the dynamics of condensed matter. Techniques such as small-angle neutron scattering (SANS), Time-of-Flight spectroscopy, and neutron spin-echo (NSE) are most likely to benefit from longer-wavelength neutrons [11]. Additionally, neutron imaging instruments operated with VCN spectra would benefit from enhanced contrast, as the neutron capture cross section scales with $1/v$. Figure 1.3 shows the scattering triangle in a generic SANS experiment. The k-vector

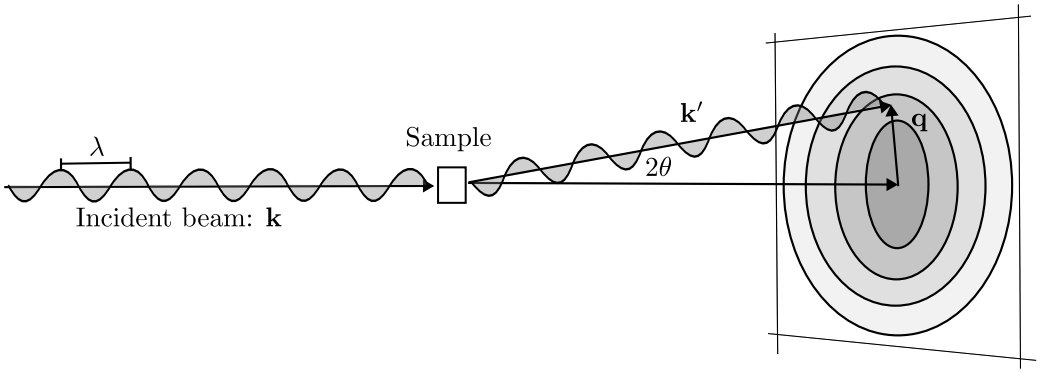

Figure 1.3.: Conceptual depiction of a Small Angle Neutron Scattering (SANS) instrument, including the scattering triangle, which illustrates the relation 1.7. Figure adapted from [30].

of the incident beam $\mathbf{k}$ has a modulus of $|\mathbf{k}| = 2\pi/\lambda$. In the typical case of elastic scattering in a SANS instrument the modulus of the $\mathbf{k}$-vector of the outgoing neutron does not change: $|\mathbf{k}| = |\mathbf{k}'|$. This results in the expression for the scattering vector $\mathbf{q} = \mathbf{k} - \mathbf{k}'$:

$$q = |\mathbf{q}| = \frac{4\pi \sin(\theta)}{\lambda} \,. \tag{1.7}$$

One can see from Equation 1.7, that longer wavelengths λ would allow for smaller $\mathbf{q}$-transfer under the same angle θ, which would result in larger length scales being accessible. Additionally, the same $\mathbf{q}$-transfer θ becomes larger, resulting in a higher resolution. Following [31] we can deepen this analysis: A typical SANS instrument is a long-baseline pinhole setup. The beam is usually collimated by two apertures. The first one at the sample position and the second one, having twice the diameter, at the same distance as the detector downstream of the sample position. The resolution of a SANS instrument can be related to the minimum accessible q value (q_{min}). For a pinhole setup, the radius of the beam spot at the detector is four times the radius

of the aperture at sample position (r_s), which results in:

$$q_{\min} = \frac{8\pi r_s}{\lambda_{\max} L_f} \ . \tag{1.8}$$

Here, L_f represents the final flight path, and λ_{max} denotes the maximum wavelength utilized in the instrument's operation. Similarly, we can define the maximum attainable value of q ($q_{\max}$) with the following equation:

$$q_{\max} = \frac{2\pi r_{\max}}{\lambda_{\min} L_f} \ , \tag{1.9}$$

where $r_{\max}$ represents the distance from the center of the scattering pattern to the farthest detector pixel, while $\lambda_{\min}$ corresponds to the minimum wavelength employed in the setup.

In terms of "neutron economics" or efficiency, F. Mezei points out, that a longer-wavelength beam requires less stringent beam collimation, for a comparable q-resolution [11]. Thus, larger wavelengths enable lower collimation and larger sample sizes in both dimensions across the beam while maintaining the same angular resolution. Similarly, the wavelength band at the sample ($\delta\lambda$) can be higher for an incoming VCN to achieve the same relative monochromaticity $\delta\lambda/\lambda$. This results in a gain of efficiency proportional to λ^5, matching the decay in flux of a Maxwellian spectrum. Hence, a long-wavelength tail that decays at a rate less than λ^{-5} will have corresponding performance gains (either in data rate or resolution, or a balanced gain in both). A comprehensive design study of potential SANS and imaging instruments for the lower ESS moderator is presented in [12, Section 8].

These simplified considerations do not encompass the drawbacks associated with the utilization of very long-wavelength neutrons. These include increased absorption and scattering probabilities, as well as the substantial influence of gravity on their trajectories. Increased absorption imposes more stringent demands on all materials employed within the neutron beam path, especially neutron beam windows in the source, sample, guides, cells, and surrounding environments. Combined with the increased scattering probability, it favors the use of thin samples to mitigate self-shielding due to absorption and multiple scattering. While the effects of gravity can theoretically be mitigated through instrumentation [12], they may introduce complexity and additional absorption concerns. Consequently, enhancing the performance and advancing the scientific capabilities of neutron scattering techniques with VCN require substantial improvements in flux.

The neutron community has recognized the possible benefits of a high-intensity VCN source for more than two decades. A dedicated workshop in 2005 [31] served as the first forum to explore potential sources and applications. The workshop laid out multiple material and design options for future VCN sources. Despite these proposed plans, the PF2 instrument at the Institute Laue-Langevin [32] remains the only VCN beamline available to the community to this day. A limited understanding of potential moderator materials and incomplete thermal scattering libraries (TSL) have hindered the practical design of new sources. This situation changed with the HighNESS project [33, 34, 35]. Alongside conducting a design study for a second moderator [12] at the European Spallation Source (ESS) [36], which includes neutron scattering instruments and the neutron-antineutron oscillation experiment (NNBAR) [19, 20], a key objective was to develop a comprehensive database of TSL for various promising materials. This includes the use of nanodiamonds as VCN reflectors [37, 38] and superfluid helium as a UCN converter [39, 40].

Within the framework of this project, the present thesis investigates deuterated clathrate hydrates as a novel moderator material, which could significantly enhance slow neutron fluxes at the European Spallation Source (ESS) and other future neutron sources. It focuses on the manufacturing, structure, and dynamics of these compounds, and how they can be exploited for neutron moderation and reflection. This research was conducted through an extensive neutron scattering campaign over the last three years, including neutron diffraction at D20, neutron

spectroscopy at IN5, Panther, and IN1-Lagrange, as well as transmission experiments at the fundamental physics beamlines at the Institut Laue-Langevin (ILL) and the Paul Scherrer Institute (PSI).

1.3. Outline and Contribution to the Field

The present thesis is structured as follows: Chapter 2 introduces the most pertinent theoretical concepts constituting this work. This includes concepts of neutron scattering length, double differential and total cross section, the dynamical structure factor, and neutron moderation and neutron conversion.

These concepts are key to understand why clathrate hydrates are a particularly promising moderator material for very cold neutrons, and what underlying neutron scattering mechanisms facilitate the slowdown of neutrons. This process is discussed in Chapter 3, along with a brief overview of previous proposals for neutron cool-down methods based on spin-dependent nuclear and magnetic scattering. The chapter gives a brief introduction into the interdisciplinary field of clathrate hydrates and introduces localized excitations of confined molecules and magnetic scattering of confined paramagnetic species.

The experimental results presented in this work are structured in three main parts, corresponding to the structure, dynamics and total neutron cross sections of clathrate hydrates. Chapter 4 introduces a novel and reliable manufacturing technique of a particular promising binary hydrate, hosting deuterated tetrahydrofuran (THF-d) and dioxygen (O_2) as guest molecules. Although this binary hydrate has been produced before, we present a different manufacturing method, which can not only easily be scaled up for producing large amounts of material, but is also effective in maximizing the yield of the desired hydrate. Chapter 4 presents the first test of this new method together with neutron diffraction data from the obtained samples, confirming the structure and providing an estimate of the cage occupancy. In addition, novel data on the thermal expansivity of the obtained material are presented.

Understanding the production and structure of the clathrate hydrate in question allowed us to proceed to study the dynamics of these compounds. Of particular interest are Einstein modes of the confined molecules (THF and O_2), as well as magnetic scattering of the intramolecular zero-field splitting of the triplet ground state of confined O_2, discussed in Section 3.3. These excitations were studied using the ILL's time-of-flight spectrometers IN5 and Panther. The vibrational spectrum was investigated at the instrument IN1-Lagrange. The results of these inelastic neutron scattering experiments, together with a description of the instruments, the applied corrections to the data and data reduction methods are presented in Chapter 5.

Besides the collective excitations characteristic to the cage structure of a CS-II hydrate (see Section 3.1), we identified rattling motion of the confined THF/THF-d molecule, which might be particularly effective for neutron slowdown. Furthermore we measured for the first time the magnetic down-scattering of confined O_2 in the binary clathrate hydrate. The experimental effort was accompanied by a computational study to develop a database of thermal scattering libraries of various hydrate compounds for design studies of future neutron sources. The results of these studies are given in [41, 42], with a focus on hydrates hosting THF and O_2. The vibrational spectrum measured at IN1-Lagrange confirmed molecular dynamics (MD) simulations and density functional theory (DFT) calculations conducted on these hydrates. The experimental work complemented by simulations allow for detailed descriptions of neutron interactions within these materials, enabling precise modeling of neutron transport and moderation processes.

Chapter 6 presents various experiments conducted to determine the total neutron cross section of fully deuterated clathrates in the cold and very cold neutron spectrum. Experimental data

on the total neutron cross section, σ_t, serve as a critical benchmark for validation of the novel thermal scattering libraries. It is also essential for determining the neutron transparency of the moderator with respect to down-scattered neutrons.

The measurement of σ_t shows that, while the Bragg scattering of CS-II hydrates is accurately described within our model, there appears to be a mesoscopic structure that gives rise to small-angle scattering. While this structure remains vague, we established a way to model this contribution in a hard-sphere [38] and an empirical Guinier model. Since there are no instruments dedicated for neutron cross section measurements, this chapter gives a more detailed description of the respective experimental setup, and explains the employed methods of data acquisition and reduction. This instructional description should allow future experimenters using these techniques to learn from our mistakes and adopt some of the key insights.

The final chapter 7, provides a comprehensive summary of this thesis. It examines the broader implications of the results and identifies potential directions for future research.

2. Theoretical Concepts

2.1. Neutron Interactions with Matter

As mentioned in Chapter 1 the neutron participates in all four fundamental interactions of nature. For studying condensed matter only the *strong nuclear force* and *electromagnetism* are relevant. While gravitational attractions are typically small enough to be neglected, the weak nuclear force is mainly significant insofar it causes *beta*-decay and limits the neutron lifetime (τ_n). The strong force only acts over a very short distance of the order of $10^{-15}\,\mathrm{m}$. The interaction between a free neutron and a nucleus strongly depends on the number of neutrons and protons in the nucleus and the combined spin of the system. The short range of the strong force allows neutrons to penetrate deeply into condensed matter [43].

The electromagnetic interaction arises on account of the neutron's intrinsic magnetic dipole moment (see Table 1.1). As a result, the neutron interacts with variations in the magnetic flux, enabling the study of magnetism through neutron scattering techniques. In this work, inelastic magnetic scattering is particularly important, as it enables neutron slowdown in a process that is discussed in detail in Section 3.3.

2.1.1. Scattering Kinematics

A generic scattering event of a neutron with initial wavevector $\mathbf{k}$ and energy E, scattered at an angle θ into a final state with wavevector $\mathbf{k}'$ and energy E' is depicted in Figure 2.1. The vector

$$\mathbf{q} = \mathbf{k} - \mathbf{k}' \tag{2.1}$$

is referred to as the *scattering vector*. Together with the vectors $\mathbf{k}$ and $\mathbf{k}'$, it forms the *scattering triangle*, depicted in Figure 2.1. From the de Broglie relation $p = \frac{h}{\lambda} = \hbar k$ it is apparent that $\hbar\mathbf{q}$ denotes the momentum transferred from the neutron to the sample, while

$$\hbar\omega = E - E' \tag{2.2}$$

is the transferred energy. The quantities $\mathbf{q}$ and ω, are usually referred to as *momentum transfer* and *energy transfer*. The constant $\hbar$ often gets omitted. This already allows an important distinction between neutron scattering events: When the initial energy matches the final $E = E'$ the scattering process is termed *elastic*, whereas if $E \neq E'$, it is said to be *inelastic*. Applying the cosine rule to the scattering triangle gives [43, Equation 1.16]:

$$q^2 = k^2 + k'^2 - 2kk'\cos(2\theta) = \frac{2m_n}{\hbar^2}\left(E + E' - 2\sqrt{EE'}\cos(2\theta)\right), \tag{2.3}$$

with $|\mathbf{k}| = k$, $|\mathbf{k}'| = k'$, $|\mathbf{q}| = q$ and the kinetic energy of a non-relativistic neutron $E = \frac{p^2}{2m_n} = \frac{\hbar^2 k^2}{2m_n}$. For elastic scattering the scattering triangle becomes isosceles ($|\mathbf{k}| = |\mathbf{k}'| = k$) and the above equation can be written as [43, Equation 1.17]:

$$q = 2k\sin(\theta) = \frac{4\pi}{\lambda}\sin(\theta)\,. \tag{2.4}$$

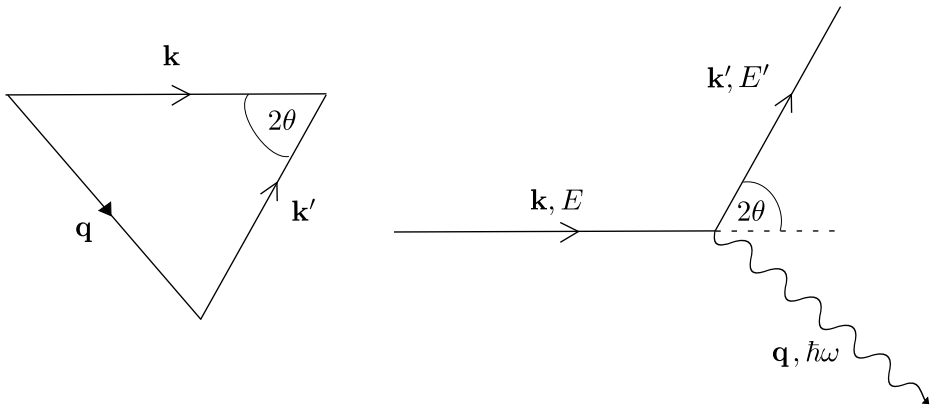

Figure 2.1.: Representation of a generic scattering event (right) and the corresponding scattering triangle (left). A neutron, initially characterized by the wavevector $\mathbf{k}$ and energy E, scatters through an angle 2θ to a final state represented by the wavevector $\mathbf{k}'$ and energy E'. The scattering vector $\mathbf{q}$, derived from the difference between the initial ($\mathbf{k}$) and final ($\mathbf{k}'$) wavevectors, completes the *scattering triangle* along with these wavevectors. Figure adapted from [43, Figure 1.10].

2.1.2. Cross Sections

The introduction of the neutron cross section and the mean free path allows for a first quantitative characterization of neutron reactions with matter. Consider a beam of neutrons with a flux density of Φ neutrons per unit of time and area passing through a layer of thickness dx, containing N identical atomic nuclei per cm^3.[1]

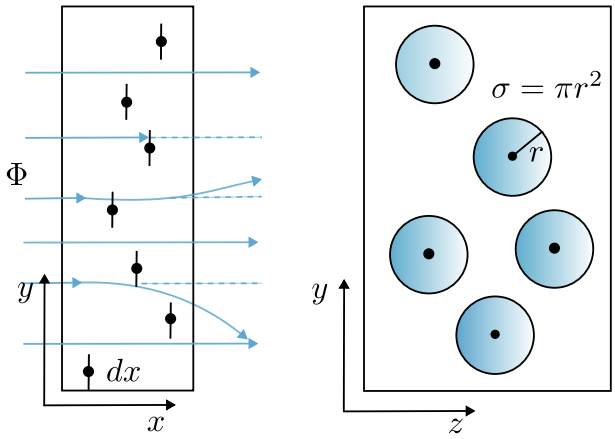

Figure 2.2.: A collimated neutron beam of the flux Φ penetrating a layer of thickness dx containing N identical atomic nuclei per cm^3 (left) and the illustration of the cross section σ (right). Figure adapted from [44, Figure 2.80].

Due to nuclear reaction of the neutrons with the atomic nuclei a part $d\Phi$ of the incident neutrons are scattered and deflected, while another part will be absorbed (see Figure 2.2). The *cross section* σ for the interaction of the neutron with the nucleus can now be defined as the area $\sigma = \pi r^2$ around the nucleus, through which the neutrons must pass to interact with the

[1] This introduction of the concept of the cross section and the resulting exponential reduction of the beam intensity (for photons called the *Beer-Lambert law*), can be found in most introductory physics text books. Consider e.g. [44, 2.8]. An introduction into the neutron cross section specifically is given in [45, 1.3.1].

nucleus. Along the distance dx the number Φ of neutrons changes due to interaction by

$$\frac{d\Phi}{dx} = -\Phi\sigma N \ . \tag{2.5}$$

Solving this equation exhibits the exponential reduction in beam intensity:

$$\Phi = \Phi_0 \exp\left(-N\sigma x\right) , \tag{2.6}$$

where Φ_0 is the initial neutron flux. The cross section has dimension cm^2, following from the quantities $N[\mathrm{cm}^{-3}]$ and $x[\mathrm{cm}]$. Since the typical values of σ are usually very small, the unit barn is used, where $1\,\mathrm{barn} = 10^{-24}\,\mathrm{cm}^2$. Scattering ($\sigma_s$) and absorption ($\sigma_a$) cross sections are separate entities. Each of these cross sections is further subdivided into various partial cross sections, comprising aspects like elastic and inelastic scattering, neutron capture, fission, and more. The sum of all of these partial cross sections is called the *total cross section*, thus [45, Equation 1.3.3]:

$$\sigma_t = \sigma_s + \sigma_a \ . \tag{2.7}$$

The cross section per cm^3, or the probability that the neutron interacts along a path of 1 cm is given by the *macroscopic cross section* [45, Equation 1.3.4]:

$$\Sigma_t = \sigma_t N \ , \tag{2.8}$$

where N is the number density, calculated as $N = \frac{\text{mass density}}{\text{atomic weight}} \times N_A$, with N_A representing Avogadro's number. For materials that contain molecules, with atoms of different cross sections Equation 2.6 becomes:

$$\Phi = \Phi_0 \exp\left(-N_{\mathrm{mol}} \sum_i \left(n_i\sigma_i\right) x\right) \ , \tag{2.9}$$

where $N_{mol} = \frac{\text{mass density}}{\text{atomic weight}} \cdot N_A$ and n_i is the number of atoms of type i with the cross section σ_i.

Another commonly used quantity is the *mean free path*, which is defined as the distance a neutron can travel on average before it interacts. This quantity is calculated by summing all possible distances, each weighted by its frequency of occurrence, and then dividing by the probability of a collision occurring after any given distance, thus [45, Equation 1.3.12]:

$$\Lambda = \int_0^\infty x \exp\left(-\Sigma_t x\right)\Sigma_t \mathrm{d}x = \frac{1}{\Sigma_t} \ . \tag{2.10}$$

The mean free path is equivalent to the inverse of the macroscopic cross section. Likewise to the cross section one can distinguish between the mean free path for scattering Λ_s and absorption Λ_a. Finally the *mean time between two collisions* can be defined as

$$\tau = \frac{\Lambda}{v} \ , \tag{2.11}$$

for a neutron travelling at a constant speed v. The total scattering cross section accounts for all scattered neutrons. Scattering experiments however are typically focused on the scattering occurring in a specific direction. The *differential scattering cross section* is defined as the number of neutrons scattered per second into the solid angle $\mathrm{d}\Omega$ about a given direction:

$$\frac{\mathrm{d}\sigma}{\mathrm{d}\Omega} = \frac{\#n}{\Phi_0 \, \mathrm{d}\Omega} \ . \tag{2.12}$$

Finally, the *double differential cross section* is defined as the number of neutrons $\#n$ scattered per second into the solid angle $\mathrm{d}\Omega$ about a given direction with a final energy between E' and $E' + \mathrm{d}E'$ [46]:

$$\frac{\mathrm{d}^2\sigma}{\mathrm{d}\Omega \mathrm{d}E'} = \frac{\#n}{\Phi_0 \, \mathrm{d}\Omega \, \mathrm{d}E'} \ . \tag{2.13}$$

2.1.3. Scattering from Nuclei

The scattering of neutrons from an isolated bound nucleus is discussed in [47], where an explicit derivation can be found. This section follows key aspects of this derivation to introduce the *scattering amplitude*, the *scattering length* and its relation to the cross section. Neglecting spin effects, the neutron wavefunction can be written as $\psi(\mathbf{r})$. The incident neutron is described by a plane wave, $\psi(\mathbf{r}) = \exp(i\mathbf{k} \cdot \mathbf{r})$, where $\mathbf{k}$ is the wavevector aligned with the neutron's motion. The scattering process is governed by the Schrödinger equation for the nuclear potential $V(\mathbf{r})$ [47, Equation 2.1]:[2]

$$\left[\nabla^2 + k^2 - \frac{2m}{\hbar^2} V(\mathbf{r})\right] \psi(\mathbf{r}) = 0. \tag{2.14}$$

At large distances ($r \to \infty$), where $V(\mathbf{r}) = 0$, the wavefunction becomes a superposition of the incident plane wave and a scattered spherical wave. The scattered wave introduces the scattering amplitude $f(\theta)$, which quantifies the angular distribution and magnitude of the scattering. For slow neutrons, where the range of the nuclear interaction ($\sim 1 \times 10^{-15}\,\mathrm{m}$) is much smaller than the neutron wavelength ($\sim 1\,\text{Å}$), the scattering is isotropic (s-wave scattering). In this case, the wavefunction simplifies to [47, Equation 2.3]:

$$\psi(\mathbf{r})\big|_{r>r_0} = \exp(\mathrm{i}\mathbf{k} \cdot \mathbf{r}) + f\frac{\exp(\mathrm{i}kr)}{r}. \tag{2.15}$$

Note that in this case f does not depend on θ. The scattering cross section σ_s can be expressed by the flux of scattered neutrons divided by the flux of incident neutrons. This results in:

$$\sigma_s = 4\pi|f|^2. \tag{2.16}$$

Similarly, the absorption cross section σ_a can be calculated by relating the incoming and outgoing neutrons, resulting in:

$$\sigma_a = \frac{4\pi}{k}\mathrm{Im}(f) - 4\pi|f|^2. \tag{2.17}$$

Consequently, the total cross section becomes:

$$\sigma_t = \sigma_s + \sigma_a = \frac{4\pi}{k}\mathrm{Im}(f). \tag{2.18}$$

An important result is that the scattering amplitude is inherently complex, with its imaginary component being directly proportional to the nucleus' total cross section.

When the neutron energy is sufficiently far from the nearest resonance, a relationship can be established between the real and imaginary parts of the scattering amplitude, resulting in an expression for the scattering length b. As a simple case, consider a nucleus without absorption such that $\sigma_t = \sigma_s$. In this scenario Equation 2.18 simplifies, for $E \to 0$, to:

$$\mathrm{Im}(f) = \frac{\sigma_s}{4\pi}k \to 0\,, \tag{2.19}$$

and the scattering amplitude becomes real. Looking at the s-component of the wave function ψ_0, or more specifically the function $u(r) = r\psi_0(r)$ in this limiting case[3], one finds that it will form a straight line. For $k \to 0$, this leads to [47, Equation 2.10]:

$$u\,(r)\big|_{r>r_0} = r + \lim_{k\to 0}(f)\,. \tag{2.20}$$

[2] A full treatment is given in the works of V.F. Turchin [47] and V.F. Sears [48].

[3] This is done because $u(r)$ follows a simpler differential equation than $\psi_0(r)$ (see [47, Equation 2.7 et seq.]).

We identify the point where this line intersects the horizontal axis (see Figure 2.3) as the *scattering length* [47, Equation 2.11] [4]:

$$b = \lim_{k \to 0}(f)\,. \tag{2.21}$$

It can be interpreted as the effective radius of a rigid sphere with radius r_0. In this model, $V(r) = 0$ for $r > r_0$ and $V(r) = \infty$ for $r < r_0$, preventing the neutron from entering the sphere. The wave function vanishes at $r = r_0$, and for $k \to 0$, this is the only point where $u(r) = 0$, making the scattering length $b = r_0$. Naturally, the interaction between a neutron and a nucleus is more complex than that with a simple "rigid sphere". For some isotopes, the scattering length can even take negative values. However, for most nuclei, it remains positive and is generally on the same order of magnitude as the nuclear radius [47].

Figures 2.4a and 2.4b display the bound coherent scattering lengths $\bar{b}$ of natural elements, as functions of atomic number and mass number, respectively. For the former, the scattering lengths are averaged over isotopes and weighted by natural abundances. A gradual increase in scattering lengths is observed for larger nuclei. Some outliers are labeled with their chemical symbols.

To account for negative scattering lengths, the simple 'rigid sphere' model must be extended. The neutron-nucleus interaction can be qualitatively described as a potential well with depth V_0 and radius r_0. For $V_0 \gg E_n$, the wave function $u(r)$ of an s-neutron inside the nucleus is given by [47]:

$$u(r) = C \cdot \sin(Kr)\ , \tag{2.22}$$

where $K = \sqrt{2MV_0/\hbar^2}$ represents the magnitude of the neutron wavevector inside the nucleus. By matching the wave function inside and outside the nucleus for $k \to 0$, which forms a straight line as described above, we find

$$b = r_0 - \frac{\tan(Kr_0)}{K}\ , \tag{2.23}$$

which gives a negative scattering length if,

$$\tan(Kr_0) > Kr_0\,. \tag{2.24}$$

In fact this semi-phenomenological approach describes not only the negative scattering lengths but also the variations that occur in the natural distributions of elements and isotopes (shown in Figure 2.4a and 2.4b). This has been shown explicitly by [49], with what the authors call a "random potential model". By varying K in Equation 2.23* between $[\frac{\pi}{2}, \frac{5\pi}{2}]$ one finds a distribution of the neutron scattering length b, that can be compared to the natural distribution. Figure 2.5 shows the comparison of the experimental case (blue histogram) as a function of $b' = b/A^{(1/3)}$, with the measured scattering length b and the mass number A. For the calculated ratios b/R to be on the same scale, it is assumed that $R = R_0 A^{(1/3)}$ with R_0 being a free parameter, which is found to be $R_0 = 1.4\,\mathrm{fm}$ [49]. Although this approach has some ambiguities, it is remarkable that a simple square well potential can qualitatively capture the natural distribution of neutron scattering lengths.

For the case in which neutrons can also be absorbed, the limit $\lim_{k\to 0}(f)$ is complex and as can be seen from Equation 2.18, σ_t and σ_a increase with $1/v$ for $k \to 0$. However, since for the considered (thermal) energy range $\mathrm{Im}(f) \ll |f|$†, the imaginary part of the scattering amplitude gets usually neglected and we can write the scattering amplitude as the negative scattering length:

$$\psi\left(\mathbf{r}\right)|_{r>r_0} = \exp\left(\mathrm{i}\mathbf{kr}\right) - b\ \frac{\exp\left(ikr\right)}{r}\ . \tag{2.25}$$

[4] The scattering length of a free nucleus is sometimes denoted by a, as e.g. in [47].

*The formulation in [49] is slightly different and the parameter is called α.

†Even for an absorber as strong as boron $\mathrm{Im}(f)/|f| \sim 0.04$ (see [47]).

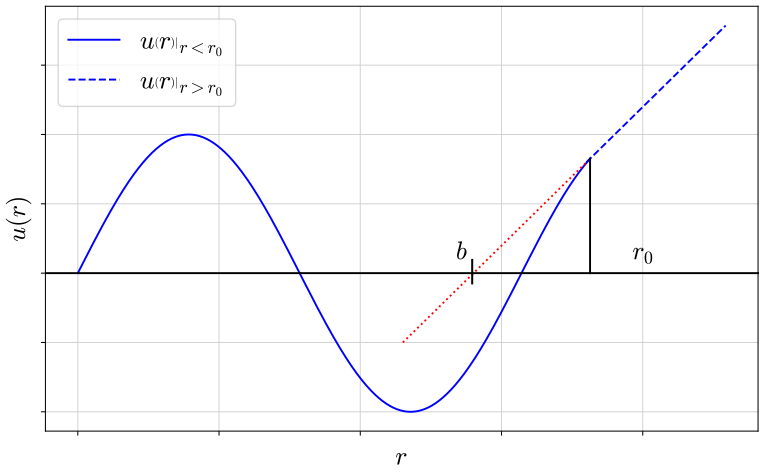

Figure 2.3.: The wave function $u(r)$ of a thermal neutron scattering from the potential well of a nucleus. Figure adapted from [47, Figure 2.1]

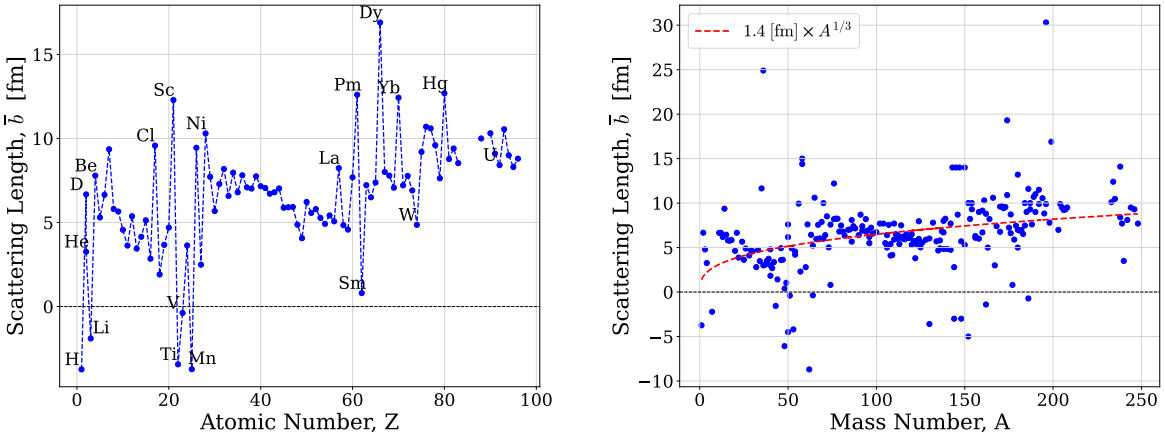

(a) The distribution of neutron scattering lengths as a function of the atomic number Z.

(b) The distribution of neutron scattering lengths as a function of the mass number A.

Figure 2.4.: The distribution of neutron scattering lengths for the natural elements and deuterium (D) (a) as well as for all stable isotopes (b). ring ring length follows roughly a trend of $\propto 1.4 \cdot A^{1/3}$. The original data is taken from [50], extracted via [51].

Note that the scattering length b does not depend on the neutron's energy and the scattering cross section becomes

$$\sigma_s = 4\pi b^2 \ . \tag{2.26}$$

Equation 2.25 implies that a positive b indicates a phase shift of π upon scattering from the nucleus.

2.1.4. The Dynamical Structure Factor

Thermal neutrons carry energies low enough so that no emission of secondary particles needs to be considered during simple scattering interactions. Therefore, the scattering of unpolarized

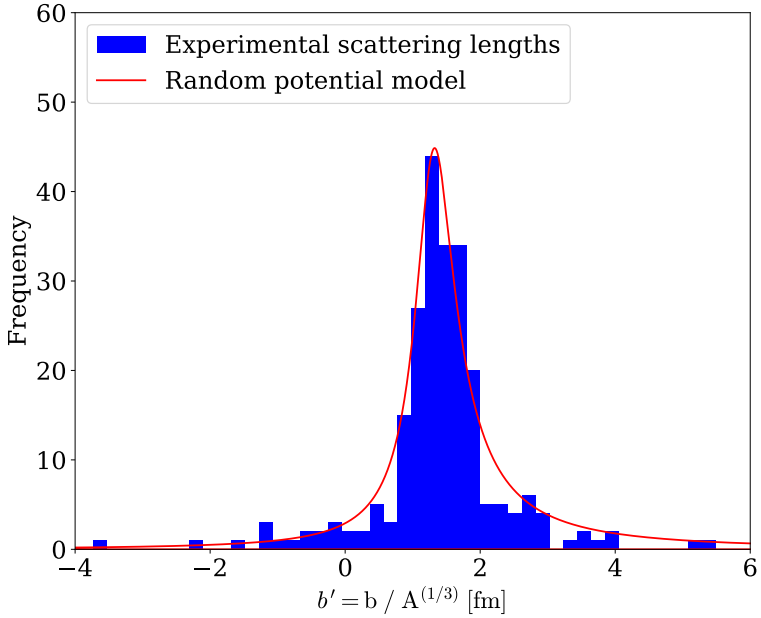

Figure 2.5.: The distribution of experimental scattering lengths of thermal neutrons (as reported in [50]) as a function of $b' = b/A^{(1/3)}$, compared to the random potential model developed in [49] (see text).

neutrons can be fully described by the double differential cross section, $\frac{\mathrm{d}^2\sigma}{\mathrm{d}\Omega \mathrm{d}E'}$, which describes the scattering of an incident neutron with wavevector $\mathbf{k}$ from a scattering system characterized by the index λ into a final wavevector $\mathbf{k}'$, leaving the scattering system in its final state λ'. Based on Fermi's golden rule, this differential cross section is related to quantum mechanical transition amplitudes, leading to what is referred to as the master equation of thermal neutron scattering. A comprehensive derivation of this equation is provided in the works of V.F. Turchin [47] and G.L. Squires [52]. It can be written as [52, Equation 2.15]:

$$\left(\frac{\mathrm{d}^2\sigma}{\mathrm{d}\Omega\,\mathrm{d}E}\right)_{\lambda\to\lambda'} = \frac{k'}{k}\left(\frac{m_n}{2\pi\hbar^2}\right)^2 \left|\langle \mathbf{k}'\lambda'|V|\mathbf{k}\lambda\rangle\right|^2 \delta(E_\lambda - E_{\lambda'} + E - E')\,. \tag{2.27}$$

The δ-function makes sure that the total energy in the process is conserved. Due to the short range of the neutron-nuclear interaction the potential V is effectively point like. For an ensemble of N nuclei, with $\mathbf{R}_j$ $(j = 1, ..., N)$ being the position vector of the jth nucleus, it takes the form of:

$$V(\mathbf{r}) = \frac{2\pi\hbar^2}{m}\sum_j^N b_j\,\delta(\mathbf{r} - \mathbf{R_j})\,. \tag{2.28}$$

Originally introduced by Enrico Fermi [53], this potential is commonly referred to as the *Fermi pseudopotential*. This allows Equation 2.27 to be brought into a form that omits the sum over all final states of the target system, replacing the potential with its Fourier transform (see [52, Section 2.3]). Conveniently, the Fourier transform of the Fermi pseudopotential yields a constant. With this the master equation for neutron scattering can be written as:

$$\frac{\mathrm{d}^2\sigma}{\mathrm{d}\Omega\,\mathrm{d}E'} = \frac{k'}{k}S(\mathbf{q},\omega)\,, \tag{2.29}$$

where $S(\mathbf{q},\omega)$ is the *dynamical structure factor* or the scattering function and is defined by

$$S(\mathbf{q},\omega) \equiv \frac{1}{2\pi\hbar}\sum_{j,j'=1}^{N} b_j b_{j'}, \int_{-\infty}^{\infty} \langle \exp\left(-\mathrm{i}\mathbf{q}\cdot\mathbf{R}_{j'}(0)\right)\exp\left(\mathrm{i}\mathbf{q}\cdot\mathbf{R}_j(t)\right)\rangle \cdot \exp\left(-\mathrm{i}\omega t\right)\mathrm{d}t\ . \tag{2.30}$$

We adapt the notation in [52, Equation 2.64] and write the expectation value in the integral of Equation 2.30 as:

$$\langle j', j\rangle \equiv \langle \exp\left(-\mathrm{i}\mathbf{q}\cdot\mathbf{R}_{j'}(0)\right)\exp\left(\mathrm{i}\mathbf{q}\cdot\mathbf{R}_j(t)\right)\rangle\ . \tag{2.31}$$

Leading to the shorter expression for the dynamical structure factor

$$S(\mathbf{q},\omega) \equiv \frac{1}{2\pi\hbar}\sum_{j,j'=1}^{N} b_j b_{j'} \int_{-\infty}^{\infty} dt\langle j', j\rangle \exp\left(-i\omega t\right). \tag{2.32}$$

2.1.5. Coherent and Incoherent Scattering

As shown above, the scattering length depends not only on the atomic species but also on the nucleus's mass number, and thus on the isotope (see Figure 2.4b). As a result, even the simplest scattering systems, consisting of a single element arranged in a lattice, will exhibit different scattering lengths at each site j, depending on the natural abundance of the element's isotopes and their respective nuclear spins. The value b_j can then appear with the relative frequency p_j, such that [52, Equation 2.60 et seq.]:

$$\sum_j p_j = 1\ . \tag{2.33}$$

The average value of b for the whole scattering system then results in

$$\overline{b} = \sum_j p_j b_j \tag{2.34}$$

and the average value of b^2 is

$$\overline{b^2} = \sum_j p_j {b_j}^2\ . \tag{2.35}$$

The distribution of isotopes is random and uncorrelated, so that the values of b_j at any two sites j depends only on p_j. Expanding on this idea, we posit that the scattering from a specific sample of a material closely approximates the scattering averaged across numerous samples that differ only in the isotopic arrangement (and the nuclear spin) among their sites. Consequently, this allows us to express Equation 2.29 as

$$\frac{\mathrm{d}^2\sigma}{\mathrm{d}\Omega\ \mathrm{d}E'} = \frac{k'}{k}\frac{1}{2\pi\hbar}\sum_{j,j'=1}^{N}\overline{b_{j'}b_j}\int\langle j', j\rangle \exp(-\mathrm{i}\omega t)\ \mathrm{d}t\ . \tag{2.36}$$

From the assumption of no correlation between different b_j of each site, follows [52, Equation 2.65]:

$$\overline{b_{j'}b_j} = (\overline{b})^2 \quad \text{for}\ \ j' \neq j \tag{2.37}$$

$$\overline{b_{j'}b_j} = \overline{b^2} \quad \text{for}\ \ j' = j \tag{2.38}$$

This allows to separate the dynamical structure factor $S(\mathbf{q},\omega)$ into two components, the *coherent* and the *incoherent* part [52, Equation 2.66 et seq.]:

$$S(\mathbf{q},\omega) = S_{\mathrm{coh}}(\mathbf{q},\omega) + S_{\mathrm{inc}}(\mathbf{q},\omega)\,, \tag{2.39}$$

with:

$$S_{\text{coh}}(\mathbf{q},\omega) \equiv \frac{1}{2\pi\hbar}(\bar{b})^2 \sum_{j,j'=1}^{N} \int_{-\infty}^{\infty} \langle j', j\rangle \exp\left(-\mathrm{i}\omega t\right) dt\,, \tag{2.40}$$

and:

$$S_{\text{inc}}(\mathbf{q},\omega) \equiv \frac{1}{2\pi\hbar}\left(\overline{b^2} - (\bar{b})^2\right) \sum_{j=1}^{N} \int_{-\infty}^{\infty} \langle j, j\rangle \exp\left(-\mathrm{i}\omega t\right) dt\,. \tag{2.41}$$

When comparing Equation 2.40 and Equation 2.41 one can see that the coherent scattering is dependent on the correlation between positions of *different* nuclei at different times. On the other hand the incoherent scattering depends on the correlation between the positions of the *same* nucleus at different times. This means that any variation in intensity with $\mathbf{q}$ due to *interference* comes from the coherent part of the scattering, while the incoherent part would produce a flat "background" (e.g. in a diffraction experiment). However, the inelastic incoherent scattering provides important information on the dynamics of the investigated material (see [43, Section 5.2.9]). It should be noted that the distribution of scattering lengths does not only depend on the isotopic distribution, but also on the spin orientation of the nuclei at different sites j. Coherent and incoherent scattering lengths or cross sections are defined and tabulated for each natural element [54]. For thermal neutrons, it can be shown that the sum of the incoherent and coherent scattering cross sections closely approximates the scattering cross section of an unbound nucleus, σ_{free}, the limit that the total scattering cross section approaches at short wavelengths [55].

2.1.6. The Harmonic Approximation

One key difficulty in evaluating the dynamical structure factor is solving the integral over states $\langle j', j\rangle$ in Equation 2.31. A common approach in crystalline solids is to decompose the nuclear position in terms of displacements $\mathbf{u}$ from equilibrium positions $\mathbf{d}$, so that:

$$\mathbf{R}_j(t) = \mathbf{d}_j + \mathbf{u}_j(t)\,. \tag{2.42}$$

In the *harmonic approximation*, the nuclei are modeled using potentials that are quadratic functions of their displacements. This is similar to the Einstein model of a crystal, where nuclei are drawn back to their equilibrium positions by spring-like forces, leading to harmonic vibrations. In this framework, it can be shown that [56, Equation N.16]:

$$\langle j, j'\rangle = \exp\left(-\mathrm{i}\mathbf{q}\cdot(\mathbf{d}_{j'} - \mathbf{d}_j)\right) \exp\left(-W_{j'}(\mathbf{q})\right) \exp\left(-W_j(\mathbf{q})\right) \exp\left(\langle(\mathbf{q}\cdot\mathbf{u}_{j'}(0))(\mathbf{q}\cdot\mathbf{u}_j(t))\rangle\right). \tag{2.43}$$

The term

$$W_j(\mathbf{q}) \equiv \frac{1}{2}\langle(\mathbf{q}\cdot\mathbf{u}_j(0))^2\rangle \tag{2.44}$$

is called the *Debye–Waller factor*, which is a measure of the time independent average squared displacement of nuclei j along $\mathbf{q}$ [52]. The time dependence in Equation 2.43 is solely present in the final exponential term, which accounts for nuclear motion. This term can be expanded using a Taylor series [57, Equation 20]:

$$\exp\left(\langle(\mathbf{q}\cdot\mathbf{u}_{j'}(0))(\mathbf{q}\cdot\mathbf{u}_j(t))\rangle\right) = \sum_{n=0}^{\infty} \frac{1}{n!}\left(\langle(\mathbf{q}\cdot\mathbf{u}_{j'}(0))(\mathbf{q}\cdot\mathbf{u}_j(t))\rangle\right)^n \tag{2.45}$$

Note, that the expectation value $\langle(\mathbf{q}\cdot\mathbf{u}_{j'}(0))(\mathbf{q}\cdot\mathbf{u}_j(t))\rangle$ correlates linear displacements of two nuclei at two different times along $\mathbf{q}$. This is directly related to an interaction in which a neutron exchanges energy and momentum with a phonon state.

2.1.7. Elastic Scattering

The first term in the expansion of Equation 2.45 when plugged into the expression for the dynamical structure factor $S(\mathbf{q},\omega)$ in Equation 2.41 or Equation 2.40, gives rise to *elastic scattering*. The expression for elastic incoherent scattering turns out to be [43, Equation 5.49]:

$$\left(\frac{\mathrm{d}\sigma}{\mathrm{d}\Omega}\right)_{\mathrm{inc}}^{\mathrm{el}} = N\sum_j \frac{(\sigma_{\mathrm{inc}})_j}{4\pi}\exp(-2W_j)\,. \tag{2.46}$$

For the expression for coherent elastic scattering one obtains [43, Equation 5.48]:

$$\left(\frac{\mathrm{d}\sigma}{\mathrm{d}\Omega}\right)_{\mathrm{coh}}^{\mathrm{el}} = N\left(\frac{2\pi}{v_0}\right)^3 \sum_{\mathbf{G}} |F_N(\mathbf{G})|^2 \delta(\mathbf{q}-\mathbf{G}), \tag{2.47}$$

In this equation $F_{\mathrm{N}}(\mathbf{G})$ is the structure factor (including the Debye-Waller factor). The normalization factor $N\frac{(2\pi)^3}{v_0}$ contains the volume of the primitive unit cell v_0 and the number of lattice points N. The Laue condition occurring in the argument of the delta function is fulfilled when the transferred wavevector $\mathbf{q}$ is equal to a reciprocal lattice vector $\mathbf{G}$. Mathematically, this is equivalent to Bragg's law:[5]

$$n\lambda = 2d_{hkl}\sin(\theta)\,, \tag{2.48}$$

where n is the diffraction order, λ the neutron wavelength, d_{hkl} the lattice spacing between neighbouring hkl- planes and 2θ the diffraction angle. We will use Equation 2.47 to determine the atomic positions within the hydrate's unit cell in the analysis of neutron diffraction data collected at D20, as discussed in Chapter 4.

2.1.8. Inelastic Scattering in the Incoherent Approximation

The terms with $n \geqslant 1$ in the expansion of Equation 2.45 represent inelastic scattering events where the incoming neutron exchanges energy and momentum with an n-phonon state. Evaluating these terms can be highly complex, often necessitating the use of approximations to make the problem solvable. A major focus of this work is the study of localized excitations in hydrate compounds, which can be exploited for neutron slowdown. In neutron scattering experiments these excitations are reflected in incoherent, inelastic scattering. The one-phonon incoherent cross section of a poly-crystalline sample can be expressed as [43, Equation 5.96]:

$$\left(\frac{\mathrm{d}^2\sigma}{\mathrm{d}\Omega\mathrm{d}E'}\right)_{\mathrm{inc}}^{1\,ph} \approx \frac{k'}{k}\sum_j \frac{(\sigma_{\mathrm{inc}})_j}{4\pi}\frac{q^2}{3m_j}\exp(-2W_j)\frac{g_j(\omega)}{2\omega}\left[n(\omega)+1\right]\,, \tag{2.49}$$

The summation is over all distinct atomic species j in the primitive unit cell. The term $\frac{(\sigma_{\mathrm{inc}})_j}{4\pi}$ represents the incoherent scattering cross section for atomic species j, normalized by 4π, and quantifies the scattering contribution from each species. The factor $\frac{q^2}{3m_j}$ arises from summing over the contributions of all phonon modes and their associated polarization vectors (see [43, Section 5.2.9] for details). The Debye-Waller factor for species j contributes as $\exp(-2W_j)$. The partial vibrational or phonon density of states (DOS) $\frac{g_j(\omega)}{2\omega}$ contains the crucial dynamical information of the sample. The factor $\frac{1}{2\omega}$ normalizes this with respect to the phonon energy, ensuring that the overall scattering intensity scales correctly with the available phonon modes. Finally, the Bose-Einstein factor $[n(\omega)+1]$ accounts for the distribution function $n(\omega)$, which represents the average number of phonons at frequency ω at thermal equilibrium:

$$n(\omega) = \frac{1}{\exp(\hbar\omega/k_{\mathrm{B}}T)-1}\,, \tag{2.50}$$

[5] This is shown in [43, 47, 52]

where k_B is the Boltzmann constant. The function $g_j(\omega)$ represents the *partial vibrational density of states*, quantifying the contribution of atom j's motion to the overall density of states.

Unlike the inelastic coherent cross section (not discussed here), the one-phonon incoherent scattering cross section (Equation 2.49), has no distinct features in $\mathbf{q}$. The scattering intensity for a given energy varies continuously with $\mathbf{q}$ with a weak $\mathbf{q}$ dependence primarily governed by the Debye–Waller factor [43]. These "dispersion-free" excitations are particularly effective for cooling neutrons to very cold temperatures, as down-scattering remains efficient even for neutrons with low $\mathbf{q}$ vectors. This enables neutron cooling through successive down-scattering events, referred to as a "cooling cascade" [58] (see Section 3.3).

Separating coherent from incoherent inelastic scattering signals in an experiment can be challenging. A practical approach to minimize the contribution from inelastic coherent scattering is to conduct measurements at high momentum transfers ($q \gg \frac{2\pi}{d}$), where d represents the nearest-neighbour distance. At such large q values, interatomic interference effects become negligible, allowing the scattering from individual atoms to be considered independently. This is the case, for example, at the instrument IN1-Lagrange, where additionally the specific energy analysis gives a q-integrated signal (see Section 5.1). Generally, at large q, the nuclear scattering can be described by the incoherent scattering formula, whereby substituting $\sigma_{\mathrm{inc},j}$ with the total scattering cross section $\sigma_j = \sigma_{\mathrm{coh},j} + \sigma_{\mathrm{inc},j}$, an approach referred to as the *incoherent approximation* [43].

The incoherent approximation is particularly useful for analyzing one-phonon scattering at large q in polycrystalline samples. However, it is also valid, at low q when the incoherent scattering is dominant. It provides a straight forward way to compute the Generalized Density of States (GDOS), $G(\omega)$, from the dynamical structure factor. The GDOS represents an average of the partial densities of states $g_j(\omega)$, which appear in Equation 2.49. Each species contributes according to its incoherent scattering cross section, weight and thermal motion [43, Equation 5.98]:

$$G(\omega) = \sum_j \frac{\sigma_j}{4\pi} \frac{1}{m_j} \exp(-2W_j)\, g_j(\omega)\,. \tag{2.51}$$

This quantity can be computed, for example, using Molecular Dynamics (MD) simulations and compared with inelastic neutron scattering data, via the relation [43, Equation 5.99]:

$$G(\omega) \propto \frac{\omega}{q^2} \frac{1}{n(\omega)+1} \frac{k}{k'} \left(\frac{\mathrm{d}^2\sigma}{\mathrm{d}\Omega \mathrm{d}E'} \right)^{1\ \mathrm{ph}}. \tag{2.52}$$

Since the single-atom total scattering cross sections (σ_j) serve as weighting factors in the definition of $G(\omega)$, the partial vibrational DOS for each atomic species can be approximated by performing a series of measurements on samples with varying isotopic compositions. This process of *isotopic substitution* or *contrast variation* was realized on the inelastic scattering experiments of multiple hydrate compounds as discussed in Chapter 5.

2.2. Neutron Moderation

The process of neutrons slowdown via multiple inelastic collisions in a cold (or thermal) medium is called *moderation*. The medium in which the collisions, hence deceleration, takes place is called the *moderator*. When fast neutrons interact with the nuclei of a scattering medium, the loss of energy occurs with the diffusion in the medium. When the neutron's energy exceeds approximately 1 eV, the atoms it collides with are effectively free and stationary before the interaction takes place [45]. For lower energies the chemical binding and their thermal motion have to be taken into account. A good moderator reduces the speed of neutrons after a small number

of collisions and has a low absorption cross section. This section introduces basic definitions of neutron fields and neutron transport and presents important results of the theory of neutron moderation.[6] The objective of this theory is to determine the spatial and spectral distribution of the neutron flux resulting from a specified distribution of sources, or more technically, from a given source and moderator configuration.

As a starting point we consider a volume element $\mathrm{d}V = \mathrm{d}x\,\mathrm{d}y\,\mathrm{d}z$ in the moderator medium with the position vector $\mathbf{r}$. Let $n(\mathbf{r}, \mathbf{\Omega}, E)\,\mathrm{d}V\,\mathrm{d}\Omega\,\mathrm{d}E$ be the number of neutrons within a volume $\mathrm{d}V$, with kinetic energies in the range $[E, E+\mathrm{d}E]$, and within a differential solid angle $\mathrm{d}\Omega$ around the unit vector $\mathbf{\Omega}$ in flight direction. Thus, $n(\mathbf{r}, \mathbf{\Omega}, E)$ in units of $\mathrm{cm}^{-3}\,\mathrm{sr}^{-1}\,\mathrm{eV}^{-1}$ describes the neutron density per cubic centimeter, per energy interval, and per flight direction. This *differential* is not necessarily stationary, but can also depend on the time t. By integration over the whole energy spectrum one obtains the total number of neutrons per volume element with a given flight direction [45, Equation 5.1.1 et seq.]:

$$n(\mathbf{r}, \mathbf{\Omega})\mathrm{d}V\mathrm{d}\Omega = \int_0^\infty n(\mathbf{r}, \mathbf{\Omega}, E)\mathrm{d}V\,\mathrm{d}\Omega\mathrm{d}E\ . \tag{2.53}$$

The quantity $n(\mathbf{r}, \mathbf{\Omega})$ is usually referred to as the *vector density*. By integration over all flight direction, one obtains $n(\mathbf{r})$ the total number of neutrons in the volume element $\mathrm{d}V$ at the point $\mathbf{r}$. The *differential neutron flux* is defined by

$$F(\mathbf{r}, \mathbf{\Omega}, E)\mathrm{d}\Omega\mathrm{d}E = n(\mathbf{r}, \mathbf{\Omega}, E)v\mathrm{d}\Omega\mathrm{d}E\ , \tag{2.54}$$

where $v = \sqrt{\frac{2E}{m_n}}$ is the neutron speed. The *differential neutron flux* is the number of neutrons at the point $\mathbf{r}$ in a given energy interval, with given flight directions in the differential solid angle $\mathrm{d}\Omega$ around $\mathbf{\Omega}$, that penetrate a unit surface area perpendicular to the direction $\mathbf{\Omega}$ per unit time [45]. Integrating the differential flux $F(\mathbf{r}, \mathbf{\Omega}, E)$, in units of $\mathrm{cm}^{-2}\mathrm{s}^{-1}\mathrm{sr}^{-1}\mathrm{eV}^{-1}$, over energy yields the *vector flux* $F(\mathbf{r}, \mathbf{\Omega})$. Finally, integrating over the solid angle:

$$\Phi(\mathbf{r}) = \int_{S^2} F(\mathbf{r}, \mathbf{\Omega})\mathrm{d}\Omega = n(\mathbf{r})\overline{v}\,, \tag{2.55}$$

yields the *flux* or *scalar flux* of neutrons, where $\overline{v}$ represents the average speed of polyenergetic neutron field. Here, S^2 denotes the surface of the unit sphere, representing all possible directions. In reactor and neutron physics the flux $\Phi(\mathbf{r})$ in $\mathrm{cm}^{-2}\mathrm{s}^{-1}$ is a widely used quantity. In contrast to fluxes encountered in other physical theories like electro- or thermodynamics the neutron flux is not a *vector*, but a *scalar* quantity. The physical significance of the neutron flux can be elaborated on a simple example, as described in [45, Section 5.1.1]:

Consider a circular disc of area $1\,\mathrm{cm}^2$ ($\pi R^2 = 1\,\mathrm{cm}^2$) anchored at $\mathbf{r}$ (see Figure 2.6). The quantity $F(\mathbf{r}, \mathbf{\Omega})\,\mathrm{d}\Omega$ represents the number of neutrons passing through the disc per second within a solid angle element $\mathrm{d}\Omega$ around its normal direction $\mathbf{\Omega}$. To compute the neutron flux, imagine the disc rotating in all directions while keeping its center fixed at $\mathbf{r}$. As it does so, it traces out a sphere of radius R with a cross sectional area of $1\,\mathrm{cm}^2$ and a total surface area of $4\,\mathrm{cm}^2$. The flux Φ quantifies the number of neutrons crossing this sphere per second. In an isotropic neutron field, where all directions are equally probable, 2Φ neutrons cross the $4\,\mathrm{cm}^2$ surface per second, each crossing once inward and once outward. Thus, $\Phi/2$ neutrons traverse $1\,\mathrm{cm}^2$ per second.

These definitions allow to characterize the behaviour of a neutron field in space and time, by finding a balance of $n(\mathbf{r}, \mathbf{\Omega}, E)\mathrm{d}V\mathrm{d}\Omega dE$ that takes into account [45, Section 5.1.2]:

1. The leakage out of the volume element $\mathrm{d}V$

[6] This follows [45], [59] and [60].

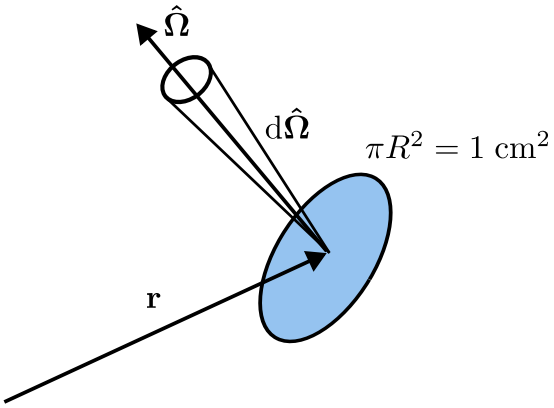

Figure 2.6.: Illustration for the definition of the *vector flux* and *flux*. Figure adapted from [45].

2. The loss due to absorption or scattering into other directions
3. Gains due to neutrons scattering from other directions or energy intervals
4. The production of neutrons by sources in the volume element $\mathrm{d}V$ (with a source density of $S(\mathbf{r}, \mathbf{\Omega}, E)$)

The equation that gives such a *neutron balance* is called *transport equation*. A simple version of that equation can be set up for the moderation of neutrons in an infinite medium with uniformly distributed sources [45, Equation 5.1.16]:

$$(\Sigma_a + \Sigma_s)\Phi(E) = \int_0^\infty \Sigma_s(E' \to E)\Phi(E')\mathrm{d}E' + S(E)\ . \tag{2.56}$$

The left hand side represents the neutrons lost per $\mathrm{cm}^{-3}\mathrm{s}^{-1}$ by absorption and scattering. The right hand side results in the number of neutrons gained from the sources ($S(E)$) or by in-scattering from energies outside the E-interval. To evaluate the term $\Sigma_s(E' \to E)$, the dynamics of particle collisions should be considered.

2.2.1. Average Energy Loss

A derivation of the neutron slowdown due to elastic collisions with the nuclei of a moderating medium is given in [60, Section 1.6]. By analyzing the neutron's average energy after a collision in the center-of-mass frame, they derive an expression for the average energy loss [60, Equation 1.23]:

$$\overline{\Delta E} = \overline{E - E'} = E\frac{1-\alpha}{2}\ , \tag{2.57}$$

where E and E' are the kinetic energies of the neutron before and after the collision respectively, α is an auxiliary quantity $\alpha \equiv \frac{(A-1)^2}{(A+1)^2}$, with A representing the mass number of the moderating material. Another quantity commonly used in reactor physics is the average *logarithmic energy loss* or *lethargy gain* ξ, which is given by [61]:

$$\xi = \ln E - \overline{\ln E'} = \int_{\alpha E_1}^{E_1} \ln\frac{E}{E'}\frac{1}{(1-\alpha)E}dE' = 1 + \frac{\alpha}{1-\alpha}\ln\alpha\ . \tag{2.58}$$

This is an energy-independent constant and characterizes the moderating capability of a nuclide with a given mass number. It allows to estimate the average number of collisions n necessary to moderate a neutron of an initial energy E to the energy E' [61]:

$$n\xi = \ln\frac{E}{E'}\ ; n = \frac{\ln E/E'}{\xi} \tag{2.59}$$

The parameter ξ decreases with the nuclide mass. Consequently, the higher the nuclide mass A, the greater the number of collisions required to slow down a fast neutron. The moderating efficiency of a nuclide (or molecule) should also hinge on the likelihood that a collision will lead to a scattering reaction rather than a capture reaction, which would effectively eliminate the neutron. This makes it convenient to multiply ξ with the ratio of the macroscopic scattering and absorption cross section. The resulting quantity $\xi\Sigma_s/\Sigma_a$, is called the *moderating ratio* and is a measure of the effectiveness of a moderator material [60]. Typical moderator materials are listed in Table 2.1. The importance of considering not only the logarithmic energy loss ξ, but also the moderating ratio $\xi\Sigma_s/\Sigma_a$ can be illustrated by comparing light water H_2O and heavy water D_2O. Despite the fact that neutrons are moderated more rapidly in light water driven by its elevated ξ value, the substantial absorption cross section (Σ_a) of hydrogen nuclides counteracts this advantage, resulting in a moderating ratio nearly 80 times lower compared to heavy water. Heavy nuclides with high absorption cross sections, e.g. ^{238}U, show diminishing moderation ratios, underlining the indispensable role of moderators in preserving a controlled nuclear chain reaction.

Table 2.1.: Moderation parameters for various materials. The number of collisions are calculated for a moderation of a neutron from 2 MeV to 1 eV by Equation 2.59. The data is extracted from [60, Table 1.4].

Substance	A	α	ξ	Number of Collisions $2\,\text{MeV} \rightarrow 1\,\text{eV}$	$\xi\Sigma_s/\Sigma_a$
H	1	0	1	14	-
D	2	0.111	0.725	20	-
H_2O	18	0.801	0.92	16	71
D_2O	22	0.834	0.509	29	5670
He	4	0.36	0.425	43	83
C	12	0.716	0.158	91	192
^{238}U	238	0.983	0.008	1730	0.0092

2.3. Thermalization of Neutrons

The treatment of the slowing down process up to this point only considers elastic collisions of high-energy neutrons from quasi stationary nuclides. These equations hold for neutrons of high energies outside of the resonance region.[7] They can be applied to calculate an energy dependent neutron density within a given source and moderator configuration up to energies of several eV. Below these energies, interactions between neutrons and matter cannot be treated like elastic collisions anymore. Instead, one has to take into account the complex nature of the neutron scattering process as well as the thermal motion of the nuclei. Since the energy of thermal neutrons is comparable to the binding energies of atoms in molecular and crystalline materials the neutron will interact with an ensemble of atoms rather than a single nucleus. Moreover, given that the wavelength falls within the range of interatomic distances, the neutron's wave function experiences coherent interference phenomena, such as diffraction. While these properties allow to study condensed matter with the means of neutron scattering, as discussed above, it makes the evaluation of the neutron transport equation and thus the determination of thermal neutron spectra and distributions rather involved and the subject of numerical simulations. These simulations require detailed input on the scattering behaviour of the moderation material, usually

[7] The resonance region is beyond the scope of this thesis. For a treatment of resonance absorption in infinite and finite media the reader is referred to [45], [59] and [60].

referred to as *scattering kernel*. This section aims to characterize general features of thermal neutron spectra and to outline the numerical computation of the thermalization process.

2.3.1. General Features of Thermal Neutron Spectra

Even though the cross section for thermal neutron scattering can be very complicated, there are general features in its behavior, with important implications for the neutron thermalization as discussed in detail in [59]. Consider again the situation of Equation 2.56, with uniformly distributed neutron sources throughout an infinite medium, allowing to ignore spatial and time dependence. Using the property of the energy dependent neutron scattering cross section $\Sigma_s(E) = \int_0^\infty dE'\Sigma_s(E \to E')$, one finds the balance relation [59, Equation 9-3]:

$$\int_0^\infty dE\Sigma_a(E)\Phi(E) = \int_0^\infty dES(E) \; . \tag{2.60}$$

Thus, in order to have a steady-state flux $\Phi(E)$ in an infinite medium, the rate at which sources appear needs to be equal to the rate at which neutrons are absorbed, as there is no leakage. In this thermalization scenario, all source neutrons start at high energies and slow down into the thermal range. Assuming no upscattering above a thermal cutoff energy E_c, the rate of neutron absorption will match the rate at which neutrons are moderated into the thermal range.

Another important property of the differential scattering cross section is the *principle of detailed balance*, which must be satisfied by any neutron scattering event from a system of nuclei in thermal equilibrium. It states that the neutron cross section for a transition from E to E' is related to the cross section for the reverse transition (E' to E) by a factor determined by the Maxwell-Boltzmann distribution $M(E)$ [62], which describes the energy distribution of particles in thermal equilibrium at a temperature T:

$$M(E) \equiv \frac{2\pi}{(\pi k_B T)^{3/2}}\sqrt{E}\exp\left(-\frac{E}{kT}\right) \; . \tag{2.61}$$

This has important consequences for the energy spectrum of neutrons within a moderator. If we consider a special case of Equation 2.56 in which we disregard the absorption within the medium and use the principle of detailed balance, we can write [59, Equation 9-8]:

$$\Sigma_s(E)\Phi_M(E) = \int_0^\infty dE'\Sigma_s(E' \to E)v'n_0M(E') = \int_0^\infty dE'\Sigma_s(E \to E')vn_0M(E) \; , \tag{2.62}$$

where $\Phi_M(E)$ is the neutron flux characterizing neutrons in thermal equilibrium at the temperature of the scattering medium:

$$\Phi_M(E) \equiv vn_0M(E) = \frac{2\pi En_0}{(\pi k_B T)^{3/2}}\sqrt{\left(\frac{2}{m}\right)}\exp\left(-\frac{E}{k_BT}\right) \; , \tag{2.63}$$

where n_0 is the neutron density in the medium. The principle of detailed balance ensures that the equilibrium spectrum of neutrons will follow a Maxwell-Boltzmann distribution, characterized by the moderator temperature T. Similar to the behavior of a highly dilute gas, the neutrons will gradually attain thermal equilibrium with the moderator material, through which they are diffusing. Such a distribution is depicted in Figure 2.7 for different moderator temperatures T.

The properties of the Maxwell-Boltzmann distribution function give the most probable neutron energy (E_T) and speed (v_T) given the temperature T of the system [59, Equation 9-10]:

$$E_T = k_BT \tag{2.64}$$

$$v_T = \sqrt{\frac{2k_BT}{m}} \; . \tag{2.65}$$

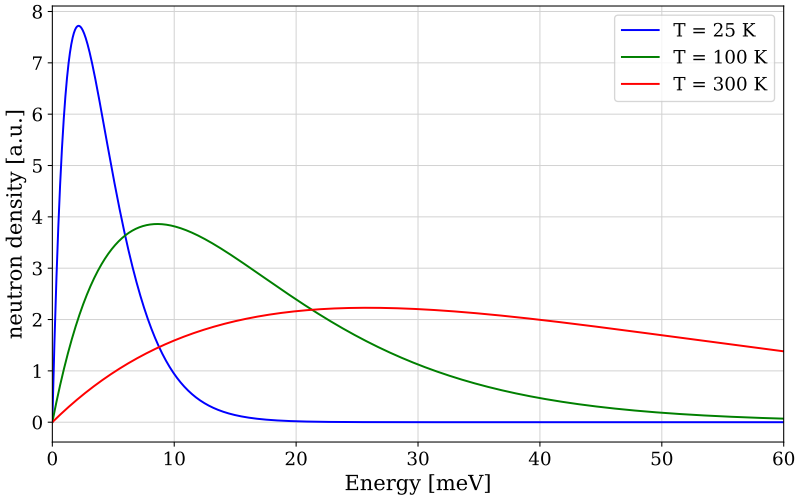

Figure 2.7.: The neutron density as a function of energy E is shown for a neutron field in thermal equilibrium with a moderator at temperatures of 25 K (typical for a cold source), 100 K, and 300 K (typical for a thermal source). The resulting spectra are Maxwell-Boltzmann distributions which are plotted as a function of energy in meV.

For a moderator at room temperature ($T = 293\,\mathrm{K}$), this gives the typical values for thermal neutrons $E_T = 25\,\mathrm{meV}$ and $v_T = 2.2 \times 10^3\,\mathrm{ms}^{-1}$.

This treatment remains valid only in scenarios free of factors that introduce non-equilibrium characteristics. Factors such as neutron absorption, leakage, or time dependence of the system can perturb the Maxwellian neutron distribution, causing deviations from thermal equilibrium. Figure 2.8 introduces two qualitative features of such spectra, namely "absorption heating" and "diffusion cooling" [59, Section 9.I.B]. If an absorption term gets introduced one will find that

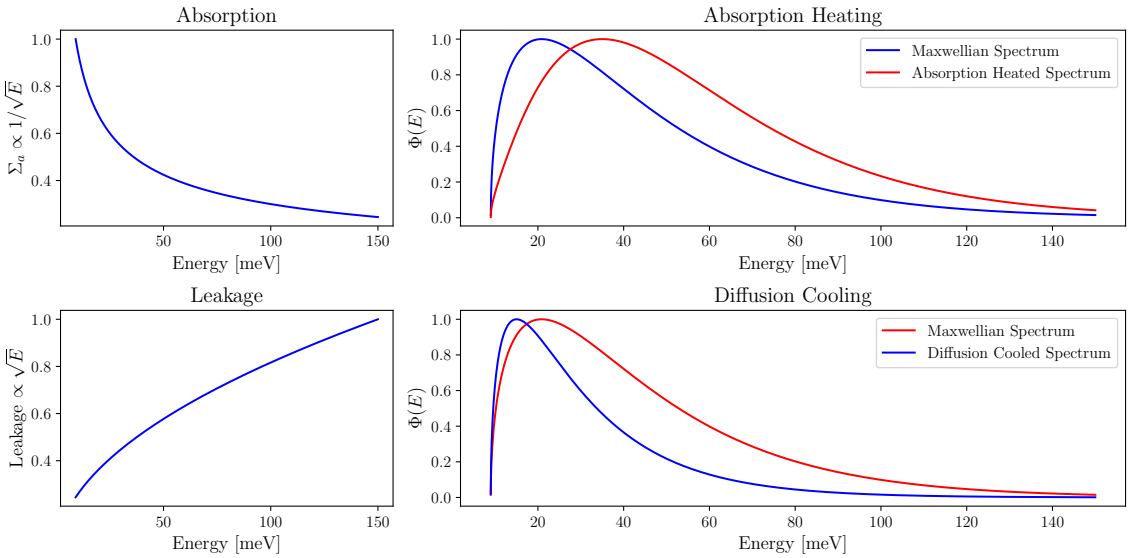

Figure 2.8.: Effects of selected non-equilibrium perturbations on normalized Maxwellian neutron spectra. This follows the discussion in [59, Section 9.I.B] (see text).

the spectrum will be shifted to higher energies, as if its effective temperature was increased. This "absorption heating" can be understood by considering the $\frac{1}{v}$-relation of the neutron ab-

sorption cross section. Since the probability of an absorption events increases with decreasing energy ($\propto \frac{1}{\sqrt{E}}$), the resulting spectrum will be shifted to higher energies. The exact opposite phenomenon occurs, when looking at neutron leakage. This can be modeled by introducing a leakage term $\propto \sqrt{E}$ to the total cross section. The leakage term acts like an effective absorption, the probability of which increases with energy. As higher energy neutrons will tend to leak more rapidly from the system, the system will be shifted to lower energies, which is referred to as "diffusion cooling". This yields to effective neutron temperature models, allowing to characterize a moderator, source configuration through a Maxwellian distribution with an effective temperature $T_n \neq T$, primarily dependent on the absorption cross section of the moderation medium, as discussed in [59, Section 9.I.C]. However, it requires a substantial amount of empirical guesswork and is insufficient to describe more intricate scenarios. A more sophisticated treatment requires calculating the neutron spectrum directly from Equation 2.56. This requires detailed knowledge of the neutron cross section in the required energy range.

2.4. Phase Space Transformation and Neutron Conversion

The state of the art of VCN and UCN production can be separated into two categories, which are both significantly different from the *spectral cooling* or *thermalization* of neutron fields in neutron moderators (discussed in Section 2.3). This has considerable consequences on the resulting spectra.

The first category is based on spectral dependent extraction of neutrons from a cold source and subsequent *phase space transformation*, which was first developed by Albert Steyerl in Garching [63] before moving to the ILL [64]. The resulting instrument, PF2, remains operational to this day and includes one of the first UCN sources available to users, as well as the only existing VCN beamline. The instrument is fed by a liquid deuterium cold source operated at 25 K. The neutrons are extracted through a vertical and strongly curved neutron guide system, that only transmits the long-wavelength tail of the liquid-deuterium moderator spectrum. The neutrons trajectory against the earth's gravitational pull leads to a deceleration of the neutrons. The neutrons that pass through are partly deviated to the VCN beam-line, while the majority is Doppler-shifted by rotating mirrors to the UCN energy range in the *Steyerl turbine* [64]. This causes a shift in the neutron velocity and an increase in beam divergence [65]. A similar concept was implemented at the Argonne National Laboratories, where the Doppler shift is facilitated by moving synthetic 'Thermica' crystals with a d-spacing of about 9.96 Å [66, 67]. The effect on the neutron spectrum is illustrated in Figure 2.9. It is important to note that these types of sources are essentially advanced methods for extracting the slowest neutrons from a cold moderator spectrum. As a result, the *phase-space density* of VCN and UCN cannot exceed the corresponding values in the cold source. This follows from Liouville's theorem, which states that the phase-space density of an ensemble of particles remains constant under canonical transformations [68]. Such transformations include spectral transformations such as reflections from moving mirrors or crystals, as in a neutron turbine, or the action of gravity in vertical neutron guides [69, 70]. In order to achieve higher fluxes of VCN, additional moderation to lower temperatures than classical cold sources is required.

The situation changes in the second category, which is typically used for UCN production and *neutron conversion* in a single inelastic scattering event [28]. In contrast to thermal and cold moderators, a UCN converter system is *not* in thermal equilibrium, which inspired the term *superthermal UCN sources* for such converters. Instead of many energy transfers of a neutron with the moderator material as discussed above, a converter acts in its simplest form as a two-level system with a ground state and an excited state separated by an energy E^*. At low temperatures, $k_\mathrm{B}T << E^*$, the excited state is practically unoccupied, such that the cross

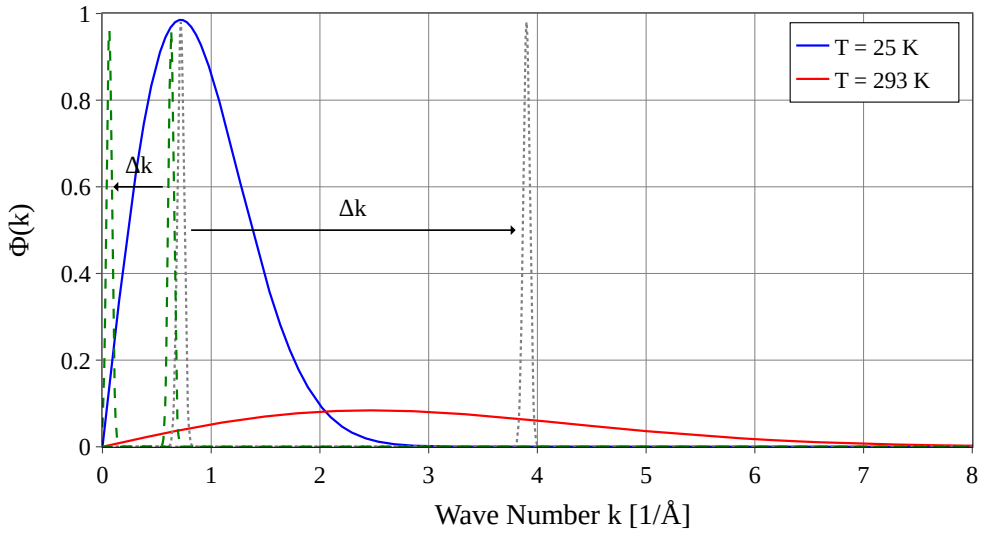

Figure 2.9.: Illustration of the phase space transformation resulting from a Doppler shift caused by a moving monochromator crystal, in contrast to moderation. It is assumed that the monochromator crystals accept a narrow Gaussian distribution around a given k. The green dashed lines represent the transformation to UCN from a wavevector $k = 0.63\,\text{Å}^{-1}$ facilitated by a decelerating 'Thermica' crystal as proposed in [66, 67]. The grey dotted lines illustrate a proposal to enhance the brightness at the sample position by Doppler shifting cold (or even ultra cold) neutrons to higher wavevectors rather than relying on thermal neutrons [71, 72]. Note that, while moderation compresses the spectrum to lower wavevectors, phase space transformations just shift a part of it.

section for down-scattering strongly exceeds that for up-scattering. In other words: At low enough temperatures, where the ground state of this two-level system is almost fully populated, the process of a neutron in the vicinity of E^* to excite the state and loose its energy is much more likely than the reverse process. This allows to formulate the following gain factor for UCN production [69, Equation 4-1]:

$$G(T) = \frac{\Sigma_{\text{down}(T)}}{\Sigma_\text{a} + \Sigma_{\text{up}(T)}}\ , \tag{2.66}$$

where $\Sigma_{\text{down}(T)}$, Σ_a and $\Sigma_{\text{up}(T)}$ are the macroscopic cross sections for down-scattering, capture and up-scattering by the converter atoms, respectively. For very low temperatures $T \to 0$, $\Sigma_{\text{down}(T)}$ will approach a constant, while $\Sigma_{\text{up}(T)} \to 0$ and Σ_a is independent of T. If Σ_a is small enough, the gain factor will, in principle, become arbitrarily large upon lowering T. This is particularly true for superfluid ^{4}He (He-II) at temperatures below $\sim$0.5 K as UCN converter. The coherent inelastic scattering from He-II can be described by a two level system with an energy gap of $E^* \equiv 1\,\text{meV}$, which corresponds to 12 K. The phonon-roton dispersion relation of He-II allows only neutrons of $E^* \equiv 1.03\,\text{meV}$ or $\lambda^* \equiv 8.9\,\text{Å}$ to down-scatter to UCN energies by excitation of a single phonon of the energy E^* (see Figure 2.10).[8] Since Σ_a of ^{4}He is exactly zero due to its nuclear configuration, $G(T)$ is dominated by the strong T-dependency of $\Sigma_{\text{up}(T)} \sim T^{-7}$. Besides superfluid helium, solid deuterium (SD_2) is a successfully employed UCN converter [73, 74]. Other materials investigated so far are α-O_2 [75, 76] and α - $^{15}N_2$ [77].

The fact that VCN and UCN spectra do not originate from thermalization with a moderator medium implies that they do not follow a Maxwellian distribution. The spectrum of the VCN

[8] The situation is actually more complex than that and the multi-phonon excitations are not negligible, see e.g. [39].

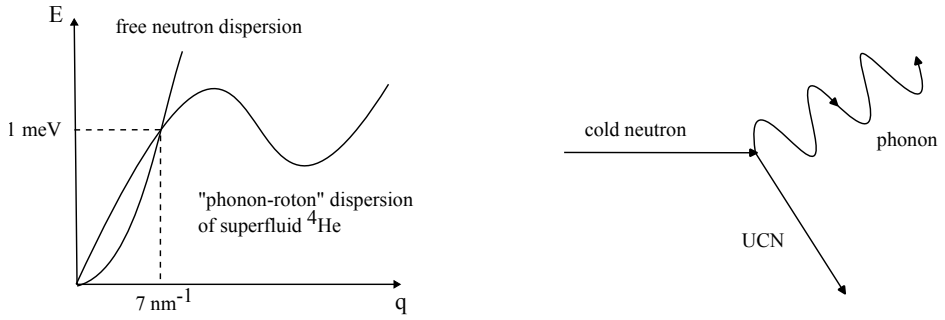

Figure 2.10.: The phonon-roton dispersion relationship of He-II (left) serves effectively as a two level system. A cold neutron of the energy $E^* \equiv 1.03\,\text{meV}$ or $\lambda^* \equiv 8.9\,\text{Å}$ can excite a phonon in the superfluid and scatter down two a UCN (right). Figure adapted from [70].

beam at PF2 is discussed in more detail in Chapter 6.3. It is strongly dependent on the geometry of the vertical curved guide, which allows energies up to about 200 µeV (20 Å) to be transmitted. This is the lower boundary of the wavelength spectrum, which reflects the long wavelength tail of the LD_2 source.

2.5. Solutions to the Transport Equation

The qualitative properties of thermalized neutron spectra shown above can be used to analytically solve the transport equation with approximate models. Such models are discussed in e.g. [59, Section 9.II]. While these models definitely have their merits, they lost some of their practical relevance due to successive improvements of computational methods.

A straightforward approach to discretization and numerical solution of the transport equation is the *multigroup diffusion method* (discussed extensively in [59, Part 3]), where the energy dependence of the neutron flux $\Phi(\mathbf{r}, E, t)$ is split into G *energy groups*, shown schematically below:

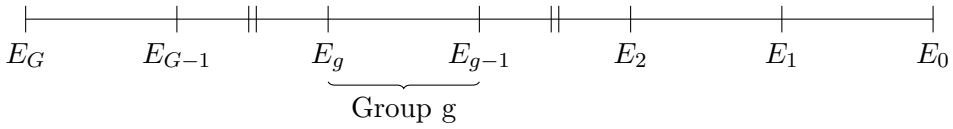

This allows to define discretized *multigroup flux* $\Phi_g(\mathbf{r}, t)$, which represents the total flux of all neutrons with energies E in the group $E_g < E < E_{g-1}$. The transport equation then becomes a set of coupled diffusion equations, where neutrons can experience a change in energy and then pass from one group to another. The infinite medium equation for our thermalization problem defined above (Equation 2.56) becomes

$$\Sigma_{t_g}\Phi_g = \sum_{g'=1}^{N} \Sigma_{s_{g'g}}\Phi_{g'} + S_g \ , \tag{2.67}$$

with the group index g. This could be evaluated for N energy groups in the sub-thermal energy range ($0 < E < 1\,\text{eV}$), with input data on the scattering kernel.

A fundamentally different approach is simulating the neutron transport for statistical relevant amount of particles, based on specified source, geometry, cross section and thermal scattering input data. This *Monte Carlo* method for neutron transport and thermalization dates back to

the efforts of neutron diffusion problems encountered in the Manhattan Project and is closely tied to the availability of general purpose computers [78, 79]. Until today, neutron transport simulations maintain their relevance across various fields including reactor physics, radiotherapy, radiation protection, and neutron scattering experiments.

2.5.1. The Monte Carlo Method for Neutron Transport

Monte Carlo methods are particularly well-suited for neutron transport due to the inherently probabilistic nature of these interactions. Based on [80], this section gives an overview of MC simulations in neutron transport emphasizing the importance of accurate thermal scattering libraries (TSL). Any Monte Carlo simulation of radiation transport typically involves several key steps:

1. Random sampling of the source.
2. Determination of the position of the next interaction.
3. Analysis of the interaction type, which may include changes in direction and energy (scattering), generation of new particles (fission), or the particle being absorbed or otherwise removed from the system (absorption).

Steps 2 and 3 are repeated until the particle is either absorbed or escapes from the considered volume. This process is illustrated in Figure 2.11. In the absence of external forces that could

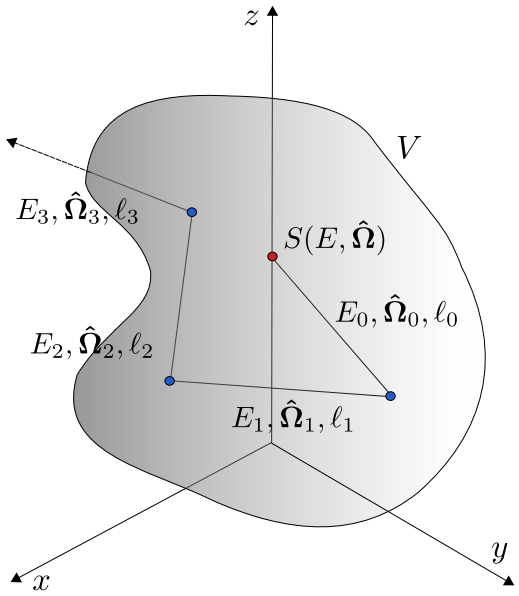

Figure 2.11.: *Markov chain* of the transport process of a single neutron starting with its appearance from a source $S(E, \hat{\mathbf{\Omega}})$ the neutron follows its trajectory $(E_0, \hat{\mathbf{\Omega}}_\mathbf{0}, l_0)$ until it interacts. This interaction possibly changes the neutron's trajectory and energy $(E_1, \hat{\mathbf{\Omega}}_\mathbf{1}, l_1)$. This process continues until the neutron is either absorbed or escapes the considered volume. This illustration is inspired by [81].

alter its trajectory, a neutron with energy E_0 sampled from the source travels in a straight line in the direction $\hat{\mathbf{\Omega}}_\mathbf{0}$. The cumulative probability of neutrons travelling a certain length ℓ can be expressed as:

$$P(\ell) = 1 - \exp(-\Sigma_t \ell) \tag{2.68}$$

The travelling distance to the first collision ℓ_0 can be obtained by sampling this distribution. Analyzing this collision requires determining the probability for each type of interaction, rep-

resented by $p_i = \frac{\Sigma_i}{\Sigma_t}$. In the case of a scattering event, it is necessary to sample the outgoing energy and direction distribution to determine the values of $\hat{\mathbf{\Omega}}_\mathbf{1}$ and E_1. These distributions are given by the scattering kernel. The neutron of E_1 is then travelling a distance ℓ_1 in direction $\hat{\mathbf{\Omega}}_\mathbf{1}$, where the next collision takes place. This process continues until a collision results in either absorption or scattering in a direction that causes the neutron to escape the volume V. In this case, the simulation continues by sampling new particles from the source until the total number of particles to be simulated N is reached. The probabilities in such a simulation depend only on the current state of the particles—characterized by their position $\mathbf{r}$, energy E, and direction $\hat{\mathbf{\Omega}}$ – and are independent of previous states. This independence is what qualifies the simulation as a *Markov chain* [80].

It can be shown that these steps, when coupled with the use of an appropriate statistical estimator for the neutron flux, offer a solution to the *transport equation* in its integral form (see e.g. [80, Chapter 2]). Considering also induced fission or radiative capture, with the respective macroscopic cross sections Σ_f and Σ_γ, requires to additionally calculate the corresponding probabilities p_f, p_γ, and scattering probability p_s, which are given by

$$p_f = \frac{\Sigma_f}{\Sigma_t}\,, p_\gamma = \frac{\Sigma_\gamma}{\Sigma_t}\,, p_s = \frac{\Sigma_s}{\Sigma_t} \tag{2.69}$$

Sampling from this probability distribution is equivalent to determining the position of a random number ξ_i in the vector of cumulative probabilities as illustrated below.

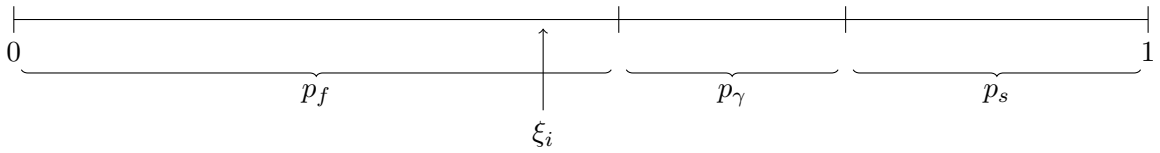

Where ξ_i is a random or pseudo-random number.[9]

Sampling can be performed randomly from the computed cumulative probability distribution, or by prioritizing regions of the distribution that significantly impact the result. The latter approach, known as importance sampling, improves accuracy by directing more samples to critical areas, or enhances performance by reducing the total number of required samples. In McStas [84], for example, this is done by assigning weight factors depending on the physical probability and the Monte Carlo sampling probability to the sampled particles (see [Section 2.2][85]).

2.5.2. Scattering Kernels for MC Simulations

To accurately model the behavior of neutrons within a moderator material, a precise characterization of the material and its interactions with neutrons is essential. In this context *scattering kernels* that include all relevant contributions of the neutron dynamical structure factor $S(\mathbf{q}, \omega)$, are key components in neutron transport simulations.

[9] The advantage of pseudo-random numbers is that they ensure reproducibility of a simulation, while behaving like random numbers. A common way to generate a sequence of such numbers is the *linear congruential method* starting with a random number *seed* ξ_0 a sequence with the recurrence:

$$\xi_{i+1} = (g\xi_i + c) \bmod M\,, \tag{2.70}$$

where g, c, and M are constants and mod stands for the modulo operator, which returns the remainder of the division. The choice of these constants has a significant effect on both the quality and the performance of the generator. Typical values are $g = 2806196910506780709$ $c = 1$, and $M = 2^{63}$ [82, 83].

To this end one of the objectives of the HighNESS project was to develop a comprehensive database of thermal neutron scattering libraries for various promising moderator, reflector, and converter materials for slow neutron sources, that allow the generation of scattering kernels in NCrystal [57, 86, 87] – a material library designed to enhance the accuracy of Monte Carlo simulations involving thermal neutron transport through primarily crystalline substances. A key strength of NCrystal is its integration with common simulation frameworks such as McStas [88], OpenMC [89], MCNP [90], and PHITS [91]. This allows the rapid integration of scattering kernels into neutronic design studies, as conducted within the HighNESS project. Moreover, NCrystal is accessible through various programming languages, including `C`, `C++`, and `Python`, allowing for individualized application across different computing environments.[10]

This work provided experimental input for the development of TSL for clathrate hydrates containing both protonated and deuterated tetrahydrofuran (THF and THF-d) [41, 93], as well as dioxygen [42]. The scattering kernels allow future design studies of VCN sources employing clathrate hydrates. They are open source and are available to the scientific community under [94].

[10] The `Python` environment is supported by Jupyter notebooks, which include tutorials and examples to assist users in using the library for their projects (see [92]).

3. Clathrate Hydrates as a Neutron Moderator

Although laboratory notes of Joseph Priestley from 1778 suggest the manufacturing of the first man-made hydrate [95], the discovery of clathrate hydrates is typically attributed to Humphry David in 1810, who found that a solid can be formed from an aqueous solution of chlorine cooled below 9 K of the melting point of water [96]. In 1823, the existence of such a solid was confirmed by Michael Faraday [97]. The taxonomy of "hydrate" or "clathrate hydrate" was developed a century later by H. M. Powell. According to Powell, clathrates are inclusion compounds in which "two or more components are associated without ordinary chemical union but through complete enclosure of one set of molecules in a suitable structure formed by another" [98]. In clathrate hydrates the hydrogen bonded water molecules arrange themselves in hollow polyhedra [99]. This host structure is capable of encapsulating a large variety of molecules (guest molecules). Although nonaqueous clathrates are subjects of research in various fields, within this work, the term 'clathrate' will be used interchangeably with 'clathrate hydrate' or 'gas hydrate'.

This section provides a concise overview of clathrate hydrates, accompanied by a selective review of significant publications in the field. For a more extensive discussion, readers are encouraged to consult [95], which has served as a standard work for many years. Although Peter Englezos' review [99] is now somewhat dated, it still offers a thorough examination of the advancements contemporary to its publication. A more recent and extensive collection of work, featuring a chapter focusing on neutron scattering of clathrate and semiclathrate hydrates, can be found in [100]. It should be emphasized that clathrate hydrates are studied across a wide range of disciplines, from fundamental solid-state physics to geology, climate science, and petroleum engineering. A brief review of hydrates in climate science is provided in Appendix 3.1. This chapter focuses on the unique physical properties of hydrates that make them promising VCN moderators, including low-energy excitations of confined molecules and atypically large crystallographic unit cells, which enable coherent elastic scattering across the cold neutron spectrum.

3.1. Hydrate Structures

The first determination of a cubic clathrate hydrate structure was achieved by M. v. Stackelberg in 1949 [101]. Two years later Claussen suggested a hydrate structure with a cubic unit cell containing 136 water molecules [102, 103, 104], which we know today as structure II hydrate. The structure I hydrate was discovered independently by Linus Pauling and Richard E. Marsh [105], in parallel to works by Muller and Stackelberg [106].

The fundamental building block for all hydrate structures is the pentagonal dodecahedron, formed by hydrogen-bonded water molecules. This is a polyhedron with 12 flat faces having 5 edges each.[1] Structure I (CS-I) is formed when these dodecahedra are arranged in space in such

[1] Interestingly enough, the pentagonal dodecahedron is one of five Platonic shapes, which in the Timaios dialogue [107], is associated with the fifth element. In this dialogue Timaios speculates about the constitution of the physical universe according to certain ancient Greek beliefs, wherein four elements – earth, water, air, and fire – were considered fundamental. Each of these elements is associated with a specific Platonic solid. The cube represents earth, while the octahedron stands for air, the icosahedron for water, and the tetrahedron for fire. The fifth element associated with the dodecahedron points beyond these elements and, as a notion of space or

a manner that they are linked through their vertices. The voids that are formed between dodecahedra, due to imprecise packing, have the shape of tetrakaidecahedra. These are polyhedra with 12 pentagonal and 2 hexagonal faces. Using the nomenclature suggested in [109], we can write $n_i^{m_i}$ for these polyhedra, where n_i is the number of edges in the face of type i and m_i is the number of faces with n_i edges. The pentagonal dodecahedron, as well as the tetrakaidecahedra of structure I can then be conveniently expressed by 5^{12} and $5^{12}6^2$ respectively.

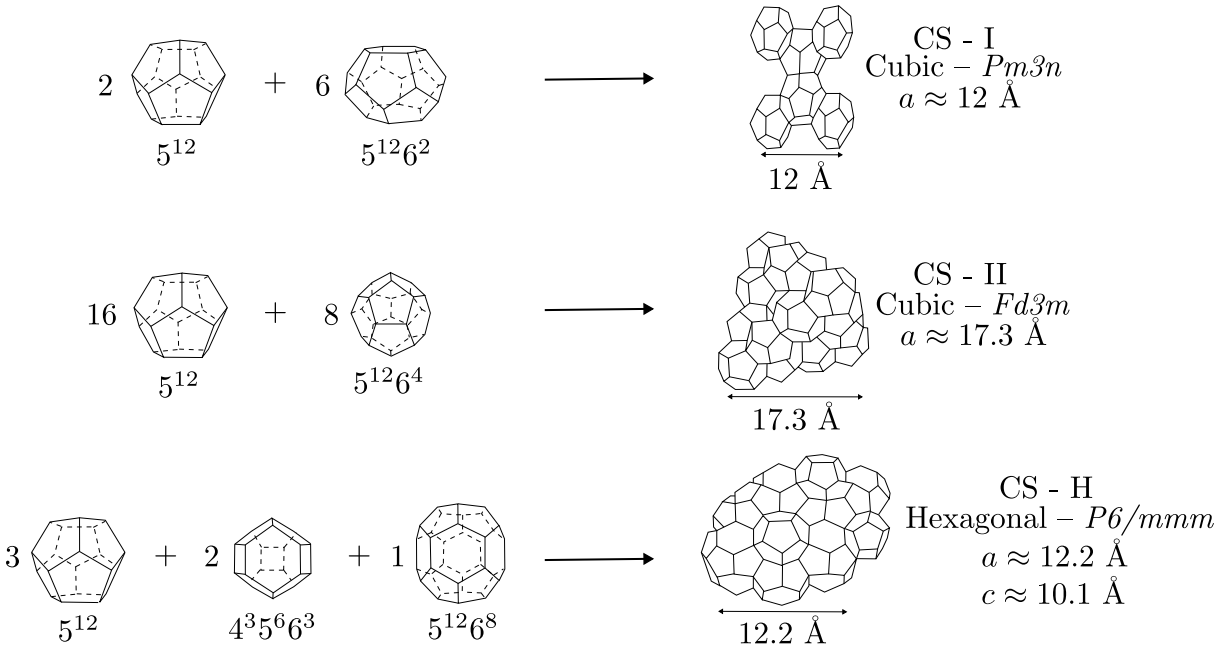

Figure 3.1.: The construction of the three most abundant hydrate structures from different polyhedral cavities. The crystallographic information of the resulting crystalline structures is given on the right. The numbers before the cages indicate the number of the respective cavities in the corresponding crystallographic unit cell. The pentagonal dodecahedron occurs in all of the structures, the other polyhedra appear in the space in between from different arangements of the 5^{12} (see text). Note that the atypically large unit cells of these structures result in high Bragg cutoffs, which play an important role in the coherent scattering behaviour of the investigated hydrate structures. Figure adapted from [95] and [110].

In the Structure II (CS-II) the 5^{12} polyhedra are arranged in such a way that they share faces. As a result a polyhedron with 12 pentagonal and 4 hexagonal faces ($5^{12}6^4$), a hexakaidecahedron, is formed. Finally, structure H is built up of layers of 5^{12} and alternating $5^{12}6^8$ and $4^3 5^6 6^3$ polyhedra. The polyhedra of the most abundant hydrate structures (CS-I, CS-II and CS-H) are summarized in Table 3.1 and Figure 3.1. It is important to note that this list is not exhaustive. By formulating the problem of hydrate inclusion compounds as a topological problem of finding three-dimensional four-connected nets[2] able to form crystallographic structures, [109] found five

aether, is associated with the movement of heavenly bodies.

In 1596 Johannes Kepler uses Platonic solids to construct the planetary orbits of our solar system in [108]. The dodecahedron is circumscribed around planet earth, while the orbit of Mars would lay on the sphere surrounding it.

[2] In [109] and related publications a three dimensional four connected net refers to a specific type of three dimensional lattice or network structure, where each node or lattice point connects to its four nearest neighbors. The four-connectedness is given by the hydrogen bonds of water-molecules, where the oxygen atom has two covalent bonded hydrogen atoms and is able to H-bond to two more hydrogen atoms as an acceptor [111].

additional hydrate structures, only three of which have been confirmed experimentally at this point [95]. The story of clathrate hydrates seems far from complete. For the context of this work, we will focus the CS-II structure hosting two specific guest molecules. The study of its specific structure is described in Chapter 4.

Table 3.1.: The geometry of the cages in the most abundant hydrate structures following the notation of [109]. The table is adapted from [95, Table 2.1]. Note that the average cavity radius depends on temperature and pressure.

Hydrate Crystal Structure	**I**		**II**		**H**		
Cavity	Small	Large	Small	Large	Small	Medium	Large
Polyhedron	5^{12}	$5^{12}6^2$	5^{12}	$5^{12}6^4$	5^{12}	$4^35^36^3$	$5^{12}6^8$
# Polyhedra per Unit Cell	2	6	16	8	3	2	1
Average Cavity Radius [Å]	3.95	4.33	3.91	4.73	3.94	4.04	5.79
# H_2O per Cavity	20	24	20	28	20	20	36
Unit Cell Formula	$2(5^{12}) \cdot 6(5^{12}6^2) \cdot 46H_2O$		$16(5^{12}) \cdot 8(5^{12}6^4) \cdot 136H_2O$		$3(5^{12}) \cdot 2(4^35^66^3) \cdot (5^{12}6^8) \cdot 34H_2O$		
Crystal System	Cubic		Cubic		Hexagonal		
Space group	Pm3n (N°223)		Fd3m (N°227)		P6/mmm (N°191)		
Lattice description	Primitive		Face centered		Hexagonal		
Lattice parameters	$a = 12\,\text{Å}$ $\alpha = \beta = \gamma = 90°$		$a = 17.3\,\text{Å}$ $\alpha = \beta = \gamma = 90°$		$a = 12.2\,\text{Å}$ $c = 10.1\,\text{Å}$ $\alpha = \beta = 90°, \gamma = 120°$		

3.2. Einstein Modes of Confined Molecules

The idea that the temperature dependency of the heat capacity ($C = \frac{dE}{dT}$) of a solid can be explained by describing each atom of the solid as a harmonic oscillator was introduced by Albert Einstein in 1907 [112]. In Einstein's model a crystal consists of N atoms that can vibrate *independently* in space, resulting in $3N$ localized harmonic oscillators with a characteristic frequency ω_E[3], such that:

$$E_n = \hbar\omega_E \left(n + \frac{1}{2}\right) , \tag{3.1}$$

where n is a natural number. The dynamics of each individual atom only depends on the temperature of the solid, not on the dynamics of surrounding atoms. By building the partition function (with $\beta = \frac{1}{k_B T}$)

$$Z = \sum_{n=0}^{\infty} \exp\left[-\beta \left(n + \frac{1}{2}\right) \hbar\omega_E\right] \tag{3.2}$$

of such a system, one can calculate its mean energy via:

$$\overline{E} = -\frac{1}{Z}\frac{\partial Z}{\partial \beta} , \tag{3.3}$$

and finally the heat capacity via:

$$C_V = \left(\frac{\partial \overline{E}}{\partial T}\right)_V . \tag{3.4}$$

This results in four connections of each oxygen atom, within the clathrate structure.

[3]Einstein's derivation in [112] looks different, but is based on the same principles.

This derivation is frequently used to introduce the concept of quantized excitations in condensed matter physics textbooks and historically accounted for the first time for the fast dropping heat capacity at low temperatures in most crystalline solids, e.g. diamonds (see [112]).

Usually aforementioned textbooks continue to point out that this model, with all its merits and simplicity falls short, in describing the actual trend of C_V at low temperatures which is not exponential in T but goes with T^3 and introduce Debye's model [113] in its place. The oscillators are no longer independent and localized; rather, they are coupled, leading to the emergence of *collective modes*. Instead of $3N$ harmonic oscillators, Debye describes the dynamics of condensed matter through quantized waves. This has various implications. In the context of this work the most pertinent is the occurrence of *dispersion relations*[4]. The specific wave mechanics of a crystal lattice only allows certain relations between the wavevector k and its frequency ω.

In the description of the dynamics of clathrate hydrates and other inclusion compounds both models come into play. While the host lattice of hydrogen bonded water molecules exhibits collective excitations with complex dispersion relations, the confined guest molecules can indeed experience localized excitations, which are therefore referred to as *Einstein modes*. The exact nature of these excitations depends on the guest molecule, particularly on its size and mass. While the rattling motions of molecular hydrogen or noble gases in a hydrate cage can be approximated as harmonic oscillators [114, 115], larger molecules usually exhibit more complex dynamics. Dependent on the mass of the guest molecule, the excitations can also exhibit coupling to the host lattice, as described in [116, 117, 118]. This has notable implications on the thermodynamic properties of clathrate hydrates. The thermal conductivity $\kappa(T)$ is about an order of magnitude lower than that of ice Ih [118, 119, 120], and it exhibits characteristic features at certain temperatures for different guest molecules. The thermal expansivity $\alpha(T)$ shows a low onset temperature and strong non-linearity, dependent on the guest molecule and cage occupation (see Section 4.1.3).

While the complex dynamics of clathrate hydrates are interesting to study in and of itself, for their application as moderator, it is important to note that the localization of these excitations implies the absence of a dispersion relation. This in turn has substantial effects on the moderation properties of the material. The cross section for inelastic neutron scattering involving collective excitations, such as phonons, for a neutron of energies $E < k_\mathrm{B}T_\mathrm{D}$, in a cold medium with the Debye temperature T_D is proportional to $(\frac{E}{k_\mathrm{B}T_\mathrm{D}})^3$ for single phonon emission[5] [121]. Localized excitations, on the other hand, do not have this limitation and allow for an efficient neutron slowdown even at lowest neutron temperatures. An important caveat in this context is that for most clathrate hydrates, including the ones considered in this study, the guest and host dynamics are not completely decoupled. Depending on the mass, size and chemical composition of the guest molecule the coupling can range from a light perturbation to an integration of the guest motion into some eigenmodes of the host lattice, as observed for the xenon hydrate (see [116]). The dynamics of the hydrates identified as promising as VCN moderators are discussed in Chapter 5.

[4] In the original publication Debye assumes the simple dispersion relation $\omega = v_s k$, with v_s being the speed of sound.

[5] The cross sections for processes of higher order drop even faster with decreasing energy.

3.3. Achieving Very-Low Neutron Temperatures via Magnetic Cooling

3.3.1. Magnetic Cooling in a Spin-Polarized Medium

In Section 2.4, we discussed how we can think of the inelastic coherent scattering of cold neutrons from He-II as a two level system. Another such system, that in fact was proposed before superfluid He-II is spin-polarized deuterium (D_2) [122]. The nuclei of deuterium have positive magnetic moments and we assume perfect polarization along a strong magnetic field. The neutron's magnetic moment (μ_n) is negative[6], in a strong magnetic field $\mathbf{B}$ the high-energy magnetic state of the neutron would cause the spin (σ) to be aligned parallel, while μ_n would be aligned anti-parallel to the magnetic field. Due to the conversion of angular momentum this state is not allowed to scatter of a nucleus and flip its spin to the anti-parallel direction. The situation changes when an AC field is applied. If this field is resonant at a frequency ω, so that $\hbar\omega = 2\boldsymbol{\mu}_n \cdot \mathbf{B}$, with $\boldsymbol{\mu}_n$ being the vector of the magnetic moment of the neutron, it is able to induce transitions between the spin states of the neutron. This state can now scatter from a spin-polarized deuteron and induce a spin-flip, resulting in an increase of potential energy of both the neutron and the deuteron within the magnetic field [70]. Due to energy conservation this increase needs to be compensated with a decrease of the neutron's kinetic energy by an amount of [70]

$$\Delta = 2\mathbf{B} \cdot (\boldsymbol{\mu}_n + \boldsymbol{\mu}_D) \,, \tag{3.5}$$

where μ_D is the deuteron's magnetic moment[7]. Since (magnetic) up-scattering of the neutron is suppressed by conservation of angular momentum, this perfectly spin-polarized moderator could serve as an effective two-level system for neutron cool-down. However, as pointed out already by Namiot, who proposed his idea in [122], the down-scattering could only be facilitated in very small steps. He noted that, for the cooling mechanism to become effective the neutrons need to be pre-moderated below 12 K. Despite assuming unrealistic conditions, as a field as strong as 30 T, and 100% polarisation, the energy loss in a single magnetic down-scattering event, Δ, would only be about 5 µeV and the pre-moderation temperature much lower than from any available CN source. The physical limit of this approach is determined by the magnitude of the nuclear magnetic moment, $\boldsymbol{\mu}_N$. However, this changes when paramagnetic systems are considered.

3.3.2. Magnetic Cooling in a Paramagnetic System

The energy transfer during neutron spin-flip scattering with an electron is about three orders of magnitude higher than with a nucleon, due to the significant mass difference between the proton and electron, occurring in the Bohr and nuclear magnetons, defined as:

$$\mu_B = \frac{e}{2m_\mathrm{e}}, \hbar \,, \quad \mu_N = \frac{e}{2m_\mathrm{p}}, \hbar; . \tag{3.6}$$

The ratio between these two quantities is the ratio between the proton and electron mass, which is a well known physical constant, $m_\mathrm{p}/m_\mathrm{e} = 1836.15$ [124]. As a consequence the energy loss Δ of one magnetic down-scattering from an electron is typically a fraction of a meV rather than a µeV in down-scattering from a nucleus in Namiot's proposal. Simple paramagnetic species respond to external magnetic fields, whereas magnetic molecules can exhibit a phenomenon known as *zero-field splitting*. This phenomenon causes the splitting of magnetic energy levels, enabling inelastic magnetic neutron scattering even in the absence of an external field [58]. These paramagnetic excitations are typically non-dispersive, meaning that the inelastic magnetic scattering is not

[6] μ_n points in the exact opposite direction as the spin (σ).
[7] $|\boldsymbol{\mu}_D| \approx 0.857\,\mu_N$ [123].

constrained by a magnon dispersion relation. This property facilitates neutron slowdown through an inelastic, incoherent "cooling cascade." This concept, detailed in [58], identifies molecular oxygen (O_2), with its spin-triplet ground state ($^3\Sigma_g^-$), as a particularly promising candidate for such applications. Without external magnetic fields and considering unpolarized neutrons, the double differential magnetic scattering cross section per atom/molecule is given by [42]:

$$\frac{d^2\sigma_{\text{mag}}}{d\Omega dE\prime} = \frac{b_{\text{mag}}^2}{2}\sqrt{\frac{E\prime}{E}}\left(S_{\text{mag},+}(\mathbf{q},\omega) + S_{\text{mag},-}(\mathbf{q},\omega) + S_{\text{mag},0}(\mathbf{q},\omega)\right) . \tag{3.7}$$

The cross section is composed of three components corresponding to different scattering processes: up-scattering, $S_{\text{mag},+}(\mathbf{q},\omega)$, down-scattering, $S_{\text{mag},-}(\mathbf{q},\omega)$, and elastic scattering, $S_{\text{mag},0}(\mathbf{q},\omega)$. These functions are dependent on temperature T, the zero-field splitting constant D, and the magnetic form factor of the oxygen molecule. When the O_2 molecules are considered unoriented, the magnetic scattering relies only on the polar scattering angle through the magnetic form factor. As a result, $S_{\text{mag}}(\mathbf{q},\omega)$ reduces to $S_{\text{mag}}(q,\omega)$, and the scattering kernels are expressed by [42][8]:

$$S_{\text{mag},\pm}(q,\omega) = \exp\left(-\left(\langle u^2\rangle + \frac{\ln(2)}{\Gamma_{\text{mag}}^2}\right)q^2\right) g_{\pm}(T)\delta(\hbar\omega \pm D) \tag{3.8}$$

and

$$S_{\text{mag},0}(q,\omega) = \exp\left(-\left(\langle u^2\rangle + \frac{\ln(2)}{\Gamma_{\text{mag}}^2}\right)q^2\right) g_0(T)\delta(\hbar\omega) . \tag{3.9}$$

In these expressions, $\langle u^2\rangle$ represents the mean-squared displacement of the molecular center, which varies with temperature and was neglected in the original treatment [58] to describe neutron slowdown by magnetic scattering in a moderator preferentially kept below 2 K. The term $\Gamma_{\text{mag}} = 15\,\text{nm}^{-1}$ denotes the half-width at half-maximum (HWHM) of the magnetic form factor, which is typically approximated by a Gaussian function [125]. The zero-field splitting constant D characterizes the energy difference between the spin states of the oxygen molecule. The temperature dependence of the scattering functions is captured by the thermal averages of the spin matrix elements, represented by the functions $g(T)$:

$$g_-(T) = \frac{4}{3}\frac{1}{1+2\exp\left(-\frac{D}{k_{\text{B}}T}\right)}, \tag{3.10}$$

and

$$g_+(T) = g_0(T) = \frac{4}{3}\frac{\exp\left(-\frac{D}{k_{\text{B}}T}\right)}{1+2\exp\left(-\frac{D}{k_{\text{B}}T}\right)} . \tag{3.11}$$

The functions $g_\pm$ account for the spin state distribution at a given temperature T. These functions include thermal averages of spin matrix elements corresponding to transitions between the magnetic states of the triplet state, as illustrated in Figure 3.2a. The quantum numbers $m = -1, 0, 1$ characterize the projection of the spin $S = 1$ of the oxygen molecule onto the molecular axis. In a magnetic scattering event with a neutron, if the molecular spin state transitions from $m = 0$ to $m = \pm 1$, the neutron loses the energy corresponding to the field splitting constant D. Conversely, in a transition from $m = \pm 1$ to $m = 0$, the neutron gains the energy D.[9] Note that the factor $\exp\left(-\frac{D}{k_BT}\right)$ between g_- and g_+ ensures that the description of the scattering processes is consistent with thermodynamic equilibrium by fulfilling the principle of detailed balance:

$$S_{\text{mag},+}(q,-D) = \exp\left(-\frac{D}{k_BT}\right) S_{\text{mag},-}(q,D) . \tag{3.12}$$

[8] The treatment of the magnetic neutron scattering theory follows [42, 58]

[9] This is because the eigenvalues of the Hamiltonian for the spin states $m = 0$ and $m = \pm 1$ are $-2D/3$ and $D/3$, respectively. A derivation is provided in [58, Appendix].

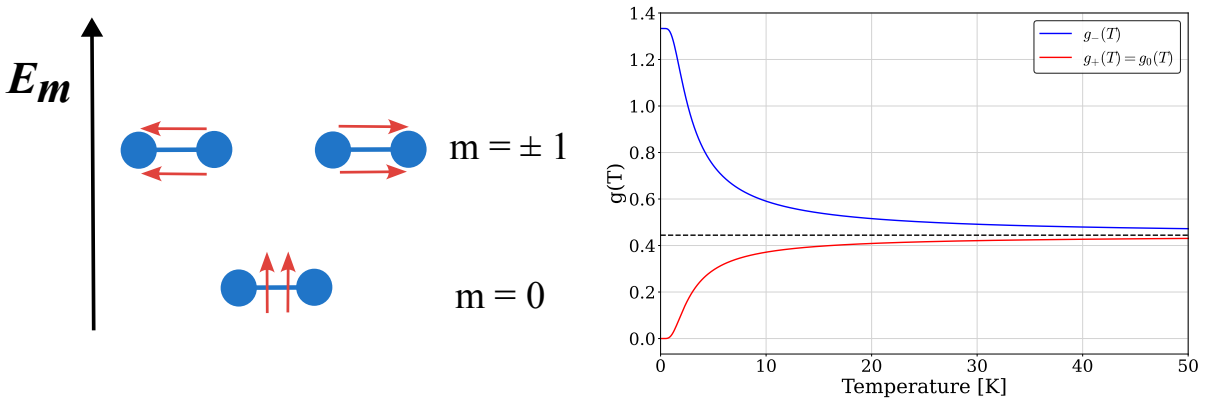

(a) Energy levels and spin states of the triplet ground state of O_2.

(b) Temperature dependence of paramagnetic scattering $g_\pm(T)$.

Figure 3.2.: Energy levels of the triplet ground state of O_2. (a) The oxygen molecule is illustrated with two filled circles. The arrows represent the paired electron spins of the triplet state. The quantum numbers $m = \pm 1$ correspond to the spin orientation parallel or anti-parallel to the oxygen molecular axis, while $m = 0$ corresponds to the spin perpendicular to it. The functions $g_\pm(T)$ depicted in (b) contain the thermal averages of spin matrix elements (see text). As temperature increases, the difference between $g_-(T)$ and $g_+(T)$ decreases, approaching the asymptotic value of 4/9. To calculate $g(T)$, a field splitting constant of $D = 0.4\,\text{meV}$ was used.

The magnetic scattering cross sections are obtained by integrating the double differential cross section over all possible final neutron energies and directions. This leads to the following expressions for the up-scattering, down-scattering, and elastic scattering cross sections:

$$\sigma_{\text{mag},\pm}(E) = \frac{\sigma_{\text{mag}}}{2} c_\pm g_\pm(T) f_\pm(E,T)\,, \tag{3.13}$$

and

$$\sigma_{\text{mag},0}(E) = \frac{\sigma_{\text{mag}}}{2} g_0(T) f_0(E,T)\,, \tag{3.14}$$

where $\sigma_{\text{mag}} = 4\pi b_{\text{mag}}^2 \approx 3.66\,\text{b}$. The factors $c_\pm$ are given by

$$c_+ = \sqrt{1 + D/E} \tag{3.15}$$

$$c_- = \begin{cases} \sqrt{\left(1 - \frac{D}{E}\right)} & \text{for } E \geqslant D \\ 0 & \text{for } E < D \end{cases} \tag{3.16}$$

The functions $f_\pm(E,T)$ and $f_0(E,T)$ account for the form factor and are defined as:

$$f_\pm(E,T) = \frac{1}{4c_\pm AE} \left(\exp\left(-AE(1-c_\pm)^2\right) - \exp\left(-AE(1+c_\pm)^2\right)\right) \tag{3.17}$$

and

$$f_0(E,T) = \frac{1 - \exp(-4AE)}{4AE}\,. \tag{3.18}$$

The parameter A is given by $A = \frac{2m_n(\langle u^2\rangle + \ln(2)/\Gamma_{\text{mag}}^2)}{\hbar^2}$. Having found an expression for the neutron down-scattering cross section, we can write the spectral conversion rate density as:

$$p\left(E'\right) = \int_0^\infty \Phi\left(E\right) \Sigma_-\left(E \to E'\right) dE\,, \tag{3.19}$$

where Σ_- is the macroscopic magnetic down-scattering cross section, defined as $\Sigma_- = N\sigma_{\mathrm{mag},-}$, with N being the number density of paramagnetic centers (O_2 molecules). The expression $p(E')$ represents the number of neutrons in a neutron field that are converted from an energy E to a lower energy $E' < E$ by a single scattering event, per unit time, volume, and energy. The assumption of a single scattering event holds when only small amounts of material are exposed to the neutron field, such as in thin conversion layers. In larger moderator volumes, the occurrence of multiple scattering events becomes significant and the dispersion-free paramagnetic excitations initiate cooling cascades. These cascades are a valuable mechanism for neutron down-scattering VCN temperatures, as they successively reduce the neutron's energy. This effect can be analyzed by defining groups of neutrons characterized by a spatial density $n_{j,E_0}dE$ within an energy interval dE centered around a specific energy E_0. The energy of each group is given by:

$$E_j = j\Delta + E_0\,, \tag{3.20}$$

where $0 \leqslant E_0 < \Delta$ defines the base energy for the group when $j = 0$. The rate constant for scattering from group j to j' is denoted by $\tau^{-1} j \to j'$, following the notation in [58]. The population of neutrons in group j can then be described by the following equation:

$$\frac{dn_j}{dt} = \underbrace{s_j}_{\substack{\text{neutron}\\ \text{sources}}} + \underbrace{n_{j+1}\tau^{-1}_{j+1\to j}}_{\substack{\text{down-scatters from}\\ \text{the group } j+1}} + \underbrace{n_{j-1}\tau^{-1}_{j-1\to j}}_{\substack{\text{up-scatters from}\\ \text{the group } j-1}} - \underbrace{n_j\tau^{-1}_{j\to j-1}}_{\substack{\text{Losses due to}\\ \text{down-scatters to}\\ \text{group } j-1}} - \underbrace{n_j\tau^{-1}_{j\to j+1}}_{\substack{\text{Losses due to}\\ \text{up-scatters to}\\ \text{group } j+1}} - \underbrace{n_j\tau_a^{-1}}_{\substack{\text{Losses due to}\\ \text{absorption}}}\,. \tag{3.21}$$

The first term s_j describes homogeneously distributed sources of neutrons within the system. The second and third terms account for the influx of neutrons into group j from adjacent energy groups: down-scattering from group $j + 1$ and up-scattering from group $j - 1$, respectively. Conversely, the fourth and fifth terms describe the loss of neutrons from group j due to down-scattering to $j - 1$ and due to up-scatters to group $j + 1$. The final term represents losses due to neutron absorption, characterized by the rate constant τ_a^{-1}, which is defined as

$$\tau_{\mathrm{a}}^{-1} = v\Sigma_{\mathrm{a}}\,. \tag{3.22}$$

Note that this term remains constant across all groups since $\Sigma_a \propto 1/v$. The resulting system of first-order differential equations can be expressed in matrix form and solved as detailed in [58]. This yields an analytical stationary solution for the neutron spectrum in a homogeneous neutron field within an infinite moderator material. While the specifics of this solution are beyond the scope of this discussion, two key aspects are worth emphasizing:

1. The non-dispersive nature of inelastic (down-)scattering from paramagnetic species enables the removal of energy from neutrons in consistent steps of Δ. This step-wise energy reduction leads to significant gains in the production of VCN and UCN, compared to the single-step neutron conversion discussed in Section 2.4.
2. The energy removed in a single spin-flip inducing down-scattering event is substantially higher when scattering from electrons rather than nuclei. Unlike the micro-eV scale energy removal proposed by Namiot [122], which requires extremely high magnetic fields, the zero-field splitting of O_2 facilitates magnetic down-scattering in increments of $\Delta = 0.4\,\mathrm{meV}$. Consequently, the cooling cascade from O_2 is significantly more effective, enabling a substantial enhancement of the long-wavelength tail of cold neutron spectra within reasonable moderator sizes.

3.3.3. Host Structures for Paramagnetic O_2

After identifying the cooling mechanism, [58] discusses various host structures for O_2. The considered host structures are summarized in Table 3.2, supplemented by the binary clathrate

hydrate hosting THF-d and O_2. A suitable host structure can accommodate high densities of O_2, while preventing the magnetic ordering typically observed at low temperatures in crystalline oxygen [76, 126]. Dioxygen can also be intercalated into the fcc lattice of C_{60} crystalline molecules. A maximum of one O_2 can be trapped per 60 unit resulting in a maximum number density of $1.38 \times 10^{21}\,\mathrm{cm}^{-3}$ [127]. Another material considered by [58] is dioxygen embedded in a helium matrix, in so called van der Waals clusters, which would result in remarkably low absorption and number densities of up to $1.46 \times 10^{21}\,\mathrm{cm}^{-3}$ [128].

Table 3.2.: Rate constant for neutron absorption and achievable number density in three media hosting dioxgyen at low temperature as given in [58]. The values are given for bulk matter and with the indicated O_2 filling fractions of cages.

Host	Cage structure	Number Density [cm^{-3}]	τ_a^{-1} [s^{-1}]
D_2O	CS-II Deuterate, $O_2 \cdot D_2O$ (86%)	4.16×10^{21}	7.49
D_2O	Binary CS-II Deuterate, THF-d$\cdot O_2 \cdot D_2O$ (80%)	2.58×10^{21}	13.97
carbon	Octahedral Voids in fcc-C_{60} (70%)	0.97×10^{21}	63.9
^{4}He	^{4}He Van Der Waals Clusters	1.46×10^{21}	0.122

Even though the vanishingly small absorption of the ^{4}He inclusion compound makes it a strong candidate, the advantages of using deuterated clathrate hydrates are threefold:

1. they also exhibit weak neutron absorption,
2. they enable the highest storage densities of O_2 without magnetic ordering,
3. and allow for the introduction of additional guest molecules, which can contribute to the neutron slow-down via localized excitations.

4. Manufacturing and Structure Determination of THF-d and THF-d – O_2 Hydrates

This chapter introduces a novel manufacturing technique of a particular promising binary hydrate hosting deuterated tetrahydrofuran (THF-d) and dioxygen (O_2) as guest molecules. While this binary hydrate has been produced before from a slurry by constantly stirring a solution of one part THF in 17 parts of water, pressurizing it with O_2 and slowly decreasing the temperature [129, 130], we present a different manufacturing method, which is not only easily scalable for producing large amounts of material, but also effective in maximizing the yield of CS-II hydrate and the cage occupancy of O_2.

The application of clathrate hydrates in a moderator requires a reliable method of producing large quantities of the material. Since the moderator has to be cooled to temperatures well below 4 K to be most effective, and the clathrate hydrates have only a low thermal conductivity, it is proposed to immerse a porous block of packed powder in super-fluid helium serving as an effective and neutron non-absorbing medium for cooling. The production of the THF-d clathrate hydrate powder and the addition of the dioxygen can for practical reasons not be done in-situ in the moderator tank, so that a cold transfer of the material is necessary after its preparation.

This chapter presents the first test of this method, along with a neutron diffraction study of the obtained samples, which confirms the structure and provides an estimate of the cage occupancy. Large parts of this chapter are to be published in an article under the title *A Manufacturing Technique for Binary Clathrate Hydrates for Cold and Very Cold Neutron Production.*

4.1. Manufacturing of THF-d – O_2 Deuterates

The manufacturing technique of THF-d – O_2 hydrates presented here follows three basic steps:

1. Forming THF-d hydrates from a stoichiometric solution of THF-d/17D_2O.
2. Grinding the THF-d hydrate into a fine powder providing a large reaction surface.
3. Exposing the powder to a high pressure O_2 atmosphere.

The preparation of THF hydrates is described in Appendix G. It should be added that the evaporation at room temperature of water (or heavy water) can be neglected compared to that of THF (or THF-d). For THF-d we observed an evaporation rate of 0.6 mg/minute from an open 17 ml vial. The most precise way to achieve an almost exact stoichiometric ratio is adding slightly more THF than necessary and monitoring the evaporation. The materials used in this process are provided in Table 4.1.

Previous studies have shown the feasibility of creating clathrate hydrates starting from hexagonal ice (Ih) [116, 131, 132]. However the grain sizes achieved by grinding ice Ih with a mortar in liquid nitrogen is in the 10 to 100 µm range, with a broad Gaussian distribution [133]. In addition, manual grinding in a mortar is hardly feasible for the amount of material that is needed for moderator applications, which depending on the size of the moderator run from 100 g to several kg.

Table 4.1.: The materials used for the manufacturing of binary clathrate discussed in this work.

Component	**Supplier**	**Purity**
Dioxygen O_2	Air liquide	$\geqslant 99.5\%$
THF (C_4H_8O)	Eurisotop	$\geqslant 99.9\%$
THF-d (C_4D_8O)	Eurisotop	isotopic purity $\geqslant 99.5\%$
Heavy water (D_2O)	Eurisotop	isotopic purity $\geqslant 99.9\%$

Grinding THF-d Deuterate into Fine Powder

Milling already formed THF-d hydrates, rather than grinding ice Ih as a starting point to form the binary hydrate has multiple advantages. Not only does milling allow to produce high quantities of fine powders, it also provides a smaller and narrower distributed grain size, suggesting faster and more uniform hydrate formation. Moreover, using THF-d hydrates rather than ice Ih as a starting material changes the necessary thermodynamic conditions for the formation of a binary THF-d – O_2 hydrate, allowing its formation at lower pressures (see Fig. 4.1).

An important condition to fulfill in this process, particularly when preparing powders of deuterates, is to maintain low temperatures while preventing the condensation of H_2O from the laboratory atmosphere. The latter, which could alter both the stoichiometry and the isotopic composition of the sample, can be kept well under control by handling the deuterate in a dry nitrogen or argon atmosphere within a glove box or bag.

Preliminary tests indicated that the thermal mass of the 50 ml jar pre-cooled to liquid nitrogen temperature was sufficient to mill for over 4 minutes at SI500rpm before the jar temperature exceeded 270 K. As milling cycles of 60 s to 100 s yielded similar powders, a shorter time per cycle (90 s) was chosen to avoid compromising the CS-II structure. The potential introduction of stacking disorders during the grinding and milling of THF-d hydrates was described in [134]. This makes it imperative to validate the structure of these powders.

For the milling we used a RETSCH PM100 planetary ball mill, equipped with a stainless steel grinding jar with a volume 50 ml and grinding balls with diameters of $\varnothing = 5$ mm, $\varnothing = 10$ mm and $\varnothing = 20$ mm.[1] The finest powder was obtained with 10 balls of $\varnothing = 5$ mm.

The process was carried out as follows: In a glove bag, the stoichiometric solution THF-d/17D_2O was poured into a thin-walled aluminum pan in liquid nitrogen. The solid deuterate forms at the bottom of the aluminum pan within less than a second. It can then be transferred together with the stainless steel balls into the grinding jar, which is under argon and in liquid nitrogen. After the transfer, the jar is closed in the argon atmosphere and placed in the ball mill. To reduce the heat exchange with the environment, the contact surfaces between the jar and the mill were insulated with Teflon and the jar was wrapped in aluminum foil, which also avoided condensation of air humidity on it.

Following milling, the jar was transferred back into the glove bag, reopened under an argon atmosphere, and the cold powder was transferred into a container for neutron scattering analysis of the THF-d deuterate or into the pressure cell for creation of the binary clathrate (next section).

[1] This configuration was chosen to produce the small quantities required for this work. The same mill allows to use jars up to 500 ml.

Dioxygen Gassing

To prepare the binary THF-d – O_2 deuterate, the powder was kept at dry ice temperatures and inserted into a 9.8 ml pressure cell made of stainless steel. The cell was flushed with O_2, sealed with indium wire, and tightly closed. Subsequently, the cell was maintained at a constant temperature of 274.15 K and a pressure of 10 MPa. This was facilitated by a water bath with a temperature controller and a pump controller that compensated for pressure loss due to O_2 uptake in the hydrate, ensuring homogeneous filling. A flow chart of this process is depicted in Fig. 4.2. Figure 4.1 shows established hydrate dissociation curves for the O_2-water system and

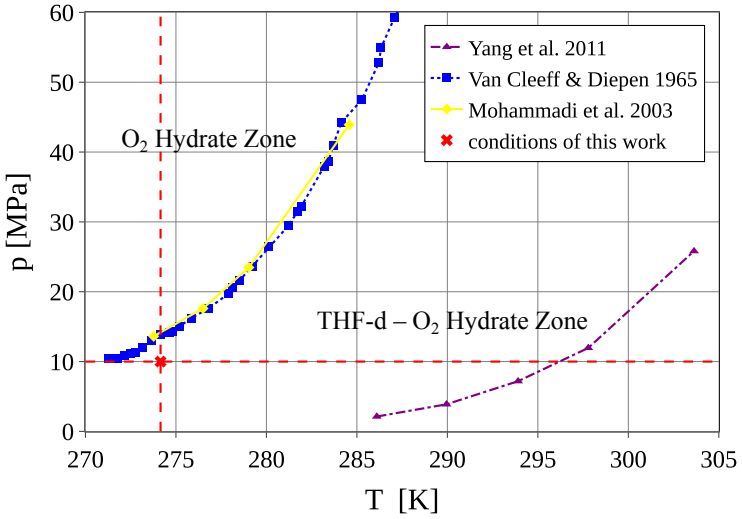

Figure 4.1.: Reported dissociation curves for THF-d – O_2 and O_2 deuterate indicating the respective hydrate stability zones. The temperature and pressure conditions for our preparation were chosen to lie just outside the O_2-hydrate zone.

[130] for the O_2-THF water system, as reported in [130, 135, 136]. Temperature and pressure for our preparation were chosen to lie just outside the O_2-hydrate zone yet securely within the O_2-THF-hydrate zone, optimizing yield of the binary hydrate. Typically, clathrate formation rates are higher in the initial stages and become slow after several days [131]. After 10 days[2] at 274.15 K and 10 MPa the hydrates were cooled to liquid nitrogen temperatures, the pressure in the cell was slowly released and the THF-d – O_2 deuterate was extracted under an argon atmosphere.

4.1.1. Neutron Diffraction at D20

The powder samples of THF-d - and THF-d – O_2 deuterates were filled under argon atmosphere and liquid nitrogen into cylindrical sample containers made from vanadium, with an inner diameter of 6 mm and a wall thickness of 0.1 mm. The high-intensity two-axis diffractometer D20 at the Institut Laue-Langevin was operated using the (115) reflection of a Germanium(113) monochromator at a wavelength of $\lambda = 1.546$ Å. At a takeoff angle of 90°, this results in a lattice-spacing resolution of $\Delta d/d = 3 \times 10^{-3}$. The high flux at D20 allows to obtain diffraction patterns between double scattering angles of 4° and 150° with satisfactory statistics in about 30 min. The objective of the experiments at D20 was to validate that (1) the ball milling procedure described above preserves the CS-II structure and (2) the whole sample preparation prevents intake of water from air humidity at non-negligible levels. In a first step, neutron diffraction experiments

[2] This time was mostly defined by instrumental constraints and should be increased for higher cage filling factors.

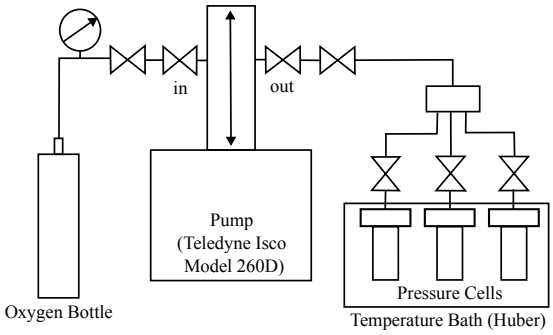

Figure 4.2.: Schematic of the apparatus for transforming THF-d hydrates into binary THF-d - O_2 deuterate. The oxygen bottle is connected via a pressure gauge with the pump system (*Teledyne Isco Model 260D*), that supplied a constant pressure of 10 MPa, compensating for the O_2 uptake of the hydrate. The gas was then distributed on three identical pressure cells separated by a valve (*Top Industrie*). The cell's temperature was kept steadily at 274.15 K with a temperature controller (*Huber pilot one*). The conditions for the pressurization were chosen based on the reported literature. See [130, 135, 136] for the data depicted in 4.1.

were performed using a sample of the milled material before gassing. For comparison, the same experiments were also performed for a sample prepared by manual grinding in a mortar instead of milling. Both data sets were then compared with previous data obtained from THF-d deuterate produced by quenching a stoichiometric solution [93]. In a subsequent step, the manually ground and ball-milled samples were pressurized with O_2 as described above, and the resulting THF-d – O_2 deuterates were investigated. The ball mill sample was divided into two sub-samples from the top and bottom of the pressure cell, respectively. Comparison of the diffraction data from these samples allowed us to detect a possible difference of O_2 content due to the different location of the powder with respect to the oxygen inlet valve.

To evaluate the thermal expansion, as described in Section 4.2.3, the two binary samples were measured at temperatures ranging from 1.5 K to 80 K, and the simple THF-d deuterate from 2 K to 100 K, in increments of 5 K.

4.1.2. Rietveld Refinement

The raw data were analyzed to derive thermal expansion, and structure refinements were performed in Fullprof [137, 138]. The Rietveld method [139], a crystallographic least-squares refinement method, was employed to validate the structure. This method provides information on lattice constants, positional and thermal parameters, as well as guest occupancies for every crystalline phase within the sample. It's important to note that instrumental and background parameters are established concurrently with the parameters of the structural model. As a result, the estimated standard deviations derived from such a method partly reflect instrumental and sample imperfections but not necessarily other systematic errors.
The THF-d molecule was treated as a rigid body, with its position and orientation within the large cage as free fitting parameters. The O_2 molecule was treated as a free atom at the corresponding site. In addition to the phase under investigation (THF-d deuterates and binary THF-d – O_2 deuterates), the refinement included the aluminum of the sample environment and residual hexagonal ice. Phase fractions are determined through a scale factor as part of a multi-pattern refinement procedure (see e.g. [140]). This allows for quantitative analysis of the mass percentage of each phase in the sample. The weight percentage W_j for the phase j can be

calculated as in [141]:

$$W_j = \frac{S_j Z_j M_j V_{cj}}{\sum_i^N S_i Z_i M_i V_{ci}} \,, \tag{4.1}$$

with S, Z, M and V being the scale factor, the number of formula units per unit cell, the mass of one formula unit and the unit-cell volume, for each phase j and i, respectively. Fullprof also accounts for the multiplicities of each site, for occupation numbers unequal to 1, via the factor f_j, and the micro absorption of neutrons (Brindley factor t_j) of each phase [142]:

$$W_j = \frac{S_j Z_j {f_j}^2 M_j V_j / t_j}{\sum_i^N S_i Z_i {f_i}^2 M_i V_i / t_i} = \frac{S_j \cdot \mathrm{ATZ} \cdot V_j}{\sum_i^N S_i \cdot \mathrm{ATZ}_i \cdot V_i} \,, \quad \text{with } \mathrm{ATZ} = Z_j {f_j}^2 M_j / t_j. \tag{4.2}$$

Since the two phases within the refinement have very similar absorption t_j is ~ 1. In a stochiometric compound f_j reduces to 1, as the multiplicities are calculated by dividing the Wyckoff multiplicity m of a particular site by the general multiplicity M [142]. This is the case for the THF-d deuterate, where Equation 4.2 reduces to Equation 4.1. In the case of non-stochiometric compounds, as in the binary THF-d – O_2 deuterate, these multiplicities are calculated by

$$f = \frac{Occ\, M}{m} \,, \tag{4.3}$$

where Occ is the occupation number used in the refinement. This allows to compute the cage occupancy of the O_2 in the small cages, by allowing the occupation number Occ of the respective O_2 to be a free refinement parameter and using Equation 4.2 to calculate the weight percentage.

4.1.3. Determination of the Thermal Expansivity

The thermal expansivity is isotropic for a cubic crystalline structure and is defined as the partial derivative of the lattice parameter a with respect to temperature, under constant pressure p [143, 144]

$$\alpha = \frac{1}{a}\left(\frac{\partial a}{\partial T}\right)_p \,. \tag{4.4}$$

The expansion of the cell parameter at a reference temperature T_0, $a_0 = a(T_0)$, to a temperature T can then be expressed as

$$a(T) = a_0(1 + \alpha \Delta T) \,, \tag{4.5}$$

where $\Delta T = T - T_0$. Generally α is a function of temperature. Since the T-dependency of α is small, it can be expanded around some $\alpha_0 = \alpha(T_0)$ and approximated by [145, 146, 147]

$$\alpha(T - T_0) \approx \alpha_0 + \alpha_1(T - T_0) + \alpha_2(T - T_0)^2 \,. \tag{4.6}$$

This quantity can be determined from the raw data independently of any refinement. Given a high-quality diffractogram, a peak-finding algorithm (see e.g., [148]) can identify a number of N peaks. The positions of these peaks in 2θ are then monitored as a function of temperature. Since the determination of the peak maximum is limited by the angular resolution of the instrument[3], this process can be improved by fitting each of the peaks with a Lorentzian peak shape function over its FWHM and compute the peak center μ and its standard deviation σ. Using Bragg's law (Equation 2.48), the lattice spacing can then be expressed by

$$d_{hkl} = \frac{\lambda}{2 \sin(\theta)} \tag{4.7}$$

[3] This was 0.5 deg for the configuration in which the reported data was obtained.

The parameter μ in d-spacing can then be plotted with their respective σ as a function of T. The thermal expansivity $\alpha(T)$ can then be obtained using Equation 4.5 by computing the relative expansion of the lattice spacing from a reference temperature T_0

$$\alpha(T) = \frac{\Delta d}{d\Delta T} = \frac{d(T) - d(T_0)}{d(T_0)(T - T_0)} \,, \tag{4.8}$$

for all measured T and finding the coefficients α_0, α_1 and α_2 from Equation 4.6 that fit the data.

4.2. Results

4.2.1. Fine Powders of THF-d Deuterates

Prior to investigating the binary hydrate samples, we confirmed through neutron diffraction that the CS-II structure consistently forms as a polycrystalline solid with minimal residual ice. This was observed regardless of whether the solution was quenched in liquid nitrogen or slowly cooled in a cryostat, as presented in [93]. However, the diffraction data also revealed clear texture effects. Figure 4.3 presents diffractograms of two distinct samples of THF-d deuterates: solidified in bulk (a), and milled with a ball mill (b). A rotation of the sample allows for an examination of the influence of texture on the diffraction pattern. Notably, rotations by 40 ° and 90 ° exhibit a clear effect in the intensity profile of the bulk sample, while minimal effects are observed in both the milled and ground samples (not shown). This demonstrates the successful mitigation of texture through grinding and milling, with the structure remaining fully intact. This conclusion is supported by the consistent peak positions in the diffractograms, as verified through the Rietveld method.

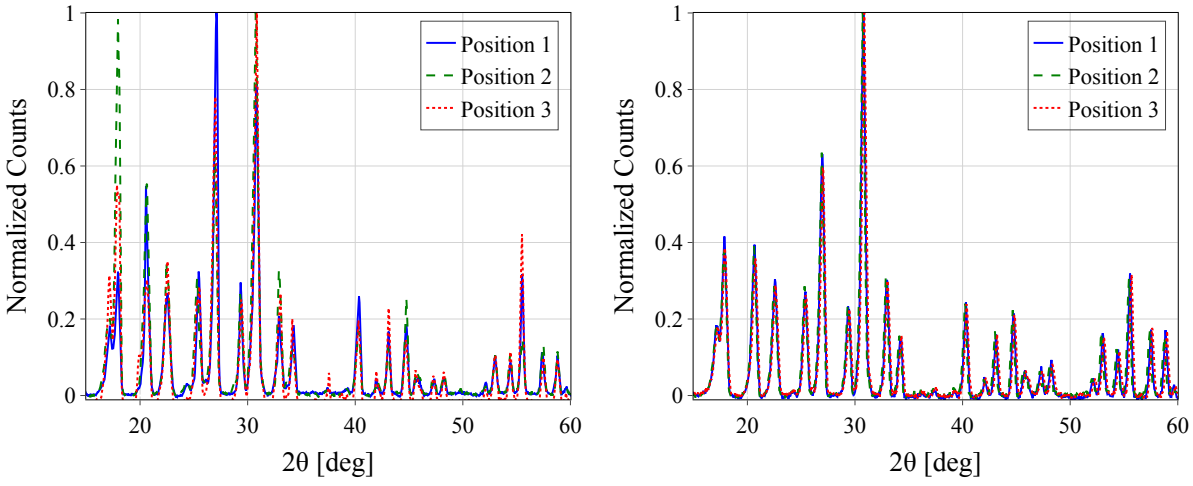

(a) THF-d deuterate solidified in bulk.

(b) THF-d deuterate milled with a ball mill.

Figure 4.3.: Diffraction patterns measured for three different angular positions of the sample in the beam (0 °, 40 °, 90 °) for three diffrent samples of THF-d deuterate in a limited range of $2\theta = [15\,°, 60\,°]$, at a temperature of 2 K. While the bulk sample (a) shows clear texture (manifesting as a change of the intensity profile as a function of the sample rotation), the three data sets from the milled sample (b) match almost perfectly. The powder ground with a mortar (not shown) shows a very similar behavior to the milled sample.

4.2.2. Structure Analysis of the Binary THF-d – O_2 Deuterate

A comparison of the THF−d and THF-d – O_2 is shown in Figure 4.4. The two samples show very similar peak positions, while exhibiting different intensity profiles. This provides clear evidence that the cubic *Fd3m* structure typical for CS-II hydrates is maintained throughout the manufacturing process. Furthermore it indicates a change of the *structure factor*, by the introduction of O_2 into the the 5^{12} cages. A complete Rietveld refinement of the THF-d – O_2

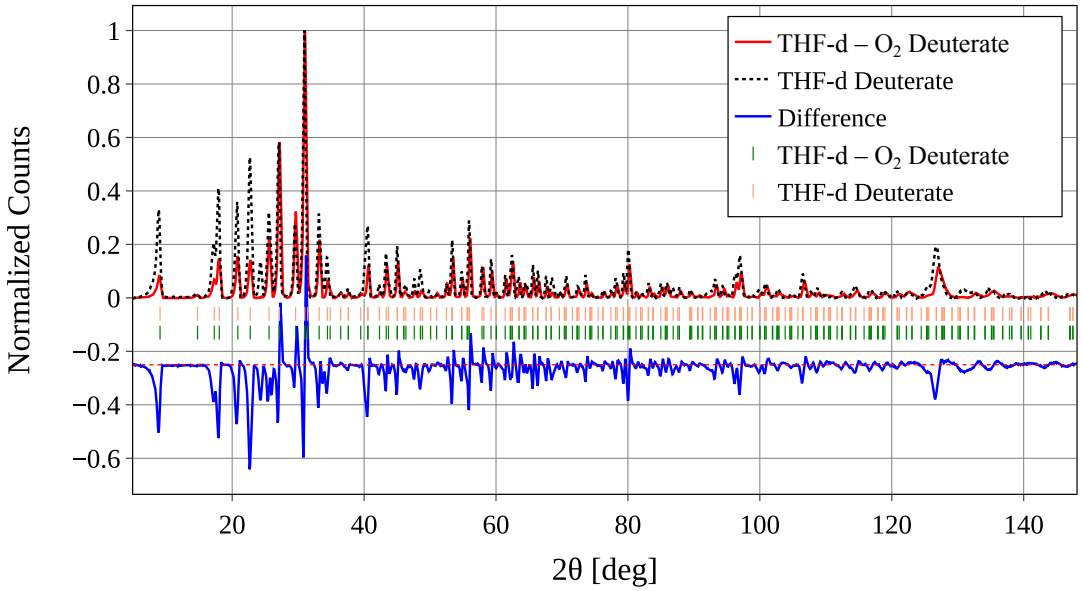

Figure 4.4.: Comparison of the diffraction patterns of a powder of THF-d deuterate (black dotted line, peak position indicated in light salmon) and the bottom sample of THF-d – O_2 deuterate (red line, peak position indicated in green) at a temperature of 2 K. The difference of the two diffractograms is given in blue and shifted along the vertical axis by −0.25 indicated by a red dashed line for better visibility. See text for details.

deuterate, as depicted in Figure 4.5a, confirms the CS-II structure. At 2 K, the determined lattice parameter is $a = 17.12202 \pm 0.00031$Å, which agrees reasonably well with the reported data in [129] (see also Section 4.2.3).

The reliability factors of the refinement [149] at a base temperature of 2 K for a refinement spanning the entire 2θ-range ($4.5\,^\circ - 148.5\,^\circ$) are computed as $R_p = 18.0$, $R_{wp} = 20.7$, $R_e = 2.85$. These factors can be further reduced to $R_p = 12.5$, $R_{wp} = 14.0$, $R_e = 2.21$ by limiting the 2θ-range to $4.5\,^\circ - 60.5\,^\circ$. Both the top and bottom samples (see Section 4.1) exhibit very similar purity of the CS-II hydrate phase, with weight percentages of $99.41 \pm 1.67\%$ for the top sample and $98.78 \pm 2.02\%$ for the bottom sample. The primary impurity is assumed to be residual ice Ih, with weight percentages of $0.59 \pm 0.27\%$ and $1.22 \pm 0.20\%$. Similar results were obtained for temperatures ranging from 2 K to 80 K.

One of the primary objectives of this study was to estimate the O_2 occupation within the 5^{12} cages. In this context, it is assumed that the larger $5^{12}6^4$ cages are exclusively and fully occupied by the significantly larger THF-d molecule (see Figure 4.5b). The longest end-to-end distance within the THF-d and oxygen molecules, calculated from the molecular coordinates provided in [150] and [151], is 4.16 Å and 1.23 Å, respectively. Although the occupation of the $5^{12}6^4$ cages is not entirely excluded, it is considered negligibly small based on the stoichiometric composition of the THF-d deuterate (see also [129]). The occupation of 5^{12} cages was determined by treating the occupation number *occ* of the oxygen within the cage as a free fitting parameter. Given that

its site has a Wyckoff multiplicity of $m = 32$, and the general multiplicity of the *Fd3m* space group is $M = 192$, the cage occupation of O_2 can be calculated using Equation 4.3.

The refinements of the data of the top and bottom sample at 2 K gave very comparable occupation numbers of 0.798 ± 0.015 and 0.801 ± 0.011 respectively, indicating a homogeneous formation of the deuterate throughout the pressure cell. As a counter check we can compare the computed volume density of the hydrate with the one of a fully occupied THF – d and THF-d – O_2 deuterate, which is 1.29 g/cm^3 for the evaluated cell parameter. The volume density of the refined structure can be calculated by adding up all the mass contributions of the unit cell divided by its volume

$$\rho = \sum_{j}^{N} \frac{f_j M j}{a^3} \ , \tag{4.9}$$

which results in 1.257 g/cm^3 and 1.258 g/cm^3 for the top and bottom sample respectively. The difference to the fully occupied deuterate of about 0.03 g/cm^3 accounts for 20 % of the 5^{12} cages being empty.

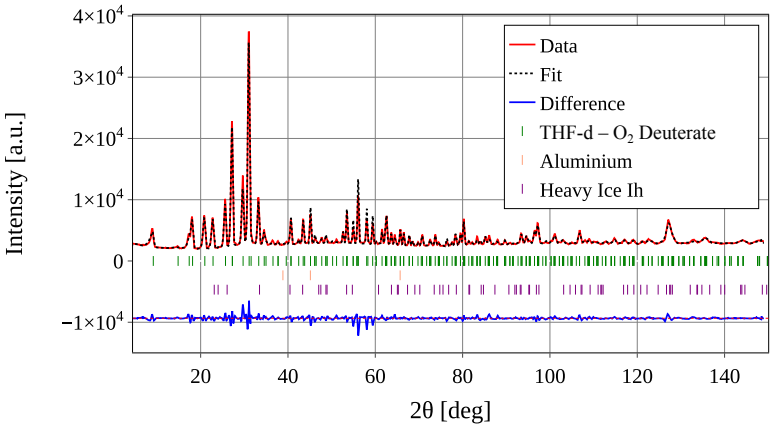

(a) Diffractogram of the THF- and THF-d – O_2 deuterate.

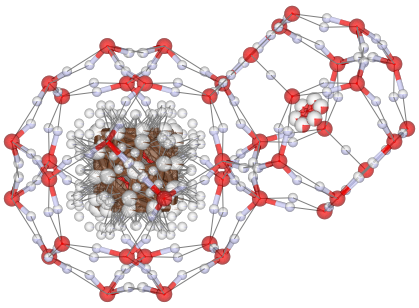

(b) One $5^{12}6^4$ cage occupied with a THF-d molecule and one 5^{12} cage occupied with an O_2 molecule.

Figure 4.5.: Diffractogram of the bottom sample of the THF-d and THF-d – O_2 deuterate (a), one representative $5^{12}6^4$ cage occupied with a THF-d molecule and one 5^{12} cage with O_2 computed from the refined pattern (b). The original data is depicted in red. The fit from the refinement (dashed black) was obtained through a multi phase Rietveld refinement. The residuals are depicted in blue and shifted by -9.4×10^{-5} along the vertical axis indicated by a red dashed line. The peak positions for each considered phase are indicated by vertical lines. The reliability factors for a refinement over the given 2θ-range are computed to be $R_p = 18.0$, $R_{wp} = 20.7$, $R_e = 2.85$.

4.2.3. Thermal Expansivity

Figure 4.6 shows the diffractograms of the THF-d – O_2 deuterate bottom sample during cool-down arranged as a heatmap. The colorbar indicates the normalized counts while T is plotted on the vertical axis. Magnifying the range from $2\theta = [54°, 64°]$ clearly shows how the lines deviate from the vertical due to thermal expansivity of the sample. The parameters of the peak finding algorithm, described in Section 4.1.3, were carefully selected to prioritize those peaks in the analysis, with the highest prominence, i.e. $N = 19$ peaks for each given temperature for the THF-d – O_2 deuterate and $N = 15$ for the THF – d deuterate. Recalling that each peak corresponds to a specific lattice plane distance d_{hkl}, the temperature dependence of this lattice

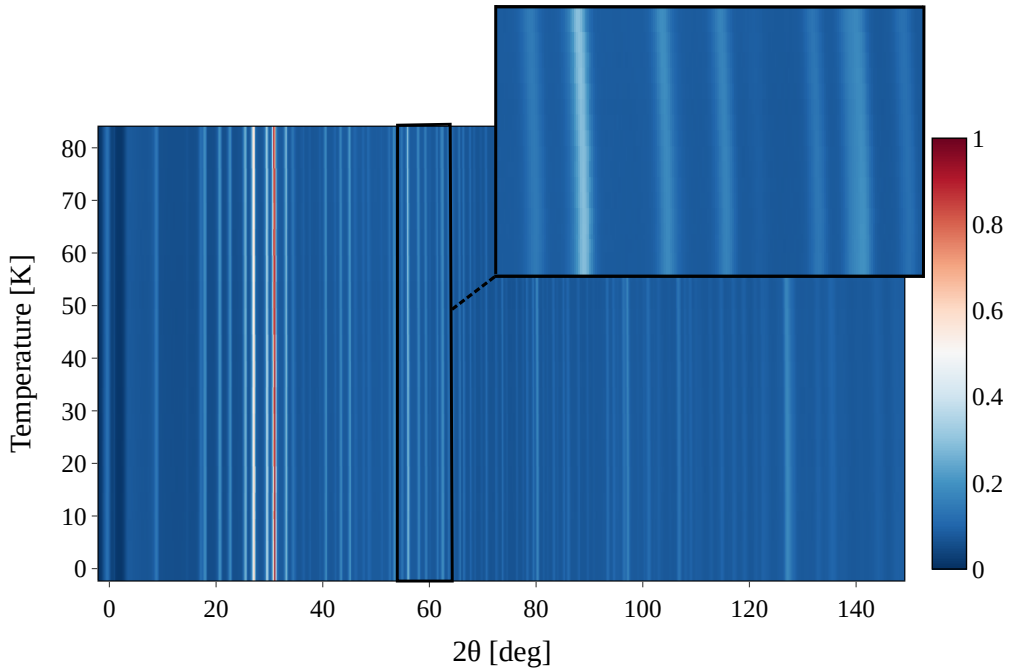

Figure 4.6.: Heatmap of the diffractograms measured at temperatures from 1.5 K to 80 K. The colorbar indicates normalized counts. The range $2\theta = [54^\circ, 64^\circ]$ is magnified in the upper right corner.

spacing can be calculated using Equation 4.8. Calculating $\Delta d/d$ for each diffractogram and computing the average yields:

$$\overline{\alpha}(T) = \frac{\overline{\Delta d}}{d\Delta T} = \frac{1}{N}\sum_{i=0}^{N}\frac{d_i(T) - d_i(T_0)}{d_i(T_0)(T - T_0)} \,. \tag{4.10}$$

Figure 4.7a presents the computed values of $\frac{\Delta d}{d}$ across all measured temperatures T_j for both the THF-d – O_2 and the THF–d deuterate. The solid lines represent a fit using Equation 4.6. The fit parameters are given in Table 4.2. To estimate the uncertainty of the fit parameters, a Monte Carlo method was employed. Generating data sets with random variations within the specified uncertainty of the original data and performing fits on these data sets allows to compute the average fit parameters and their corresponding uncertainties.

In the subsequent step, the calculated thermal expansivity was employed for cross-checking the thermal expansion derived from the refinement. The lattice parameter refinement was conducted using the Le Bail method [142, 152]. This method focuses on refining the lattice parameter for a predetermined space group rather than performing a full refinement. The reliability factors obtained were $R_p = 6.74$, $R_{wp} = 8.13$, and $R_e = 2.39$ for the THF-d – O_2 deuterate, and $R_p = 7.01$, $R_{wp} = 8.50$, and $R_e = 2.85$ for the THF–d deuterate at $T = 2\,\mathrm{K}$. Similar results were observed at other temperatures.

Figure 4.7b illustrates the expansion of the lattice parameter a as a function of temperature. The circles represent computed values of a using the Le Bail method. The solid lines depict $a(T)$ as in Equation 4.5, utilizing the $\alpha(T)$ values from Figure 4.7a, and a_0 denotes the lattice parameter at the base temperature of $T = 2\,\mathrm{K}$, which is $17.0867 \pm 3.2 \times 10^{-4}$Å for the THF-d – O_2 deuterate and $17.1094 \pm 4.1 \times 10^{-4}$Å for the THF–d deuterate, respectively.

Table 4.2.: Fit parameters for the thermal expansivity $\alpha(T)$ described in Equation 4.6 for the two investigated samples.

	THF-d – O_2 Deuterate	THF-d Deuterate
α_0	$-2.56 \times 10^{-5} \pm 9.9 \times 10^{-6}$	$-3.17 \times 10^{-5} \pm 2.5 \times 10^{-5}$
α_1	$4.00 \times 10^{-6} \pm 6.5 \times 10^{-7}$	$-2.34 \times 10^{-6} \pm 1.3 \times 10^{-6}$
α_2	$3.06 \times 10^{-7} \pm 8.3 \times 10^{-9}$	$2.49 \times 10^{-7} \pm 1.3 \times 10^{-8}$

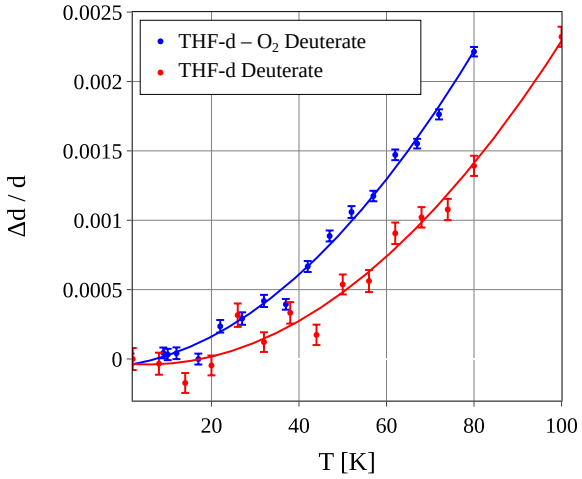

(a) Average values of $\frac{\Delta d}{d} = \alpha \Delta T$ calculated from diffractograms taken at temperatures between 2 K and 100 K. The solid line depicts a fit for the thermal expansivity $\alpha(T)$.

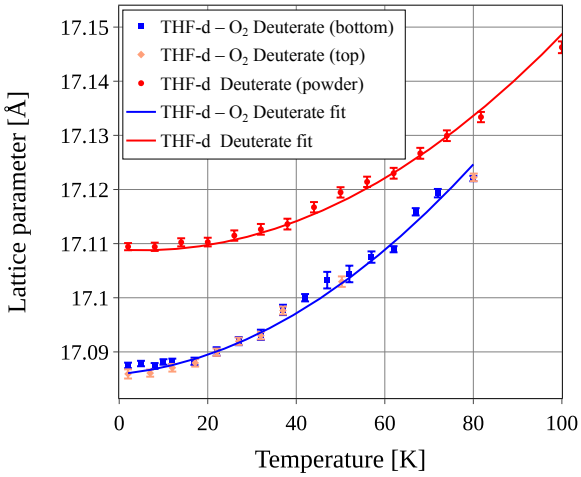

(b) Thermal expansion of the lattice parameter a. The circles depict the lattice parameters calculated in Fullprof using the Le Bail method. The solid lines use the computed $\alpha(T)$ and Equation 4.5.

Figure 4.7.: Thermal expansivity $\alpha(T)$ calculated as outlined in Equation 4.8 (left) and expansion of the lattice parameter of THF-d – O_2 deuterate and THF – d deuterate (right). The thermal expansion of the lattice parameter compares the values obtained with the Le Bail method (blue, red and pink circles) with the prediction resulting from $a(T) = a_0\,\alpha(T)$ (solid lines), where $a_0 = a(T_0 = 2\,\mathrm{K}) = (17.0867 \pm 3.2 \times 10^{-4})$Å for the the THF-d – O_2 deuterate and $(17.1094 \pm 4.1 \times 10^{-4})$Å for the THF – d deuterate respectivly.

4.3. Discussion and Conclusions

The apparent reduction in unit cell size for the binary THF-d – O_2 deuterate, compared to THF – d deuterate, might raise concerns about the reliability of the Rietveld refinement results. However, this outcome is not only supported by the raw data but also consistent with existing literature. Figure 4.8 displays the peak positions in the specified temperature range between $2\theta = 20°$ and $2\theta = 57°$. The peak positions of THF – d deuterate are visibly shifted towards lower angles, indicating a larger unit cell. In fact, the ratio of two identical hkl-plane distances d_{hkl}, calculated from the first peak position in Figure 4.8 using Equation 4.7, corresponds to the ratio of their respective lattice parameters determined by the Le Bail method. For the samples at $T = 2\,\mathrm{K}$, this is expressed as:

$$\frac{d_{O_2}}{d_{\mathrm{no}\,O_2}} = \frac{\sin\left(\theta_{\mathrm{no}\,O_2}\right)}{\sin\left(\theta_{O_2}\right)} = 99.84 \pm 0.008\% \,. \tag{4.11}$$

In comparison the ratio of the lattice parameters calculated with the Le Bail method at the same temperature is:

$$\frac{a_{O_2}(T = 2\,\mathrm{K})}{a_{\mathrm{no}\,O_2}(T = 2\,\mathrm{K})} = \frac{17.087(5)}{17.109(4)} = 99.871 \pm 0.004\% \,. \tag{4.12}$$

It is worth noting though, that the values obtained for the lattice parameter of the binary deuterate $a(T = 80\,\mathrm{K}) = (17.122 \pm 0.001)\,\text{Å}$ is slightly larger than the one reported for the corresponding hydrate in [129] ($a(T = 100\,\mathrm{K}) = (17.1143 \pm 0.0005)\,\text{Å}$). This difference could be attributed to both deuteration and the filling of the 5^{12} cages. The contribution of the cage filling, which is not reported in [129], can significantly impact the unit cell expansion, particularly at higher temperatures [132]. Deuteration generally weakens H-bonds in ice Ih and clathrate hydrates, resulting in longer bond distances [132], which could contribute to the observed discrepancy. The values of the lattice parameter of the THF-d deuterate seem to be in reasonable agreement with the literature [145, 147, 153], which shows variations of up to 0.03 Å at comparable temperatures. The observed shrinking of the unit cell upon the introduction of

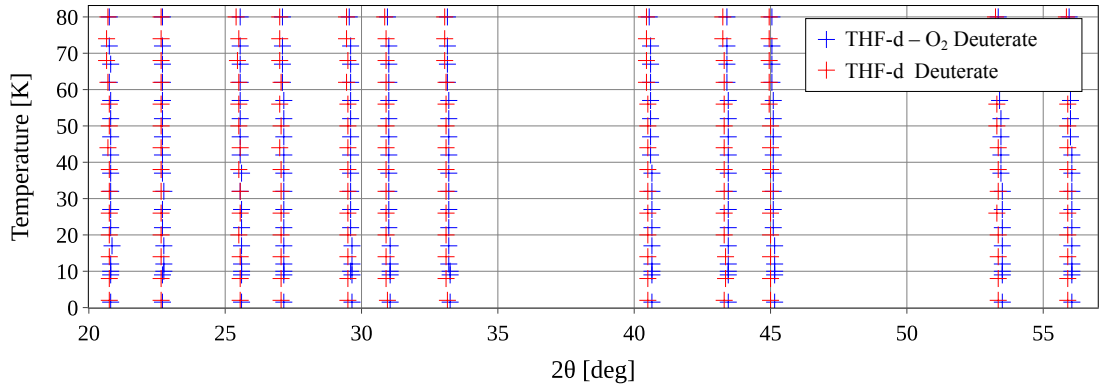

Figure 4.8.: Selected peak positions in a 2θ range between 20° and 57° for the measured temperature range. The peak positions of the THF – d deuterate are consistently shifted towards lower angles compared to the THF-d – O_2 deuterate, indicating a larger unit cell.

dioxygen into the 5^{12} cages could be attributed to guest-host attraction at low temperatures. Molecular dynamics simulations indicate an expansion of the H_2O network in the CS-I structure when the cages are left empty [154, 155]. This explanation finds support in data on N_2- and Ne-hydrates reported by [156], which shows a lattice shrinkage compared to the empty CS-II structure, and a larger lattice parameter for the significantly smaller Ne atom.

The analysis of thermal expansion proved to be more complex than anticipated. Earlier published data shows a large variety in the lattice parameter [145, 147, 153] and its thermal expansion [145, 147, 157]. This variation could be due to differences in cage filling and preparation methods, isotopic effects, or experimental uncertainties, as described in [132]. The strong non-linearity at low temperatures is characteristic of the composition of clathrate hydrates as an Einstein solid [158, 159]. The low frequencies of the guest molecule's rattling modes allow for excitations at very low temperatures. This is exactly the property, that we intend to exploit for neutron moderation. It is also visible in the thermal expansivity of the lattice parameter, which is heavily influenced by the coupling of these modes with the lattice structure [117].

The low onset temperature of this Einstein modes explain the particular form of $\alpha(T)$ observed in Figure 4.7a. It also accounts for the steeper increase in the thermal expansivity of THF-d – O_2 deuterate compared to THF – d deuterate. The higher abundance of O_2, nearly twice as much, allows for a wider range of rattling excitations, resulting in increased expansivity at

low temperatures. This effect vanishes at higher temperatures when the excitation spectrum is dominated by acoustic modes of the host lattice.

Further exploration of this effect would require additional data at higher temperatures and a more sophisticated expansion model, as complex interplay between guest-host interactions and lattice dynamics makes the study of thermal expansion in clathrate hydrates an intricate subject. Elements of such a model have been introduced by the authors of [132].

5. Inelastic Neutron Scattering Studies

5.1. Basic Principles of the Employed Time-of-Flight Spectrometers

Section 6.1 discusses the use of the time-of-flight technique to measure the spectrum of a white beam. The principle is based on the fact that the kinetic energy of a non-relativistic particle is given by $E = \frac{1}{2}mv^2$. If a chopper is employed to define the starting time of a bunch of neutrons, and we have precise knowledge of their flight path D, we can calculate their velocity v and hence their kinetic energy E by recording the arrival time t:

$$v = \frac{D}{t} \,. \tag{5.1}$$

In most cases in solid-state physics, however, one is not primarily interested in the properties of the neutron beam itself (although these properties are crucial for a successful experiment) or the transmission through a sample, but rather in the dynamics of the sample. To adapt the time-of-flight technique to study the dynamics of a sample, there are, in principle, two options:

1. Illuminate the sample with a monochromatic neutron beam and analyze the time-of-flight of the scattered neutrons, determining the energy gains and losses of the neutrons in the sample. This is called *direct geometry time-of-flight*.
2. Illuminate the sample with a wide-spread pulse of neutrons with a known energy distribution and analyze the final energy of the scattered neutrons using an analyzer crystal. The time-of-flight provides spectral information on the incoming neutron beam, and the known final energy allows conclusions to be drawn about the dynamics in the sample. This is called *indirect-geometry time-of-flight*.

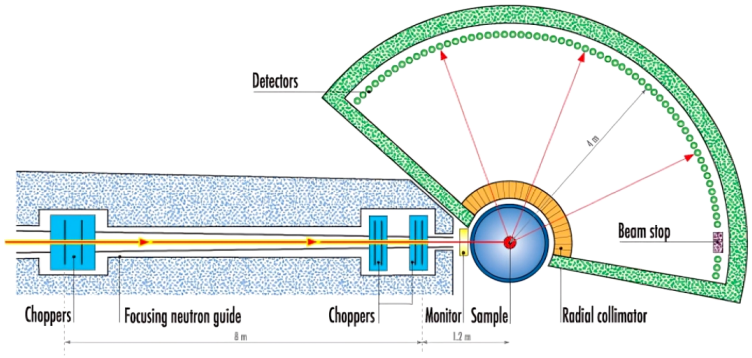

Figure 5.1.: Schematic of the IN5 spectrometer at the Institute Laue-Langevin. Image taken from [160].

The choice between direct- and indirect-geometry depends on the specific requirements of the experiment, including the desired energy resolution, the range of energy transfers to be studied, and the nature of the sample dynamics. In the context of this work, two direct geometry time-of-flight spectrometers – Panther and IN5 – and one indirect-geometry scanning spectrometer – IN1 - LAGRANGE – were used. These are briefly described in this section.

Figure 5.1 shows a schematic of the IN5 spectrometer. The continuous cold, white neutron beam is pulsed by an initial pair of choppers, which also pre-select a narrow wavelength distribution $\Delta\lambda$. The incident wavelength λ is then further refined by two additional pairs of choppers. This refinement is achieved by controlling the phase difference in the choppers' rotation. By adjusting this phase difference, the specific wavelength band that is transmitted can be selected. The sequence of choppers serves multiple functions, by carefully tuning the phase two choppers select the wavelength band, while one removes the harmonics $n\lambda$ and another one resolves possible frame overlaps. It is important to note, that tuning the width of the wavelength band involves a trade-off between neutron flux at the sample and the achievable energy resolution. While narrower bands enhance the instrument's resolution, they also result in a significant reduction in the number of neutrons reaching the sample. During a regular reactor cycle, the flux at the sample of IN5 reaches approximately $6.83 \times 10^5\,\mathrm{n/cm^2/s}$ at $\lambda = 5\,\text{Å}$ [160].

Despite this trade-off, the result is a monochromatic, pulsed neutron beam that illuminates the sample. The scattered neutrons are detected by a large array of ^{3}He position-sensitive detectors (PSDs) that allow for the determination of the scattering angle and hence the transferred q-vector. Through time-of-flight information, the energy transfer can also be determined. With a high incident wavelength and a large detector array with high angular resolution, IN5 is optimized for probing low energy transfer processes, in the order of magnitude of 0.1 to 250 meV [160].

Panther (**P**olarisation **an**alysis with **ther**mal neutrons) [161], on the other hand, is a "hybrid" direct geometry time-of-flight spectrometer designed for high flux and medium resolution at intermediate energy transfers (7.5 to 171 meV) [162]. Its schematic is given in Figure 5.2. It has also proven to be an ideal instrument for studying the host lattice dynamics of our hydrate system at intermediate energy transfers.

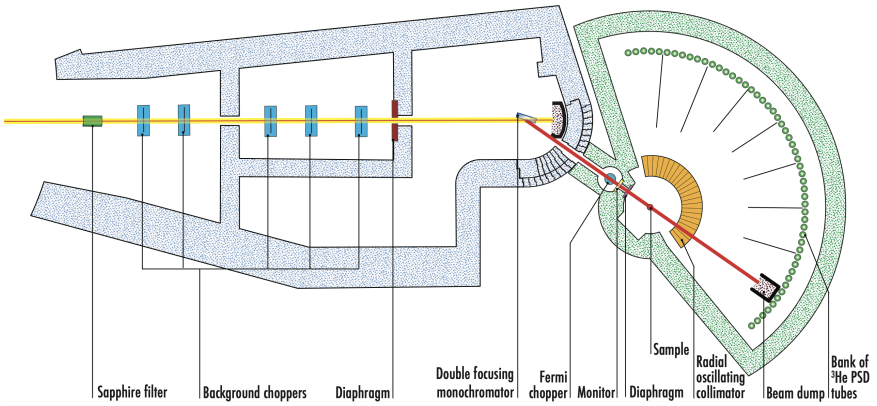

Figure 5.2.: Schematic of the Panther spectrometer at the Institute Laue-Langevin. Image taken from [162].

Panther uses thermal neutrons, which makes the use of choppers for monochromatization impractical, as it would require relatively large distances between the choppers and high angular velocities. This necessitates the use of a curved monochromator crystal to select the incident wavelength, giving it the name "hybrid" direct geometry time-of-flight spectrometer. Consequently, the flight chamber hosting the sample environment and the array of PSDs needs to be movable around the monochromator axis to allow the selection of different incident wavelengths. Finally, a Fermi chopper between the monochromator and sample position defines the origin in time ($t = 0$) and shapes the neutron pulse. A Fermi chopper usually consists of a rotating stack of neutron-absorbing material. Spinning at the right velocity, it not only gives the beam a pulsed structure but also allows slower neutrons to pass through the chopper before faster

ones, resulting in *time focusing*. This ensures that all neutrons that have undergone the same energy transfer arrive at the detectors simultaneously, which has beneficial consequences for the instrument's energy resolution [163].

Vibrational Spectrometry

The instrument IN1-Lagrange (**La**rge **Gr**aphite **An**alyzer for **G**enuine **E**xcitations) employs a different approach to analyze energy transfers to the sample. It is an indirect-geometry spectrometer that uses a set of monochromating crystals to scan through available incident energies by moving the instrument around the monochromator axis, rather than monitoring the time-of-flight of an incoming neutron pulse of a known spectrum. The focusing pyrolytic graphite analyzer crystals reflect only neutrons with a final energy of $E' = 4.5\,\text{meV}$.[1] With four available monochromators – Si(111), Si(311), Cu(220), and Cu(331) – the instrument covers an energy range from 4.5 to 500 meV. The energy resolution, $\frac{\Delta E}{E}$, is approximately 2%, though it varies depending on the selected monochromator and Bragg reflection. For the Si monochromators the resolution is limited by the mosaicity of the crystal to about 0.8 meV. In general, the reflected wavelength band broadens at shallower Bragg angles, which correspond to higher energy transfers, leading to a reduction in resolution [164]. In addition to the lower resolution, the interpretation of the data becomes challenging at higher energy transfers due to the diminished intensity caused by the Debye-Waller factor and the presence of harmonics and combinations in the vibrational spectrum.

It is important to note that, for each energy transfer point, all neutrons that fulfill the Bragg condition at the analyzer crystal are reflected towards the same detector. As a consequence, no q-dependence can be extracted from the data. The resulting information is not the dynamic structure factor $S(q, \omega)$, but rather $S(\omega)$ without any q information.

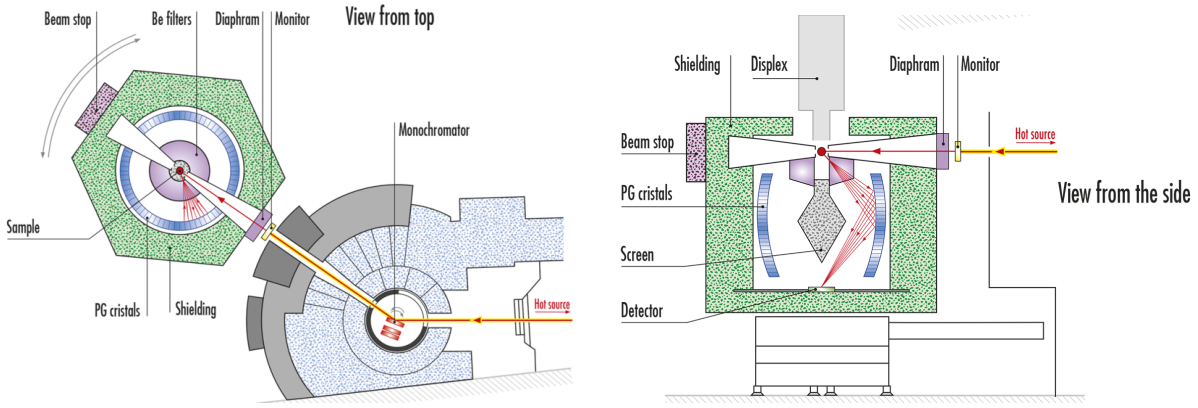

(a) View from top.

(b) View from side.

Figure 5.3.: Schematic of IN1-Lagrange at the Institute Laue-Langevin. Images taken from [165].

[1] In fact, this is not the whole story. Due to Bragg's law $n\lambda = 2d\sin(\theta)$, the analyzer crystals also allow for harmonics, i.e., reflections with $n > 1$. These reflections are suppressed with Be filters; see Figure 5.3.

5.2. Self-Shielding and Multiple Scattering

5.2.1. Attenuation and Self-Shielding

The transmission of neutrons through a material can be described with the Beer-Lambert law, Equation 2.6. This is described in detail in Chapter 6. In a direct-geometry time-of-flight experiment neutrons pass a certain amount of sample material before and after the scattering event of interest. Consequently, the count rate at the detector is attenuated, as a function of the energy dependent macroscopic cross section an the path the neutron travels through the sample. This scenario, as discussed in [43, Chapter 10.1.1] is depicted in Figure 5.4. The neutron travels a distance L_i, before scattering within a volume dV and leaving the material after traveling the distance L_f through the sample. Due to the finite thickness of the sample the neutron beam is attenuated exponentially according to Equation 2.6; this is referred to as *self-shielding* or *self-attenuation*. To calculate the transmission (T) through the sample and correct for self-shielding, one needs to solve the integral [43, Equation 10.5]:

$$T = \frac{1}{V}\int_V \exp\left(-\Sigma_t(\lambda)L - \Sigma_t(\lambda')L'\right)dV \ . \tag{5.2}$$

While for limited sample geometries this integral can be evaluated analytically, it must in general be evaluated numerically. Tabulated values are given in [166, 167]. It can be shown that the angular dependency of the self-shielding is minimized for cylindrical and particularly hollow cylindrical samples geometries (see [168, 169]). Principally, any geometry with rotational symmetry along the axis perpendicular to the scattering plane will have favorable attenuation properties.

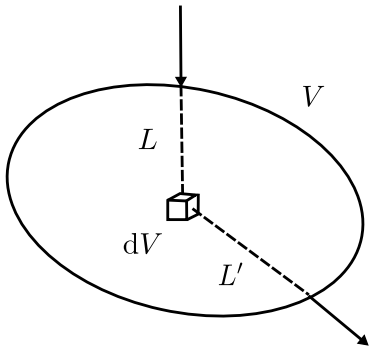

Figure 5.4.: The path of a neutron through the sample for the calculation of the attenuation factor. Figure adapted from [43].

5.2.2. Using Monte Carlo Simulations for Self-Shielding Corrections

A common approximation that is made is to only consider elastic scattering for self-shielding corrections, i. e. assuming that $\Sigma_t(\lambda) = \Sigma_t(\lambda')$. If one also wants to take inelastic scattering into account, and possibly also the sample environment in addition to the attenuation due to the sample, one needs to resort to simulation tools.

A convenient way to address this in the context of analyzing data from direct geometry spectrometers at the ILL is using *Mantid* [170, 171], specifically the `DirectILLSelfShielding` algorithm [172], which uses `MonteCarloAbsorption` [173] as a backbone. This algorithm employs a MC simulation to determine the correction factors at each position in the detector array for each recorded time-of-flight channel. The sample material geometry as well as the sample container are specified beforehand. The simulation does not account for the specific crystalline

structure of the material. It rather calculates the average cross section per atom and then uses the Hamilton-Darwin approach [174, 175] as described in [176]. The algorithm then samples from random scattering points within the sample and calculates through the sample and container objects. The self-attenuation factor is computed for each neutron track according to Equation 5.2, and the average attenuation factor is assigned to each point in the detector array and time-of-flight channel.

Figure 5.5 presents the calculated attenuation factors for the measured vanadium standard at Panther. The heatmap illustrates the attenuation factor for each of the 73728 PSD spectra in the array as a function of time-of-flight in microseconds. The obtained attenuation factors, ranging from $T = 0.962$ to $T = 0.978$ for the annular vanadium standard with a thickness of 125 µm, align well with the expectations estimated using a slab approximation, as discussed in [43, Chapter 10.1.1]. This approximation assumes $\Sigma_t(\lambda) = \Sigma_t(\lambda') = 10.18\,\mathrm{b} \times 0.0722\,\mathrm{cm}^{-3}$, small angles of θ, and approximates the annular sample as a slab with a thickness of 250 µm, resulting in $T = 0.968$.

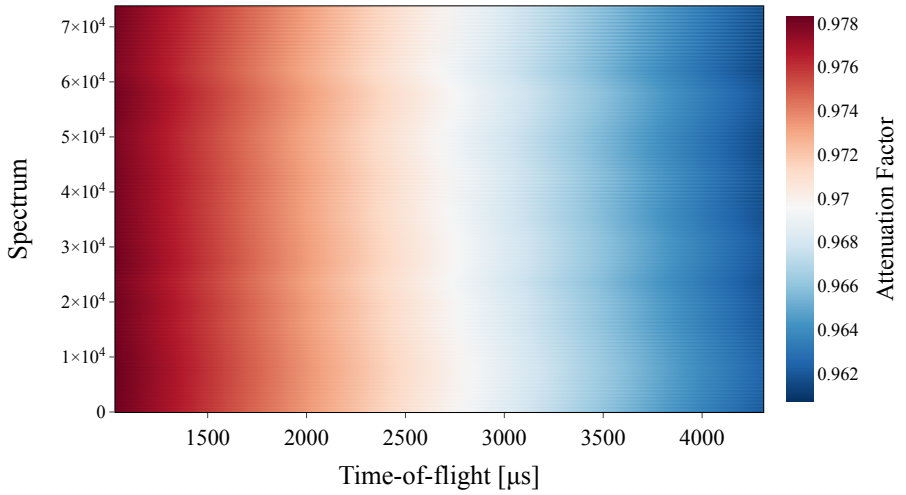

Figure 5.5.: Heatmap of attenuation factors for the vanadium standard at Panther, obtained using the `DirectILLSelfShielding` algorithm in Mantid. The attenuation factors are shown for each of the 73728 detectors as a function of time-of-flight in microseconds. It is evident that neutrons with larger time-of-flight (longer wavelength) exhibit stronger attenuation. This is due to the $1/v$-dependence of the neutron absorption cross section of vanadium.

The dimensions of the final samples are listed in Table 5.2. The attenuation factors for the hydrate samples remain nearly constant over the time-of-flight range. This is due to the small absorption fraction of the total cross section. The average attenuation factors obtained through simulations using the `DirectILLSelfShielding` algorithm are provided in Table 5.1 and compared with an elastic approximation through a thin slab.

5.2.3. Multiple Scattering

Another intrinsic source of uncertainty in neutron scattering experiments, arising from the finite size of the sample, is *multiple scattering*. For specific materials or large sample geometries, the probability that a neutron, having already scattered once, will undergo additional scattering can be significant.

Even though *self-shielding* and *multiple scattering* are related phenomena, they are distinct: self-shielding primarily affects the number of neutrons from the initial beam reaching the de-

Table 5.1.: Comparison of the average attenuation factor obtained with Monte Carlo Simulations using `DirectILLSelfShielding` with an approximation of a thin slab of thickness $2d$, with d being the wall thickness of the hollow cylinder (see Table 5.2).

Compound	Slab Approximation	MC Simulation
THF · H_2O	0.8927	0.8767
THF · D_2O	0.9625	0.9577
THF-d · H_2O	0.9668	0.9672
THF-d · D_2O	0.9078	0.8861

tector, whereas multiple scattering adds parasitic intensity to the signal from single scattering events. When at least one incoherent scattering event is involved, multiple scattering generally contributes only as a diffuse background. A particularly challenging situation occurs with multiple Bragg scattering, which may result in either a decrease in the intensity of expected Bragg peaks or the emergence of peaks at forbidden positions.

A derivation for an analytical expression for multiple scattering within the sample is given in [43, Chapter 10.1.2]. The fraction of scattered neutrons can be written as the sum of neutrons that scattered once (f_1) and the ones that scattered more than once (f_m):

$$f = f_1 + f_2 + \cdots + f_n = \sum_{i=1}^{n} f_i = f_1 + f_m \,, \tag{5.3}$$

where each fraction can be calculated recursively through an effective scattering function, which includes self-shielding as well as multiple scattering (see [43]). A commonly made assumption is that the ratio of neutrons scattered j times to those scattered $j-1$ times is constant, such that $\frac{f_j}{f_{j-1}} = \frac{2}{f_1} = \Delta$ [55, 177, 178]. This allows to estimate the fraction of multiple scattered neutrons via

$$\begin{aligned} f_m &= f_1 \frac{\Delta - \Delta^n}{1-\Delta} \\ &\approx f_1 \frac{\Delta}{1-\Delta} \end{aligned} \,. \tag{5.4}$$

In the last step we used that for $\Delta < 1$, $\Delta^n \ll 1$. This shows that it is sufficient to estimate the first and second-order contributions in order to asses the effect of multiple scattering. However, solving an expression for double scattering alone can be quite challenging and requires numerical methods. This process is outlined for different geometries in [55].

Another way to estimate multiple scattering is through Monte Carlo simulations. Although this method is computationally more expensive than solving analytical expressions, it avoids many associated limitations. By using an appropriate scattering kernel, the commonly made assumption of isotropic scattering can be relaxed. Additionally, intermediate energy transfers during scattering can be incorporated, and the geometries of the sample and its environment are not restricted to "simple" cases.

One approach to setting up such a simulation is through ray tracing using OpenMC [89] or McStas [88]. If Δ is the primary focus, these virtual experiments can be simplified. By tracing the trajectory of each neutron passing through the sample, the fractions f_1, f_2, …, f_n can be readily obtained from the result.

5.2.4. The Optimal Sample Geometry

The most convenient way to deal with multiple scattering is to minimize its occurrence. This can be accomplished by selecting an appropriate sample geometry and optimizing its dimensions.[2]

From the perspective of self-shielding, rotational symmetry is essential, allowing for the use of cylindrical and annular cells. In many direct-geometry spectrometers, as well as in instruments employing large arrays of detectors or analyzer crystals, hollow cylinders are preferred as the sample geometry. This allows for maximizing the sample size relative to the beam width, which, in instruments using cold neutrons, is typically on the order of 1 cm. At the same time, this geometry minimizes the sample volume and the associated path length through the sample, thereby reducing multiple scattering.

Optimizing Sample Thickness

The annular thickness of the hollow cylinder d is a trade-off between maximizing the signal of scattered neutrons and minimizing multiple scattering. The neutron-scattering rule-of-thumb is that the sample should act as a "10% scatterer" [43, 179], meaning that 10% of the neutrons entering the sample undergo at least one scattering event. The rationale behind this is that approximately 10% of the initially scattered neutrons will experience a second scattering event, and about 10% of those will scatter again, and so on. Therefore, a "10% scatterer" yields, for all intents and purposes, a tolerable level of multiple scattering within the sample.

For a hollow cylinder with an annular thickness d that is significantly smaller than its inner and outer radii ($d \ll R_1, R_2$), the scattering probability can be approximated by [179]:

$$S \approx \frac{\Sigma_s}{\Sigma_t} \left(1 - \exp -\pi \Sigma_t d\right) . \tag{5.5}$$

This represents the probability that a neutron will scatter at least once within the sample, followed by either exiting the sample, being absorbed, or undergoing additional scattering. Generally, this approximation tends to overestimate the actual scattering probability. Solving Equation 5.5 for t gives

$$d \approx -\frac{1}{\pi \Sigma_t} \ln \left(1 - \frac{S \Sigma_t}{\Sigma_s}\right) . \tag{5.6}$$

For samples that exhibit low absorption, so that $\Sigma_t \approx \Sigma_s$ and following the 10 % rule, we can write

$$d \approx -\frac{1}{\pi \Sigma_t} \ln (0.9) \approx \frac{1}{30 \Sigma_t} . \tag{5.7}$$

Table 5.2 shows the optimal annular sample thicknesses d using the 10% rule calculated with Equation 5.6 and the actual values of d as used in the experiment.

Estimation of Multiple Scattering with Monte Carlo Simulations

In order to quantify the fraction of multiple scattering within the chosen sample geometry, we designed an OpenMC model of a hollow cylinder that mimics the exact dimensions of the sample. The hollow cylinder is defined by an inner radius of $r_{\text{inner}} = 0.74$ cm and an outer radius

[2] Another important consideration is that multiple scattering requires a longer traversal distance within the sample. As a result, any absorber present within the sample naturally reduces the likelihood of higher-order scattering events, though this reduction in scattering is accompanied by a decrease in the overall flux. In some cases, however, this effect can be strategically exploited by intentionally adding absorbing materials to the sample.

Table 5.2.: Calculated annular sample thickness using the 10% rule and Equation 5.6.

Sample	THF $\cdot H_2O$	THF $\cdot D_2O$	THF-d $\cdot H_2O$	THF-d $\cdot D_2O$
Σ_s [cm^{-1}]	5.639	1.614	4.692	0.667
Σ_t [cm^{-1}]	5.661	1.619	4.710	0.667
d, 10% rule [cm]	0.0059	0.0208	0.0071	0.0503
actual d [cm]	0.005	0.005	0.005	0.010

of $r_{\text{outer}} = 0.75\,\text{cm}$, both of which extend infinitely along the x-axis for simplicity. This configuration creates a thin cylindrical shell filled with THF-d deuterates, a material whose scattering kernel is generated using NCrystal to account for inelastic scattering within the sample. The entire setup is enclosed by a large spherical boundary with a radius of $r = 100\,\text{cm}$, which acts as a vacuum boundary. This ensures that any particles reaching the boundary are considered to have left the simulation domain.

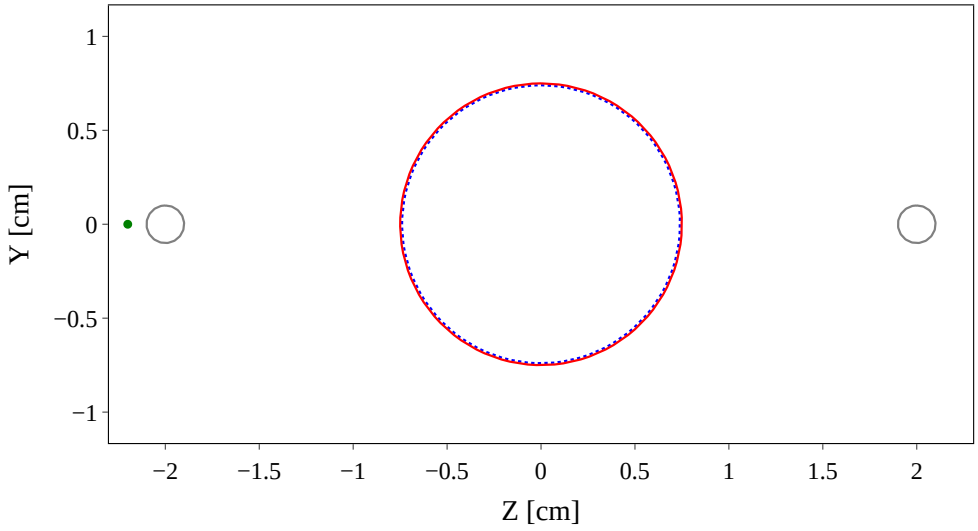

Figure 5.6.: YZ view of the simulated geometry for evaluating multiple scattering in a hollow cylinder. The blue dotted line indicates the inner wall of the cylinder, and the red line indicates the outer wall, constituting a wall thicknes of $t = 0.1\,\text{mm}$ Small spherical detector regions, shown in grey, are positioned along the z-axis at $z = -2\,\text{cm}$ (incident detector) and $z = 2\,\text{cm}$ (transmitted detector), each with a radius of $r = 0.1\,\text{cm}$. The source is located at $(0, 0, -2.2\,\text{cm})$, emitting particles monodirectionally towards the positive z-axis with energies uniformly distributed between 1 meV and 10 meV.

Figure 5.6 shows a YZ view of the simulated geometry. The inner wall of the hollow cylinder is indicated by the blue dotted line, and the outer wall is indicated by the red line. Incident and transmitted particles are detected using small spherical detector regions placed along the z-axis, before and after the cylinder. The incident detector is placed at $z = -2\,\text{cm}$, and the transmitted detector is at $z = 2\,\text{cm}$, with each detector having a radius of $r = 0.1\,\text{cm}$. They are both indicated in grey. This setup allows the calculation of the cross section through the simulation, providing a cross-check. A point source, located at $(0, 0, -2.2\,\text{cm})$, emits particles monodirectionally towards the positive z-axis, with energies uniformly distributed between 1 meV and 10 meV. The simulation operates in a fixed source mode with a defined number of particles and batches. Tallies are implemented to measure the flux in the incident and transmitted detector regions, while particle tracks are saved to capture detailed trajectories and interactions

for subsequent analysis. The calculated cross section from the simulated transmission is given in Figure 5.7. The agreement with the used NCrystal model for both the deuterated and protonated version indicates that the simulation is working properly.

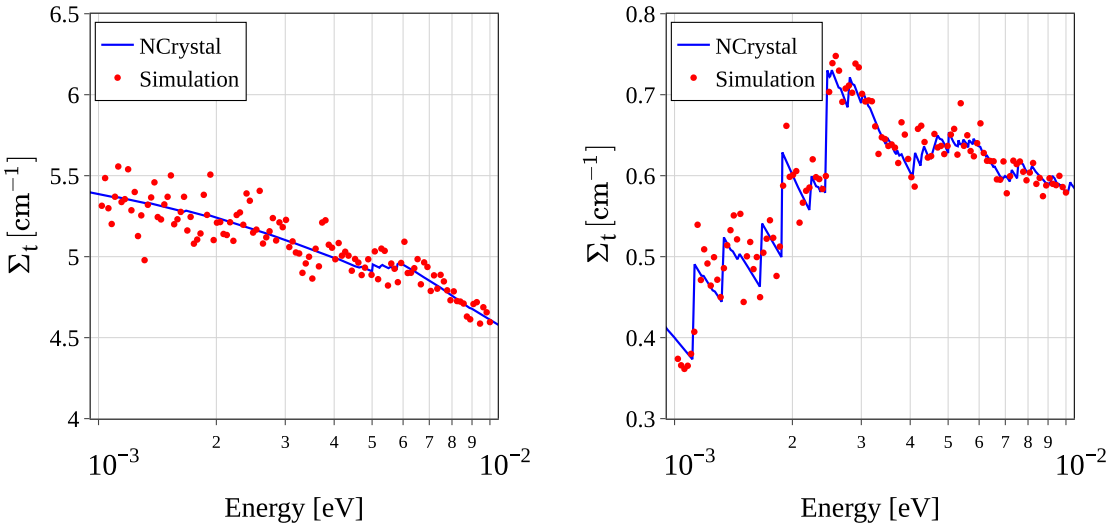

(a) Fully protonated sample.

(b) Fully deuterated sample.

Figure 5.7.: Simulated cross section of transmission through a hollow cylinder, as used at Panther and IN5, plotted as a function of energy. The blue line represents the input cross section used in the simulation, while the red markers indicate the cross section derived from the transmitted flux. The agreement between the simulated and calculated data validates the accuracy and reliability of the simulation.

The fraction of multiple scattered neutrons can be evaluated using the stored particle tracks. By scanning through each track and extracting the direction vectors, we can identify changes in the direction of the particle that are indicative of scattering events within the material. By recording the total number of scattering events for each track, we can calculate the fraction of single- and double-scattered neutrons. A total of $N = 44991$ analyzed particle tracks resulted in 5180 neutrons that scattered once, 129 that scattered twice, and 3 that scattered three times for the fully deuterated sample. The resulting multiple scattering fraction is with 0.29% negligible. The fraction of neutrons scattered more than once to neutrons scattered once is 2.6%.

Furthermore, this approach also enables testing the validity of Equation 5.4. The fractions f_1 and f_2 obtained from the simulation are used to calculate $\Delta = \frac{f_2}{f_1}$, and subsequently f_m. This also yields a fraction of 0.29%. It is important to note that the fraction of scattered neutrons is larger than the value estimated by Equation 5.5. This discrepancy arises because the scattering kernels account for Bragg scattering, which is not included in calculations based solely on tabulated values.

For the fully protonated sample, analysis of $N = 44991$ particle tracks for $t = 0.05\,\mathrm{mm}$ revealed 19720 neutrons scattering once, 1567 scattering twice, 134 scattering three times, and 10 scattering more than three times. The resulting multiple scattering fraction is 0.38%, this is again in very good agreement with the value obtained from Equation 5.4, which is 0.378%. The fraction of neutrons scattered more than once to neutrons scattered once is 7.9%.

5.3. Calibration to Absolute Units

Inelastic neutron scattering experiments allow the calibration of the measured intensity, thus converting the raw data into a cross section in absolute units of $[\mathrm{b\,sr^{-1}\,meV^{-1}}]$. For a quantitative analysis of the scattering kernel of clathrate hydrate samples, this is essential. A quantitative analysis of the moderation properties is feasible only if the scattering properties are known in absolute units. The possibility of calibration arises from the accurately known nuclear scattering lengths and amplitudes, along with typically minor and manageable corrections for self-shielding outlined above. A common approach, which was also employed here and is described in [43] involves measuring a standard sample with a known cross section.

For precise calibration, it is essential that the standard is measured under the same scattering geometry as the sample and occupies the same area within the neutron beam. To achieve this, we scanned the beam profile, as detailed below, to ensure that the neutron flux incident on the standard was identical to that on the sample. Vanadium is commonly used as a standard due to its consistent and well-characterized scattering properties. The fact that vanadium scatters almost exclusively incoherently, with $\sigma_{\mathrm{inc}}(V) = 5.08\,\mathrm{b}$ (see [51]), allows for the straightforward calculation of the calibration factor across the entire detector array. The differential cross section of the sample per atom (p. a.) in absolute calibrated units is given by [43, Equation 10.32]:

$$\left(\frac{\mathrm{d}\sigma}{\mathrm{d}\Omega}\right)_{S,\text{p. a.}} = \frac{\sigma_{\mathrm{inc}}(V)}{4\pi}\frac{\rho_V}{\rho_S}\frac{A_r(S)}{A_r(V)}\frac{C_S}{C_V}\,. \tag{5.8}$$

Here, A_r, ρ and C denote atomic weight, mass density, and normalized count rates associated with the sample and the vanadium standard, respectively.

While Equation 5.8 shows the principle of the vanadium calibration method, there are a few things to consider when applying this method to direct-geometry time-of-flight spectrometers. Firstly, on such an experiment one does not measure the differential cross section $\left(\frac{\mathrm{d}\sigma}{\mathrm{d}\Omega}\right)$, but rather $\left(\frac{k}{k'}\frac{\mathrm{d}^2\sigma}{\mathrm{d}\Omega\mathrm{d}E'}\right)$. Consequently C_S and C_V are functions of energy transfer, in terms of normalized counts per unit energy. For Equation 5.8 to be valid, the quantity C_V needs to be integrated over an appropriate energy range. In practice, this is done numerically in a separate procedure as discussed in [177]. Furthermore, the vanadium data needs to be corrected for self-attenuation and multiple scattering as described in 5.2.3, as well as the Debye-Waller factor as discussed below.

5.4. Measurement Procedure and Data Reduction

The dynamic structure factor $S(q,\omega)$ of these hydrates was determined using the instruments IN5 and Panther at the ILL. These experiments, carried out in spring 2021 as experiment 1-10-42 on IN5 [180] and experiment 1-10-49 on Panther [181], aimed to measure $S(q,\omega)$ over a large fraction of (q,ω)-space, which was made possible by the wide and complementary kinematic range of the two instruments.

Prior to the measurements, the vertical intensity profile of the beam was mapped using a low-density polyethylene (LD-PE) ring with a diameter of 1.45 cm and a height of 1.4 mm, placed at the bottom of a sample container. The LD-PE ring scatters strongly and almost isotropically. By vertically scanning the ring through the beam and monitoring the scattered signal, we were able to infer the vertical intensity profile of the beam. The integrated normalized counts on the detector array as a function of the position of the LD-PE ring are shown in Figure 5.8 for both instruments IN5 and Panther. The intensity profile is not flat and varies for each selected initial wavelength. Consequently, a small deviation in the vertical extension of the sample and

the vanadium standard can lead to significant errors in normalization. To mitigate this, we positioned the upper edge of the sample and the standard at a z-position that approximately corresponds to the average intensity over the vertical extension of the sample. This condition is met for a height between $z = 31\,\text{mm}$ and $z = 51\,\text{mm}$ for IN5 and $z = -21\,\text{mm}$ and $z = -1\,\text{mm}$ for Panther.

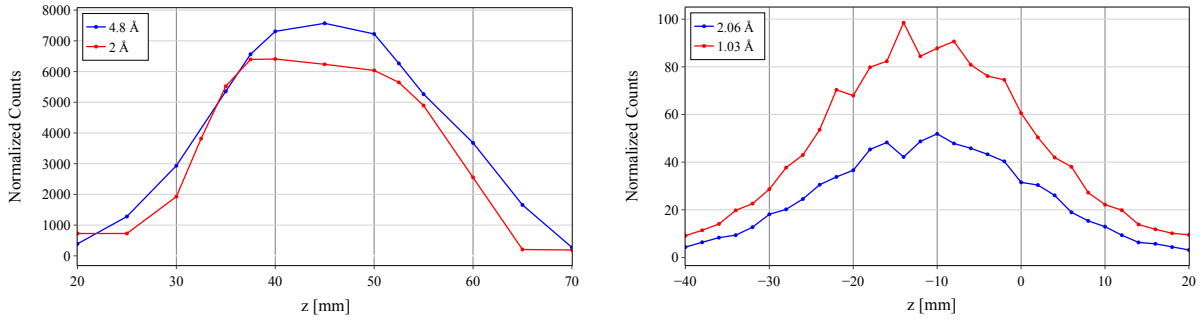

(a) IN5 (b) Panther

Figure 5.8.: Integrated normalized counts on the detector array as a function of the height of the LD-PE ring, showing the vertical intensity profiles of the neutron beam for the IN5 and Panther instruments (see text). The intensity profiles exhibit significant variations at different incident wavelengths. Thus, precise vertical alignment of the sample and the vanadium standard is crucial to ensure accurate normalization.

Table 5.3.: Differently deuterated and protonated samples prepared for the spectroscopy experiments [180] and [181]. The deuteration of either the guest molecule or the host lattice highlights different parts of the sample in the scattering signal.

	Abbrev.	Host Lattice	Guest Molecules
Fully protonated	THF · H_2O	136 H_2O	8 C_4H_8O
Deuterated cage	THF · D_2O	136 D_2O	8 C_4H_8O
Deuterated guest	THF-d · H_2O	136 H_2O	8 C_4D_8O
Fully deuterated	THF-d · D_2O	136 D_2O	8 C_4D_8O

The samples, prepared as described in Appendix G, are summarized in Table 5.3. A significant advantage of forming the hydrate from the liquid solution is the simple isotopic substitution in both the guest and host molecules. The distinct neutron cross sections of hydrogen (H) and deuterium (D) allow for contrast variation in spectroscopy experiments. By substituting one of the liquid components with its deuterated counterpart – water (H_2O) with heavy water (D_2O) and THF (C_4H_8O) with THF-d (C_4D_8O) – four different sample contrasts were obtained, as detailed in Table 5.3.

The annular sample cells were dimensioned to minimize self-attenuation (which was corrected for, see Section 5.2.1) and multiple scattering (see Section 5.2.3). The resulting masses and dimensions of the samples are summarized in Table 5.4. These data were used for self-shielding corrections and normalization to absolute units. For the vanadium standard, we rolled a sheet of 99.8 % V from Goodfellow [182] into a hollow cylinder within the Al sample container with the outer diameter of $\text{ø}_{\text{outer}} = 1.5\,\text{cm}$. The same standard was used in both experiments.

The experimental configurations at IN5 and Panther are summarized in Table 5.5. The measurement protocol included, in addition to the four samples, measurements of the respective empty sample cells for background corrections and a vanadium standard for normalization.

Table 5.4.: Dimensions and masses of the samples measured at experiment 1-10-42 on IN5 [180] and experiment 1-10-49 on Panther [181]. The uncertainties in the masses are ± 0.05 mg.

Sample	**ø$_{\text{inner}}$ [cm]**	**ø$_{\text{outer}}$ [cm]**	**Mass Panther [mg]**	**Mass IN5 [mg]**
THF · H_2O	1.39	1.40	45.3	42.6
THF · D_2O	1.39	1.40	45.9	46.6
THF-d · H_2O	1.39	1.40	44.3	43.4
THF-d · D_2O	1.48	1.50	101.0	101.3
Vanadium	1.487	1.50	707.8	707.0

Table 5.5.: Configurations for measurements conducted on ILL's TOF spectrometers. The overlap with the incident wavelength at 2 Å enables a crosscheck of the absolute units calibration.

Instrument	Panther	IN5
Incident energies E [meV]	77.1, 19.3	20.5, 9.1
Incident wavelength λ [Å]	$\sim$ 1.03, 2.06	$\sim$ 2.0, 3.0
Temperature [K]	1.5	1.5

Data Reduction

The data reduction was done in Mantid [170, 171] which serves as a successor for LAMP (Large Array Manipulation Program) [183, 184] for the data reduction and visualization at most neutron scattering instruments at the ILL. A great advantage of Mantid is that, while the computationally heavy algorithms are coded in `C++`, they can be called using python scripts.

The first step in every data reduction in Mantid is collecting and preprocessing the raw neutron scattering data with the `DirectILLCollectData` [185] algorithm. The algorithm merges the indicated runs saved in NeXus files and normalizes the detector spectra with the monitor counts and identifies the elastic peak position (EPP) with a fitting procedure. This allows calibration of the incident energy E by using the relation:

$$E = \frac{m_n D^2}{2t_{\text{el}}^2} \tag{5.9}$$

where t_{el} is the time-of-flight corresponding to the elastic peak. The total flight path D corresponds to the sum of the primary flight path D_1 between the Fermi chopper and the sample and the secondary flight path D_2 between the sample and the detector. This is done for the respective runs of vanadium, the empty cells and the samples. The raw data for the fully deuterated sample at an incident energy of $\lambda = 2$ Å recorded on IN5 is shown in Figure 5.9. This illustration shows the entire detector array integrated over the whole time-of-flight spectrum. Each of the visible Debye-Scherrer cones corresponds to a lattice plane distance d_{hkl} that fulfills the Bragg condition $\lambda = 2d_{hkl}\sin(\theta)$.

The vanadium data is integrated over the time-of-flight range of the elastic peak. This allows for masking faulty detectors that show no signal and provides the total scattering intensity of the vanadium standard, which is crucial for normalization to absolute units. The corresponding algorithm to this process is `DirectILLIntegrateVanadium` [186]. As a final step before computing $S(q,\omega)$ the empty container signal is subtracted and the data is corrected by the self-shielding factor, as calculated in Section 5.2.1. At this point the data corresponds to the double differential cross section per unit time, i.e., $\frac{\mathrm{d}^2\sigma}{\mathrm{d}\Omega \mathrm{d}\tau}$. The final reduction step normalizes the

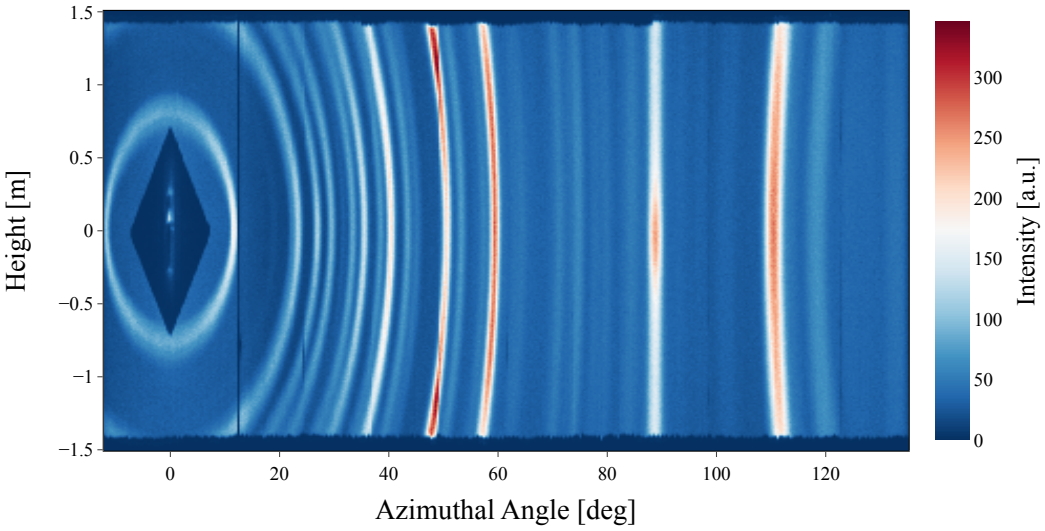

Figure 5.9.: Raw neutron scattering data for the fully deuterated sample at an incident wavelength of $\lambda = 2\,\text{Å}$ recorded on IN5 [180]. The detector array is integrated over the time-of-flight spectrum, showing Debye-Scherrer cones that correspond to lattice plane distances d_{hkl} fulfilling the Bragg condition. Note that the detector array is physically oriented to the left of the beam-stop, from a downstream perspective. For better readability, the data has been inverted.

data to absolute units of $[\text{b}\,\text{sr}^{-1}\,\text{meV}^{-1}]$ using the vanadium standard, as described in Section 5.3 and then converts it to units of energy transfer to obtain $\frac{\text{d}^2\sigma}{\text{d}\Omega\text{d}E} = \frac{\text{d}^2\sigma}{\text{d}\Omega\text{d}\hbar\omega}$. This is done using the algorithm `DirectILLReduction` [187].

A derivation of the conversion from time-of-flight τ to energy transfer $\hbar\omega$ is given in [43, Section 10.3.3]. Applying this conversion allows to write the the dynamical structure factor for a spectrum recorded at a given detector pixel of the detector array in cylindrical coordinates (φ, z), as

$$\left(\frac{\text{d}\sigma}{\text{d}\Omega\,\text{d}\hbar\omega}\right) = \left(\frac{\text{d}\sigma}{\text{d}\Omega\,\text{d}\tau}\right)\frac{(\tau-\tau_1)^3}{m_n D_2^2}\,. \tag{5.10}$$

Here, D_2 is fixed and correspond to the flight path of the neutron from the sample position to the detector. For direct geometry spectrometers, such as the one used here τ_1 is also fixed and corresponds to the time-of-flight of neutrons with the initial wavelength λ. Note that here φ is not the scattering angle but the azimuthal angle relative to the beam axis. Obtaining the actual $S(q,\omega)$ from $S(\varphi, z, \omega)$ requires an additional transformation. The scattering angle 2θ can be calculated from the coordinates (φ, z) of the recorded scattering event using the known geometry of the instrument. This quantity allows to calculate the wavevector transfer q from the known relation of the scattering triangle (see Equation 2.3):

$$q = \sqrt{k^2 + k'^2 - 2kk'\cos(2\theta)}\,. \tag{5.11}$$

This relation gives the characteristic shape of the $S(q,\omega)$ related to the kinematic range of the instrument, i.e. the possible values of energy and wavevector transfers that can occur during the interaction of incident neutrons with a sample. As an example, the kinematic range of Panther is illustrated in Figure 5.10 for the two incident wavelengths that have been used in the experiment.

The transformation of $S(2\theta,\omega)$ to $S(q,\omega)$ requires the calculation of another Jacobian deter-

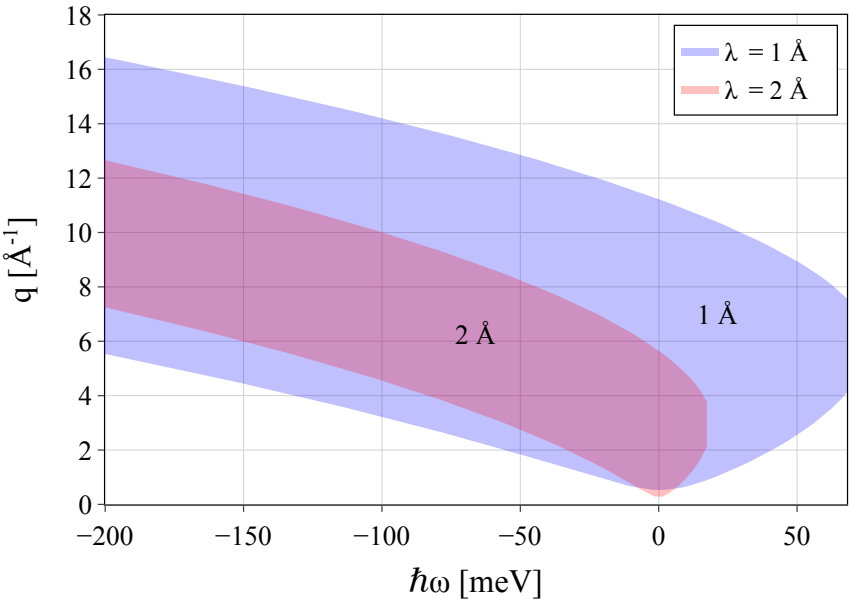

Figure 5.10.: Kinematic range of the Panther instrument for two incident wavelengths λ used in the experiment. Shaded areas show possible energy and wavevector transfers based on Equation 2.3.

minant, which requires the derivative

$$\frac{\partial q}{\partial \theta} = \frac{\partial}{\partial \theta}\left(\sqrt{k^2 + k'^2 - 2kk'\cos(2\theta)}\right), \tag{5.12}$$

so that

$$\frac{\partial q}{\partial \theta} = \frac{kk'\sin(2\theta)}{\sqrt{k^2 + k'^2 - 2kk'\cos(2\theta)}}. \tag{5.13}$$

This ultimately establishes the relationship between $S(2\theta, \omega)$ and $S(q, \omega)$, expressed as:

$$S(q,\omega) = S(2\theta,\omega)\frac{\sqrt{k^2 + k'^2 - 2kk'\cos(2\theta)}}{kk'\sin(2\theta)}. \tag{5.14}$$

The Jacobian is not explicitly calculated in Mantid. However, the normalization process in the algorithm used to transform $(2\theta, \omega)$ to (q, ω) (`SofQWNormalisedPolygon` [188]) uses a normalization, that numerically reflects the derivative in Equation 5.13.

Once $S(q, \omega)$ is obtained one can infer the structure of the sample by integrating energy to obtain $S(q)$, resembling a diffractogram. To study the dynamics, $S(\omega)$ can be obtained by integrating over a specified q-range. This quantity can be interpreted as a density of states or frequency distribution function, as it provides information about the distribution of energy transfers (ω) without differentiating between different momentum transfers.

Consistency Verification of the Vanadium Normalization

As a sanity check of the data reduction routine, the correction factors, and the vanadium normalization, we can again refer to the well-known scattering properties of vanadium. Figure 5.11 shows the dynamical structure factor obtained from the data reduction routine described above, normalized to absolute units.

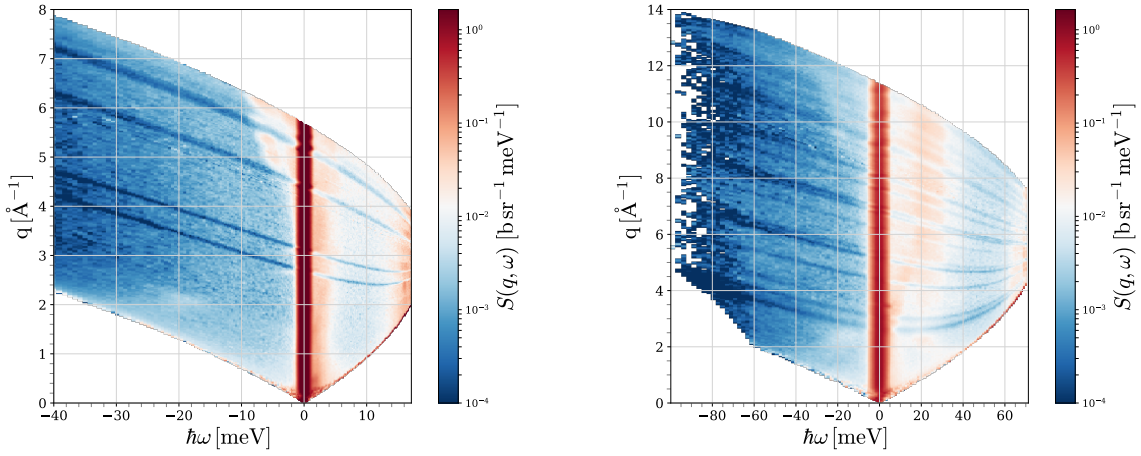

(a) $\lambda = 2\,\text{Å}$. (b) $\lambda = 1\,\text{Å}$.

Figure 5.11.: Dynamical structure factor $S(q,\omega)$ of vanadium obtained from the data reduction routine described above and normalized to absolute units. The data was obtained at Panther in Experiment 1-10-49 [181]. This serves as a validation of the applied correction factors and normalization process, utilizing the well-known scattering properties of vanadium. The dispersing energy gaps, tracing the outline of the kinematic region, originate from aluminum Bragg peaks at constant scattering angles.

By integrating the data over ω, we obtain the structure factor $S(q)$ for the vanadium standard, as illustrated in Figure 5.12. The results are presented in units of [mb sr^{-1}] for a q range from 1 to 2.5 Å. This q-range was chosen to avoid interference from the Bragg peaks of the aluminum environment and to minimize the influence of the Debye-Waller factor. To correct for the Debye-Waller factor, an estimate of the mean square displacement $\langle u^2 \rangle$ of the vanadium atoms is required, which can be calculated using the formula [189]

$$\langle u^2 \rangle = \frac{3\hbar^2}{2A_r(V)k_B\Theta_D}\left(1 + 2\frac{T}{\Theta_D}\right), \tag{5.15}$$

where $\hbar$ is the reduced Planck constant, $A_r(V)$ represents the atomic mass of vanadium, Θ_D denotes the Debye temperature, and T is the temperature of the vanadium standard. At a temperature of 5 K and with $\Theta_D = 380\,\text{K}$ this value allows us to compute and correct for the Debye-Waller factor, given by

$$\exp\left(-\frac{1}{3}\langle u^2 \rangle q^2\right). \tag{5.16}$$

Integration over solid angle introduces an additional factor of 4π and yields the scattering cross section of vanadium, which is $\sigma_s = 5.1\,\text{b}$ [51].

The results of the vanadium cross section show excellent agreement with the literature value for normalization on IN5 (see Table 5.6). This indicates that the normalization routine and the underlying algorithms are consistent. However, for the experiments conducted on Panther, there seems to be an underestimation of the scattering magnitude of the vanadium standard by approximately 4% and 9%, at $\lambda = 2.06\,\text{Å}$ and $\lambda = 1.03\,\text{Å}$ respectively. Since this effect depends on the incident wavelength λ, it may be due to the wavelength-dependent detector efficiency that is not yet well characterized. The wavelength overlap between these two instruments allows for an additional valuable cross-comparison of the normalization procedure with the sample measurements. This is discussed in Section 5.5.

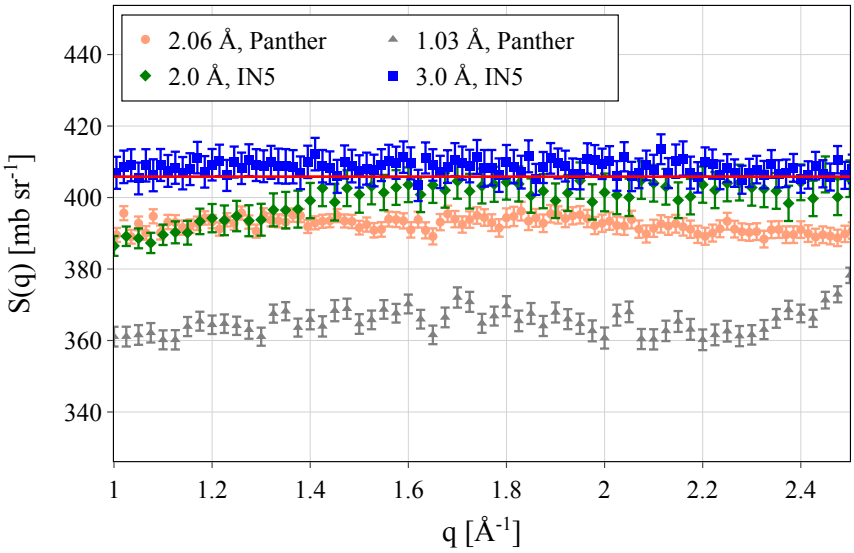

Figure 5.12.: Self consistency test of the incoherent cross σ_s of the vanadium standard. $S(q)$ was calculated in absolute units of $\mathrm{mb\,sr^{-1}}$. The solid red line denotes the well known scattering cross section of vanadium $\sigma_s = 406\,\mathrm{mb\,sr^{-1}}$ [51]. The isotropic scattering signal is constant in q, the integration over solid angle yields the results given in Table 5.6

Table 5.6.: Self-consistency test of the incoherent cross section σ_s of the vanadium standard. The established literature value is $\sigma_s = 5.1\,\mathrm{b}$.

Configuration	σ_s [b]
2.06 Å, Panther	4.93 ± 0.028
1.03 Å, Panther	4.65 ± 0.031
2.0 Å, IN5	5.05 ± 0.063
3.0 Å, IN5	5.14 ± 0.056

5.4.1. Presentation of Results obtained at Panther

Figure 5.13 and Figure 5.14 show the $S(q,\omega)$ maps measured at Panther for the incident wavelengths 2.06 Å and 1.03 Å. The samples listed in Table 5.3 were measured at a temperature of 1.5 K. The neutron dynamical structure factor was calculated from the raw data as described above. The normalization to absolute units was facilitated with a vanadium standard.

In the investigated energy region, the dynamics of the sample are dominated by the translational spectrum of the host structure. These lattice excitations result in two distinct peaks at approximately 7 meV and 10.5 meV, which are characteristic for all CS-II hydrate structures (see, e.g. [100, 116, 117, 190, 191]). Although these excitations are present in both the protonated and deuterated cage structures, they are particularly well visible in the THF-d $\cdot$ H_2O sample at an incident wavelength of 2.06 Å, as shown in Figure 5.13b. This is because the scattering contribution of the deuterated THF-d molecule is small compared to the protonated H_2O cages.

At higher energy transfers, as observed for the lower incident wavelength $\lambda = 1.03$ Å in Figure 5.14, the librational bands of the water molecules in the host structure become visible. This is preceded by a characteristic gap between translational bands and librational bands. The size of this gap is influenced by the mass of the molecular constituents. For deuterated host lattices, the vibrational excitations occur at lower energies compared to their protonated counterparts,

resulting in a smaller gap. This is because the increased mass of deuterons in the deuterated molecules lowers the librational frequencies, shifting the librational band to lower energies. It begins at around 55 meV for D_2O and at the higher energy end of the instrument's range, around 70 meV for H_2O. The vibrational energy spectrum is closer investigated in Section 5.7. This can be observed when comparing the samples with D_2O cages (see Figures 5.14a and 5.14c) with those with H_2O cages (see Figures 5.14b and 5.14d).

The dynamical behavior becomes more evident when looking at q slices through the dynamical structure factor $S(q, \omega)$, i.e. the average of the signal within a given interval in q. The data collected at Panther at a temperature of $T = 1.5\,\mathrm{K}$ are presented in Figure 5.15. These averages were calculated over the range of $q = [3.0, 5.0]\ \mathrm{Å}^{-1}$ for an incident wavelength of $\lambda = 2.06\,\mathrm{Å}$ and over $q = [6.0, 8.0]\ \mathrm{Å}^{-1}$ for $\lambda = 1.03\,\mathrm{Å}$, as shown in Figures 5.15a and 5.15b. The results were obtained using the `LineProfile` [192] algorithm in Mantid. For the incident wavelength of $\lambda = 2.06\,\mathrm{Å}$, characteristic peaks were observed at approximately 7.5 meV and 10.5 meV for the protonated host lattices and slightly red-shifted excitations for the deuterated ones. Additionally, lower-energy peaks around 3 meV and 4.9 meV, particularly prominent in the THF $\cdot$ D_2O sample, are indicative of localized excitations of the THF molecule. These low-energy excitations are more distinct in the data obtained from the IN5 instrument (see Section 5.4.2), which provides higher energy resolution and lower incident wavelengths.

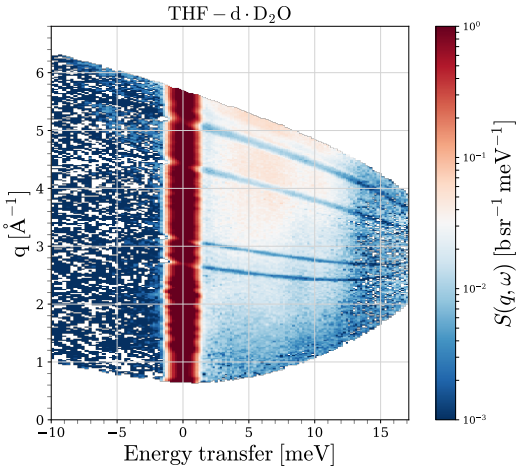

(a) Panther, 2.06 Å, THF-d ·D_2O.

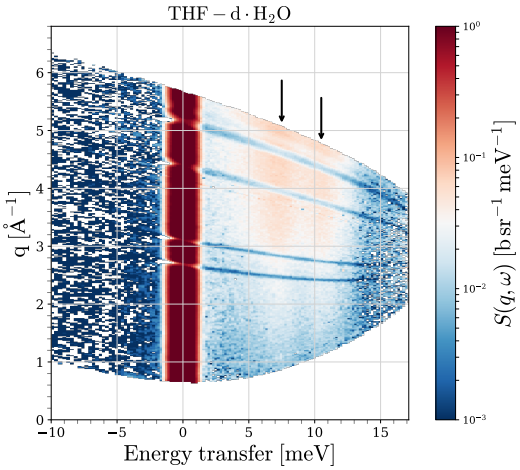

(b) Panther, 2.06 Å, THF-d · H_2O.

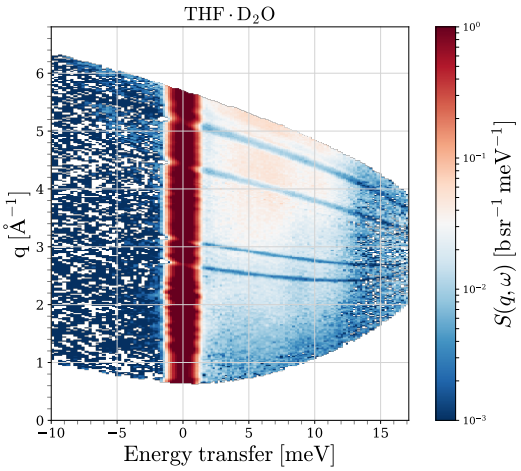

(c) Panther, 2.06 Å, THF · D_2O.

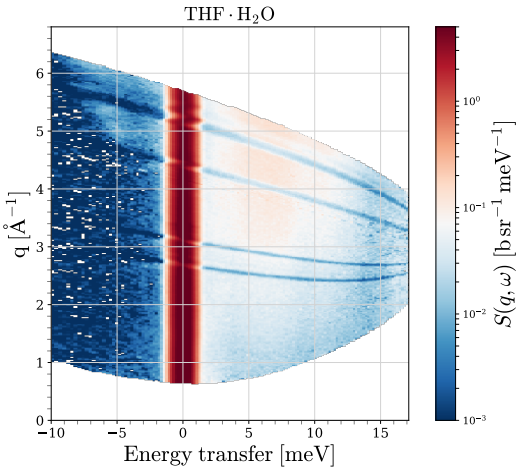

(d) Panther, 2.06 Å, THF · H_2O.

Figure 5.13.: Dynamical structure factor $S(q, \omega)$ for the hydrate samples listed in Table 5.3, at a temperature of 1.5 K and an incident wavelength of $\lambda = 2.06$ Å, presented in absolute units. The impact of isotopic substitution is evident when comparing THF-d · H_2O (b) with THF · D_2O (c). Note that the colorbar scales differ between subplots. The protonated host lattice clearly shows the characteristic CS-II cage excitations at about 7.5 meV and 10.5 meV indicated with two black arrows. The localized excitation of the THF molecules within the D_2O cage is more subtle but becomes evident when examining an averaged q slice. The dips in the signal at constant scattering angles are due to Bragg scattering from the sample container and environment. Although this is corrected for, the textured aluminum still leaves a residual artifact.

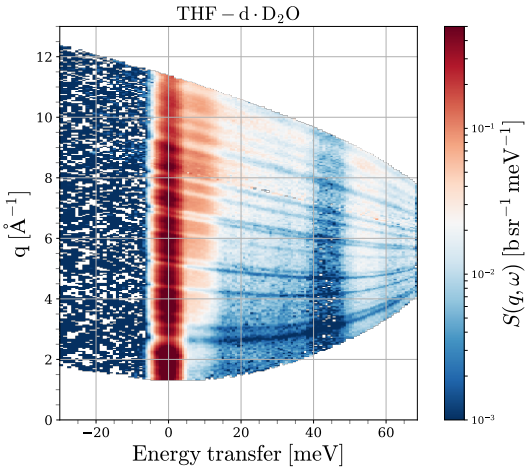

(a) Panther, 1.03 Å, THF-d $\cdot D_2O$.

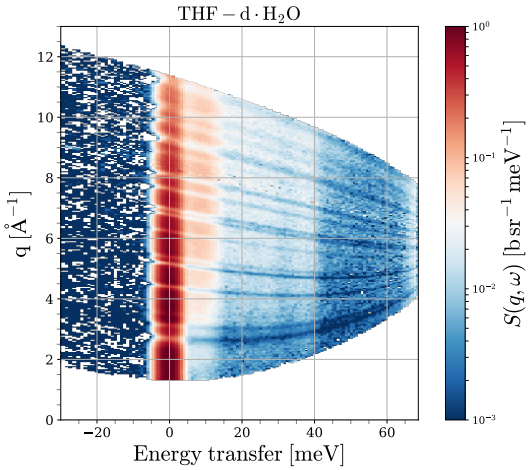

(b) Panther, 1.03 Å, THF-d $\cdot H_2O$.

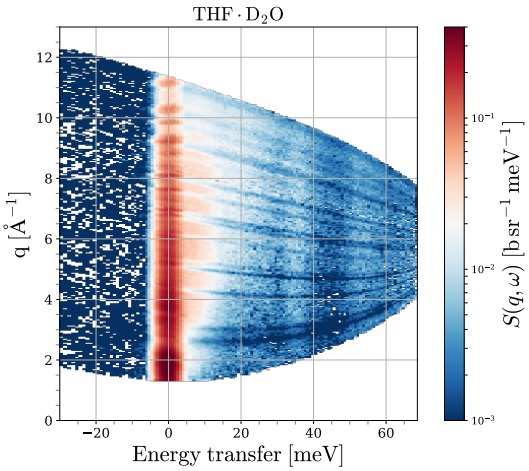

(c) Panther, 1.03 Å, THF $\cdot D_2O$.

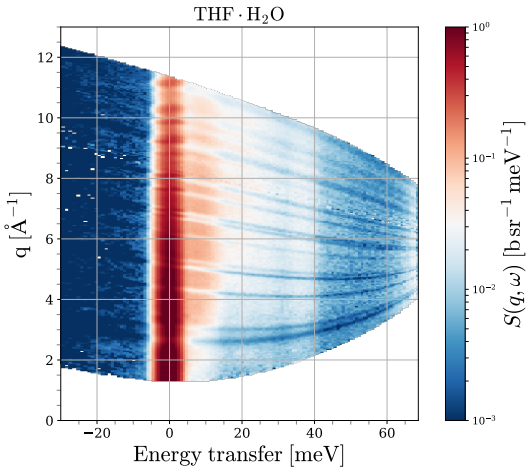

(d) Panther, 1.03 Å, THF $\cdot H_2O$.

Figure 5.14.: Dynamical structure factor $S(q, \omega)$ for the hydrate samples listed in Table 5.3, at a temperature of 1.5 K and an incident wavelength of $\lambda = 1.03$ Å, presented in absolute units. Note that the colorbar scales differ between subplots. The low incident wavelength allows measurements over the entire phonon range. The gap between phonons and librational modes differs for H_2O (40 meV–64 meV) and D_2O (40 meV–48 meV) due to the higher mass of deuterons. The dips in the signal at constant scattering angles are due to Bragg scattering from the sample container and environment. Although this is corrected for, the textured Al still leaves a residual artifact.

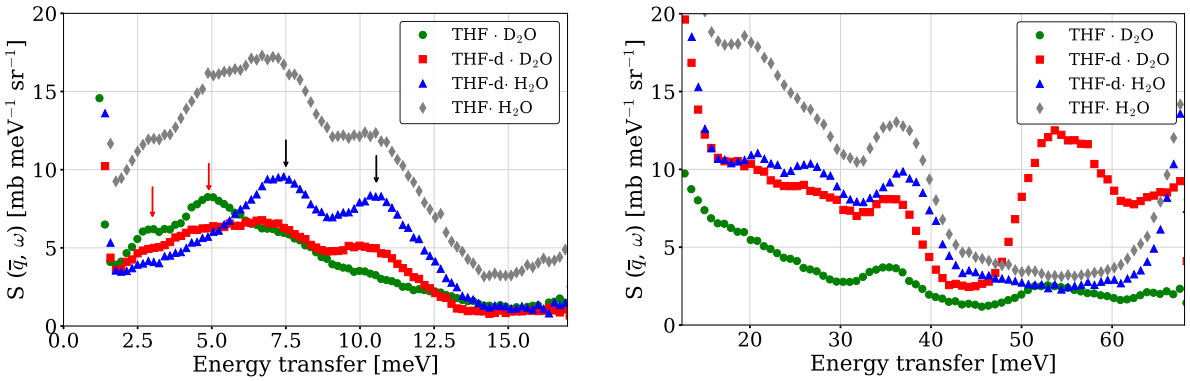

(a) Panther, $\lambda = 2.06\,\text{Å}$

(b) Panther, $\lambda = 1.03\,\text{Å}$

Figure 5.15.: Averaged q slices through $S(q,\omega)$ for the samples listed in Table 5.3 of the THF-hydrate measured at Panther at a temperature of $T = 1.5\,\text{K}$. The averages are computed over the ranges $q = [3.0, 5.0]\,\text{Å}^{-1}$ for the incident wavelength $\lambda = 2.06\,\text{Å}$ (a) and $q = [6.0, 8.0]\,\text{Å}^{-1}$ for $\lambda = 1.03\,\text{Å}$ (b), indicated by $\overline{q}$. The excitations of the lattice are indicated by black arrows, the localized excitations of the THF molecule are indicated by red arrows. The characteristic gap between phonons and librational modes for H_2O (40 meV–64 meV) and D_2O (40 meV–48 meV) are visible in (b). See text for details. The data is available in [181].

5.4.2. Presentation of Results obtained at IN5

Figure 5.16 and Figure 5.17 present the $S(q,\omega)$ maps measured on the IN5 instrument for incident wavelengths of 2.0 Å and 3.0 Å. The samples listed in Table 5.3 were again measured at a temperature of 1.5 K. The computation of the dynamical structure factor and the normalization to absolute units was conducted in the same manner for both instruments, utilizing the same vanadium standard to ensure that the dynamical structure factors $S(q,\omega)$ can be directly compared. For the incident energy of 2 Å the results obtained at IN5 instrument mirror those observed at Panther. A quantitative comparison is given in Section 5.5. The excitations of both the guest and host are red-shifted for deuterated components. This phenomenon also observed on Panther, becomes apparent when considering a simple harmonic oscillator model, where the frequency ω is given by:

$$\omega = \sqrt{\frac{k}{m}}\,, \tag{5.17}$$

with k being a force constant and m the mass of the atom or molecule. Changing the mass of the oscillating molecules effectively tunes the frequency of the oscillator, and consequently, the measured energy transfer. The mass ratio of H_2O to D_2O, as well as THF to THF-d, is approximately 9/10. Using Equation 5.17, and assuming that k does not change upon deuteration, this results in an energy transfer ratio of about 5.1%, which aligns with our observations.

The q slices were taken, averaging over q between $q = [3.0, 5.0]\,\text{Å}^{-1}$ for an incident wavelength of $\lambda = 2.0\,\text{Å}$ and at $q = [2.75, 3.25]\,\text{Å}^{-1}$ for $\lambda = 3.0\,\text{Å}$. The spectra obtained for $\lambda = 2.0\,\text{Å}$ display behavior identical to that observed with the Panther instrument, confirming the consistency of the experimental results across different instruments. The only apparent difference is a slightly higher magnitude of the scattering of the THF-d · D_2O sample.[3]

[3] This could stem from a slightly different cage occupation for the sample used at Panther. Since THF evaporates much faster than water at atmospheric conditions, the THF content and hence the cage occupation could slightly vary, with the time between the preparation of the solution and the in-situ formation of the hydrate.

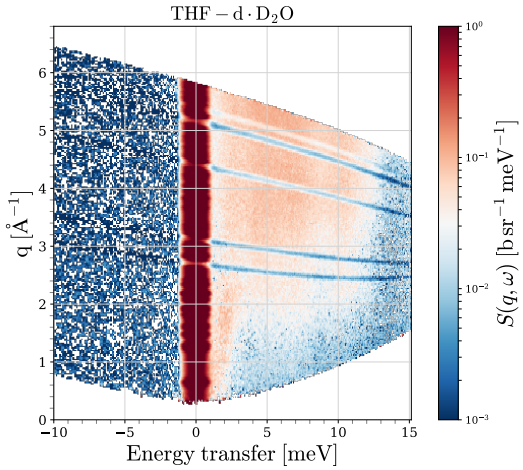

(a) IN5, 2.0 Å, THF-d $\cdot D_2O$.

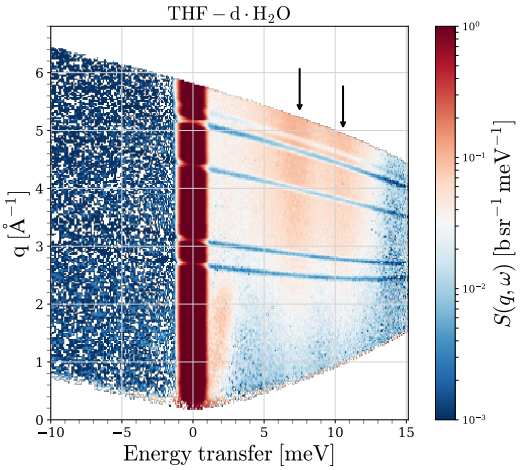

(b) IN5, 2.0 Å, THF-d $\cdot H_2O$.

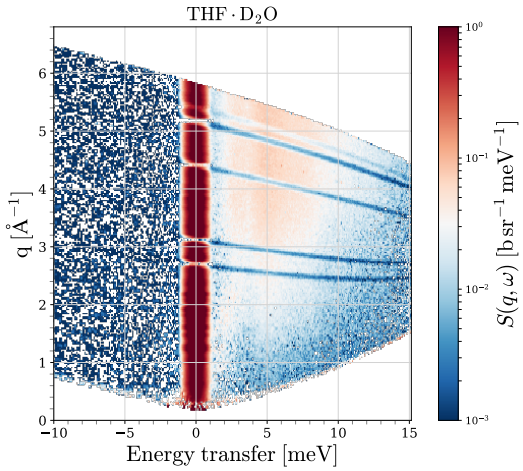

(c) IN5, 2.0 Å, THF $\cdot D_2O$.

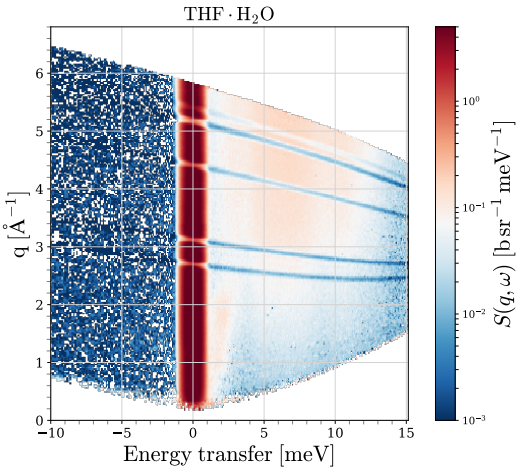

(d) IN5, 2.0 Å, THF $\cdot H_2O$.

Figure 5.16.: Dynamical structure factor $S(q, \omega)$ measured at IN5 for the hydrate samples listed in Table 5.3, at a temperature of 1.5 K and an incident wavelength of $\lambda = 2.0$ Å, presented in absolute units. The impact of isotopic substitution is evident when comparing THF-d $\cdot H_2O$ (b) with THF $\cdot D_2O$ (c). The protonated host lattice clearly shows the characteristic CS-II cage excitations at 7 meV and 10.5 meV, as indicated by black arrows, which are also visible in the data sets of Panther. The localized excitation of the THF molecules within the D_2O cage is more subtle but becomes evident when examining a q slice. The dips in the signal at constant scattering angles are due to Bragg scattering from the sample container and environment. Although this is corrected for, the textured Al still leaves a residual artifact.

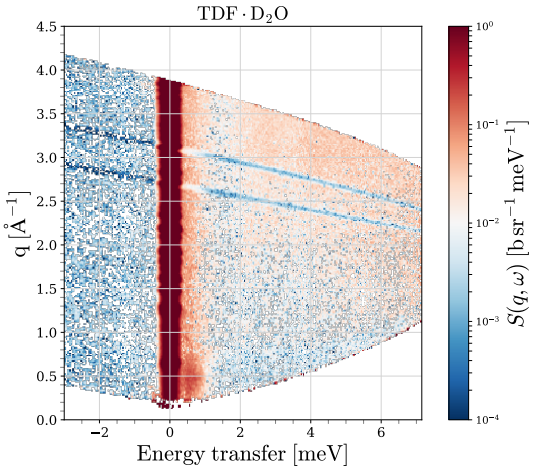

(a) IN5, 3.0 Å, THF-d · D_2O.

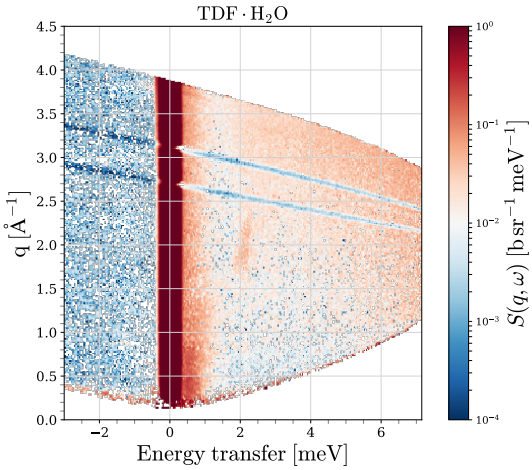

(b) IN5, 3.0 Å, THF-d · H_2O.

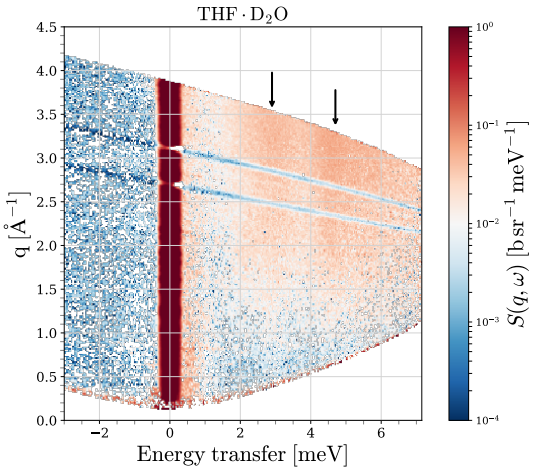

(c) IN5, 3.0 Å, THF · D_2O.

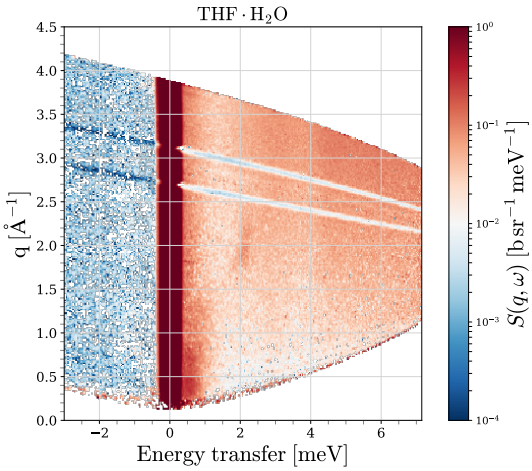

(d) IN5, 3.0 Å, THF · H_2O.

Figure 5.17.: Dynamical structure factor $S(q, \omega)$ measured at IN5 for the hydrate samples listed in Table 5.3, at a temperature of 1.5 K and an incident wavelength of $\lambda = 3.0$ Å, presented in absolute units. For the lower incident wavelength the isotopic substitution is evident when comparing THF · D_2O (c) with THF-d · D_2O (a). The excitations of the guest molecule are located at lower energy and show very distinct peaks at about 2.9 meV and 4.7 meV, best visible in the THF · D_2O sample (c) and indicated by black arrows. These localized excitations are particularly promising for moderation to the VCN range. The dips in the signal at constant scattering angles are due to Bragg scattering from the sample container and environment. These artefacts are at slightly different positions compared to Panther due to the texture of the Al-container.

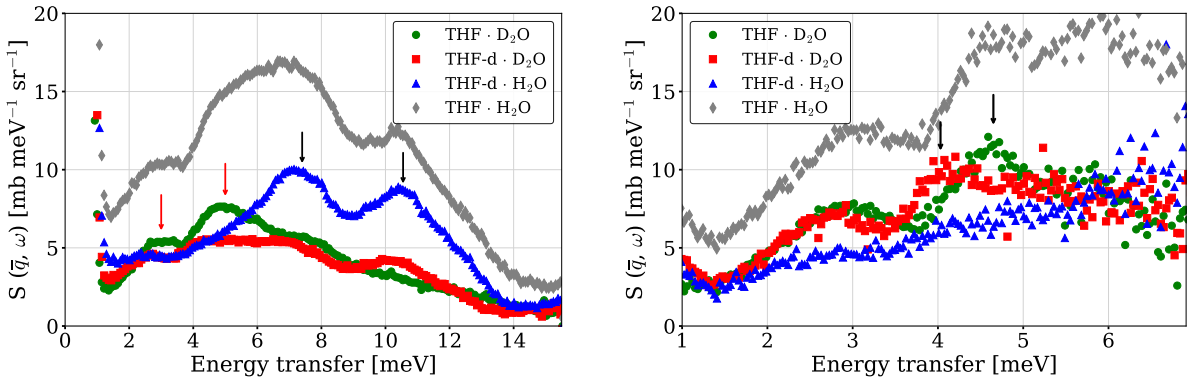

(a) IN5, $\lambda = 2.06\,\text{Å}$ (b) IN5, $\lambda = 3.0\,\text{Å}$

Figure 5.18.: Averaged q slices through $S(q,\omega)$ for the samples listed in Table 5.3 measured at IN5 at a temperature of $T = 1.5\,\text{K}$. The averages are computed over the ranges $q = [3.0, 5.0]\ \text{Å}^{-1}$ for the incident wavelength $\lambda = 2.0\,\text{Å}$ (a) and $q = [2.75, 4.25]\ \text{Å}^{-1}$ for the incident wavelength $\lambda = 3.0\,\text{Å}$ (b). The characteristic excitations of the lattice are indicated by black arrows, the localized excitations of the THF molecule are indicated by red arrows in (a). The energy shift to lower energies of the deuterated guest molecule are indicated by black arrows in (b). See text for details. The data is available at [180].

The q slice for $\lambda = 3.0\,\text{Å}$, shown in Figure 5.16c, provides further information on the dynamics of the confined THF molecule. The higher resolution of IN5 enables a more accurate determination of the excitation energies. For the protonated THF molecule, the localized excitations are resolved at 3.0 meV and 4.7 meV. In the deuterated THF-d molecule, these excitations shift to lower energies, specifically 2.7 meV and 4.1 meV, since the higher mass of the THF-d molecule decreases the rattling frequency. These localized excitations are particularly promising for moderating neutron energies into the very cold neutron (VCN) range, as they show hardly any q-dependence and allow for sequential down-scattering.

5.5. Statistical Evaluation of Data Consistency Between IN5 and Panther

To verify the data reduction and normalization approach, we can make use of the overlap in incident wavelengths between the datasets obtained at Panther and IN5 and compare them directly. Figure 5.19 shows a direct comparison of the averaged q slices averaged over $q = [3.0, 5.0]\ \text{Å}^{-1}$ obtained from the datasets taken at Panther and IN5 using a similar incident wavelength of about 2 Å. These excitation spectra show a good overall agreement between the data taken on the two different instruments. Both datasets show the same features in a very similar overall scattering magnitude.

A more systematic comparison of the full data sets is complicated by the different kinematic ranges and resolutions of the instrument. This leads not only to different binning and sizes of the data, but the $S(q,\omega)$ maps are also differently shaped, which complicates a systematic comparison. One way to circumvent that is comparing the $S(2\theta,\omega)$ data, which are both mapped on a rectangular grid instead of the $S(q,\omega)$ which has a skewed shape characteristic for the instrument. Figure 5.20 shows $S(2\theta,\omega)$ for the THF · D_2O sample measured at Panther and IN5. Even though the $S(2\theta,\omega)$ data has the overall same shape, the binning and energy range

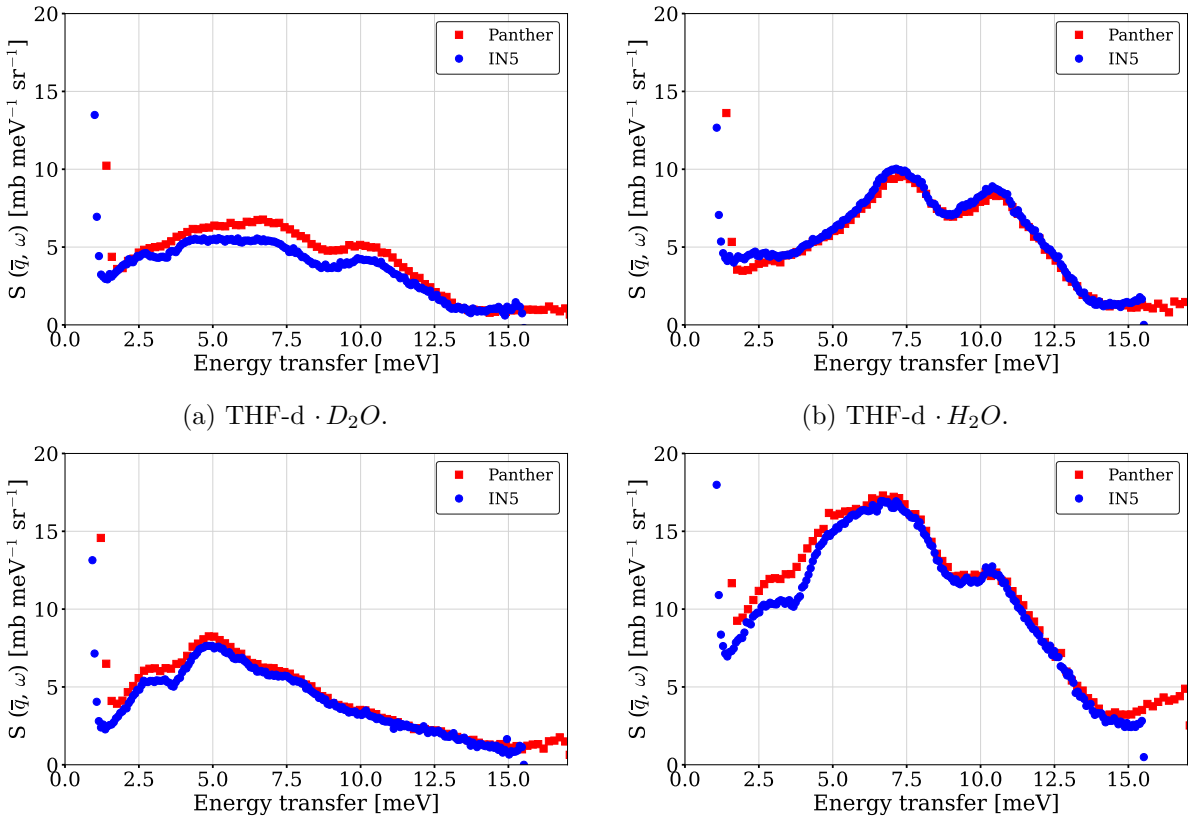

(a) THF-d $\cdot D_2O$.

(b) THF-d $\cdot H_2O$.

(c) THF $\cdot D_2O$.

(d) THF $\cdot H_2O$.

Figure 5.19.: Comparison of the averaged q slices at $q = [3.0, 5.0]$ Å^{-1} obtained from the datasets taken at Panther and IN5 using a similar incident wavelength of about 2 Å. The q slices were obtained using the algorithm `LineProfile`. Data is available under [180, 181].

of the two instruments is quite different. While the Panther data has a finer angular binning, IN5 has a much larger energy range, with higher resolution. This results in a $[2\theta \times \hbar\omega]$ grid of $[610 \times 226]$ for Panther and of $[349 \times 704]$ for IN5.

Comparing the datasets requires mapping them onto a common grid. This can only be done for the shared $[2\theta \times \hbar\omega]$ coverage, which is $2\theta = [13\,^\circ, 136\,^\circ]$ and $\hbar\omega = [-80\,\text{meV}, 15\,\text{meV}]$. Given the resolution constrains of the respective instrument, we define the new grid as $[2\theta \times \hbar\omega]$ as $[330 \times 220]$. The data can be mapped onto this grid after interpolation. In order to analyse the difference between the repsective data sets we introduce the Weighted Squared Error (WSE) [193, 194, 195]:

$$\text{WSE}(2\theta_i, \omega_i) = \frac{(S_1(2\theta_i, \omega_i) - S_2(2\theta_i, \omega_i))^2}{\sigma_1^2(2\theta_i, \omega_i) + \sigma_2^2(2\theta_i, \omega_i)}\,, \tag{5.18}$$

where $\sigma_1(2\theta_i, \omega_i)$ and $\sigma_2(2\theta_i, \omega_i)$ are the uncertainties associated with the datasets S_1 and S_2. This quantity calculates point-wise the squared difference between these two datasets and weighs it by their respective uncertainties. To better visualize this quantity over the whole dataset and show systematic differences between the data, the Weighted Normalized Root Square Error (WNRSE), denoted W_σ, is introduced. This metric normalizes the WSE by the maxima of the first dataset, providing a dimensionless quantity between 0 and 1:

$$W_\sigma(2\theta_i, \omega_i) = \frac{\sqrt{\text{WSE}(2\theta_i, \omega_i)}}{\max(S_1) - \min(S_1)}\,, \tag{5.19}$$

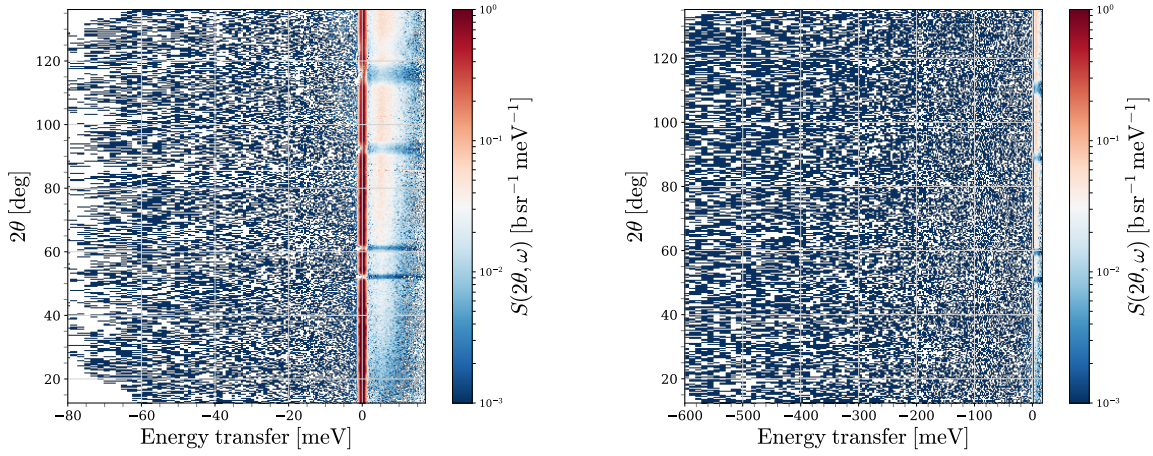

(a) Panther, $\lambda = 2.06\,\text{Å}$, THF · D_2O

(b) IN5, $\lambda = 2.0\,\text{Å}$, THF · D_2O

Figure 5.20.: Comparison of $S(2\theta, \omega)$ maps for the THF · D_2O sample measured at Panther and IN5. The Panther data, with a smaller kinematic range and lower resolution, is represented on a $[610 \times 226]$ grid, while the IN5 data, covering a larger energy range, is mapped on a $[349 \times 704]$ grid.

where $\text{WSE}(2\theta_i, \omega_i)$ is the Weighted Squared Error at each grid point defined above, and $\max(S_1)$ and $\min(S_1)$ are the maximum and minimum values of the dataset S_1 over the grid. This makes it a useful metric for visualizing the relative differences between the datasets across the grid. Figure 5.21 shows W_σ for the two datasets $S_{\text{IN5}}(2\theta, \omega)$ and $S_{\text{Panther}}(2\theta, \omega)$ in its full range and in the region of interest between $[2\,\text{meV}, 15\,\text{meV}]$ for the THF · D_2O sample measured at an incident wavelength of about 2.0 Å. The WNRSE indicates systematic aluminum artifacts. Since each instrument shows these features at slightly different positions, this leads to two distinct lines across the map for each Al Bragg peak. The elastic peak's shoulder at small scattering angles is also linked to the presence of aluminum. Since these features are not inherent to the sample, we mask these areas for the calculation of additional statistical metrics. The maskes are illustrated in Figure 5.22

From the Weighted Squared Error the Weighted Mean Squared Error can be calculated by summing over the whole grid and dividing by the number of data points N so that

$$\text{WMSE} = \frac{1}{N} \sum_{i=1}^{N} \frac{(S_1(2\theta_i, \omega_i) - S_2(2\theta_i, \omega_i))^2}{\sigma_1^2(2\theta_i, \omega_i) + \sigma_2^2(2\theta_i, \omega_i)}\,. \tag{5.20}$$

This quantity can be normalized the same way as the WSE:

$$\overline{W_\sigma} = \frac{\sqrt{\text{WMSE}}}{\max(S_1) - \min(S_1)}\,. \tag{5.21}$$

This dimensionless number between 0 and 1 provides a measure for the similarity of the two datasets. Notably, the WMSE is a very similar measure to the reduced χ-squared (χ^2_{red}), which is given by

$$\chi^2_{\text{red}} = \frac{1}{N-1} \sum_{i=1}^{N_{\text{valid}}} \frac{(S_1(2\theta_i, \omega_i) - S_2(2\theta_i, \omega_i))^2}{\sigma_1^2(2\theta_i, \omega_i) + \sigma_2^2(2\theta_i, \omega_i)}\,. \tag{5.22}$$

The normalization factor of $\frac{1}{N-1}$, corresponds to the degrees of freedom, which are generally given by $K = N - P$, where N is the number of independent data points and P the number

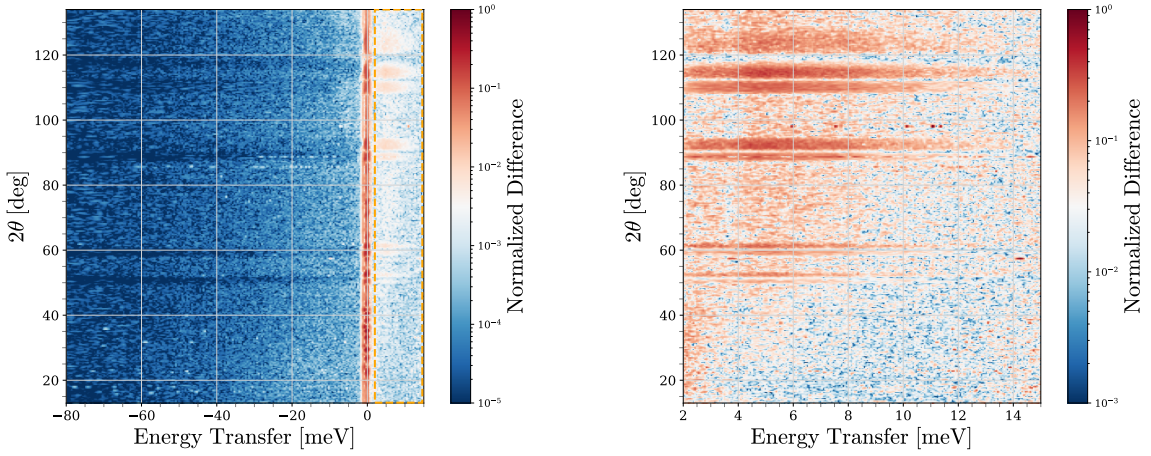

(a) W_σ, $\lambda = 2.06\,\text{Å}$, THF · D_2O (b) W_σ (zoom), $\lambda = 2.0\,\text{Å}$, THF · D_2O

Figure 5.21.: Comparison of the Weighted Normalized Root Square Error (WNRSE) W_σ between the datasets $\sigma_{\text{IN5}}(2\theta, \omega)$ and $\sigma_{\text{Panther}}(2\theta, \omega)$ for the THF · D_2O sample, measured at an incident wavelength of approximately 2.0 Å. The region of interest outlined in dashed orange in (a) is enlarged in (b). The WNRSE systematically highlights the aluminum artifacts, which appear at slightly different positions on each instrument, resulting in two lines across the map for each Bragg peak of Al. The shoulder of the elastic peak at small scattering angles is also attributed to the aluminum.

of independent parameters of the fitting model [195]. In our context, where two data sets are compared this reduces to $N-1$. While the WMSE and reduced chi-squared reflect the magnitude of the differences between datasets another interesting measure is the linear correlation between the two datasets. A standard measure to evaluate that is the Pearson Correlation Coefficient (PCC), given by [196]:

$$r = \frac{\sum_{i=1}^{N}(S_1(2\theta_i,\omega_i) - \overline{S_1})(S_2(2\theta_i,\omega_i) - \overline{S_2})}{\sqrt{\sum_{i=1}^{N}(S_1(2\theta_i,\omega_i) - \overline{S_1})^2 \sum_{i=1}^{N}(S_2(2\theta_i,\omega_i) - \overline{S_2})^2}}\,. \tag{5.23}$$

The PCC, usually denoted by r, can also incorporate weights based on the associated uncertainty of the datasets, which gives:

$$r_w = \frac{\sum_{i=1}^{N} w(2\theta_i,\omega_i)(S_1(2\theta_i,\omega_i) - \overline{S_1})(S_2(2\theta_i,\omega_i) - \overline{S_2})}{\sqrt{\sum_{i=1}^{N} w(2\theta_i,\omega_i)(S_1(2\theta_i,\omega_i) - \overline{S_1})^2 \sum_{i=1}^{N} w(2\theta_i,\omega_i)(S_2(2\theta_i,\omega_i) - \overline{S_2})^2}}\,, \tag{5.24}$$

where the weights $w(2\theta_i, \omega_i)$ are given by $w(2\theta_i,\omega_i) = \frac{1}{\sigma_1(2\theta_i,\omega_i)^2 + \sigma_2(2\theta_i,\omega_i)^2}$. The quantities $\bar{S}_1$ and $\bar{S}_2$ are the mean values of the datasets S_1 and S_2, respectively. The Pearson correlation coefficient varies between -1 and 1, where 1 signifies a perfect positive correlation, -1 signifies a perfect negative correlation, and 0 indicates no correlation. A weighted Pearson coefficient close to 1 suggests that, despite observed differences in WMSE or reduced chi-squared, the datasets likely exhibit similar overall trends and directions. This means that the two datasets, while perhaps differing in scale or noise, fundamentally agree in how they change with respect to each other.

The three introduced measures were computed for the data pairs of all four samples measured at IN5 and Panther respectively. The results are given in Table 5.7. The overall low WMSE and reduced chi-squared as well as PCC close to 1 suggests a good agreement of the datasets

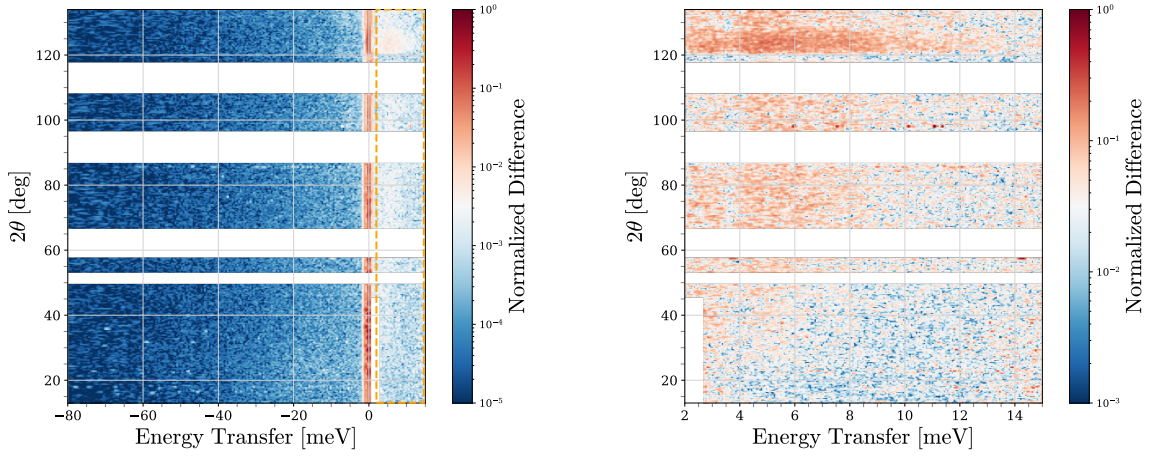

(a) W_σ, $\lambda = 2.06\,\text{Å}$, THF · D_2O (b) W_σ (zoom), $\lambda = 2.0\,\text{Å}$, THF · D_2O

Figure 5.22.: Applied mask for the comparison of the Weighted Normalized Root Square Error (WNRSE) W_σ between the datasets $S_{\text{IN5}}(\theta, \omega)$ and $S_{\text{Panther}}(\theta, \omega)$ for the THF · D_2O sample. The region of interest outlined in dashed orange in (a) is enlarged in (b). The aluminum artefacts are masked and not taken into considerations for the statistical comparison.

in both overall trend and magnitude. The WNRMSE (W_σ) values range from 1.20×10^{-4} to 1.86×10^{-4}. This indicates that the datasets are highly similar, when masking the Al artefacts of the sample container and environment.

Table 5.7.: Statistical Metrics for the masked datasets in the energy transfer region from 0 meV to 15 meV.

Dataset Pair	W_σ	χ^2_{red}	r_w
THF · H_2O	1.56×10^{-4}	1.186	0.938
THF · D_2O	1.20×10^{-4}	0.716	0.910
THF-d · D_2O	1.66×10^{-4}	1.252	0.907
THF-d · H_2O	1.86×10^{-4}	1.242	0.914

The reduced chi-squared values further support this conclusion, although THF · D_2O sample exhibits a value of 0.716. This value, being below 1, suggests that the uncertainties in one or both datasets may be overestimated. The weighted PCC, all close to 1, indicate a strong linear relationship between the datasets. This strong correlation and high level of agreement in trend and magnitude across the two instruments suggests that the measurement techniques, applied corrections, and normalization to absolute units are robust and reliable.

5.6. Experimental Dynamical Structure Factor of Binary Hydrates Hosting THF-d and O_2

In addition to the collective excitations of the host lattice, observed between approximately 7 meV and 40 meV, and the localized excitations of the THF molecule around 3 meV and 4.7 meV, the magnetic excitation of dioxygen presents a particularly promising avenue for VCN moder-

ation, as detailed in Section 3.3. Magnetic scattering at the field splitting constant D, from confined O_2 has been previously reported in CS-II, O_2 hydrates [116] and in O_2 intercalated in C_{60} (buckyballs) [127]. This section reports, for the first time, the observation of magnetic down-scattering from binary clathrate hydrates hosting THF-d in the large cages ($5^{12}6^4$) and O_2 in the small cages (5^{12}), as prepared according to the methods outlined in Chapter 4. This represents a significant advancement, as it allows for scalable manufacturing at moderate pressure conditions; while providing pronounced magnetic down-scattering to facilitate a cooling cascade to VCN temperatures.

5.6.1. Normalization of Binary Hydrate Samples Using an Internal Standard

Since the samples are prepared from a powder with an unknown packing fraction η, the normalization process is more nuanced than for bulk samples prepared from a liquid solution. However, the scattering magnitude of the lattice excitations measured in the fully deuterated sample from experiment 1-10-49 at an incident wavelength of 4.8 Å can serve as an internal standard. As described above the data from experiment 1-10-49 at IN5 is normalized with a vanadium standard. By comparing these lattice excitations with those of the binary hydrate, which share the same physical origin, we can derive a scaling factor to normalize the binary hydrate data effectively. There is however an additional subtlety. Due to the limited energy resolution and kinematic range of the instrument, the neutron down-scattering from the host lattice, can not be measured in the same experiment as the magnetic down-scattering. This required an additional measurement of the neutron up-scattering from the lattice excitations at elevated temperatures.[4] Figure 5.23 shows data for the THF-d deuterate (THF-d $\cdot$ D_2O) at 100 K, normalized to absolute units as described above next to the dynamical structure factor of the binary THF-d – O_2 deuterate (THF-d $\cdot O_2 \cdot D_2O$) without normalization. These measurements were taken as part of experiment 1-10-49 [181] and experiment 1-10-57 [197].

One can see from first glance similar features with different scattering magnitudes. This becomes more obvious when looking at a q average, as depicted in Figure 5.24. The average is taken in a range of $q = [1.5, 2.5]$ Å^{-1}, and shown for three different samples. The two binary THF-d – O_2 deuterate samples (A) and (B), differ in manufacturing. While sample (A) was prepared from a powder of THF-d – deuterates manually ground in a mortar, sample (B) was prepared from a ball-milled powder. All samples show characteristic excitations at 6.9 meV and 10.2 meV, these are equivalent to the excitations in the Stokes regime as depicted in Figure 5.17a. Using the THF-d deuterate (green triangles) as a reference, scaling factors were determined for the two binary hydrate samples (A) and (B) by minimizing the squared differences between their spectra and the reference spectrum. This was done by computing the ratio of dot products between the comparison datasets (A/B) and the reference dataset around these two maxima ($[-11.5, -4]$ meV). The uncertainties were estimated from the residuals of the data after applying the fitted scaling factors. This procedure yields scaling factors of 1.128 ± 0.006 for sample (B) and 1.956 ± 0.012 for sample (A). Applying these factors to the $S(q, \omega)$ maps allows quantification of magnetic scattering relative to the localized excitations of the THF-d molecule.

[4] In the context of inelastic neutron scattering experiments the neutron down-scattering, so processes where the neutron ends up loosing energy is often referred to scattering in the *Stokes* regime. Up-scattering, or energy gain of the neutron, is referred to as *anti-Stokes* scattering.

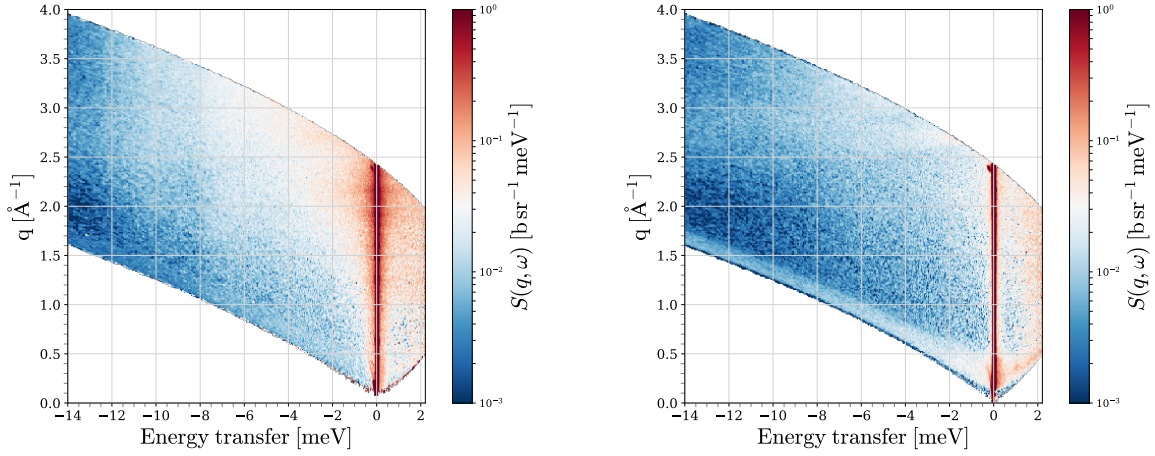

(a) IN5, $\lambda = 4.8$ Å, THF-d · D_2O, 100 K

(b) IN5, $\lambda = 4.8$ Å, THF-d ·O_2 · D_2O, 100 K

Figure 5.23.: Comparison of the dynamical structure factors for the THF-d deuterate (THF-d · D_2O) measured at 100 K with the data for the binary THF-d – O_2 deuterate (THF-d ·O_2 · D_2O) for normalization purposes. The THF-d deuterate data, obtained from experiment 1-10-49 [181], serve as a reference for normalizing the binary deuterate samples. This normalization is based on the lattice excitations observed on the anti-Stokes side, with the sample being normalized to a vanadium standard. The binary deuterate data were acquired in experiment 1-10-57 [197].

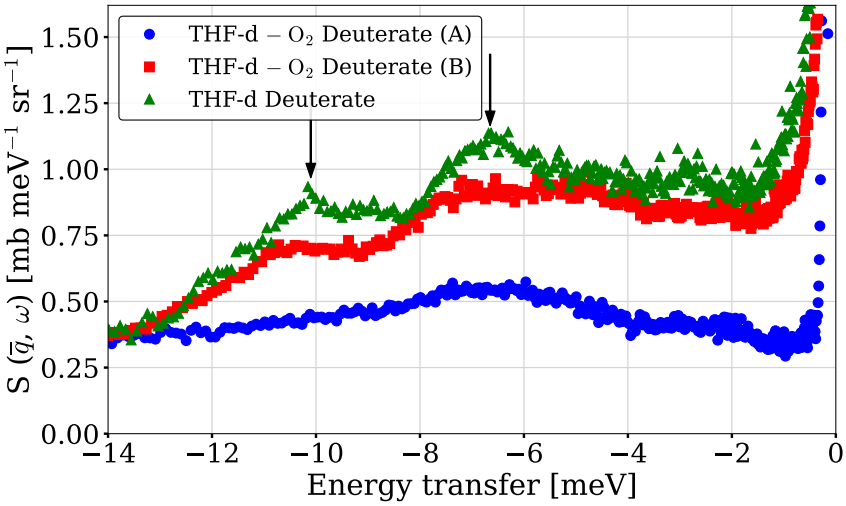

Figure 5.24.: Averaged q slice comparison over $q = [1.5, 3.5]$ Å^{-1} for three different samples. The figure shows the THF-d deuterate (green triangles) alongside two binary THF-d – O_2 deuterate samples prepared using different methods: (A) manually ground in a mortar (blue circles) and (B) ball-milled (red squares). The characteristic excitations at -6.7 meV and -10.1 meV are observed in all deuterated samples, and correspond to the Stokes regime excitations shown in Figure 5.17a. Scaling factors of 1.128 ± 0.006 and 1.956 ± 0.012 were determined for samples (B) and (A), respectively, using the THF-d deuterate as a reference (see text). These factors can be applied to the $S(q, \omega)$ maps to quantify the magnetic scattering relative to the localized excitations of the THF-d molecule.

5.6.2. Magnetic Scattering in Binary Hydrates

The dynamical structure factor of the two samples of THF-d – O_2 deuterate, measured at IN5 with an incident wavelength of 6.25 Å and a temperature of 1.5 K, is presented in Figure 5.25. The scaling factors determined from the anti-Stokes scattering of the host lattice excitations at 100 K are applied. The sample prepared from a powder ground in the ball mill (Sample B, Figure 5.25b) shows a significantly stronger magnetic signal as the sample prepared from a powder ground in the mortar (Sample A, Figure 5.25a).

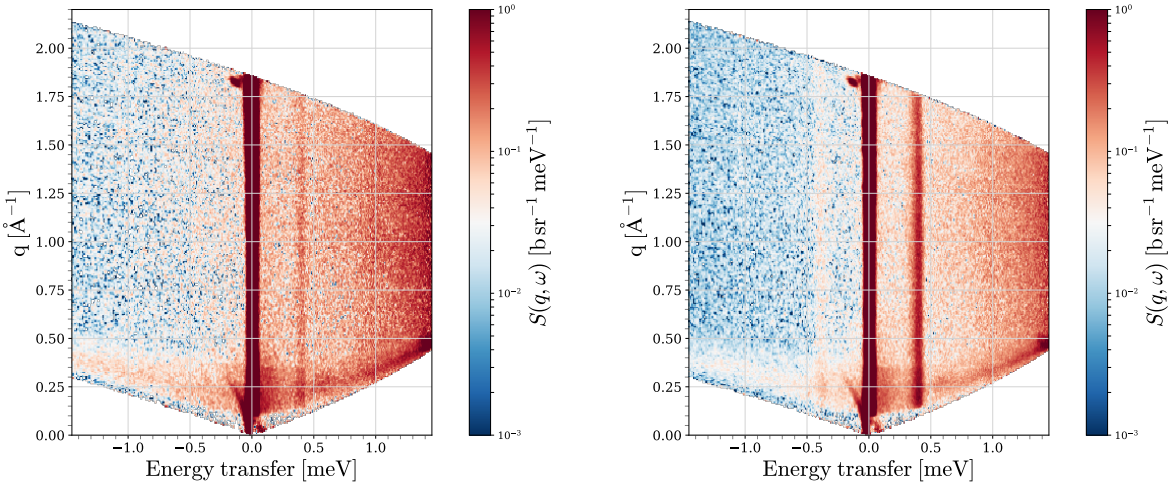

(a) IN5, $\lambda = 6.25$ Å,THF-d $\cdot O_2 \cdot D_2O$, 1.5 K, Sample A

(b) IN5, $\lambda = 6.25$ Å, THF-d $\cdot O_2 \cdot D_2O$, 1.5 K, Sample B

Figure 5.25.: Dynamical structure factor $S(q,\omega)$ of THF-d – O_2 deuterate samples measured at IN5 with an incident wavelength of 6.25 Å and a temperature of 1.5 K. The figure compares the magnetic signal strength between two samples: Sample A, prepared from a powder ground in a mortar (a), and Sample B, prepared from a powder ground in a ball mill (b). The scaling factors, determined from the anti-Stokes scattering of host lattice excitations at 100 K, have been applied. Sample B exhibits a significantly stronger magnetic signal compared to Sample A. The intensity spot at $q \approx 1.9$ Å^{-1} and the increased intensity at low q across the energy transfer spectrum are instrumental artifacts. The latter arises from the focusing neutron guide. Focusing the beam on the sample causes divergence at the detector position. This results in a halo around the beam stop, which is visible in the signal.

This result is highlighted by Figure 5.26, showing a q slice of the two datasets shown above averaged over $q = [0.75, 1.75]$ Å^{-1}. The peak of Sample B, depicted with blue squares, is significantly higher than the one of Sample A (red circles). This suggests a higher occupancy of O_2 in the small cages of Sample B in comparison to Sample A, emphasizing the critical role of small and uniform grain sizes during pressurization in the hydrate manufacturing process.[5] In combination with the diffraction data presented in Chapter 4, this clearly shows that the demonstrated manufacturing technique leads to CS-II hydrate structures with a high O_2 occupancy of the small cages.

The population of the spin sub-levels of O_2 in its triplet state ($^3\Sigma_g^-$), and consequently the inelastic magnetic scattering cross section, depends on temperature, as discussed in Section 3.3

[5] Although the grain size distribution was not quantified, optical observations strongly suggest that the powder prepared in the ball mill is finer and more uniform.

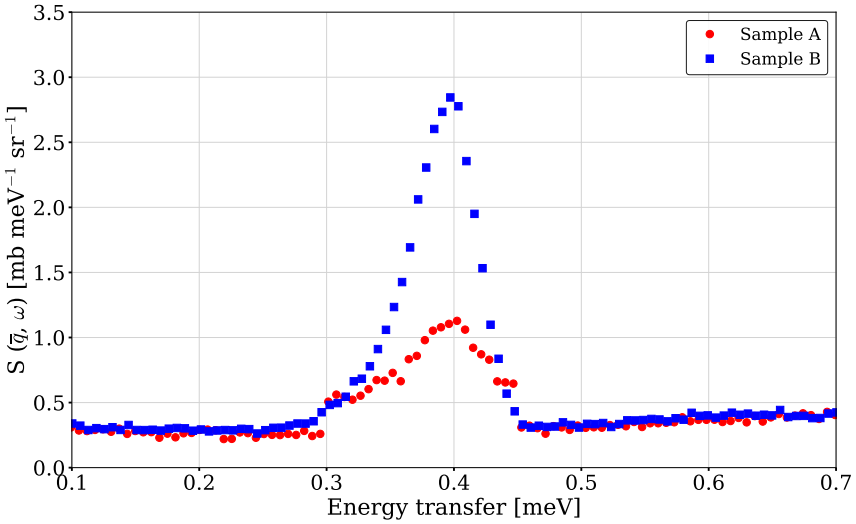

Figure 5.26.: Comparison of averaged q slices over $q = [0.75, 1.75]$ Å^{-1} for the THF-d – O_2 deuterate samples A and B at a temperature of 1.5 K. The peak corresponding to Sample B (blue squares) is significantly higher than that of Sample A (red circles), indicating a greater occupancy of O_2 in the small cages of Sample B. This result highlights the importance of small and uniform grain sizes during pressurization in the hydrate manufacturing process. Combined with the diffraction data presented in Chapter 4, this finding demonstrates that the manufacturing technique used effectively produces CS-II hydrate structures with a high O_2 occupancy in the small cages.

(see also [198] [58]). As a result, the magnetic peak in $S(q, \omega)$ is highly temperature-dependent, as shown in Figure 5.27. The temperature dependence is reflected in the dynamical structure factor, which, at low temperatures, follows the course of the function $g_{\pm}$ depicted in Figure 3.2b. At low temperatures, neutron down-scattering dominates, while up-scattering increases with rising temperature and saturates around 7.5 K. At 20 K g_+ and g_- have reached their asymptotic value and the up- and down-scattering are balanced.

Alongside these temperature-dependent scattering dynamics, the peaks exhibit increasing broadening as the temperature rises. The width of the peaks at ± 0.4 meV expands progressively with temperature, indicating an effect that surpasses the limits of instrumental resolution. This broadening could stem from various factors, including perturbations of the O_2 triplet state, which may depend on the molecular orientation within the hydrate cages, as suggested in [42]. These perturbations could lead to variations in the magnetic interaction, resulting in a distribution of the field splitting constant D and, consequently, broader peaks. This hypothesis is further supported by the slight shift of the peak center to lower values of D as the temperature increases.

The exact origin of this broadening, however, remains uncertain and may involve several contributing factors beyond molecular orientation. One possibility is the breakdown of the spin triplet ground state of molecular oxygen at elevated temperatures due to interactions between oxygen and the host lattice, which might hinder the coupling of the two unpaired electrons in the ground state [199]. Another potential cause could be the coupling of the librations of trapped oxygen with the acoustic phonons of the crystal [200], or molecular reorientation processes that affect the intrinsic characteristics of the spin triplet state of oxygen [127].

Further investigation into these effects could be facilitated by additional experiments with higher instrumental resolution. Beam time has already been granted at the backscattering spec-

trometer IN16B in the BATS configuration at the Institut Laue-Langevin [201].[6] A systematic measurement of a temperature curve extending beyond 20 K would allow for precise quantification of both the peak broadening and the potential shift of the peak center. Such detailed analysis would provide input for further modeling efforts. While there is inherent value in completing this picture of the interplay between the dynamics of the confined O_2 molecule and its triplet ground state, such details appear of minor importance for the application of the binary hydrate in neutron moderation. A natural next step in this endeavor would be to extend the OpenMC simulation study of O_2-containing inclusion compounds described in [42, Section 5] to fully deuterated hydrates hosting THF-d and O_2. The presented data could be used to adapt the phenomenological extension of the magnetic scattering model.

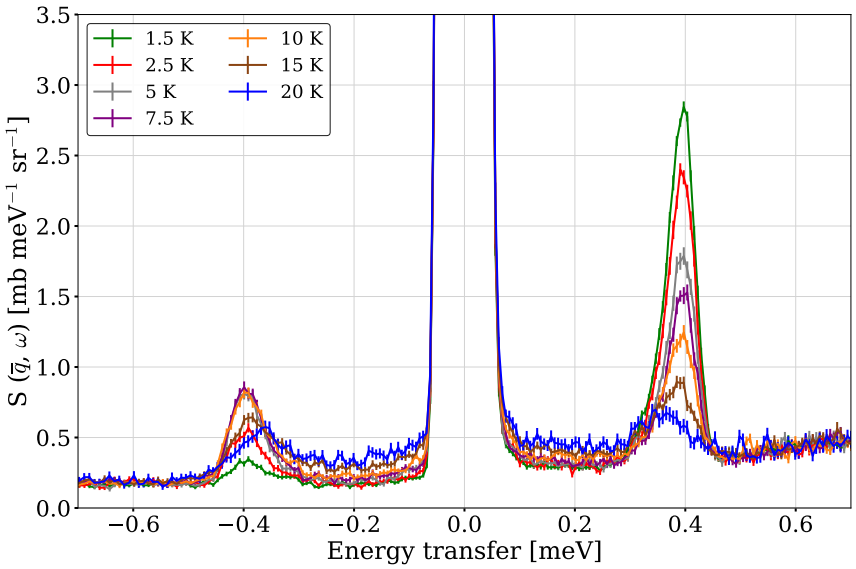

Figure 5.27.: Temperature dependence of the magnetic excitation in $S(q, \omega)$ for O_2 in its triplet state ($^3\Sigma_g^-$) (sample B). The signal is averaged over a q interval of $q = [0.75, 1.75]$ Å^{-1}. The figure illustrates how the inelastic magnetic scattering cross section varies with temperature, reflecting changes in the population of spin sub-levels. Additionally, a broadening and slight shift of the peaks can be observed, possibly due to a temperature-dependent perturbation of the field splitting constant D (see text).

5.7. Vibrational Energy Spectrum of Hydrate Samples: Experimental Measurements and Simulations

To model the dynamics within the hydrate scattering kernel density functional theory (DFT) calculations and molecular dynamics (MD) simulations were carried out by our collaborators within the HighNESS project [12, 41].[7] For the following comparison, the vibrational density of states (DOS) was obtained from the MD trajectories by calculating the velocity autocorrelation function (VACF) using the GROMACS software package [202]. The VACF is defined as:

$$C_v(t) = \langle \mathbf{v}(0) \cdot \mathbf{v}(t) \rangle , \tag{5.25}$$

[6] Unfortunately, the experiment could not be conducted as part of this thesis because BATS was temporarily decommissioned. It is scheduled to be carried out in 2025, extending beyond the timeframe of this thesis.
[7] The data is available at [94].

where $\mathbf{v}(t)$ is the velocity of a particle at time t, and the angle brackets denote an ensemble average. The DOS can be obtained by calculating the Fourier transform of VACF. Specifically, the DOS $g(\omega)$ is given by:

$$g(\omega) = \int_{-\infty}^{\infty} C_v(t) \exp(-i\omega t)\, dt \tag{5.26}$$

In practice, because the VACF obtained from simulations is discrete, the DOS is calculated using a discrete Fourier transform. These results were then cross-checked with the DOS data in the `.ncmat` files created within the collaboration [94] and compared to the experimental data. The

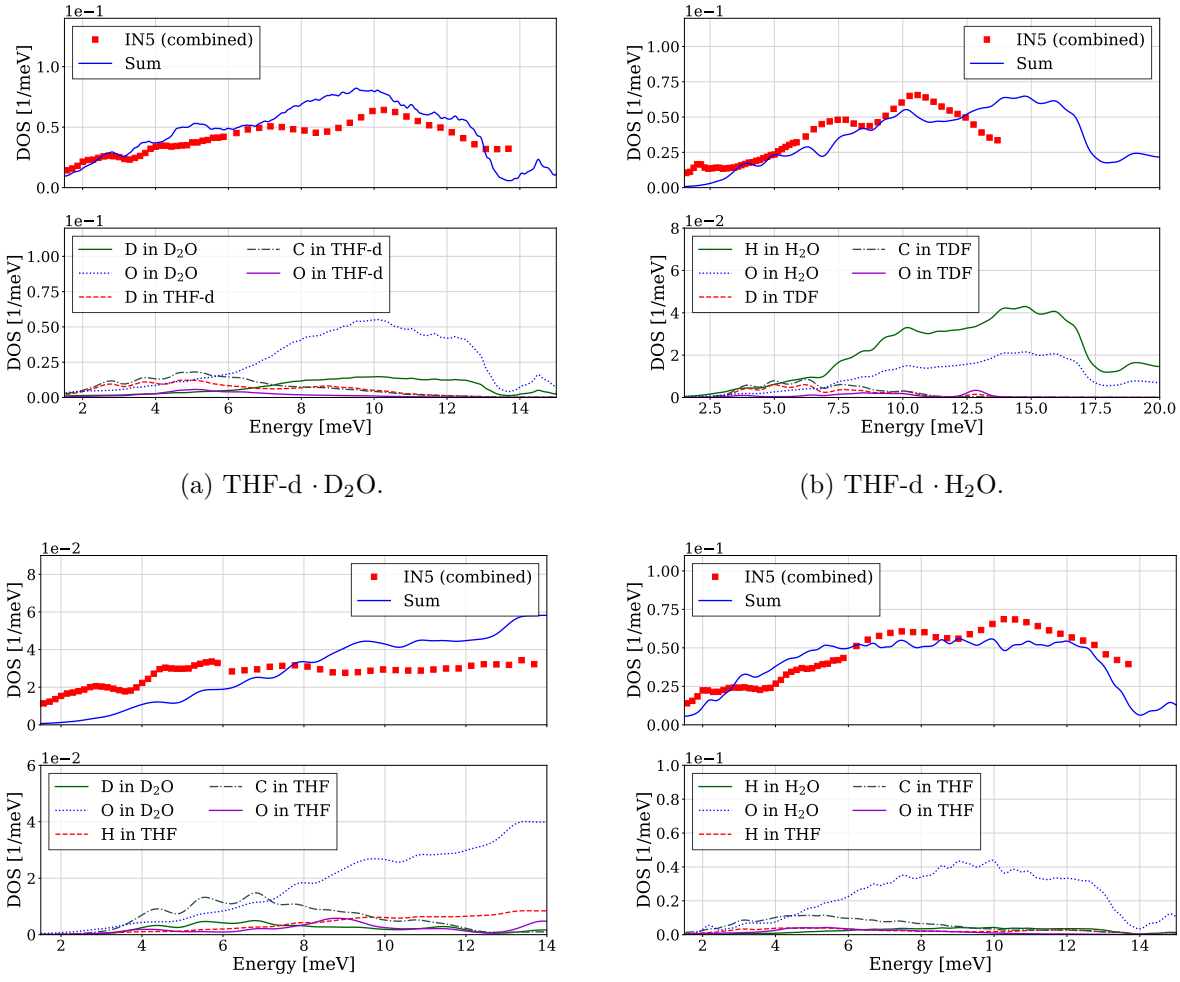

(a) THF-d $\cdot D_2O$.

(b) THF-d $\cdot H_2O$.

(c) THF $\cdot D_2O$.

(d) THF $\cdot H_2O$.

Figure 5.28.: Comparison of the normalized density of states (DOS) of the hydrate samples under study, as computed in the incoherent approximation of the data obtained at IN5 [181] at a temperature of 1.5 K, against the results of the molecular dynamics simulations. The simulation accurately captures the translational modes of the host lattice and the rattling of the THF-d molecule. However, the double peak feature of the translational band of the hydrate cage is less pronounced in the simulation, potentially due to peak overlap with low-energy THF excitations or simulation limitations. The general trend of a redshift in deuterated samples is well captured by the simulation, although a slight blue shift in the protonated components of partly deuterated samples is observed, as seen in both THF-d $\cdot$ H_2O and THF $\cdot$ D_2O.

DOS is normalized and weighted by the neutron cross section of the respective atomic species. This weighting factor is given by the equation:

$$w_i = \frac{f_i \sigma_i}{\sum_j f_j \sigma_j}, \tag{5.27}$$

where f_i is the fraction of atomic species i in the compound and σ_i the respective neutron scattering cross section. The sum in the denominator runs over all atomic species j in the compound, ensuring that the weighting factors are normalized.

As demonstrated above, the low-energy excitation spectrum of the hydrates under study are best captured by neutron time-of-flight instruments. Once the dynamical structure factor is obtained, the density of states of the sample can be computed using the incoherent approximation (see Section 2.1.8) within the Mantid framework and compared to the hydrate model established within the HighNESS collaboration. The algorithm `ComputeIncoherentDOS` [203] explicitly calculates the generalized phonon density of states in the incoherent approximation from a measured $S(q, \omega)$ workspace. The normalized results are presented in Figure 5.28.

The translational modes of the host lattice and the rattling of the THF-d molecule are well captured by the simulation. However, as previously discussed in [41], the double peak feature of translational band of the hydrate cage is less pronounced in the simulation compared to the experiment. This discrepancy may be due to the overlap of the peak with low-energy excitations of the THF molecule in the experiment or an inherent discrepancy within the simulation approach. The rattling modes of the THF-d show three distinct peaks at 2.79 meV, 3.72 meV and 4.85 meV in the simulation are only reflected by two peaks at 2.71 meV and 4.25 meV in the experiment. This could be due to the weak signal of the peak and the limited energy resolution of the instrument. This hypothesis is supported by the fact third rattling excitations is clearly visible in the protonated confined THF see Figure 5.28c. The general trend of a redshift of the deuterated or partly deuterated samples is well represented in the simulation. However in the partly deuterated samples (THF-d $\cdot H_2O$ and THF $\cdot D_2O$) the simulations exhibit a small blue shift in the excitation associated with the protonated component, compared to the respective experimental results. This can be observed in the three peaks associated with the THF in THF $\cdot D_2O$ as well as in the lattice peaks associated with the H_2O in THF-d $\cdot H_2O$.

5.7.1. Vibrational Energy Spectrum Measured at IN1-Lagrange

The time-of-flight data presented above provide high-resolution structural and dynamical information into the clathrate hydrate compounds under study. However, the resolution at high energy transfers with time-of-flight techniques is inherently limited. To explore higher-energy excitations, such as the librations of the water network and molecular vibrations beyond the limits of time-of-flight methods, we used the IN1-Lagrange vibrational spectrometer. IN1 allows for the investigation of excitations up to 500 meV, though the resolution at higher energy transfers is limited, and both the appearance of harmonics and the Debye-Waller factor complicate data interpretation. Nevertheless, these experiments allow us to not only identify the full translation and libration bands, but also to pinpoint the bending and stretching modes of water and tetrahydrofuran within the hydrate compounds, providing a benchmark for validating density functional theory calculations and ab initio molecular dynamics simulations across the entire excitation spectrum.

The isotopic substitution, which had already proven valuable in the time-of-flight measurements, was applied again for the experiments at IN1-Lagrange. In addition to the samples listed in Table 5.3, two samples of binary deuterates hosting THF-d and O_2 were also investigated. These two samples, designated (A) and (B), were from the same batches as the (A) and (B) samples discussed in Section 5.6.2. Both samples exhibited similar characteristics, with

sample (B) showing slightly higher intensities, which is likely attributable to a higher powder packing density (η) achieved by the finer powder produced through ball milling. In this section, only the data from the better-performing sample, sample (B), are presented.

Figure 5.29 shows the spectra of the fully deuterated and fully protonated samples of the simple hydrate. The first row presents experimental data from IN1-Lagrange [197]. The data were normalized to monitor counts and corrected with the empty sample cell. The datasets from different monochromators, Cu(220), Si(311), and Si(111) (see [165]), are manually stitched. The second and third rows display the neutron-weighted DOS for the host lattice and guest molecule, respectively, as simulated by [41].

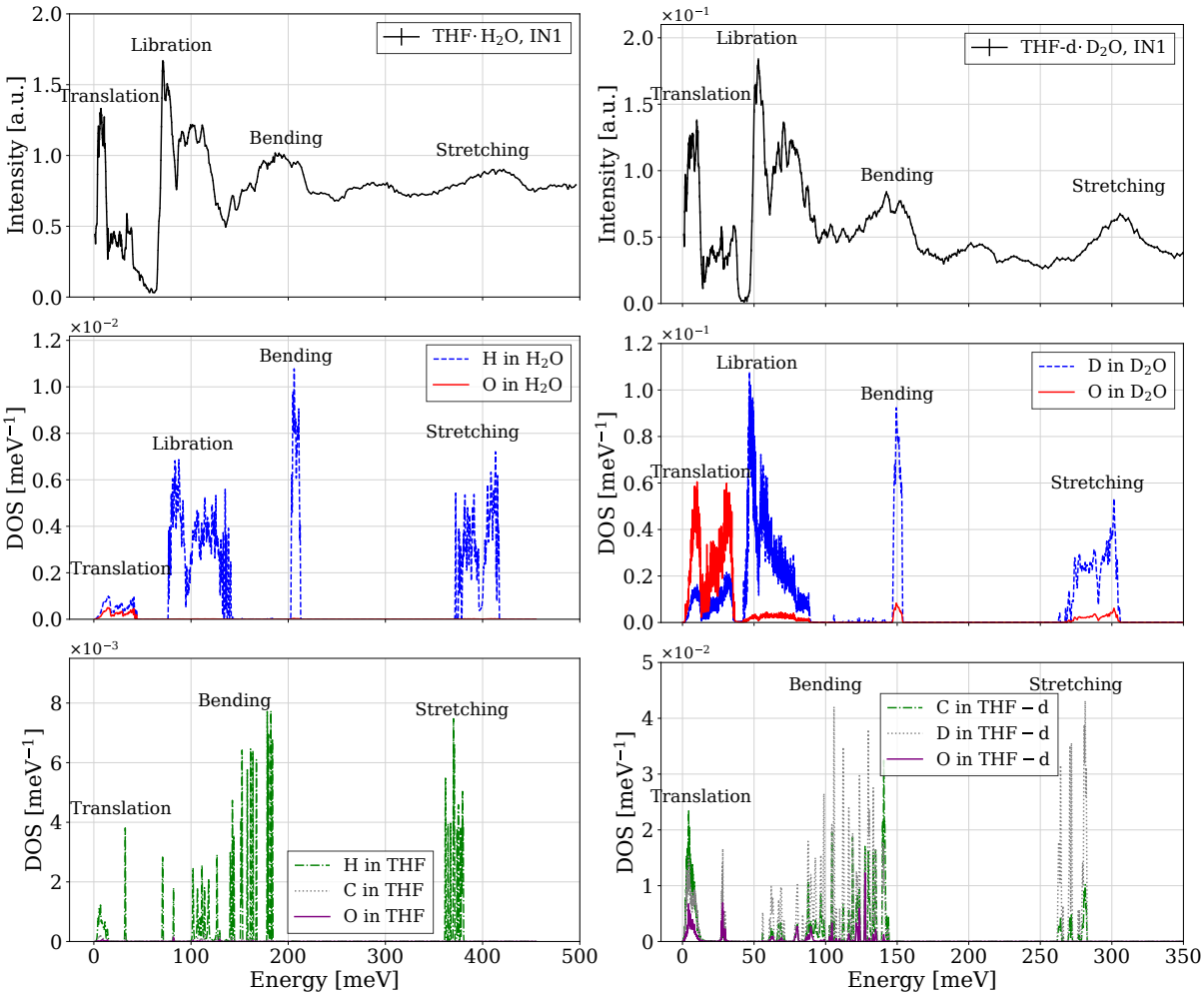

Figure 5.29.: Vibrational spectra of the mixed samples THF · D_2O and THF-d · H_2O as measured at IN1-Lagrange [197] and simulated with Molecular Dynamics [41]. The first panel shows the experimental data. The datasets from different monochromators – Cu(220), Si(311) and Si(111) (see [165]) – are manually stitched. The second and third panels show the computed density of states of the host and the cage respectively. The computed DOS is weighted according to the neutron cross section of each constituent. Note that the y-axis are different. The experimental data is accurately represented by the simulation, which serves as the foundation for the inelastic scattering component of the scattering kernel.

The mixed samples THF-d · H_2O and THF · D_2O are shown in Figure 5.30. At first glance, the separation of the stretching contributions into two distinct regions is striking. This separation arises because the O-D and C-D stretching modes occur at significantly lower energies compared

to the O-H and C-H stretching modes, resulting in two distinct peaks in the experimental data. These features are clearly visible in the experimental data and accurately captured by the MD simulation. The broad peak between the excitations, which are labeled as bending and stretching, represents harmonics of the low-energy excitations. These appear as expected at different energies for the protonated and deuterated sample.

The normal modes of the THF molecule are most clearly observed in the THF · D_2O sample (see Figure 5.30, left) and appear at the predicted positions, as discussed in detail below, where the higher-energy contributions to the vibrational spectrum are briefly analyzed.

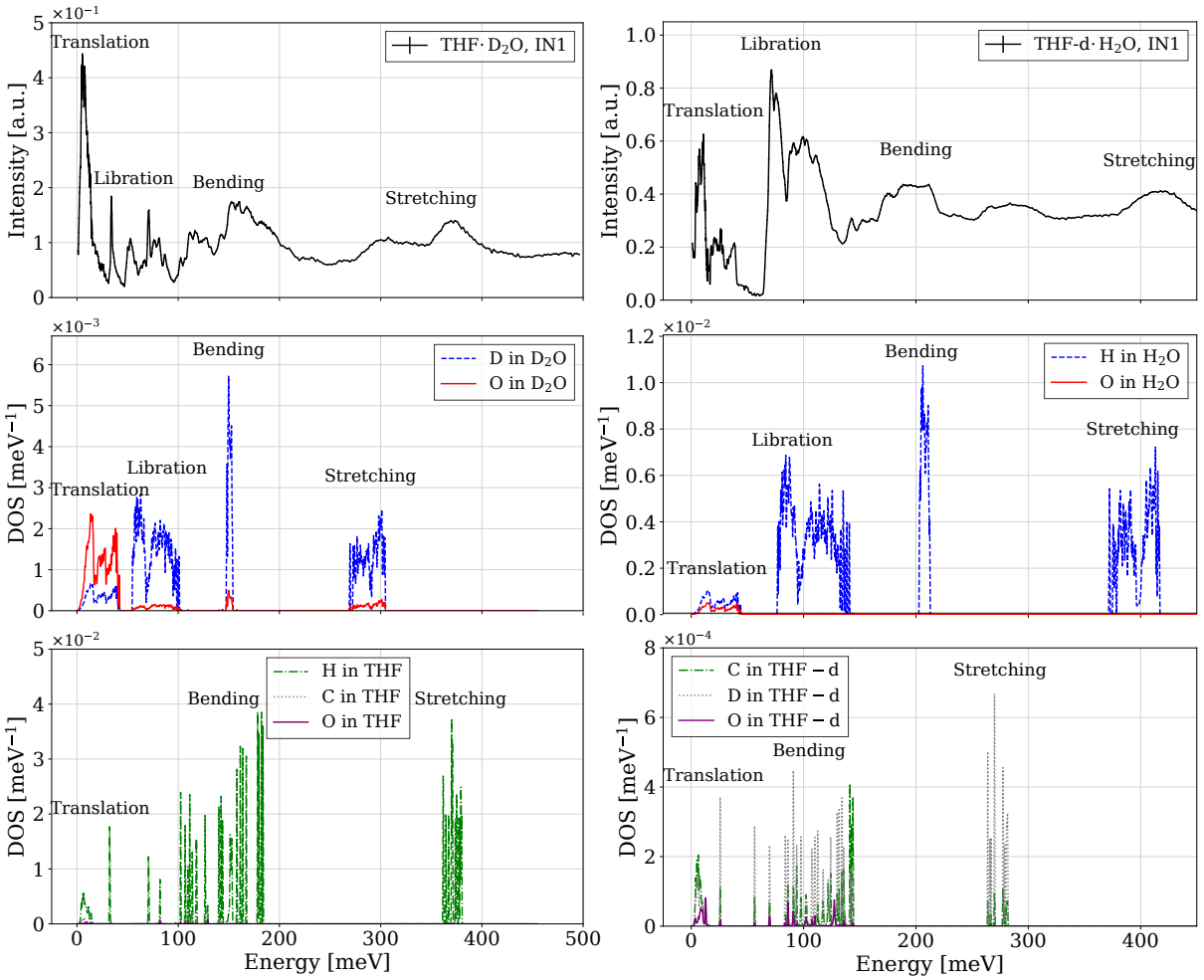

Figure 5.30.: Vibrational spectra of the mixed samples THF · D_2O and THF-d · H_2O as measured at IN1-Lagrange [197] and simulated with Molecular Dynamics [41]. The first panel shows the experimental data. The datasets from different monochromators are manually stitched. The second and third panels show the computed density of states of the host and the cage respectively. The computed density of states (DOS) is weighted by the neutron cross section of each constituent. The experimental data is accurately represented by the simulation, which serves as the foundation for the inelastic scattering component of the scattering kernel.

Low-Energy Dynamics

The data of the fully deuterated sample corresponds accurately with the results measured at Panther with an incident wavelength of 1 Å with lower resolution. The two distinct peaks, typically attributed to hydrogen bond stretching at the end of the translational band, can be

observed in the two peaks around 25 meV and 37 meV at Panther, followed by the characteristic gap and librational bands, i.e. hindered rotation of the H_2O/D_2O molecules (rocking, twisting, wagging) beginning at approximately 50 meV. Both features are well captured by the MD simulation. These excitations are blue-shifted in the fully protonated sample. Hydrogen bond stretching is observed at around 26 meV and 38 meV, consistent with Panther data. The librational band, with its first maximum at 71 meV, is partially captured and only indicated in the Panther data.

Librational Bands

Figure 5.31 explicitly shows experimental data of the librational bands of the fully deuterated and fully protonated sample taken at IN1, compared with data of hexagonal (Ih) [204] and cubic ice (Ic) [205], respectively. The librational bands are highly sensitive to the specific structure of the hydrogen bond network. As a result, they shift to higher energies, around 71 meV for the hydrate and 51 meV for the deuterate, compared to 69 meV for iceIh and 49 meV for deuterated iceIh. A similar shift in methane hydrates, as reported in [206], is attributed to increased rotational restrictions resulting from the formation of the hydrate's cage structure, which leads particularly to higher energy wagging modes.

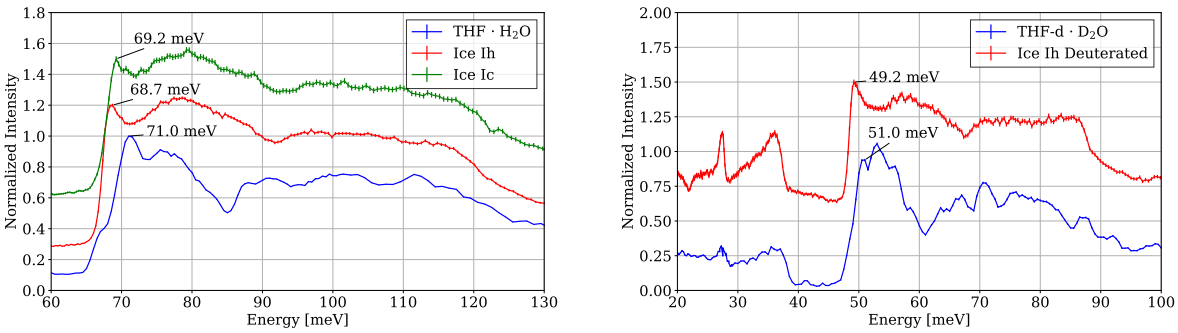

(a) Ice Ih [204], ice Ic [205] and THF hydrates

(b) Deuterated ice Ih [207] and THF-d deuterates

Figure 5.31.: Librational bands of the fully protonated and deuterated samples compared to hexagonal and cubic ice. The data is normalized to the librational peak and then shifted along the y-axis. The hydrate and deuterate samples exhibit a shift to higher energies, approximately 71 meV and 51 meV respectively, relative to ice (69 meV) and deuterated ice (49 meV). This shift reflects increased rotational restrictions in the hydrate's cage structure, consistent with observations by [206], where higher energy wagging modes in methane hydrate were linked to its more organized hydrogen-bond network.

The position of the librational bands as well as its shape is well represented by the simulations of all variations of hydrates shown in Figure 5.29 and Figure 5.30.

Bending

The librational signals are superimposed with the normal modes of the confined THF/THF-d molecule, indicated with "Bending" in the DOS data. These modes can be observed best in data of the THF · D_2O sample (see Figure 5.30). Due to its composition and geometry, the THF molecule exhibits significantly more bending excitations compared to the water cage structure. The normal modes of an isolated THF molecule can be computed using the direct method, relying on ab-initio calculations [208]. With knowledge of the molecular structure and

bonding, the atomic forces and displacements are determined, allowing for the calculation of the vibrational density of states. These calculations were carried out on the relaxed molecule using DMOL3, an ab-initio simulation tool within the Materials Studio software package [209]. The eigenmodes were obtained from the diagonalized dynamical matrix.

The results between 60 meV and 200 meV are shown in Figure 5.32 (red) in comparison with the experimental data of the THF · D_2O sample (blue) and the summed up contributions of the DOS of the confined THF molecule (green). The normal modes of the isolated molecule, calculated using material studio were used to compute a theoretical spectrum using the `Abins` algorithm in Mantid [210]. The agreement suggests that the confined molecule behaves just like an isolated molecule within its cage.

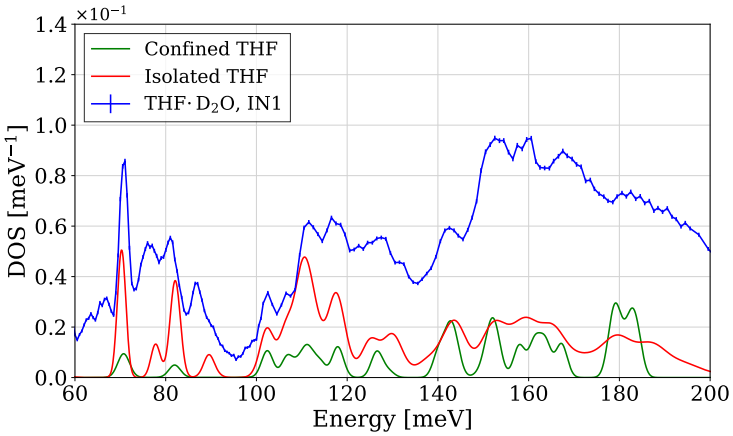

Figure 5.32.: Theoretical spectrum of the normal modes of an isolated THF molecule computed with Materials Studio [209] and `Abins` [210] (red) in comparison with the vibrational spectrum of the THF · D_2O sample recorded on IN1 (blue) and the summed up contributions of the DOS of the confined THF molecule (green), as shown in Figure 5.30.

Previous investigations have characterized the excitation spectrum of THF in its crystalline, liquid, and gaseous states [211]. In contrast to the very good agreement between the experimental data and the normal modes of both an isolated and a confined molecule, the data differ significantly from the spectrum of solid THF, as reported in [211] (see Figure 5.33). Depending on the mode, the confinement induces either a blue- or redshift of up to 2 meV, compared to the solid THF.

This effect warrants further investigation. Given the extensive Raman spectroscopy data available in the literature, complementing the presented results with such data would also enable a direct comparison between the dynamics of confined, liquid, and gaseous THF, enhancing our understanding of the influence of confinement on the vibrational dynamics of THF.

Stretching

The visibility of the stretching band is constrained by the parameters discussed above: at high energy, and consequently at high q vector transfers, the resolution is reduced due to the shallower Bragg angles of the monochromator, the signal is damped by the Debye-Waller factor, and overlaid with harmonics.

Nonetheless, valuable information can be obtained by comparing the forms of the stretching peaks across different samples. Notably, the shoulder of the stretching peak for the fully deuterated THF-d sample, positioned at approximately 265 meV (see Figure 5.29), coincides

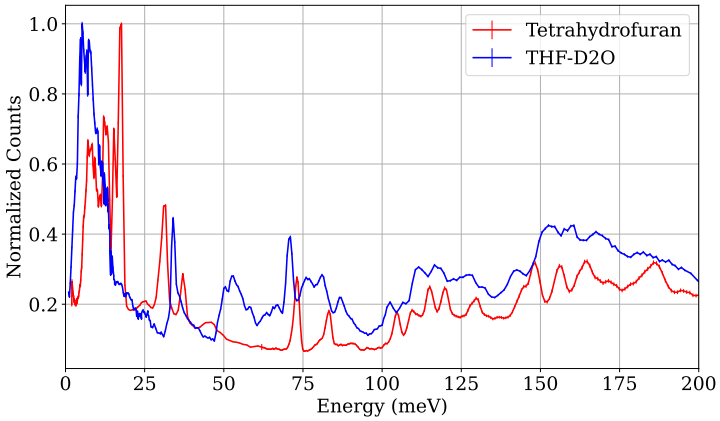

Figure 5.33.: Comparison of the vibrational spectrum of THF confined in the $5^{12}6^4$ D_2O cages recorded on IN1 to solid tetrahydrofuran [211]. Depending on the mode, the confinement causes a blue- or redshift by up to 2 meV.

with a distinct peak in the THF-d · H_2O sample (see Figure 5.30) and can be attributed to D-C stretching. A similar pattern is observed when comparing the distinct C-H stretching peak of the THF · D_2O sample with the stretching of the fully protonated sample, although here the shoulder extends more gradually into a slope.

The double peak predicted for O-H and O-D stretching in the simulations for all four different variations is not discernible in the neutron scattering data. However, the presence of this feature is well-known and attributed to the energy gap between the symmetric and asymmetric stretching modes of the H_2O/D_2O molecules [212]. This feature manifests in various forms across all water and ice-based compounds and has been measured and systematically compared for CS-I and CS-II methane hydrates with Raman spectroscopy [213].

Vibrational Spectrum of the Binary Deuterate

The vibrational spectrum of the binary clathrate hydrate hosting O_2 and THF-d (sample B) is depicted in Figure 5.34. Both the experimental data and the corresponding simulation show a notable resemblance to the THF-d deuterate. This similarity is further illustrated in Figure 5.35, where the two normalized vibrational spectra are superimposed for direct comparison. The MD simulation suggests that the O_2 guest molecule in the clathrate hydrate primarily engages in low-energy rattling modes within its cage, occurring at energies significantly below 10 meV (see Figure 5.34). These modes, although present, do not exhibit sufficient intensity to significantly affect the spectral signals within this range. Conversely, the stretching mode of the confined O_2, predicted at approximately 190 meV, is noticeable as a broad excess signal within this energy domain. Notably, peaks at 27.3 meV and 34.5 meV, along with a shoulder at 46.5 meV, are indicative of hydrogen-bond stretching and the onset of the librational band in deuterated ice Ih, suggesting residual heavy ice in the sample.

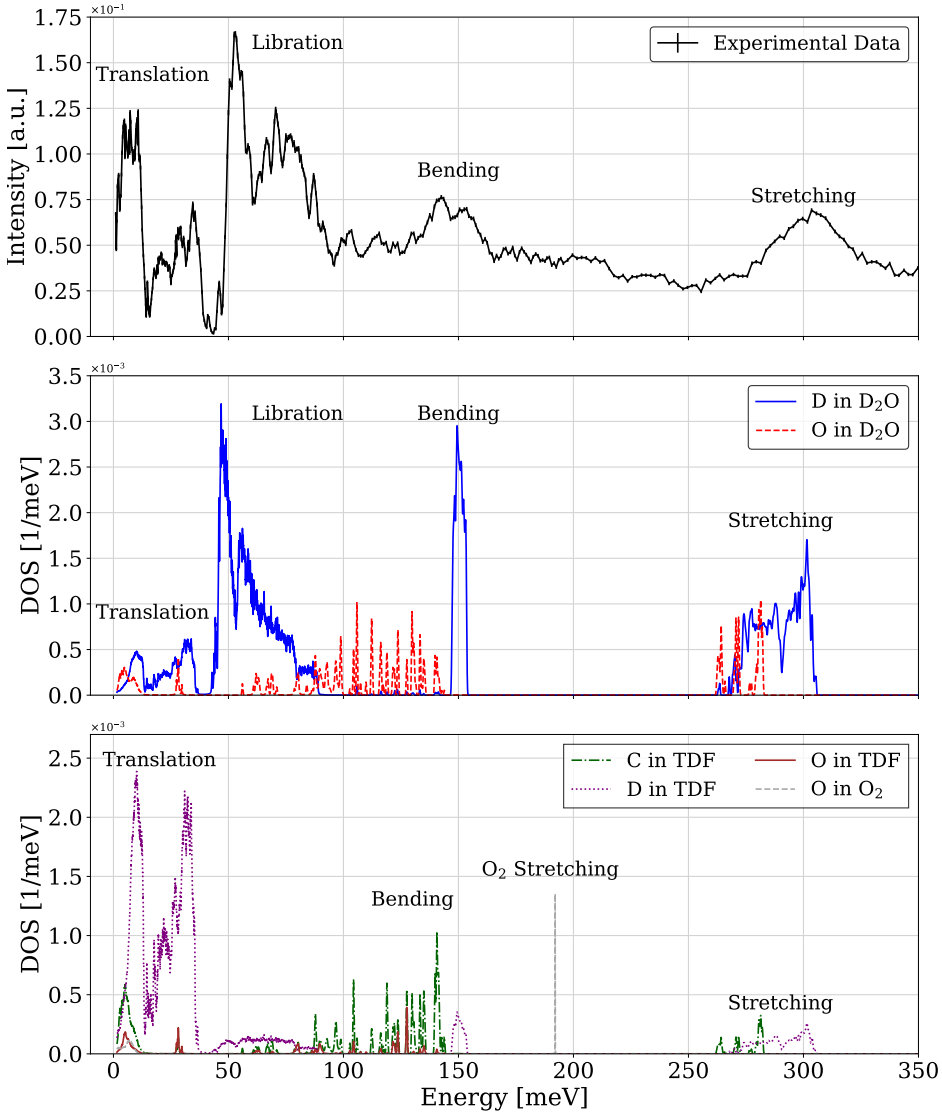

Figure 5.34.: Vibrational spectrum of the binary deuterate THF-d $\cdot O_2 \cdot D_2O$ as measured at IN1-Lagrange [197] and simulated with Molecular Dynamics [41]. The first panel shows the experimental data. The datasets from different monochromators are manually stitched. The second and third panels show the computed density of states of the host and the cage respectively. The computed density of states is weighted by the neutron cross section of each constituent. The experimental data is accurately represented by the simulation, which serves as the foundation for the inelastic scattering component of the scattering kernel.

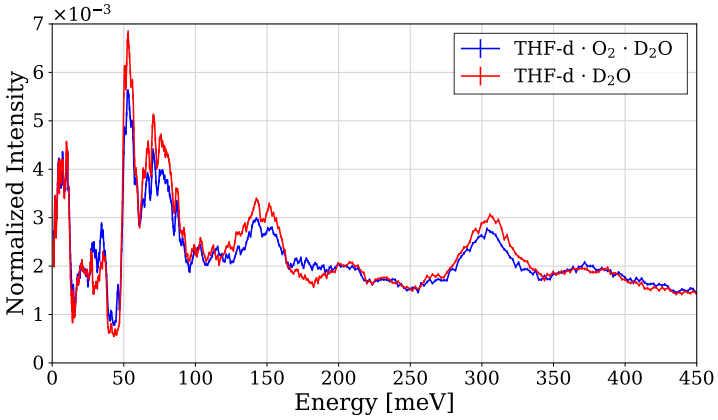

Figure 5.35.: Comparative display of normalized vibrational spectra between THF-d · D_2O and THF-d · O_2 · D_2O. The vibrational spectra are largely similar, though the O_2 stretching mode is indicated at approximately 190 meV. Additional peaks at 27.3 meV and 34.5 meV, together with a shoulder at 46.5 meV, indicate the presence of residual heavy ice.

5.8. Conclusions

The inelastic scattering study of fully and partially deuterated THF hydrates at IN5 and Panther enabled us to measure the dynamical structure factor $S(q, \omega)$ in absolute units of [b sr^{-1} meV^{-1}], providing essential experimental input for the development of the thermal scattering libraries (TSL) within the HighNESS project. The TSL within NCrystal are openly available online [94]. Measuring in absolute units proved challenging due to the complexity of calibration and the need to account for systematic errors, such as multiple scattering and self-shielding across different instruments. However, the overlap in the incident neutron wavelength range between Panther and IN5 allowed for cross-validation of the data, increasing the reliability of the measurements and providing confidence in the accuracy of the employed methodology. We identified a diverse range of low-energy excitations, encompassing both the low-frequency rattling modes of the confined THF molecules and the distinct translational modes characteristic of the CS-II hydrate structure. The dynamical features can be exploited for neutron slow-down to very low temperatures.

Additionally, we performed the first measurements of magnetic down-scattering of neutrons from paramagnetic dioxygen confined within a binary clathrate hydrate. A comparison between two binary hydrate samples, both prepared from THF-d deuterates but with different powdering methods – one using a mortar and the other milled with a ball mill – demonstrated that the fine powder produced by the ball mill exhibited significantly higher O_2 uptake compared to the coarser grains from the mortar. The temperature-dependent dynamical structure factor of the binary hydrate further supports the magnetic scattering model for O_2, initially proposed in [58] and refined in [41].

While the temperature dependence of the magnitude of the magnetic scattering appears to be well modeled, as shown in Figures 3.2b and 5.25a, further investigation into the observed temperature-dependent peak broadening is warranted. To this end, a complementary measurement at the backscattering spectrometer IN16B at the ILL has been granted. By measuring the magnetic excitations with enhanced resolution and at temperatures above 20 K, we can explore whether the observed peak broadening is related to molecular orientation, as suggested by [42].

The vibrational spectra of fully and partially deuterated THF hydrates, measured at IN1-

LAGRANGE, enabled the validation of the simulation input for the thermal scattering libraries of these compounds across the whole excitation spectrum. The observed librational band of the fully protonated sample, shows similar features to other hydrates, attributed to the restricted rotational degrees of freedom in the hydrate phase. The bending of the THF molecule confined in the $5^{12}6^4$ cage was found to be remarkably consistent with the normal modes of isolated THF molecules. Interestingly, these results diverge significantly from previously established data for crystalline and liquid THF. This could be an interesting subject for further investigation and can help understanding the vibrational dynamics of confined THF.

6. Determination of the Total Neutron Cross Section

The concept of the neutron cross section as it pertains to interactions with matter, was previously introduced in Chapter 2. We emphasized the importance of precise material characterization for Monte Carlo (MC) simulations that model neutron slow-down and moderation. The total neutron cross section σ_t serves as a critical benchmark in validating these MC simulations. It is also essential for determining the neutron transparency of the moderator with respect to down-scattered neutrons. In principle, the aforementioned quantities can be calculated if the material's structure is known at all relevant length scales. This includes the mesoscopic structure of packed crystallites, which contributes to small-angle neutron scattering due to fluctuations in scattering-length density. These fluctuations are influenced by the manufacturing processes discussed in Chapter 4. Consequently, measurements of cold neutron (CN) and very cold neutron (VCN) transmission serve as effective tools for both benchmarking our model and directly characterizing neutron transport through the manufactured material. Such measurements provide direct access to the macroscopic total scattering cross section, $\Sigma_\mathrm{t} = \sigma_\mathrm{t} N$ and the neutron's mean free path, $\Lambda = \Sigma_\mathrm{t}^{-1}$. While neutron scattering instruments, as discussed in Chapters 4 and 5, employ advanced techniques to analyze the scattering angle, energy, or spin of scattered neutrons, neutron transmission experiments examine the neutrons that pass through the sample and remain unscattered. Figure 6.1 illustrates the schematic of such an experiment.

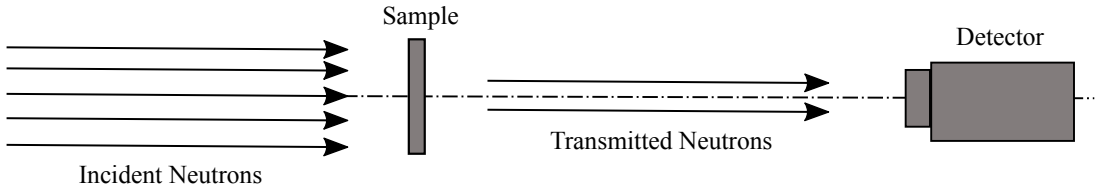

Figure 6.1.: Principle of a measurement of the total neutron scattering cross section σ_t through transmission. Figure adapted from [45, Figure 4.1.1].

Guided by equation 2.6 in Section 2.1.2, we find the following expression for the count-rate in the detector behind a sample (Figure 6.1) of a thickness d:

$$\dot{Z}_1 = \dot{Z}_0 \exp\left(-N\sigma_\mathrm{t} d\right) , \tag{6.1}$$

where $\dot{Z}_0$ is the count rate at the detector with no sample in the beam.[1] The transmission T through the sample is defined as the ratio of the measured count-rates with and without the sample being present in the beam

$$T = \frac{\dot{Z}_1}{\dot{Z}_0} , \tag{6.2}$$

[1]The count-rate $\dot{Z}_1$ is related to the neutron flux Φ over a wavelength dependent detector efficiency ϵ and the solid angle Ω subtended by the detector. The notation$\dot{Z}$ represents the time derivative, $\frac{\mathrm{d}Z}{\mathrm{d}t}$.

one can thus derive the total neutron cross section as:

$$\sigma_{\mathrm{t}} = \frac{1}{Nd} \ln\left(\frac{1}{T}\right) = \frac{1}{Nd} \ln\left(\frac{\dot{Z}_0}{\dot{Z}_1}\right) \ . \tag{6.3}$$

To ensure the accuracy of transmission experiments, measurements of the count rates with ($\dot{Z}_1$) and without ($\dot{Z}_0$) the sample must be conducted under identical conditions. This includes maintaining the experimental setup consistent and correcting for any beam fluctuations during the experiments.[2] There are several contributions that give rise to the total cross section attenuating neutron beams in the cold and very cold range:

1. σ_{a} for absorption or neutron capture,
2. σ_{inel} for inelastic scattering,
3. $\sigma_{\mathrm{coh}}^{\mathrm{el}}$ for coherent elastic scattering or Bragg-scattering
4. $\sigma_{\mathrm{inc}}^{\mathrm{el}}$ for incoherent elastic scattering
5. and σ_{inhom} or σ_{SANS} for scattering from inhomogenities in the scattering-length density of the medium leading to small angle scattering (SANS).[3]

The total neutron cross section is the sum of all these contributions

$$\sigma_{\mathrm{t}} = \sigma_{\mathrm{a}} + \sigma_{\mathrm{inel}} + \sigma_{\mathrm{coh}}^{\mathrm{el}} + \sigma_{\mathrm{inc}}^{\mathrm{el}} + \sigma_{\mathrm{inhom}} \tag{6.4}$$

All these contributions, with the exceptions of $\sigma_{\mathrm{inc}}^{\mathrm{el}}$ (see Section 2.1.5) are dependent on the neutron energy. The coherent elastic cross section $\sigma_{\mathrm{coh}}^{\mathrm{el}}$ as well as σ_{inhom} contain information about the structure of the medium. In the following, these contributions are sometimes referred to as the scattering cross section, where $\sigma_{\mathrm{s}} = \sigma_{\mathrm{inel}} + \sigma_{\mathrm{coh}}^{\mathrm{el}} + \sigma_{\mathrm{inc}}^{\mathrm{el}} + \sigma_{\mathrm{inhom}}$. A time-of-flight setup allows to measure the sum of these quantities (σ_{t}) as a function of the neutron's energy E or wavelength λ. This chapter details a variety of such setups within the cold neutron (CN) and very cold neutron (VCN) regimes, as implemented throughout the course of this thesis. The theoretical neutron scattering cross section calculated with the previously described thermal scattering libraries are described in [41]. They can be used to compute scattering kernels and cross sections using the open-source software package NCrystal [57, 86, 87]. The resulting cross section for the THF-d deuterate is shown in Figure 6.2. It is worth noting that this modeled cross section does not take into account small-angle scattering. However, as shown in this chapter, this could be an important contribution to the total cross section in the VCN range in both the bulk and the powder sample.

[2] To underscore this point, Anton Steyerl refers in [69] to Heraclitus' aphorism πάντα ῥεῖ (*panta rhei*), which would translate to 'everything is in a state of flux'. Heraclitus is also known for the metaphor: 'you cannot step into the same stream twice', which is known through fragments and Plato's Cratylus dialogue [214]. Putting this philosophy into practice translates to a careful beam monitoring during the measurements of $\dot{Z}$ and $\dot{Z}_0$. While you cannot measure the same neutron time-of-flight spectrum twice, you can indeed monitor the beam intensity and account for statistical fluctuations. Another approach is to alternate the measurements of $\dot{Z}$ and $\dot{Z}_0$ in intervals of several minutes, and average over these measurements. However, this is only practically feasible if the process can be automated.

[3] Note that for very slow neutrons with high wavelength the scattering angles are not necessarily small.

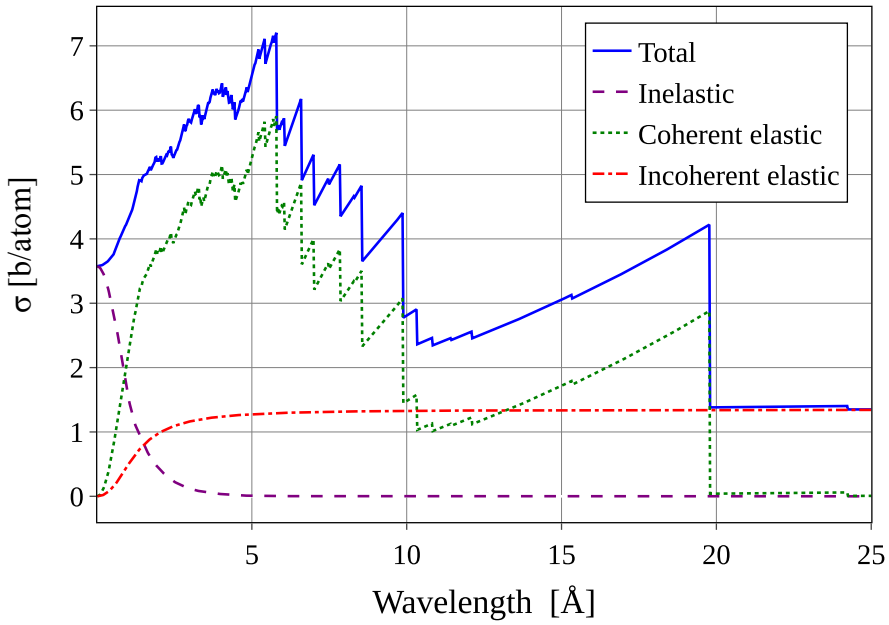

Figure 6.2.: The different contributions to the neutron scattering cross section of a CS-II hydrate hosting THF-d. The cold neutron range is dominated by coherent elastic Bragg scattering providing excellent diffuse reflection properties for moderator applications (see text). The plot was generated with NCrystal [57] based on simulations described in [41].

6.1. Neutron Transmission Experiments Using a Time-of-Flight Setup

6.1.1. Time-of-Flight Measurements

In a time-of-flight measurement, particles are emitted from the chopper opening and propagate over a distance D to a detector. By measuring the time t it takes for particles to travel this distance, their velocity v can be determined. Using de Broglie's relation, $p = mv = \hbar k = \hbar\frac{2\pi}{\lambda}$, the particle's wavelength λ can be expressed as:

$$\lambda = \frac{ht}{mD}\,. \tag{6.5}$$

To achieve this, the beam of particles is chopped into narrow bunches at the start of the flight path, located at $D = 0$, defining the time $t = 0$. Particles with different velocities will arrive at the detector at different times, allowing for the determination of their velocities based on the time-of-flight. From the distribution of arrival times $R(t)$ the time-of-flight distribution $R(\tau)$ can be evaluated and then be converted into a velocity or wavelength[4], via

$$v = \frac{D}{\tau}\,, \tag{6.6}$$

$$\frac{\mathrm{d}v}{\mathrm{d}\tau} = -\frac{D}{\tau^2} \tag{6.7}$$

[4]The distribution of arrival times can in principle differ from the the time-of-flight distribution, by e.g. a chopper offset as discussed in Appendix D. Therefore, distinct variables t and τ are used to represent these quantities.

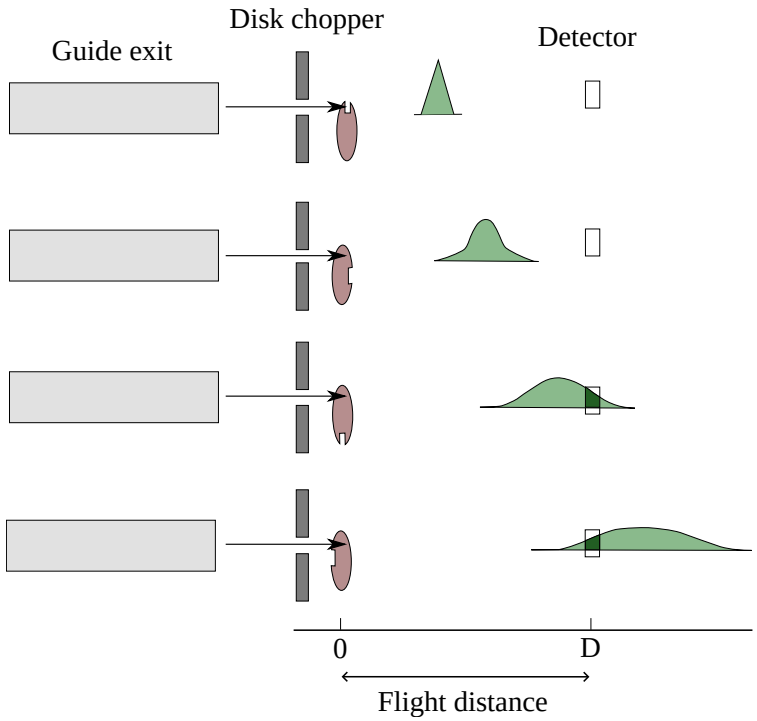

Figure 6.3.: A schematic representation of a time-of-flight measurement (adapted from [215, Figure 3.8]). The neutron beam is divided into pulses by a rotating disk chopper at $D = 0$ traveling towards the detector on the right side of the illustration. The neutron pulses spread in time according to their velocity distribution as shown from top to bottom. The change of the detector rate over one time-of-flight frame is indicated with the dark green intersection of the TOF distribution with the detector.

and

$$\lambda = \frac{h\tau}{mD} \,, \tag{6.8}$$

$$\frac{\mathrm{d}\lambda}{\mathrm{d}\tau} = \frac{h}{mD} \,. \tag{6.9}$$

For $R(\tau)$ the following relations apply:

$$\frac{\mathrm{d}R(\tau)}{\mathrm{d}v} = \frac{\mathrm{d}R(\tau)}{\mathrm{d}\tau}\frac{\mathrm{d}\tau}{\mathrm{d}v} = -\frac{\mathrm{d}R(v)}{\mathrm{d}\tau}\frac{D}{v^2} \,, \tag{6.10}$$

$$\frac{dR(\tau)}{\mathrm{d}\lambda} = \frac{dR(\tau)}{\mathrm{d}\tau}\frac{\mathrm{d}\tau}{\mathrm{d}\lambda} = \frac{\mathrm{d}R(\lambda)}{\mathrm{d}\tau}\frac{mD}{h} \,. \tag{6.11}$$

The principle of such a measurement is illustrated in Figure 6.3. A typical time-of-flight measurement obtains counts $f = (f_1, f_2, \ldots, f_n)$ at a given amount of time-of-flight channels $\tau = (\tau_1, \tau_2, \ldots, \tau_n)$. These counts are usually either normalized to a detector count rate or divided by the measurement time. In order to transform such a dataset into the wavelength domain using the equations introduced above, one has to compute the array

$$w = (w_1, w_2, \ldots, w_n) \,, \text{where } w_i = W(\tau_i) = \frac{h\tau_i}{mD} \,, \tag{6.12}$$

as well as the array

$$F = (F_1, F_2, \ldots, F_n) \,, \text{where } F_i = \frac{f_i}{\frac{\mathrm{d}W}{\mathrm{d}\tau}} = f_i\frac{mD}{h} \,. \tag{6.13}$$

The experiments described herein utilized various rotating disk choppers, typically comprising a disk with radius $\tilde{R}$ rotating at an angular frequency ω and equipped with one or more slits of width a. The width b of the modulated beam is generally determined by an aperture positioned directly upstream of the chopper disk, often referred to as a stator. As described in [215, Section 3.2.1], the resolution of a time-of-flight experiment is mainly influenced by (a) the flight distance D and (b) the opening time of the chopper, or more specifically, the chopper gating function $T(t)$. Ideally, a chopper would create a narrow particle bunch by opening and closing instantaneously, resulting in a gating function in the shape of a δ-function ($T(t) = \delta(t)$). In reality, however, the gating function has a finite and usually non-negligible width. The opening time of the gating function $T(t)$ of a rotor moving over a stator can be approximated as [215, Equation 3.37]:

$$t_0 = 2\Delta t_1 + \Delta t_2 = \frac{(a+b)}{\omega \tilde{R}} \quad . \tag{6.14}$$

This is a result of geometric considerations of the chopper window, which opens linearly for the time interval Δt_1, remains open for Δt_2 and then closes again for Δt_1. The transmission functions are repeated periodically, with the phase depending on the number of slits. The time intervals Δt_1 and Δt_2 are determined by the properties of the chopper, such as radius $\tilde{R}$, slit width a, and angular frequency ω, and the width of the stator b, as detailed in [215, Table 3.2].

The measured time-of-flight distribution $R(t)$ at the detector represents the convolution of the chopper gating function $T(t)$ with the "true" time-of-flight distribution $r(t)$. Detailed knowledge of the chopper opening function allows one to account for that and retrieve the "true" via deconvolution techniques, one of which is discussed in Appendix C. The effect of the finite detection length can be addressed by determining an effective transmission function,$T_{\text{eff}}(t)$, which accounts for both the finite opening time and the detector length, and then using this function in the deconvolution, as outlined in [215, Section 3.2.1]. For the experiments discussed here, the conversion layers in the detectors are very thin compared to the flight distances D (for ^{6}LiF $<$ mm, for ^{3}He $<$ cm). In addition, the probability of neutron conversion decreases exponentially with depth within the layer, with most neutrons converting at the beginning of the layer. Consequently, the resolution limit is primarily governed by the finite opening time of the chopper, rather than by the finite detection length.

Designing a time-of-flight measurement involves balancing these experimental constraints to optimize resolution and statistical accuracy. To demonstrate this, we compare two distinct experimental setups at PF1B, focusing on the influence of the chopper gating function on time-of-flight and wavelength resolution. Details of these two setups are discussed below. The chopper utilized in experiment 3-07-419 features a triangular gating function with an opening time of $\Delta t = (0.124 \pm 0.003)$ ms. In contrast, the chopper in experiment 3-14-431 is characterized by a trapezoidal gating function, with an opening time of $\Delta t = (1.2070 \pm 0.0031)$ ms. Details of these choppers are provided in Table 6.1. Assuming the detector response time is negligible and the electronics are sufficiently rapid, then the chopper opening time t_0 predominantly defines the resolution limit for the time-of-flight $\Delta\tau$. Given a well defined flight distance D one can calculate the resolution limit in wavelength $\Delta\lambda$ as:

$$\Delta\lambda = \frac{h}{m\frac{D}{\Delta t}} \, . \tag{6.15}$$

According to Equation 6.15, both a reduction in the opening time t_0 and an increase in the flight distance D contribute equally to enhancing the resolution. The choice of which parameter to adjust depends on the specific experimental conditions. A fundamental constraint for both parameters is the time-of-flight frame, defined as the time interval between two neutron pulses or chopper openings. Increasing the chopper disk radius ($\tilde{R}$) or reducing the number of slits can geometrically extend this interval, thereby enlarging the time-of-flight frame for a given

resolution. However, such modifications typically result in lower count rates at the detector, posing a challenge for statistically limited applications. The duty cycle of a chopper can be defined as

$$\text{Duty Cycle} = \frac{\Delta t}{t_{\text{cycle}}} \,. \tag{6.16}$$

In a time-of-flight measurement, assuming minimal losses and that the detector fully encompasses the beam's divergence, the neutron flux at the detector is the product of the continuous flux and the Duty Cycle. This typically causes a reduction in flux by a factor of 10^1 to 10^2 (see Table 6.1). Any measure that increases the time-of-flight frame, or decreases Δt for better resolution, has drawbacks on the duty cycle and eventually on the statistical accuracy of the experiments. An attempt to circumvent this problem is to use intentional frame overlaps and subsequent deconvolution, as discussed in [216]. Similar concepts in the context of total cross section measurements are discussed in Appendix C. An increase of D does not directly impact the chopper's duty cycle[5], but losses due to scattering from air or windows in and out of flight tubes need to be considered. An outline for calculating air-losses is given in Appendix B. This challenge is particularly pronounced when measurements span wide spectral ranges associated with strong variation of beam intensity, such as those encountered with the cold beam at PF1B. Here, the use of additional neutron-optical components, such as supermirrors, can be advantageous to match the dynamic range to the detector. These components can shape the spectrum, allowing different sections to be measured sequentially. This approach enables the optimization of time-of-flight parameters for specific portions of the spectrum, rather than for the entire white beam, as discussed in Section 6.2.1.

Table 6.1.: Parameters of the disk choppers used at PF1B during experiment 3-14-431 in June 2023 and experiment 3-07-419 March/April 2024.

Parameter	3-07-419	3-14-431
$\tilde{R}$ [mm]	32	124.7
a [mm]	0.25	3.07
b [mm]	0.25	6.39
ω [rad/s]	125.66	62.83
Δt_1 [ms]	0.0622 ± 0.001	0.392 ± 0.001
Δt_2 [ms]	0 ± 0.0018	0.424 ± 0.002
Δt [ms]	0.124 ± 0.03	1.207 ± 0.031
Duty Cycle [%]	0.75%	4.83%
D [m]	2.25	3.57

6.1.2. Optimizing Sample Dimensions

Unlike scattering experiments, which are discussed in Chapter 4 and Chapter 5, the signal in a transmission experiment ideally consists only of neutrons that have not interacted with the sample. As a result, the sample geometry does not need to account for self-shielding effects, which are critical in neutron scattering experiments as discussed in Section 5.2.1. On the other hand, multiple scattering can pose a concern, but it is approached differently in neutron transmission experiments compared to neutron scattering experiments. In transmission experiments, any scattered neutron detected is regarded as parasitic, not just those that have scattered multiple times. Given that the sample's thickness within the beam is crucial for accurately calculating the total neutron cross section, the primary geometrical requirement is to ensure a uniform surface

[5]However, D limits the time-of-flight frame t_{cycle}

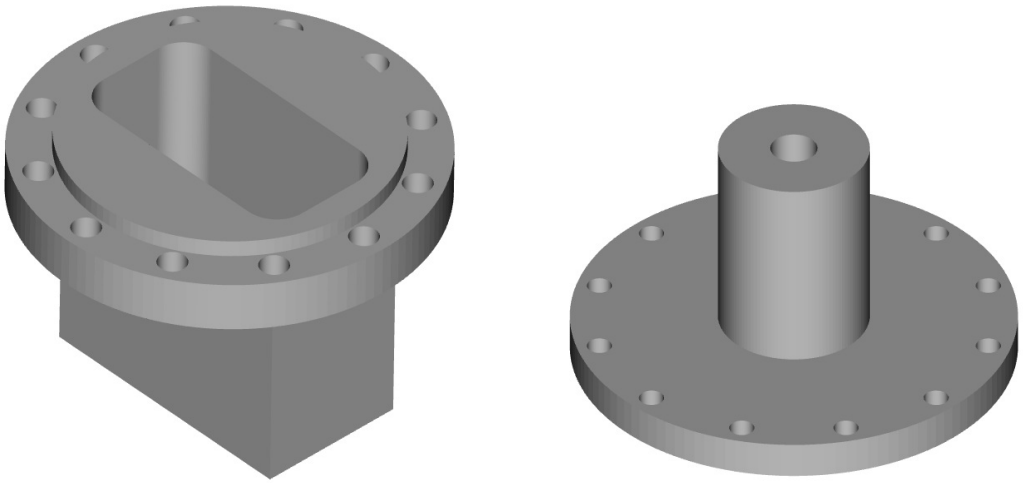

(a) Sample container. (b) Sample container lid.

Figure 6.4.: Design of the sample container for clathrate hydrate samples in transmission experiments. The cuboid design allows to reorient the sample during the experiment and measure two different sample thicknesses. The excess material at the top of the container creates an edge for an indium seal between the lid and the container. The container can be filled with the THF-d – D_2O solution to form the hydrate in situ, or filled cold with the hydrate powder. The container lid connects to the sample stick with an M8 screw, providing a thermal coupling to a nearby temperature sensor. The stick can be inserted from the top into the cryostat.

number density (number density integrated over the sample length) across the entire beam cross section.

When selecting materials for the sample container, neutron transparency is the key consideration. Although the thin, smooth surfaces of glass cells provide nearly ideal transmission properties, they proved susceptible to damage from the volume expansion of the hydrate phase. In contrast, aluminum was chosen for its durability, machinability, and excellent neutron transparency, making it well-suited for use in the cryogenic sample environment. The cuboid design of the container allows it to be used in different orientations, enabling variations in sample thickness during the experiment and facilitating the investigation of possible scattering effects. This design is illustrated in Figure 6.4. Various dimensions were employed in different experiments.

Sample Thickness

In equation 6.3, $\dot{Z}_1$ and $\dot{Z}_0$ refer to the count rates in the detector with and without the sample, respectively. For a constant beam, the total neutron counts are given by $Z_1 = \dot{Z}_1 t_1$ and $Z_0 = \dot{Z}_0 t_0$, where t_0 and t_1 are the counting times for each configuration. This allows equation 6.3 to be rewritten as:

$$\sigma_\mathrm{t} = \frac{1}{Nd} \ln\left(\frac{1}{T}\right) = \frac{1}{Nd} \ln\left(\frac{Z_0}{Z_1}\right) \ . \tag{6.17}$$

The optimal choice of d to maximize the statistical precision of σ_t is discussed in detail in [217]. Specifically, when the counting times for both with and without the sample are equal ($t_0 = t_1$), an optimal transmission of about 11% significantly reduces statistical errors. If one allows the the counting time without the sample to be shorter, achieving an even lower transmission of approximately 8% can further reduce the statistical error of σ_t.

Detector Field of View and the Role of Single and Multiple Scattering Events

Equation 6.2 is exact if the beam attenuation, which causes the change in the rate $\dot{Z}_1$, is solely due to nuclear capture σ_a and there are no sources of background. However, if the total neutron cross section is dominated by scattering σ_t, this equation is only valid provided that the scattering of the sample into the detector is negligible and only neutrons that have not scattered from the sample are counted. Depending on the sample's cross section, a transmission of 8% or 11% can correspond to sample thicknesses ranging from several fractions of a millimeter to more than 10 cm. For large samples, the probability of single and multiple scattering increases, and neutrons that scatter out of the solid angle covered by the detector might scatter back into the detector at a later stage. To circumvent this issue in neutron scattering experiments, the rule of thumb is that the probability of multiple scattering remains usually below $\sim 1\%$ if the sample attenuates the beam by no more than 90% [43]. In contrast to neutron scattering experiments, which are designed to capture the maximum solid angle, transmission experiments aim to minimize the detector's field of view. Consequently, only multiple scattering events within this narrow view contribute to parasitic signals. For instance, considering isotropic scattering: a circular detector with radius r positioned at a distance L from the sample covers a solid angle of:

$$\Omega = 2\pi(1 - \cos(\theta)) \,, \tag{6.18}$$

where

$$\theta = \arctan(r/L) \,. \tag{6.19}$$

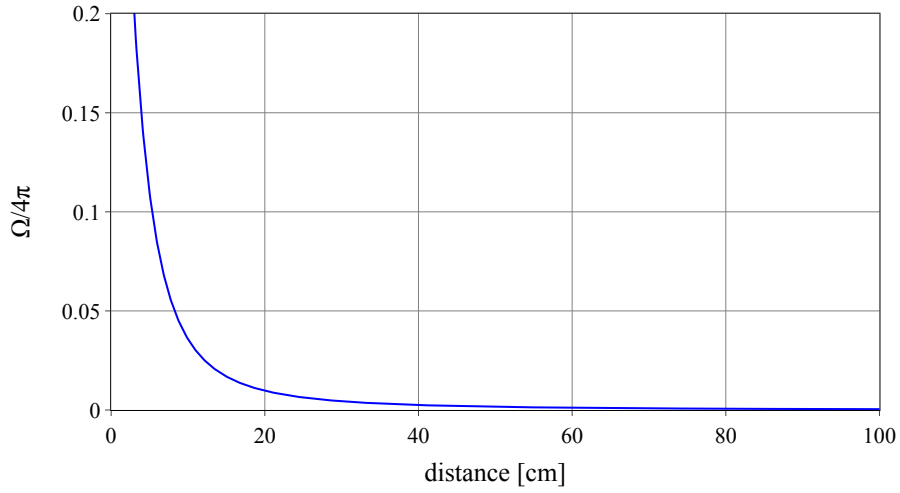

Figure 6.5.: Fraction of neutrons detected in a circular detector with radius $r = 4\,\mathrm{cm}$ for isotropic scattering, as a function of the distance from the sample.

We can estimate the scattering probability S for single scattering events within a slab of thickness d by considering the probability that a neutron travels a distance x without interacting, represented by $\exp(-\sigma_\mathrm{t} N x)$, then scatters within a differential thickness $\mathrm{d}x$, represented by $\sigma_\mathrm{s} N \mathrm{d}x$, and subsequently travels from x to d without being absorbed, the latter being is expressed as $\exp(-\sigma_\mathrm{a} N(d-x)/\cos\theta)$, where θ is the scattering angle [43]. Assuming that θ is small, such that $\cos\theta \approx 1$, simplifies the expression but may slightly overestimate the total scattering probability. This assumption is typically valid when θ is within a few degrees. By multiplying these probabilities and integrating over x, we obtain:

$$S = \frac{\sigma_s}{\sigma_\mathrm{t}} \exp(-\sigma_a N d)(1 - \exp(-\sigma_\mathrm{t} N d)). \tag{6.20}$$

Table 6.2.: Tabulated values of the scattering and capture cross sections [218] of the constituents of THF-d deuterates and binary THF-d – O_2 deuterates. An estimate of total cross section (neglecting Bragg scattering and macroscopic effects) can be calculated if the cage occupancy of the hydrate is known.

	σ_s [b]	σ_a [b]
Hydrogen	82.02(6)	0.3326(7)
Deuterium	7.64(3)	0.000519(7)
Oxygen	4.232(6)	0.00019(2)
Carbon	5.551(3)	0.00350(7)

Since the sample under investigation – fully deuterated clathrate hydrates – exhibits notably low absorption, a sample thickness that optimizes the statistical precision for equal counting times of the empty cell and the sample ($T = 0.11$, $d \approx 3.4\,\text{cm}$), as previously discussed, would unsurprisingly lead to $S \approx 0.89$. For samples with higher absorption, this value of S would naturally be smaller. For isotropic scattering events at a typical detector with a radius of 4 cm, the probability of scattered neutrons arriving at the detector is given by $S\frac{\Omega}{4\pi}$. This scenario is illustrated in Figure 6.5. At a distance of 1 m and with $S = 0.89$, this probability becomes 0.036%. Compared to the designed transmission probability of 11%, this contributes an error of 0.32%.

This demonstrates that positioning the detector sufficiently far from the sample keeps 'in-scattering' from multiple scattering events at a negligible level. Consequently, the primary limitation on sample size in a transmission experiment is not multiple scattering. In our case the sample size is dictated by the reliability of the in-situ hydrate formation. The rate and purity of hydrate formation depend on the cooling rate, necessitating adjustments in sample volumes to achieve different cooling speeds. Additionally, the sample geometry must be compatible with the cryogenic environment. For ILL cryostats, the standard diameter of the sample volume is 49 mm, which imposes an additional constraint on the design of the sample cell. As a result, actual sample thicknesses deviate from the optimal $d = 3.4\,\text{cm}$. Table 6.3 lists all different sample dimensions used in the transmission experiments described in this work.

Table 6.3.: List of the different geometries used as sample container for transmission experiments.

	Height [mm]	Length [mm]	Width [mm]	Volume [cm^3]
Geometry I	47	40	20	37.6
Geometry II	33	31	16	16.368
Geometry III	28	15	10	4.2

6.2. Transmission Experiments in the Cold Neutron Range

During the course of this thesis, three transmission experiments were conducted in the cold neutron range:

- At the multipurpose beam-line BOA, PSI, Villingen, Switzerland, in October 2022.
- At the fundamental physics beam-line PF1B at the Institut Laue-Langevin (ILL), Grenoble, France, in June 2023 [219].
- At the same beam-line in March/April 2024 [220].

The details and results of these experiments are outlined in the following section.

6.2.1. The Setup of Experiment 3-14-232 on PF1B

The PF1B beam-line faces the vertical liquid deuterium cold source via the 76 m long, $m = 2$ supermirror ballistic neutron guide *H113* with a cross section of 6 cm×20 cm [221]. A layout of the experimental setup is shown in Figure 6.6. The beam cross section was reduced in the casemate with a series of decreasing apertures to a circle with diameter 0.8 cm.

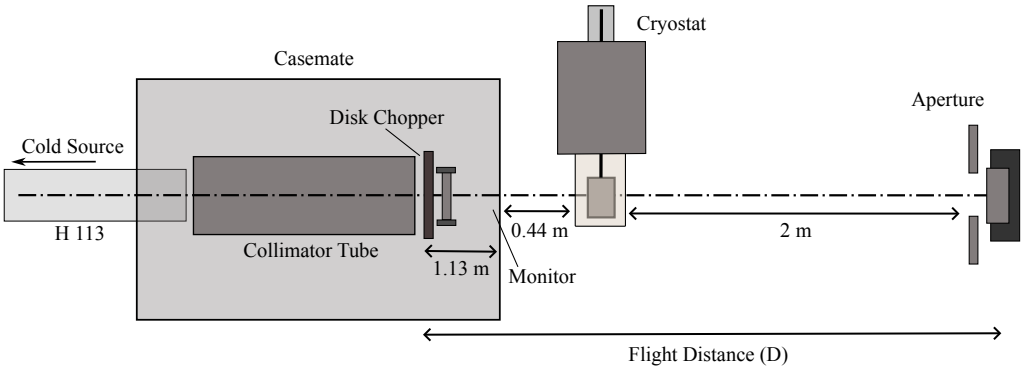

Figure 6.6.: Layout (top-view) of the experimental setup 3-14-232 at PF1B. The cold neutron beam enters from the left side through the ballistic $m = 2$ supermirror ballistic guide *H113* and passes through a collimating system containing a series of decreasing apertures under vacuum. This is followed by the chopper and a monitor detector. The beam then enters the experimental zone where it passes through the sample and hits the detector after a final aperture. The total flight distance $D = 3.57$ m.

The cryogenic sample environment was maintained by a dry cryostat equipped with a Cryomech pulse tube cold head, which utilizes a closed-loop helium refrigeration cycle to achieve cryogenic temperatures. The system used in our experiments at the ILL attained a base temperature of 4 K. The cold head is thermally coupled with the cryostat, enabling effective thermal isolation of the sample volume by shielding it from heat radiation and using an isolation vacuum to prevent convective heat transfer. The closed helium cycle continuously recycles the He gas. The compressor unit compresses and cools the gas, which is then sent back to the cold head for another cooling cycle, eliminating the need for liquid He refills.

The chopper disk had a radius of $\tilde{R} = 12.47$ cm and featured two openings separated by 180°, each with a width of $a = 3.1$ mm. It rotated at 10 Hz, producing a time interval of 50 ms between successive pulses. The width of the stator slit was $b = 6.4$ mm. The resulting parameters for the transmission function are provided in Table 6.1. This setup was a result of grouping multiple experiments on innovative reflector materials at PF1B, one of which is described in [222]. The grouping of these experiments did not fully meet the resolution requirements for our experiment, which required its repetition. The details of this reiteration are provided in the following section.

6.2.2. The Setup of Experiment 3-07-419 on PF1B

A schematic of the experimental setup is presented in Figure 6.7. The area of the beam exiting the neutron guide *H113* was reduced within the casemate using a series of apertures to a final diameter of 0.8 cm. The chopper was positioned approximately 5 cm downstream of the final aperture at the beginning of the experimental zone, followed by a monitor detector. The monitor was a ^{3}He counter with a low efficiency of $\epsilon \approx 10^{-5}$ for neutrons of 1 meV. Both the chopper and

the monitor detector were shielded using boronated polyethylene and lead bricks. The sample, together with its cryogenic environment, was mounted on a translation stage located 76 cm downstream of the chopper, allowing for movement perpendicular to the beam. The detector was placed at additional 149 cm downstream, resulting in a total flight path of $D = 225\,\mathrm{cm}$.

A particular challenge at the PF1B beam-line is the high neutron flux of $2 \times 10^{10}\,\mathrm{n\,cm^{-2}\,s^{-1}}$, which necessitates extensive shielding and effective suppression of radiation backgrounds. The background tube shown in Figure 6.7 is an aluminum tube lined with boronated rubber. This design significantly narrows the detector's field of view, thereby substantially reducing ambient backgrounds. The chopper and detector used in this setup were originally designed as a compact

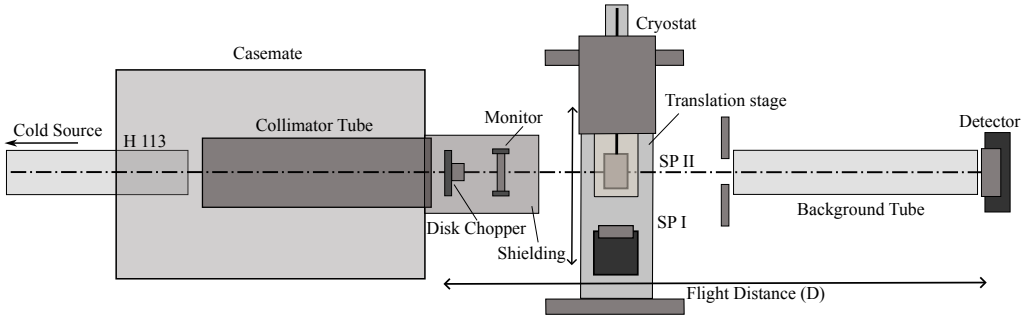

Figure 6.7.: Layout (top-view) of experiment 3-07-419 at PF1B. Compared to the setup shown in Figure 6.6 the cryostat is now equipped with a translation stage to switch easily between two sample positions SP I for calibration samples and samples that do not require a cryogenic sample environment and SP II for hydrate samples in a cryogenic sample environment.

time-of-flight device for the characterization of the GRANIT beamline [223]. The remarkably small slit size of 0.25 mm for both the rotor and stator enables a high-resolution time-of-flight setup, even with limited flight distances. The detector, shown in Figure 6.8, includes a thin ^{6}LiF conversion layer, which has weak impact on the time-of-flight resolution. The efficiency of this detector is approximately 2.5% for neutrons with an energy of 1 meV. In the setup illustrated in Figure 6.7, the detector was positioned farther from the chopper to extend the flight path and accommodate additional components. The original brushless DC motor powering the chopper was replaced with a small stepper motor, allowing the chopper to be controlled via NOMAD [224], the ILL's in-house instrument control software.

Adaption of the Setup Using a supermirror

The cold neutron beam at PF1B spans a broad spectral range from 1 Å to 40 Å [225]. Measuring such an extensive spectrum within a single time-of-flight setup presents significant challenges and necessitates considerable trade-offs.

Firstly, the peak of the spectrum imposes a limit on the required detector efficiency to prevent saturation. The spectral flux in the long-wavelength tail can be up to 10^4 times lower than the maximum flux, leading to low count rates and necessitating stringent background reduction measures. This effort was complicated by the non-negligible neutron transmission through the borated aluminum chopper disk[6], which introduced a flat background in the time-of-flight spectrum and diminished the visibility of the long-wavelength tail.

[6]Given that the absorption cross section behaves as $\sigma_a \propto 1/v$, it is reasonable to assume that most neutrons leaking through the chopper disk are in the higher energy (warmer) part of the spectrum.

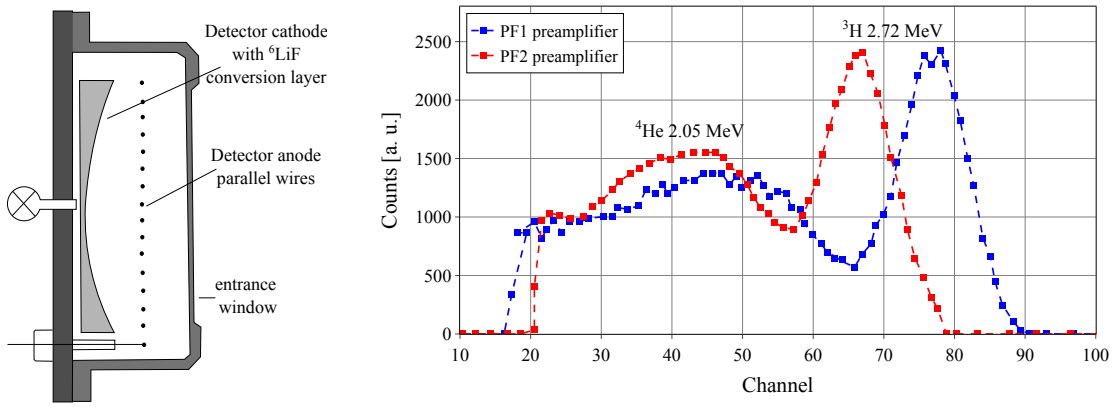

(a) Outline of the detector.

(b) Pulse height spectrum of the detector.

Figure 6.8.: Outline of the detector used in experiment 3-07-419 and associated pulse height spectra, recorded during preliminary tests with an Am/Be-source. The pulse height spectrum clearly shows the two decay products and their associated energies. The blue and red curves correspond to two different preamplifiers. Preamplifier PF1 (blue) was used for the experiment. The curved conversion layer of the detector is optimized for the time-of-flight device described in [223], but has no negative consequences for our setup.

Secondly, the time-of-flight frame size directly affects the achievable resolution when using a disk chopper, as detailed in Section 6.1. The time-of-flight resolution depends on the opening time of the disk chopper, which is in turn proportional to the chopper speed. However, the time-of-flight frame – i.e. the time required between pulses to capture the entire neutron spectrum at a given flight distance – limits how fast the chopper can spin.

This motivated the use of an $m = 3$ supermirror in the setup, tilted at an angle of approximately $1.5\,^\circ$, to achieve a cut-off wavelength of about 5.0 Å. [7] The change in the experimental

[7] The cut-off wavelength can be calculated based on the condition for specular reflection, which occurs when the perpendicular component of the the neutron's wavevector k_z is less than or equal to the critical wavevector, k_c, determined by the optical potential of the reflecting surface.

$$k_z \leqslant k_c \tag{6.21}$$

The optical potential is given by:

$$V_0 = \frac{\hbar^2}{2m} 4\pi N b = \frac{\hbar^2 k_c^2}{2m}\,, \tag{6.22}$$

where Nb is the scattering length density of the reflecting material. This allows to write the critical wavevector as $k_c = \sqrt{4\pi N b}$. The perpendicular component of the neutron's wavevector k_z can be related to the angle of incidence, θ, as:

$$k_z = \frac{2\pi \sin\theta}{\lambda}\,. \tag{6.23}$$

Solving the inequality 6.21 for θ gives an expression for the critical angle θ_c:

$$\theta < \theta_c = \arcsin\left(\frac{\lambda\sqrt{Nb}}{\sqrt{\pi}}\right)\,. \tag{6.24}$$

Using the atomic number density and neutron scattering length of nickel $N = 91.79 \times 10^{-3}\,\text{Å}^{-3}$ and $b = 10.3 \times 10^{-5}$ Å, Equation 6.24 can be simplified to $\theta_c = \arcsin\left(0.1\text{Å}^{-1}\lambda\right)$, which for small angles $\approx 0.1\text{Å}^{-1}\lambda$. The m value of a supermirror is defined as the wavelength normalized critical angle for reflection relative to nickel. For small angles this results in

$$\theta_c \approx \arcsin\left(0.1\text{Å}^{-1} m\lambda\right) \approx 0.1\text{Å}^{-1} m\lambda\,. \tag{6.25}$$

Note that the angles are in rad, so that for a mirror with an m-value of 3 the critical angle results in 0.3λ rad.

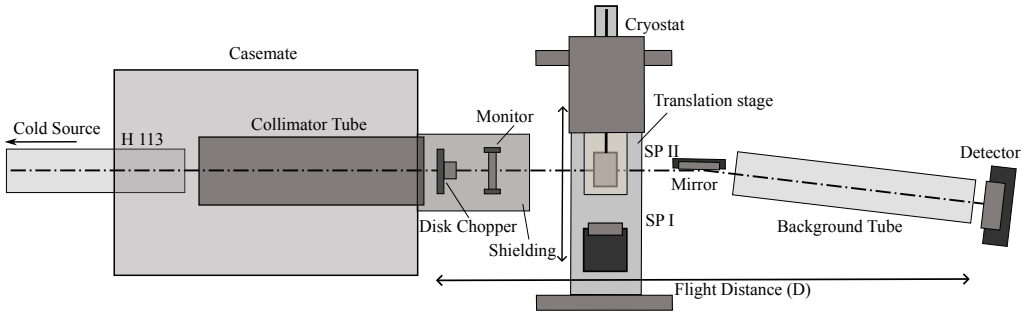

Figure 6.9.: Layout (top-view) of experiment 3-07-419 at PF1B with an $m = 3$ supermirror. The mirror was tilted to an angle of about 1.5° to achieve a cut-off wavelength of about 5 Å.

setup is illustrated in Figure 6.9.

This modification not only significantly reduced the background caused by neutron transmission through the chopper disk, but it also substantially decreased the overall flux at the detector position, thereby allowing the use of a higher efficiency detector. Additionally, this adjustment enabled the time-of-flight frame to be split into two parts. By adjusting the chopper speed, the frame of the previous setup could be cut off at around 25 Å, improving resolution in that section by reducing the chopper opening time, while the remainder of the spectrum could be recorded using the setup with the supermirror.

Wavelength Calibration

In principle, it is possible to convert a measured time-of-flight spectrum to a wavelength spectrum as outlined in Equation 6.8. This method is discussed in detail for very cold neutron (VCN) spectra in Section 6.3. Two sources of uncertainty have to be addressed: (a) accurately measuring the neutron's flight path can be challenging due to beam divergence and the finite detection volume of the neutron counter, and (b) most disk choppers have an inherent offset that depends on its angular velocity, which can be difficult to evaluate experimentally.[8] The measurement of calibration samples circumvents both of these problems. By computing the total cross section (or at least the proportional $-\ln(T)$) of materials of well-defined structure, their Bragg edges can be utilized to calibrate the wavelength spectrum, enabling the conversion from arrival times to wavelengths, as illustrated in Figure 6.10 for the calibration carried out at PF1B. The features identified in the time-of-flight spectrum can be attributed to known features in the theoretical cross section. The sharp edges of Bragg scattering are most suitable for this purpose.[9] They can be fitted using the following functional form [226, 227]:

$$\ln\left[T(t_i)\right] = \ln\left[\exp\left(-(\alpha_0 + \beta_0 t_i)\right)\exp\left(-(\alpha + \beta t_i)\right) + \left(1 - \exp\left(-(\alpha + \beta t_i)\right)\right) B(t_i, t_0, \varsigma, \tau)\right], \tag{6.26}$$

[8] Two approaches are considered in this work:

1. Determining the offset by measuring the time-of-flight spectrum at two different flight paths and evaluating the spectrum shift, as discussed in Appendix D.
2. Determining the offset using a dedicated light setup, which is detailed in Appendix F.2.

[9] This is why such a calibration is not feasible for time-of-flight measurements in the VCN and UCN ranges, as well-known materials suitable for neutron transmission usually do not exhibit *hkl*-planes with inter-planar distances $\gtrsim 4$ Å.

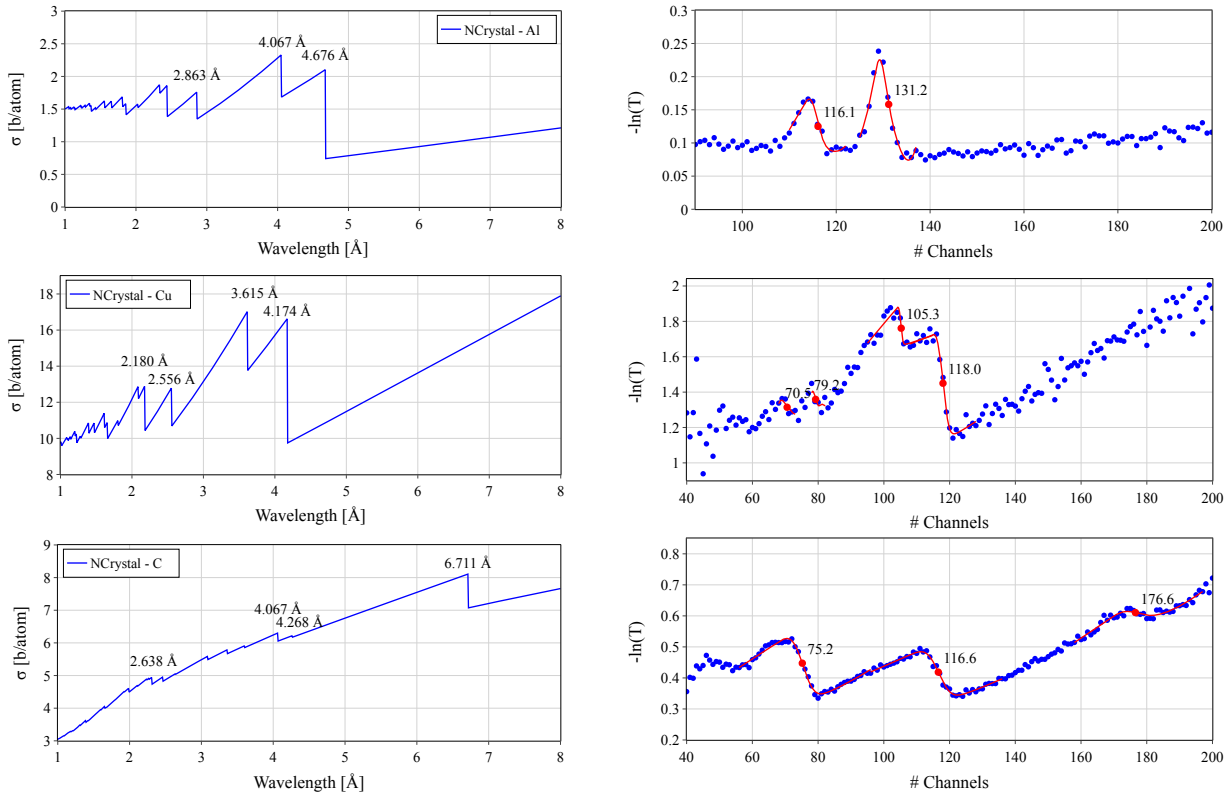

(a) Cross section computed in NCrystal [57].

(b) Experimental data of $-\ln(T) \propto \sigma_t$.

Figure 6.10.: Theoretical (a) and experimental (b) cross sections of three calibration samples measured at PF1B without the supermirror (i.e., using the setup shown in Figure 6.9) during experiment 3-07-419. The calibration was performed by fitting the measured Bragg edges using Equation 6.26 (indicated in red) and extracting the edge position t_0.
The top panel shows the results of an aluminum disk with a thickness of 21.25 mm and a diameter of 60 mm. The two highlighted edges on the left side (a) correspond to the (111) and (200) planes at 4.067 Å and 4.676 Å, respectively. These edges slgihtly deviate from their theoretical form due to texture in the aluminum alloy.
The middle panel presents a copper sample, which was created by winding copper wire into a disk with a thickness of approximately 12 mm and a diameter of 30 mm. The highlighted edges correspond to the (111), (200), (220), and (311) planes at 4.174 Å, 3.615 Å, 2.556 Å, and 2.180 Å, respectively.
The bottom panel shows a graphite disk with a thickness of 16.3 mm and a diameter of 50 mm. The highlighted edges correspond to the (002), (100), and (101) planes at 6.711 Å, 4.268 Å, and 4.067 Å, respectively. The theoretical values on the left side include some water, which is presumed to be enclosed in the graphite block, leading to high absorption and an atypical shape of the $-\ln(T)$. Since the exact positions of the edges are difficult to identify in the experimental data, they were excluded from the fit.

where

$$B(t_i, t_0, \varsigma, \tau) = \frac{1}{2}\operatorname{erfc}\left(\frac{-(t_i - t_0)}{\sqrt{2}\varsigma}\right) - \exp\left(-\frac{(t_i - t_0)}{\tau} + \frac{\varsigma^2}{2\tau^2}\right)\operatorname{erfc}\left(\frac{-(t_i - t_0)}{\sqrt{2}\varsigma} + \frac{\varsigma}{\tau}\right). \quad (6.27)$$

The parameters α_0 and β_0 define the transmission on the higher time-of-flight side of the edge, while α and β describe the jump in transmission. The parameters ς and τ represent Gaussian

Table 6.4.: Crystallographic properties of the calibration samples used at PF1B. Bragg edges are given with the precision in NCrystal. The time channel uncertainties are derived from the edge widths.

Sample	*hkl*-plane	d_{hkl} [Å]	Bragg Edge [Å]	Time Channel (t_0)	Used in Fit
Copper (cubic, $Fm\bar{3}m$)	111	2.0871	4.1742	118 ± 0.75	yes
	200	1.80748	3.61496	105.3 ± 1.24	yes
	220	1.27808	2.55616	79.2 ± 1.84	yes
	311	1.08995	2.17990	70.5 ± 2.08	yes
Graphite (hexagonal, P63/mmc)	002	3.3555	6.7110	177.7 ± 0.76	no
	100	2.13389	4.26778	117.6 ± 2.35	no
Aluminum (cubic, $Fm\bar{3}m$)	111	2.33803	4.67606	131.2 ± 2.05	yes
	200	2.02479	4.04958	116.1 ± 1.05	yes

broadening due to microstrain and crystallite size, and the asymmetry of the Bragg edge, respectively. The edge position is given by t_0. The identified set of edges can be related with a simple linear function having two free parameters (a and b), such as

$$\lambda_i = a t_i + b \,, \tag{6.28}$$

where λ_i and t_i correspond to wavelength and time bins, respectively. The resulting fit is used to convert time channels with a width of 25 µs into wavelength bins, as depicted in Figure 6.11.

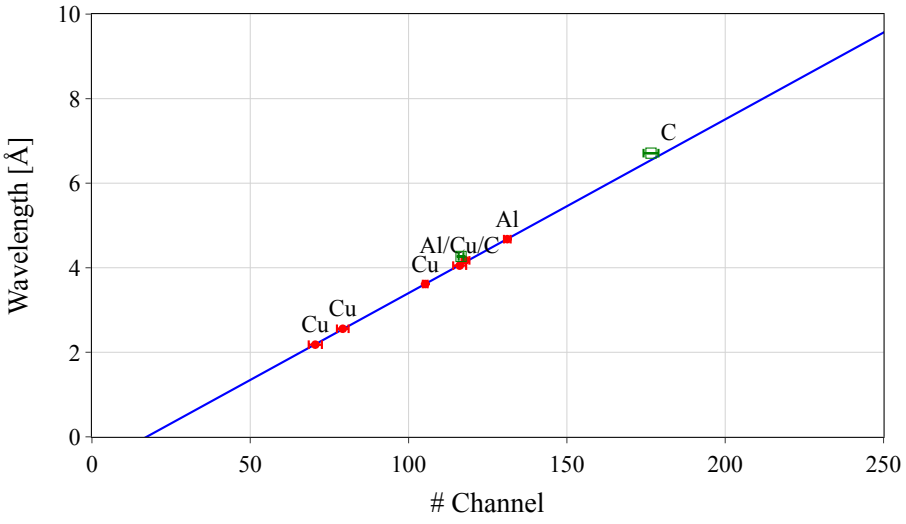

Figure 6.11.: Linear fit through the five identified Bragg edges providing the wavelength calibration for the measurements without the supermirror at PF1B (experiment 3-07-419). The open green squares refer to the Bragg edges identified in the graphite samples which were discarded for the fit. The line that passes through all the other points is given by $\lambda_i = a\, t_i + b$, with $a = (0.041 \pm 0.001)$ Å and $b = (-0.71 \pm 0.11)$ Å.

Measurement Procedure

The measurement procedure for experiment 3-07-419 was as follows: In the configuration without the $m = 3$ supermirror, the powder sample was filled into the sample container of geometry II (see Table 6.3) under an argon atmosphere. The container was then sealed, transferred to liquid nitrogen, and loaded into the cryostat at approximately 100 K. The sample volume of the cryostat was pumped out to remove excess nitrogen, ensuring a pure sample environment, before the sample was cooled to its base temperature. Transmission through the sample was measured in multiple 20 min runs, which were combined after background subtraction. Once satisfactory statistical accuracy was reached, the sample was warmed above the hydrate annealing temperature, and the liquid solution was measured at room temperature. Subsequently, the sample was cooled back to the base temperature to measure the hydrate bulk. This procedure allowed for a comparison of the bulk, powder, and liquid solution states in the same experimental configuration. As a cross-check, the cross section of heavy water was also measured at room temperature. This measurement served to verify the integrity of the experimental setup by comparing the measured cross section with well-established reference data for heavy water.

The packing fraction of the hydrate powder was evaluated from the mass of the recuperated sample. Since the sample container was filled to the top with powder, measuring the mass after melting allowed determination of the number density in powder form. The cross section was calculated after subtracting a flat background, determined from the end of the time-of-flight frame, and combining all runs using equation 6.3. This procedure was then repeated with the adapted setup using the $m = 3$ supermirror.

6.2.3. Results from CN Transmission at PF1B

Figure 6.12 shows the obtained transmission spectra through the empty container and the powder sample, both with and without the $m = 3$ supermirror. The spectra from the initial setup are indicated in pink and red, while the spectra from the adapted setup are shown in shades of blue. The resulting calculated cross sections in the relevant region are also displayed. A clear cut-off due to the supermirror is observed at approximately 6 Å in the spectra recorded with the adapted setup. The presence of intensity before this cut-off suggests that not all of the beam is reflected by the supermirror, allowing a portion of the direct beam to remain visible.

For further analysis, the cross sections measured in these two setups were stitched at a wavelength of approximately 8.3 Å. This allows to benefit from the higher count rate for shorter wavelengths in the initial setup and the extended visible wavelength range in the adapted setup. The cross-over point was chosen to maximize statistical accuracy by considering both the count rate of the spectra without mirror and the measurement time in each configuration. The same procedure was applied to the measurements of the liquid and bulk samples. Notably, for the powder sample, the expected Bragg edges are clearly visible in the experimental data, including the Bragg cut-off at approximately 20 Å.

Figure 6.13 presents the obtained cross section for the bulk sample. Compared to the powdered sample, the cross section decreases significantly. This reduction is attributed to diminished Bragg scattering in the textured polycrystalline hydrate and a smaller SANS contribution. The results from experiment 3-14-232, shown in grey, have been deconvoluted using the chopper gating function (see Appendix C). In contrast, the results from experiment 3-07-419, displayed in blue, do not require deconvolution due to the short opening times of the chopper used in this experiment. The comparison of these two experiments highlights the limited wavelength coverage of the experimental setup of experiment 3-14-232. The measurements of the liquid THF-d/17 D_2O solution and heavy water (D_2O) serve as crucial cross-checks and are presented in Figure 6.14. The cross section of heavy water (represented by salmon-colored squares) is

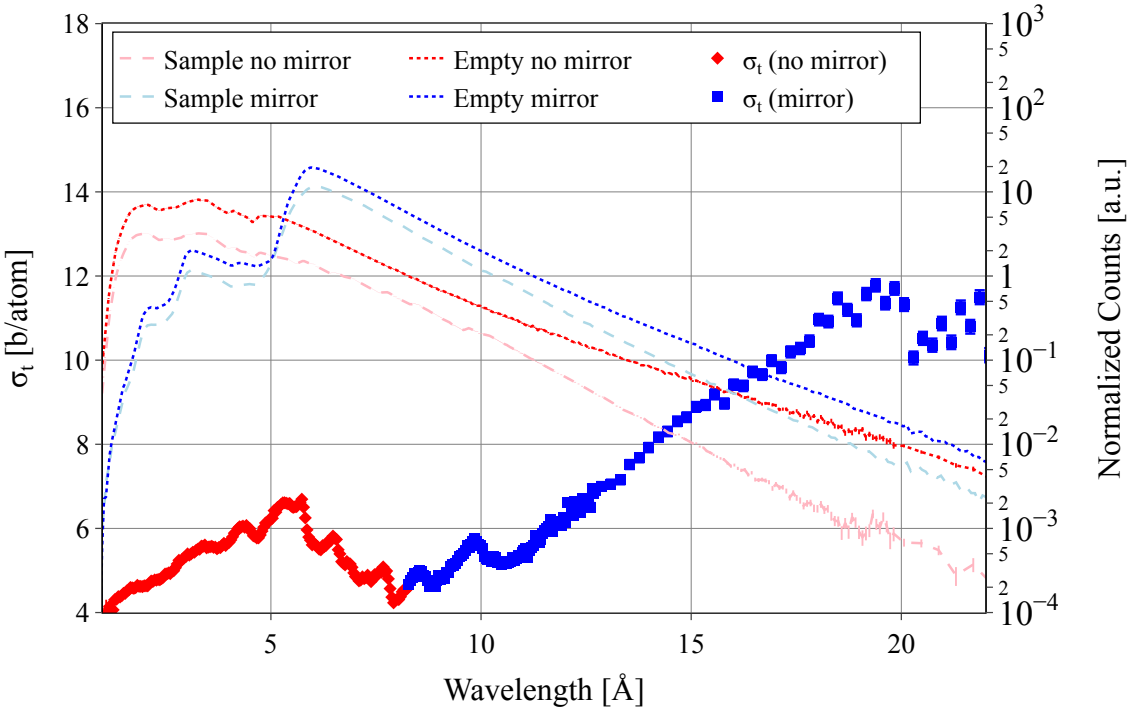

Figure 6.12.: Transmission spectra through the empty container and powder sample with and without the $m = 3$ supermirror. Spectra without the mirror are shown in pink and red, spectra with mirror in shades of blue plotted on the right axis. The cut-off at 6 Å due to the supermirror is evident, with some direct beam intensity visible before the cut-off. Cross sections from both setups were stitched at 8.3 Å to make use of higher count rates at shorter wavelengths as well as the extended wavelength range. Notably, the Bragg cut-off at $\sim$ 20 Å is clearly visible.

compared with experimental data from [228] (red dots) and [229] (grey diamonds), as well as the theoretical model from the NCrystal data library (solid blue line). The comparison shows generally good agreement, although NCrystal tends to overestimate the cross section at the characteristic peak compared to the data provided in the literature and measured in experiment 3-07-419.

The THF-d/17 D_2O solution measured at room temperature (green triangles) exhibits features similar to heavy water but at a slightly lower overall level. This discrepancy can be attributed to the different inelastic scattering properties of the two liquids, which affect the total scattering cross section per atom. Even though there are no literature values for direct comparison, the measurement of the liquid solution provides valuable verification across different experimental setups.

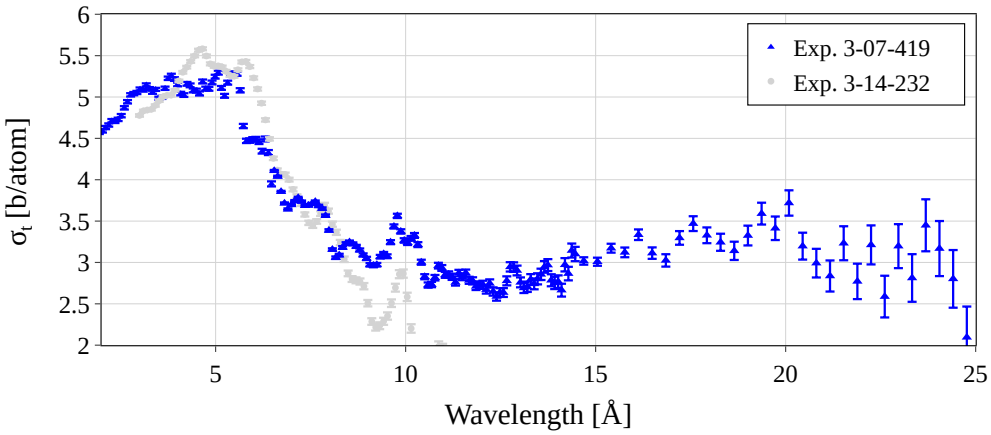

Figure 6.13.: Total cross section (σ_t) for the bulk hydrate measured at PF1B. The cross section is significantly decreased compared to the powdered sample due to reduced Bragg scattering in the textured poly-crystalline hydrate and diminishing small-angle scattering. Results from experiment 3-14-232 are shown in grey after deconvolution with the chopper gating function, while results from experiment 3-07-419 are shown in blue, where deconvolution is unnecessary due to the short chopper opening times. The observed shift is likely attributable to calibration problems in experiment 3-14-232.

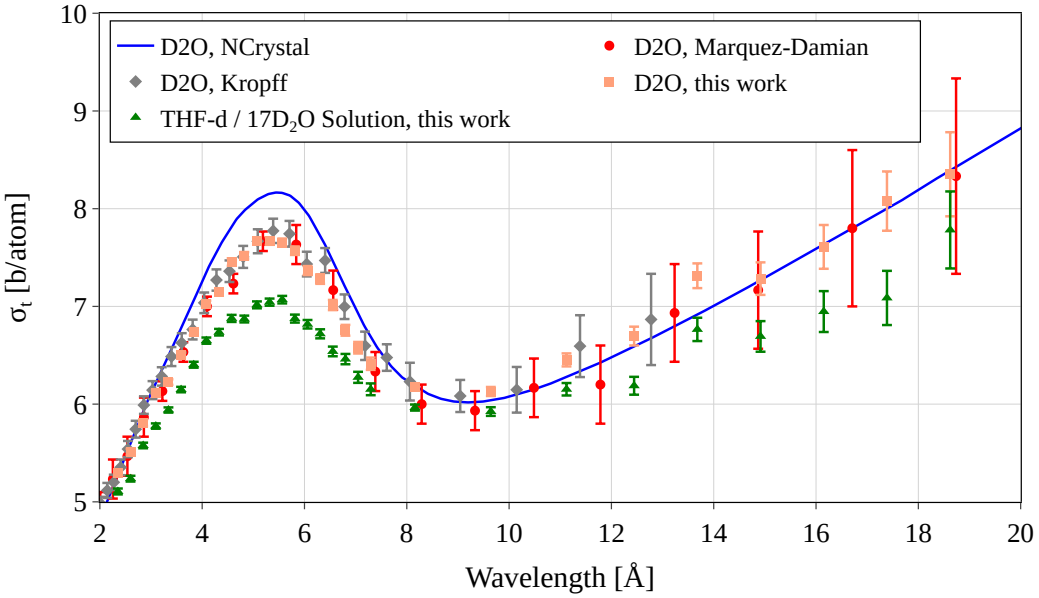

Figure 6.14.: Comparison of neutron scattering cross sections for heavy water (D_2O), THF-d/17 D_2O solution, and reference data. The cross section of heavy water measured in experiment 3-07-419 is shown with salmon-colored squares, compared to data from [228] (red dots) and [229] (grey diamonds), along with the NCrystal model (solid blue line). The THF-d/17 D_2O solution is depicted with green triangles, demonstrating similar features at a slightly lower overall level.

6.2.4. The Setup on the BOA Beamline in May 2022

The "**B**eamline for neutron **O**ptics and other **A**pproaches" (BOA) [230] is an 18 m long instrument with view on the cold source at the *Swiss Spallation Neutron Source – SINQ* at the *Paul Scherrer Institute* in Villigen, Switzerland. The experimental area is equipped with three rotating axes, adjustable translation tables, and several aperture units that can be adapted to meet various experimental needs.

An outline of the experimental setup used to investigate the total cross section of fully deuterated THF-d deuterates in bulk form in May 2022 is shown in Figure 6.15. A supermirror ($m = 4$) is placed on one rotational stage and employed to deflect only the cold part of the spectrum onto the sample. An angle of 1.04° results in a cut-off of the spectrum at 2.6 Å ($\lambda_c \approx \frac{\theta[\mathrm{rad}]}{0.1[\mathrm{Å}^{-1}]m}$). The cryostat, mounted on a rotation stage above a translation stage, operated at a base temperature of 20 K. The sample container featured a rectangular base, enabling sample thicknesses of either 20 mm or 40 mm. Sample alignment was facilitated by two apertures positioned at the sample's entry and exit points. Using a neutron camera in front of the detector, we identified the maximum transmission through the apertures, establishing the perpendicular position for a thickness of 40 mm. To measure at 20 mm, the rotation stage *rc* (see Figure 6.15) was used to rotate the cryostat by 90°.

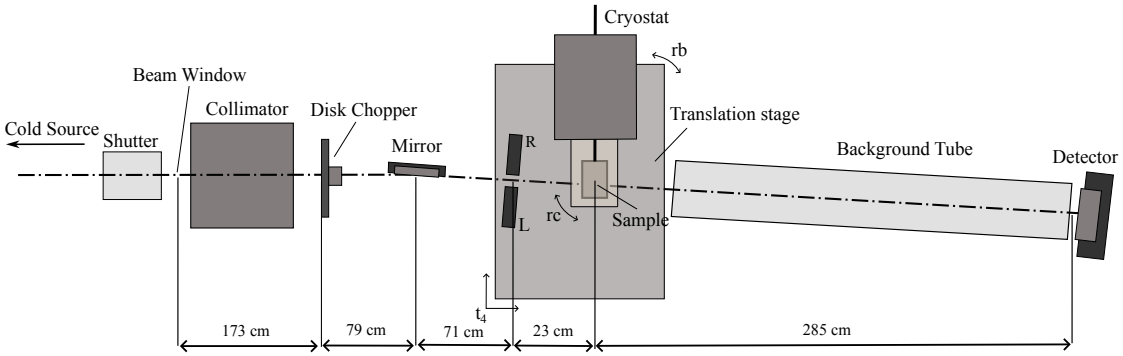

Figure 6.15.: Experimental setup for measurement of the total neutron cross section of THF-d deuterates in bulk at BOA in May 2022. The neutron beam from the cold soure enters the beam line on the left. After the collimator the beam hits the chopper. The pulsed beam is deflected by a $m = 4$ supermirror at an angle of 1.04°, this gives a wavelength cut-off at 2.6 Å. The final beam of the sample is defined by an aperture, labelled as (R,L) as an upright rectangle (10 mm × 20 mm). The cryostat at the sample position is rotatable, allowing measurements on both sides of the sample with a 90° rotation. The total time-of-flight distance adds up to 458 cm. The slab sample had dimensions of 20 mm × 40 mm × 47 mm.

The detector was a high-efficiency ^{3}He counter, with an active volume of 7.5 mm × 76 mm × 96 mm. The supermirror, combined with careful shielding of the detector and the flight tube, minimized backgrounds, enabling measurements at previously unattainable long neutron wavelengths on the BOA beam-line (see Figure 6.16).

Observations suggest that cold neutron wavelength spectra are more accurately modeled by an exponential function, $\exp(-\lambda/\lambda_1)$, combined with a short-wavelength cut-off function, rather than by a Maxwellian spectrum. This characterization holds true for the brightness spectra of both cold neutron sources at the ILL at the end of a neutron guide [225]:

$$A(\lambda) = A_0 \exp\left(-\frac{\lambda}{\lambda_1}\right) \frac{\left(\frac{\lambda}{\lambda_2}\right)^p}{1 + \left(\frac{\lambda}{\lambda_2}\right)^p} \,. \tag{6.29}$$

Table 6.5.: Parameters for Cold Neutron Wavelength Spectra

Parameter	Value
A_0	0.0199 ± 0.0003
λ_1	2.292 ± 0.011
λ_2	2.525 ± 0.011
p	4.142 ± 0.025

Table 6.5 shows the parameters for the fit shown in Figure 6.16. Unlike the spectrum given in [230] the spectrum extends beyond 20 Å.

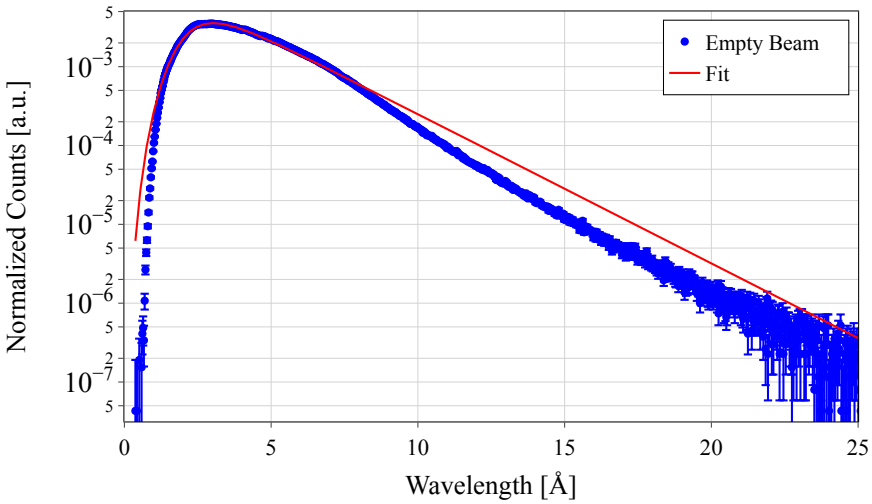

Figure 6.16.: Wavelength spectrum of the BOA beamline measured with setup described above. The spectrum is cold and has a maximum at roughly 3 Å. Unlike the spectrum given in [230] it extends beyond 20 Å. The spectrum was measured before the installation of the supermirror. The fit function is given in equation 6.29 with the parameters of Table 6.5.

Wavelength Calibration

The calibration samples used at BOA are listed in Table 6.6. The iron was powdered and placed in a thin aluminum sample container with a thickness of 20 mm in the beam. The aluminum sample was a cube with side length 50 mm, measured at different orientations to test for texture effects. The graphite was powdered and sealed in an aluminum container with a thickness of 12 mm. To save measurement time, the graphite and aluminum were measured consecutively in the same run. The resulting cross section is shown in Figure 6.17a. The calibration measurements resulted in five data points for the linear fit, as presented in Figure 6.18. The line that fits all points is given by by $\lambda_i = a\,t_i + b$, with $a = (0.0264 \pm 0.0002)$ Å and $b = (-10.1632 \pm 0.0002)$ Å. This equation is used to transform the spectra from time channels to wavelength, with t_i referring to the time-channel number.

Table 6.6.: Crystallographic properties of the calibration samples used at BOA

Sample	hkl-plane	d_{hkl} [Å]	Bragg Edge [Å]	Time channel (t_0)
Iron	110	2.0277	4.055	540.50 ± 0.60
(cubic, Im$\bar{3}$m)				
Graphite	004	1.67775	3.356	512.02 ± 0.90
(hexagonal, P63/mmc)	002	3.3555	6.711	640.27 ± 0.25
Aluminum	111	2.33803	4.676	540.01 ± 0.59
(cubic, Fm$\bar{3}$m)	200	2.02479	4.0496	562.57 ± 0.51

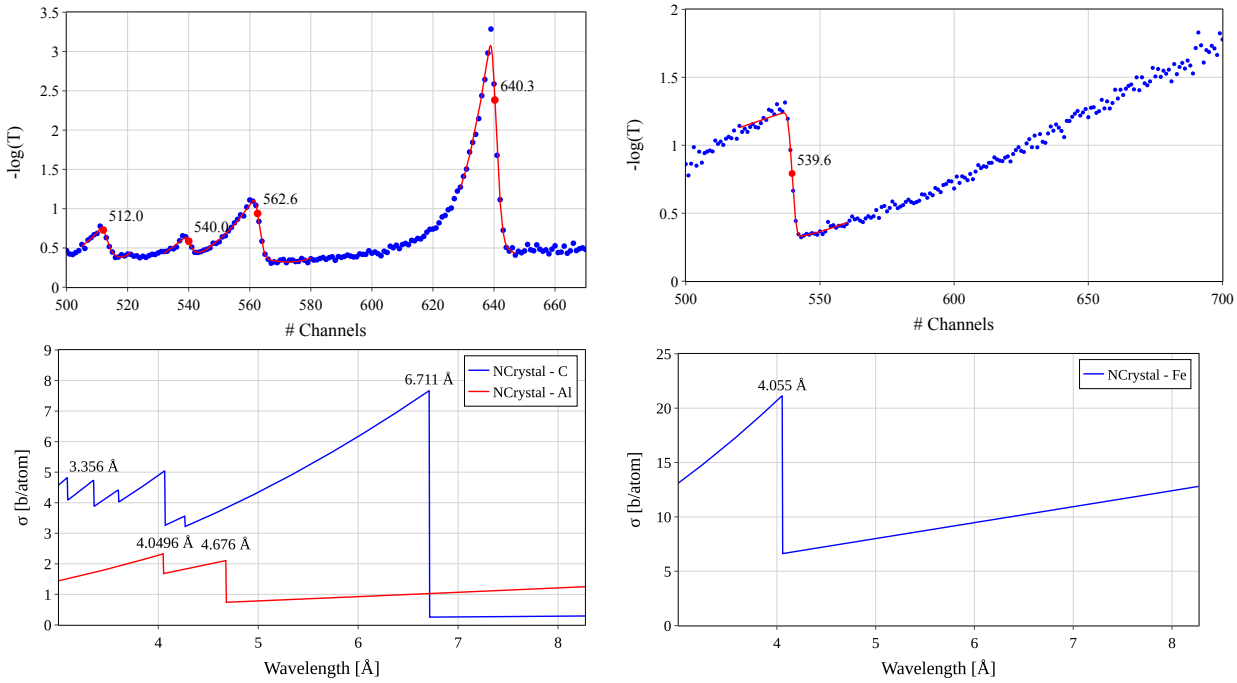

(a) Aluminum and pyrolytic graphite.

(b) Iron cube.

Figure 6.17.: Experimental (upper panel) and theoretical (lower panel) cross section of three calibration samples measured at BOA. The upper right plot shows the $-\ln(T)$ computed from the transmission through pyrolytic graphite in an aluminum container. The four highlighted edges on the left side (a) are Bragg scattering from the (004)- and (002)-plane of pyrolytic graphite at 3.356 Å and 6.711 Å and the (111)- and (200)-plane of aluminum at 4.067 Å and 4.676 Å, respectively. The edge on the right side (b) is due to the (110)-plane of iron at 4.055 Å. The theoretical cross sections are calculated using NCrystal [57]. The calibration was performed by fitting the measured Bragg edges using Equation 6.26 (indicated in red) and extracting the edge position t_0.

6.2.5. Measurement Procedure and Results from CN Transmission at BOA

The transmission data from the BOA beam line were combined, and a flat background was subtracted, which was evaluated from the mean count rate at the long wavelength end of the time-of-flight spectrum. The spectrum was then normalized to the monitor count rate, positioned upstream of the experimental zone. Subsequently, the cross section was calculated using equation 6.3. Figure 6.19 presents the resulting data. Before calculating the cross section a dynamic re-

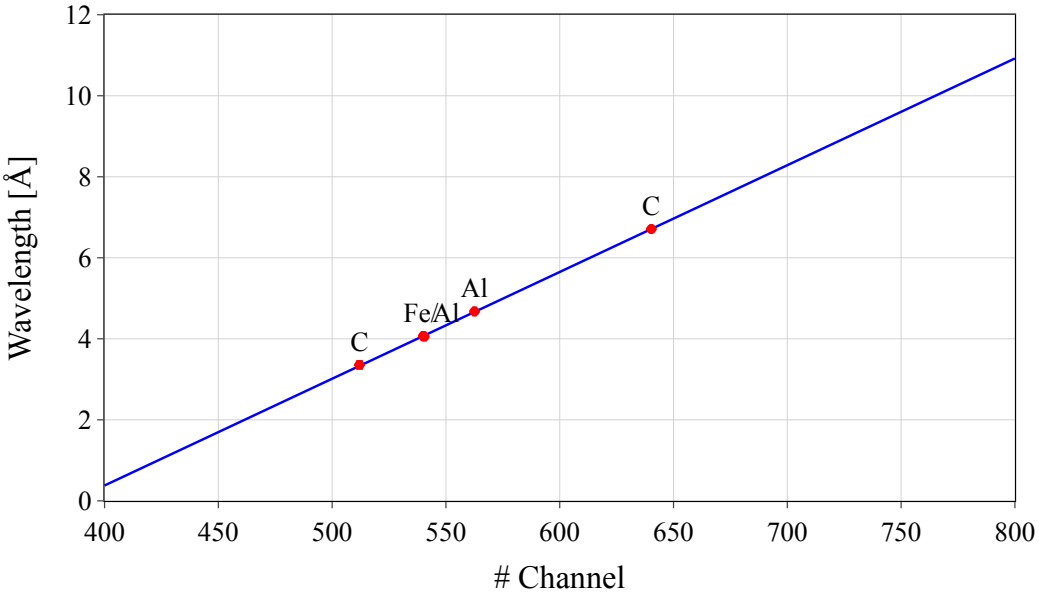

Figure 6.18.: Linear fit through the five identified Bragg edges providing the wavelength calibration for the measurements at BOA. The labels refer to respective calibration sample. The Al edge at 4.067 Å and the iron edge at 4.055 Å almost coincide. The line that passes through all the other points is given by $\lambda_i = a\,t_i + b$, with $a = (0.0264 \pm 0.0002)$ Å and $b = (-10.1632 \pm 0.0002)$ Å.

binning was applied. This combined the data from multiple bins in regions with low count rates, increasing statistical precision but reducing the wavelength resolution in these areas.

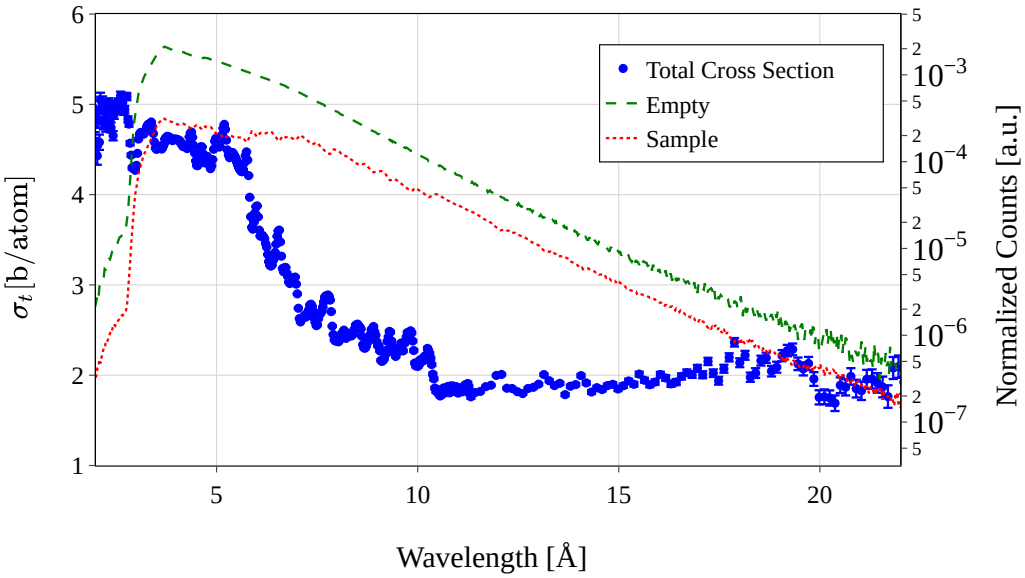

Figure 6.19.: Transmission spectrum through the empty sample container and through the sample of THF-d deuterates as well as the computed cross section for a sample thickness of 40 mm at 20 K measured at the BOA beam line.

After measuring the transmission at the base temperature, subsequent measurements at various higher temperatures were conducted, from which the corresponding cross sections were derived Figure 6.20. The cross section at 80 K (red) is similar to that at the base temperature

20 K (blue), with the difference increasing at higher wavelengths, as expected due to increased inelastic scattering. This trend becomes more pronounced at temperatures nearing the annealing point of 280 K (green). An increase of temperature preserves Bragg edges, while the contribution of inelastic scattering increases, resulting in a wavelength dependent increase of the total cross section. At temperatures above the melting point, the cross section becomes similar to that of heavy water.

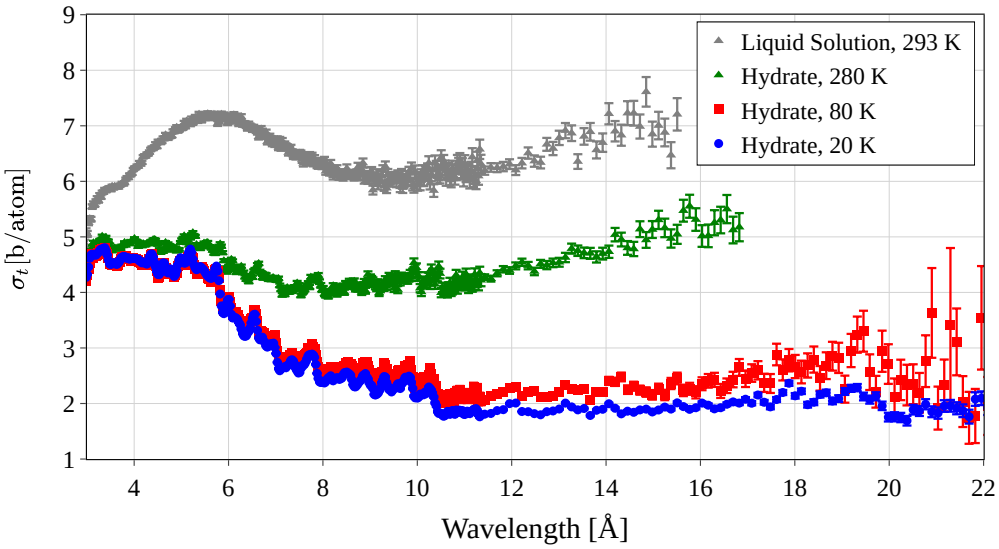

Figure 6.20.: Calculated cross section from transmission data at different temperatures (see legend). An increase of temperature above the melting temperature ($\sim$ 280 K) shows a phase transition from the hydrate phase to the liquid solution which exhibits similar properties as the cross section of heavy water.

Figure 6.21 shows the comparison of data for 20 mm and 40 mm sample thickness. While the general magnitude of the cross section is very comparable, the Bragg edges occur with different intensities. Besides the limited statistical accuracy of the measurement for 20 mm, this indicates texture in the sample, which is expected based on the results of Chapter 4. A close comparison of the low-temperature data from the 40 mm sample with the expected powder cross section (see the lower panel of Figure 6.21) shows that particularly the coherent elastic scattering seems to be damped in the measured bulk sample compared to the expected powder signal, resulting in an overall lower cross section in the Bragg region. In addition to texture within the polycrystalline hydrate phase, this could be due to significant ice impurities (see Figure 6.21).

This allows us to conclude that cooling the sample down as a bulk in its container in situ does neither form a perfect powder average nor a pure CS-II hydrate. Instead, it results in a solid solution comprising the hydrate phase, hexagonal ice, and potentially additional phases. These impurities and mixed phases hinder a systematic comparison with the calculated powder cross section. Instead, we observe Bragg scattering from both the CS-II hydrate and hexagonal ice, accompanied by a reduced intensity of coherent elastic scattering.

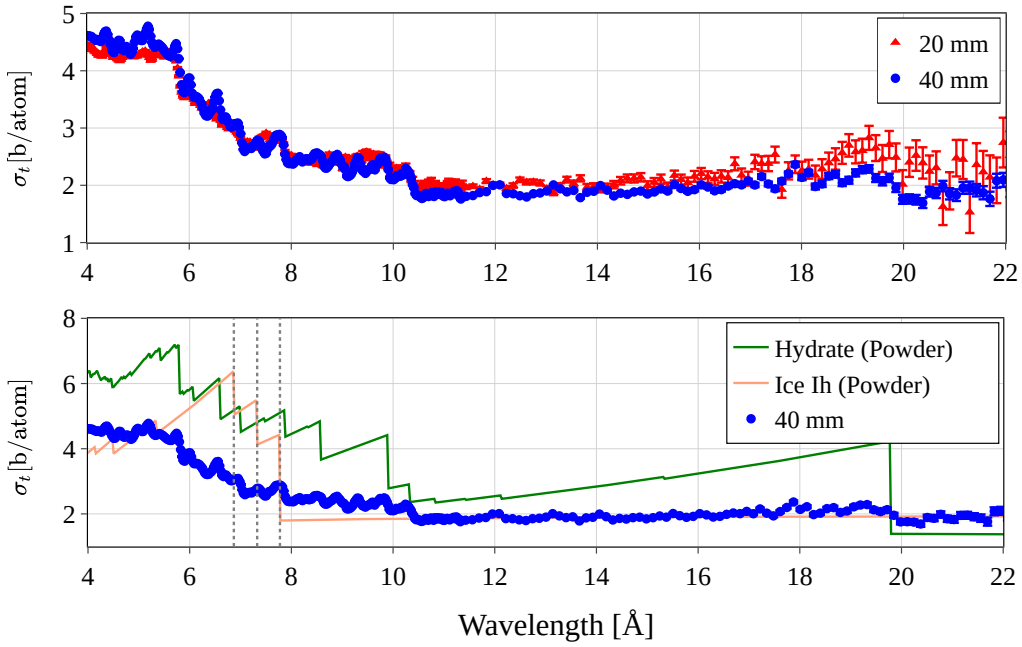

Figure 6.21.: The upper panel shows a comparison of neutron scattering cross sections for 20 mm and 40 mm sample thickness . The lower panel depicts the cross section calcultaed from the measured transmission compared to the expected powder cross section of the hydrate. The expected powder cross section of hexagonal ice based on the unit cell given by [231] is depicted in light-salmon. The Bragg edges at 6.86 Å, 7.33 Å, and 7.78 Å (corresponding to the 101- 002- and 100-plane), indicate the presence of hexagonal ice (Ih) in the sample. These impurities, along with texture within the polycrystalline hydrate phase, contribute to deviations from the expected behavior of a pure hydrate phase.

6.3. Transmission Experiments in the Very Cold Neutron Range

For the use of clathrate hydrates as a moderator material in a VCN source, the ability to effectively down-scatter and diffusely scatter thermal and cold neutrons is crucial. Additionally, the mean free path of the produced VCN is a key parameter for any material employed in such a source. This motivates direct measurements of the total neutron cross section in the VCN range. The only available instrument to conduct such an experiment is the VCN beamline at the PF2 instrument at the ILL. The PF2/VCN beamline is fed by the vertical cold source of the ILL. VCN are extracted by a neutron guide system that dips into the liquid deuterium of ILL's vertical cold source, as described in Section 2.4. The vertical and curved neutron guide[10] transmits neutrons with wavelengths between approximately 20 Å and 400 Å. The guide curvature prevents reflection of faster neutrons, while slower neutrons are unable to overcome gravity to reach the top of the guide. At the top level of the reactor building, half of the beam enters the UCN turbine to be converted into UCN, while the other half bypasses the turbine and is guided directly into the VCN cabin that houses the experimental zone of the beamline. This is depicted in Figure 6.22.

The resulting VCN beam has a cross section $A = 34\,\text{mm} \times 70\,\text{mm}$. The longitudinal axis of the cabin has an angle of $\alpha = 18.2°$ relative to the neutron beam which enters the cabin at a height of 1020 mm, relative to the cabin floor. Pre-setup components, typically including an aperture and a neutron supermirror, are positioned at the front of the optical table to deflect the beam and

[10]The guide is 12.8 m long and has a radius of curvature 13 m [232].

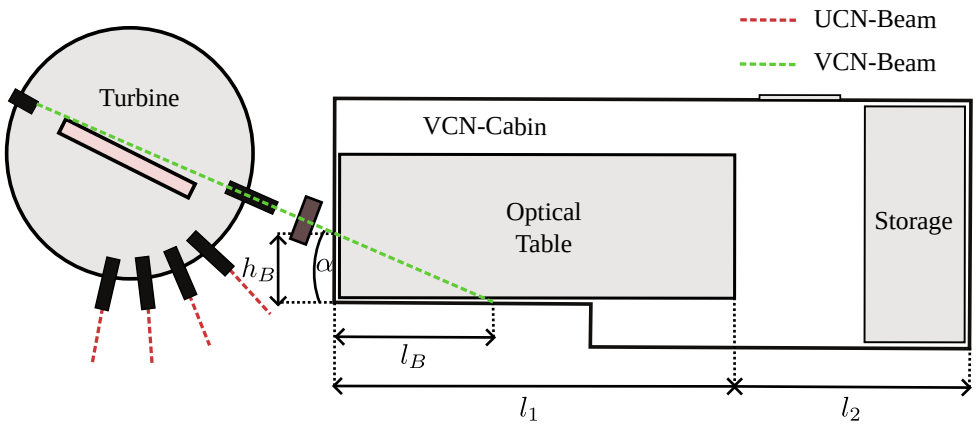

Figure 6.22.: A bird's-eye view of the VCN cabin, showing the UCN turbine at PF2. The values of the quantities defined in the figure are listed in Table 6.7. This figure was adapted from [233, Figure 3.4].

improve alignment with the cabin's axis. This mirror also shapes the neutron spectrum through the deflection. The VCN beamline supplies essential equipment for measurements, including a spatially resolving wire chamber detector, specifically the BiDim-26 [234], and basic alignment equipment [233]. A particular challenge at this beamline is the high spatial dependency of the wavelength spectrum, as discussed in [235] and [233]. A schematic of the VCN-cabin with the UCN-turbine of PF2 is shown in Figure 6.22.

Table 6.7.: Dimensions of the table and the VCN-Cabin at the instrument PF2 at the ILL.

Parameter	Value	Information
Beam Size [mm^2]	70 × 34	At the entrance port of the cabin as given in [232].
α [°]	18.2	As given in [233].
l_1 [cm]	360	Length of the table top plate.
$l_1 + l_2$ [cm]	763	Length of the cabin.
l_B [cm]	209	
h_B [cm]	69	

A spectrum of the VCN beam is given in Figure 6.23. This spectrum was obtained from the direct beam, with the setup depicted in Figure 6.24. The aperture was opened to a height of 60 mm and a width of 20 mm to allow almost the full beam cross section to be transmitted. The circular stator of the chopper, with a diameter of 10 mm was positioned in the center of the aperture.[11] The resulting spatial distribution of intensity (see Figure 6.24) shows clearly visible bright and dark spots which are a result of the specific geometry of the vertical guide system. The spectra at these spots differ, exhibiting a general trend where the maximum of the distribution shifts towards slower neutrons from top to bottom (see Figure 6.25d). At further distances there is an additional spread of the spectrum due to gravity. The vertical displacement of a neutron with a velocity v perpendicular to the Earth's gravitational field is given by

$$\Delta z = \frac{g}{2}\left(\frac{D}{v}\right)^2 , \tag{6.30}$$

where g is the local gravitational acceleration acting in z-direction and D is the neutron's flight distance. Since a slower neutron is exposed to gravity for a longer time before being detected,

[11] A comprehensive characterisation of the beam was conducted after the upgrade of the VCN beamline in May 2023. This included scanning the chopper through the whole beam cross section and analysing the spectrum at each spot. The results of this characterisation are published elsewhere.

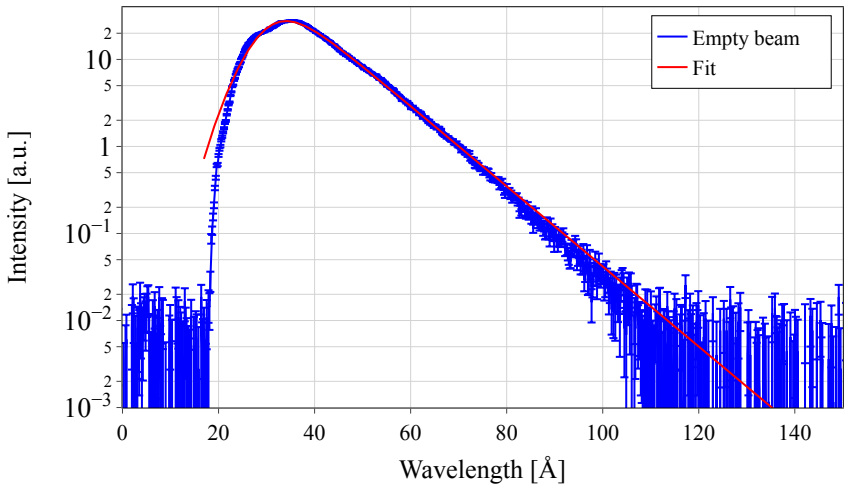

Figure 6.23.: Selected wavelength spectrum of the PF2/VCN beamline measured with setup described above. The spectrum has a maximum at roughly 36 Å. The fit function is given in equation 6.29 with the parameters of Table 6.9.

than a faster neutron, this results in an additional spatial dependency of the spectrum. For a setup like the one shown in Figure 6.26, the neutrons will experience a drop of a few millimeters due to gravity. However, the spatial dependency of the VCN beam is primarily influenced by the characteristic reflection pattern of the vertical guide rather than gravity. Nevertheless, this drop should be taken into account when aligning the experimental setup.

The biggest challenge at this beamline is finding an intensity maximum in the direct beam with a suitable spectrum and propagating it over the supermirror and through the rest of the setup. To achieve overlap with measurements on PF1B and BOA, we selected a "warmer" spot of intensity and used an $m = 5$ supermirror at the shallowest possible angle to prevent a cut-off, as shown in Figure 6.26.

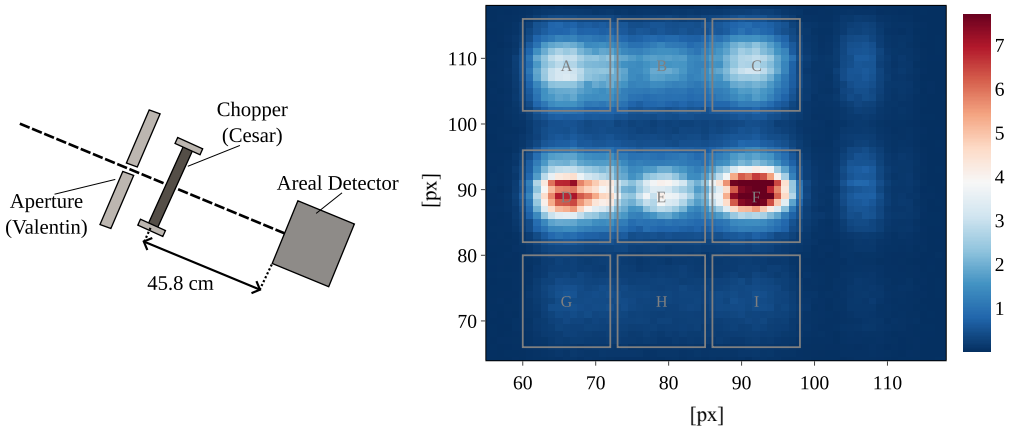

Figure 6.24.: Intensity profile of the center of the VCN beam measured in the setup depicted on the right. The color bar refers to the intensity in units of $[s^{-1}px^{-1}]$. The horizontal and vertical position on the Bidim detector in are indicated in [px], where each pixel has a size of $2 \times 2\,mm^2$. The clearly visible bright spots on the left hand side are labeled from A to I, the corresponding spectra are shown in Figure 6.25. The two bright spots on the right-hand side of the detector matrix are excluded from further analysis.

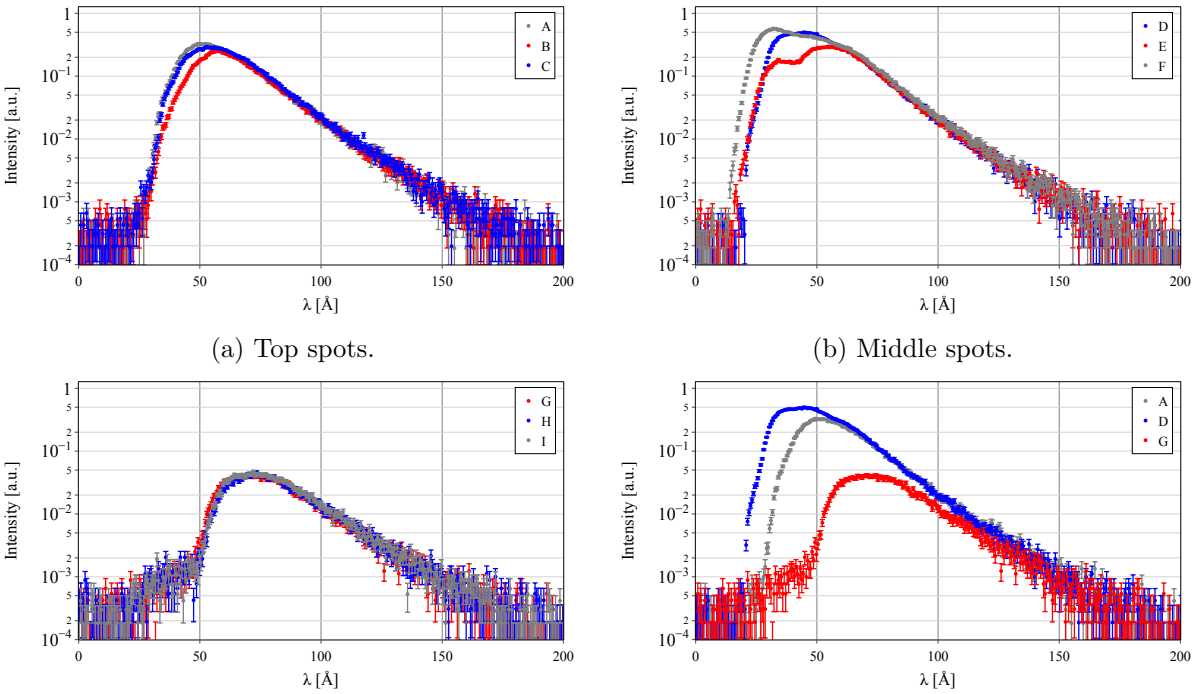

(a) Top spots.

(b) Middle spots.

(c) Bottom spots.

(d) Vertical Comparison.

Figure 6.25.: Spatial dependency of the spectrum at PF2/VCN. The letters in the legend refer to the defined ROIs in Figure 6.24. Each of the spectra was measured for 10 min.

The Setup of Experiment 3-14-232 on PF2/VCN

The transmission experiment was conducted in May/June 2023 [219], with the goal to measure the total neutron cross section of THF-d deuterates in bulk in the VCN range. The setup is given in Figure 6.26. The VCN beam entered the setup from the left, where it was initially shaped by a first aperture "Valentin".[12] Subsequently, the beam was deflected by an $m = 5$ supermirror at an angle of $\alpha_0 = 7°$ sitting on the rotational stage "Tanja", redirecting it along the optical table. The deflection angle was minimized to direct as much of the neutron spectrum as possible towards the sample. The transmitted beam served as a monitor for the experiment. The monitor detector was a ^{3}He detector called "Dunya" fabricated by A. V. Strelkov of the Joint Institute for Nuclear Research in Dubna [69, 236].

The deflected beam passed through a disk chopper ("Cesar"), with a stator aperture of 10 mm and a rotor slit width of 10 mm, resulting in an approximately triangular gating function. The aperture "Vlad" was placed in front of the cryostat for further collimation. The hydrate was solidified in the small sample container ($15 \times 10 \times 28\,\mathrm{mm}^3$). The transmitted neutrons travel the final flight path through a flight tube under static vacuum, before finally reaching the areal detector. The active area of the BiDim-26 detector is $26.5 \times 26.5\,\mathrm{cm}^2$ with a resolution of $128\,\mathrm{px} \times 128\,\mathrm{px}$ [234], resulting in a pixel size of $2 \times 2\,\mathrm{mm}^2$.

Measurement Procedure

The measurements were conducted as follows: The sample container with geometry III (see Table 6.3) was inserted into the cryostat using a sample stick. Alignment on the optical table was

[12] After a recent update of the VCN beamline the three available apertures have names beginning with the letter "V", the disk chopper is called "Cesar" and the rotational stages have names beginning with the letter "T".

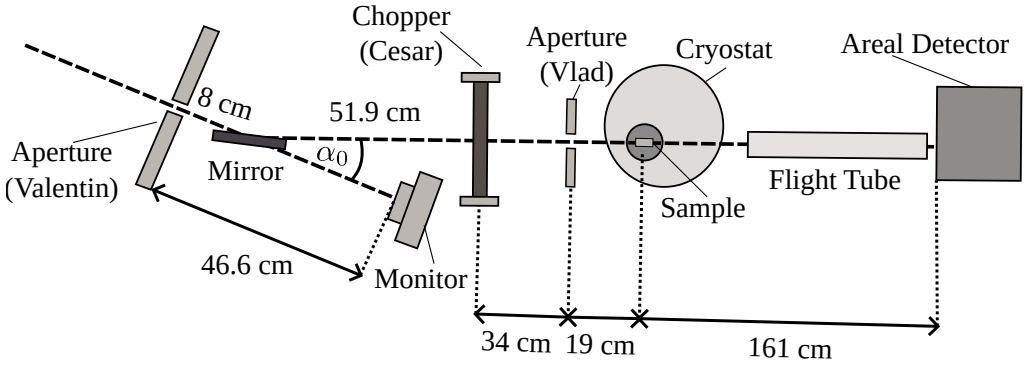

Figure 6.26.: Experimental setup for measurement of the total neutron cross section of THF-d deuterates in bulk at the VCN beamline in May 2023. See text for details.

Table 6.8.: Parameters of the chopper used at PF2/VCN.

Parameter	Value	Information
$\tilde{R}$ [mm]	165	Radius to the center of the chopper window
a [mm]	10	Width of the rotor
b [mm]	10	Width of the stator
h [mm]	21	Height of the chopper window
ω [rad/s]	62.83	Rotational speed
Δt [ms]	1.93	Chopper opening time
Duty Cycle	1.93%	
D [m]	2.141	Flight distance

achieved by physically moving the cryostat along the vertical and horizontal axes of the optical table, while height adjustments were made using the sample stick. To ensure proper angular alignment, two Cd apertures with a diameter of 8 mm and 10 mm were mounted directly at the entry and exit points of the sample container (see Figure 6.27).

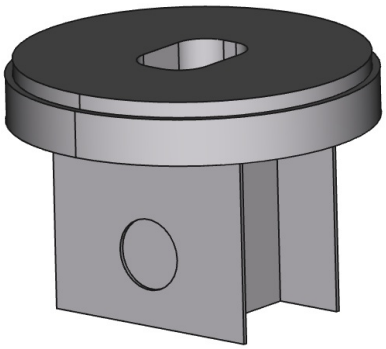

Figure 6.27.: Sample container III with two Cd apertures.

After inserting the container, the angle of the sample stick with regards to the beam was adjusted until the transmitted neutron count reached its maximum. This was made possible with a protractor disk attached to the stick, in relation to a pointer attached to the cryostat. A maximum count rate in the detector indicates that the two apertures are perpendicular to the neutron beam and the sample is well aligned. This procedure was repeated each time the sample or the empty container was placed in the beam. For an alignment error of these two

apertures of an angle $\theta \neq 90°$ their cross section with respect to the beam results in a ellipsoidal projection of the beam cross section onto the detector, instead of a circle. This ellipse has a major axis of $a = R$ and a minor axis of $b = \cos(\theta)R$, with R being the radius of the circular aperture. As a result the area of the apertures rotated by $\theta \neq 90$ is proportional to the area of the aperture multiplied by $\cos(\theta)$, so that

$$A_{\text{ellipse}} = ab\pi = R^2\pi\cos(\theta) = A_{\text{circle}}\cos(\theta) \tag{6.31}$$

Assuming a homogeneous beam the transmission of the aperture is proportional to its projected area on the detector this would result in a small error $< 1\%$ for a tilt of even $\theta = 5°$. However, as shown above the VCN beam has not only a highly inhomogenious intensity profile, but also a high spatially dependent spectrum. As a result small displacements or tilts can result in slightly different beam selections. This effect was mitigated by collimating the beam upstream with two additional apertures, finding a compromise between accepted divergence and intensity at the sample position. The necessity to realign the sample between measurements of the sample and the empty container introduces a wavelength-dependent systematic uncertainty that is not trivial to quantify. This uncertainty increase with λ, as higher wavelength neutrons, with higher divergence, are more susceptible to the effects of small tilts or displacements of the sample, and aperture. We addressed this uncertainty by measuring the sample at different orientations with respect to the beam. However, it should be noted that the mesoscopic structure can also change with orientation, as discussed below.

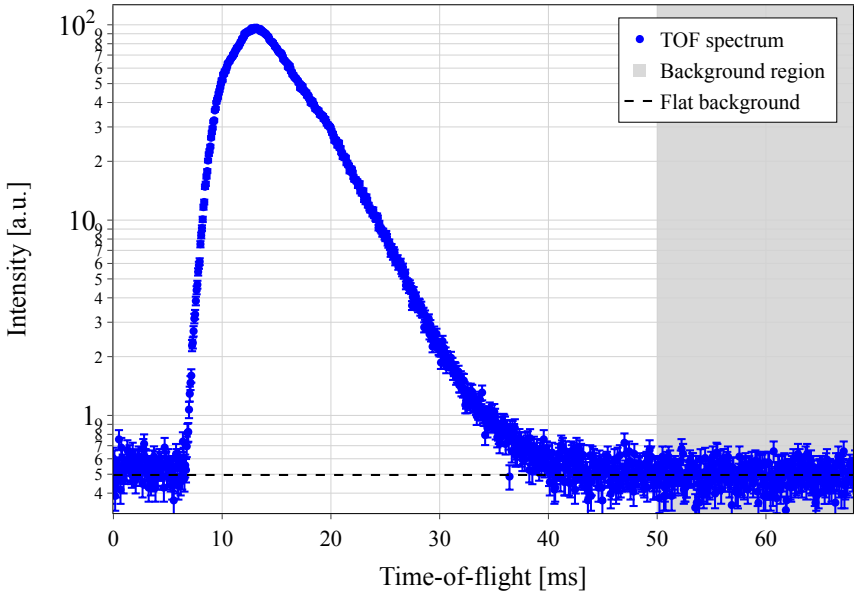

Figure 6.28.: Time-of-flight spectrum measured through the empty sample container. A flat background was subtracted, calculated as the mean intensity from the grey-shaded area at the end of the time-of-flight spectrum. This procedure was repeated for each run.

After positioning the empty cell, neutron spectra were collected in a series of 30-minute runs, each with a corresponding monitor count for the transmitted beam. These runs were later combined during analysis. Adequate statistics were typically achieved after about half a day of measurement. The cell was then removed from the cryostat, filled with the liquid sample solution, sealed, reinserted, and frozen *in situ*. Once the hydrate formed, the alignment procedure was repeated, and the sample was measured in two different orientations differing by a 90° rotation, corresponding to thicknesses of $t = 1\,\text{cm}$ and $t = 1.5\,\text{cm}$. The cryostat was capable of reaching a

base temperature of 4 K. Both the sample and the empty cell were measured at this temperature, as well as at approximately 80 K and room temperature ($\sim$ 296 K).

A flat background was subtracted, calculated from the mean intensity at the end of the time-of-flight spectrum. This process was repeated for each run, as illustrated in Figure 6.28. The normalized and background corrected spectra are then converted into the wavelength domain and the wavelength dependent total neutron cross section σ_t was calculated using Equation 6.3. Since the wavelength spectrum of the VCN beam does not cover well known features of common calibration samples, the spectrum needs to be obtained from the measured time-of-flight distribution with Equation 6.11. The determination of the chopper-offset is given in Appendix D.

With the background subtracted and the timing offset determined the spectrum can be converted into the wavelength domain and trimmed to the relevant wavelength scale. This spectrum was recorded with the setup shown in Figure 6.26. A similar parametrization as in 6.29 can be applied (see Figure 6.23), with the parameters given in Table 6.9.

Table 6.9.: Fitting parameters of the very cold neutron spectrum.

Parameter	Value
A_0	1385.57 ± 39.75
λ_1	8.88 ± 0.09
λ_2	32.03 ± 0.0963
p	9.44 ± 0.05

6.3.1. Results from VCN Transmission

Figure 6.29 presents the cross sections derived from the measurements of neutron transmission through the 10 mm and 15 mm thick hydrate bulk. The slight divergence of results from these two measurements could be attributed to alignment errors, as previously discussed, as well as to different mesoscopic structure. Additionally, variations in sample preparation and measurement conditions could contribute to these differences. The fit in the lower plot of Figure 6.29 was obtained using the mean of both configurations.

Since the VCN capture cross sections of all constituents are small (see Table 6.2), the changes in the transmitted neutron flux are primarily due to scattering. With no significant Bragg scattering expected above $\sim$ 20 Å, the scattering beyond the wavelength range of elastic incoherent scattering dominated by the deuterium is most likely due to the mesoscopic structure of the polycrystalline hydrate. Factors such as crystalline size, sample impurities, or density heterogeneities (e.g., cracks and defects) within the sample volume can cause VCN scattering. This small-angle-neutron-scattering (SANS)[13] was modelled before to describe the VCN and UCN cross section of solid deuterium (SD_2). In [237] Porod's law is used to account for scattering from crystal defects in SD_2 at low temperatures, [238] uses a Guinier approximation to account for the same effect.

Without detailed knowledge of the mesoscopic structure, modeling approaches remain limited. The Guinier model [239] offers a straightforward method to describe the scattering at small q. This model assumes uniformly distributed, non-interacting particles of a phase 1 embedded within a matrix of phase 2, where each particle in phase 1 is of identical size. Additionally, all phase 1 particles are described by a generalized radius of gyration (R_g) [238]. The radius of

[13]This type of scattering does not necessarily occur under small angles for VCN.

gyration represents the root-mean-square distance of the particle's mass distribution from its center of mass, serving as a measure of both shape and size.

Instead of particles we can think of defects in the hydrate uniformly distributed in the polycrystalline structure. Whether this is an accurate representation of the mesoscopic structure or not, it gives a first point of reference in modelling the SANS contribution of the total cross section and allows to derive an empirical expression for elastic scattering in the low q regime, employing the Guinier approximation, which is given by [239]:

$$\frac{d\sigma_{\text{Guinier}}}{d\Omega}(q) = C \exp\left(-\frac{q^2 R_{\text{g}}^2}{3}\right) \tag{6.32}$$

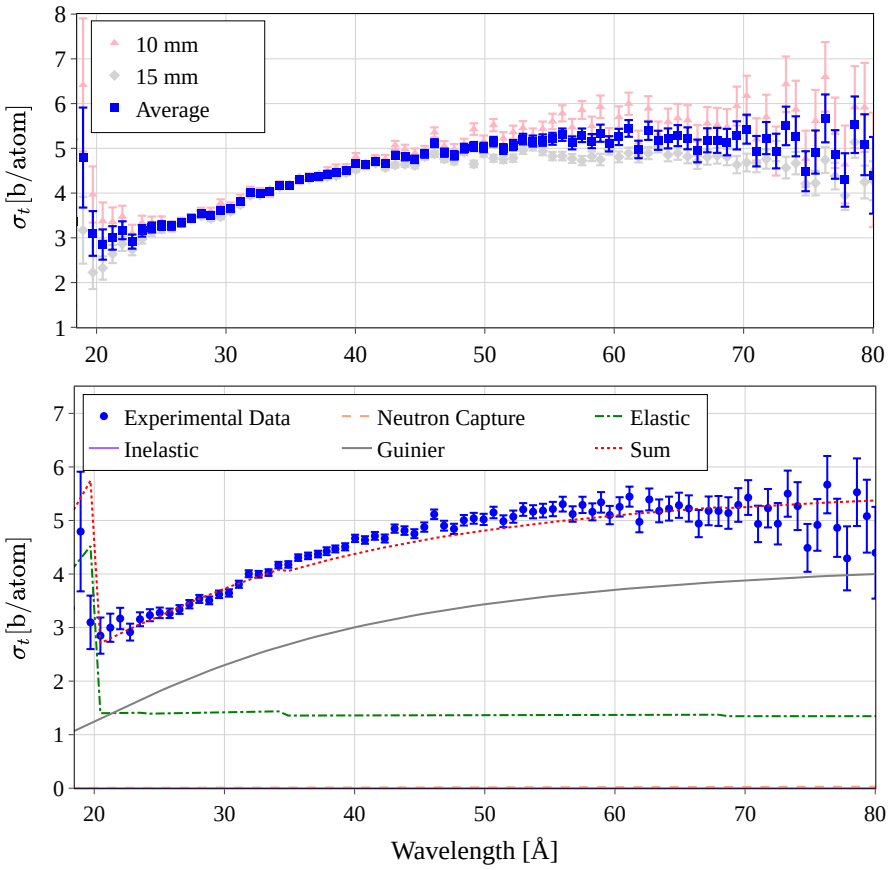

Figure 6.29.: The upper panel shows the total cross sections σ_{t} calculated from VCN transmission data for configurations with thicknesses $t = 1\,\text{cm}$ (light pink triangles) and $t = 1.5\,\text{cm}$ (grey diamonds) at $T \approx 4\,\text{K}$. The divergence at higher wavelengths ($\gtrsim 50\,\text{Å}$) may stem from alignment errors or mesoscopic structural differences between the different sample orientations. The lower panel displays the mean of the derived cross sections for both configurations (blue circles), along with a fitted curve that includes known contributions to the cross section calculated using NCrystal, as well as a small-angle scattering component modeled with the Guinier approximation.

The SANS contribution to the total cross section is obtained by integrating Equation 6.32 over the solid angle dΩ (see Appendix E), yielding:

$$\sigma_{\text{Guinier}}(\lambda) = \frac{3C\lambda^2}{4\pi R_g^2}\left[\exp\left(-\frac{4\pi^2 R_g^2}{3\lambda^2}\sin^2\left(\frac{\theta_{\text{min}}}{2}\right)\right) - \exp\left(-\frac{4\pi^2 R_g^2}{3\lambda^2}\sin^2\left(\frac{\theta_{\text{max}}}{2}\right)\right)\right], \tag{6.33}$$

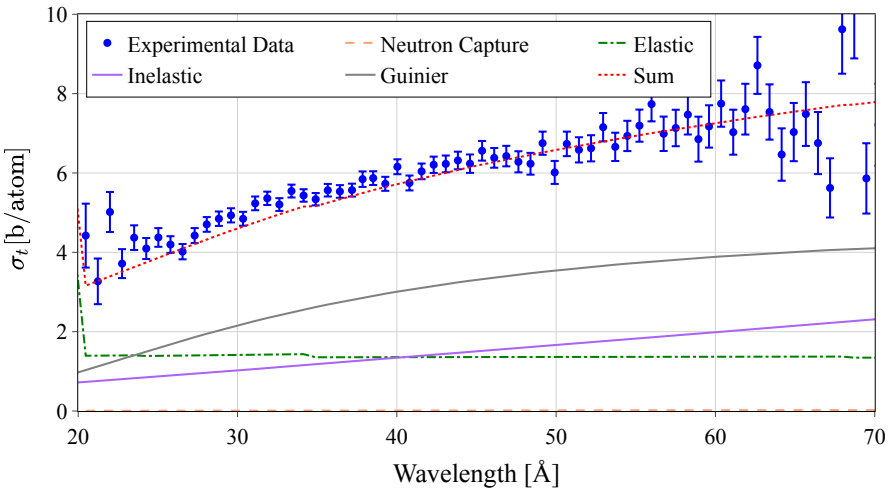

Figure 6.30.: Total cross sections σ_t calculated from VCN transmission data through the 15 mm sample at 80 K.

where C and R_g are fitting parameters, with C acting as a scale factor. The transmission setup accepts small angles down to $\theta_{min} = 2°$ and a maximum angle of $\theta_{max} = 180°$. Performing a non-linear least squares fit (e.g. [240]) gives $C = 1.41 \pm 0.04$ and $R_g = (10.12 \pm 0.57)$ Å. For the cross section measured at 80 K a similar behaviour can be observed, as depicted in Figure 6.30. Since the structural properties of the sample do not change significantly between 4 K and 80 K, the small-angle scattering, approximated by the Guinier model, remains consistent. An independent fit yields a similar SANS contribution as at 4 K. This implies that any variations in the cross section at 80 K are not due to changes in the mesoscopic structure of the polycrystalline hydrate. The increase in the cross section at 80 K can solely be attributed to an increase in inelastic scattering, as indicated by the solid purple line in Figure 6.30. This inelastic scattering is due to enhanced thermal vibrations and other dynamic processes within the material at the higher temperature. As the temperature rises, these inelastic processes become more significant, contributing to the overall increase in the neutron scattering cross section.

As a cross-check, the inelastic scattering cross section can be determined by subtracting the 4 K cross section (see Figure 6.31). The difference agrees with the inelastic scattering cross section calculated using NCrystal, validating the model's accuracy. Furthermore, the cross section of the liquid THF-d/17 D_2O solution, shown in red, provides a valuable reference point. This allows for a cross-check of the scattering magnitude against the known cross section of heavy water, shown in Section 6.4.

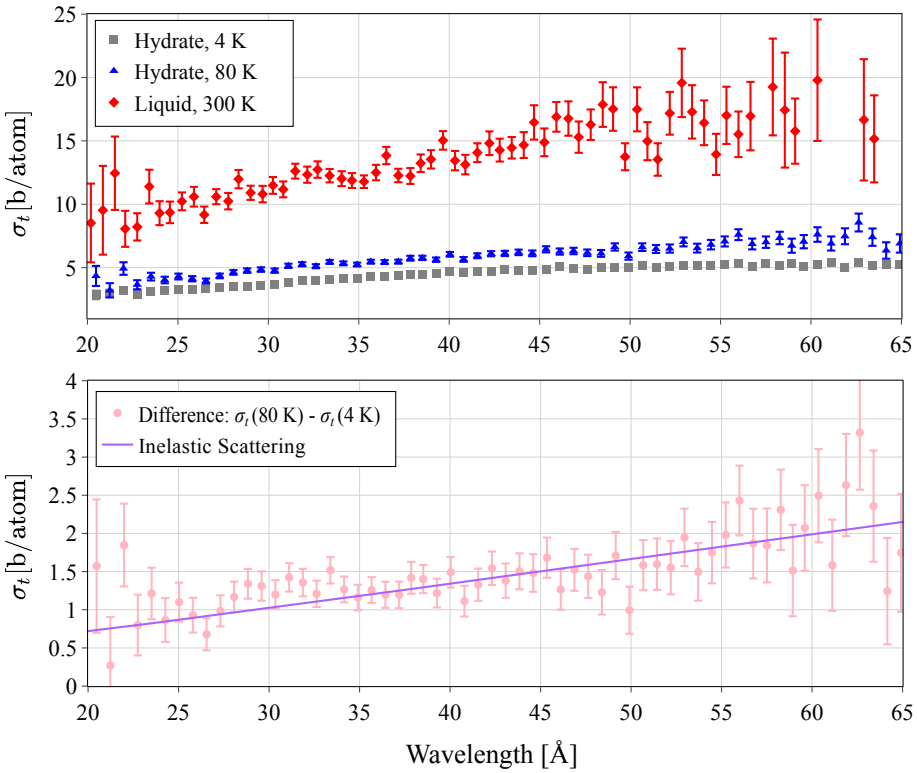

Figure 6.31.: Comparison of VCN scattering cross sections at different temperatures. The 4 K cross section (blue triangles, see also Figure 6.31) is subtracted from the 80 K cross section (grey squares), yielding the inelastic scattering cross section (light pink dots).

6.4. Comparison of Results and Discussion

6.4.1. Heavy Water and Liquid THF-d/17 D_2O Solution

As mentioned above, the liquid solution provides an important internal standard among the various conducted transmission experiments. The mesoscopic crystalline structure of the bulk sample can depend significantly on the inner surface of the sample container and the solidification process, particularly the temperature protocol used for hydrate formation. Similarly, the size distribution of the powder depends on the manufacturing technique, thus influencing the resulting SANS contribution.

In contrast, the total cross section of the liquid THF-d/17 D_2O solution depends solely on its exact stoichiometry and temperature, both of which can be carefully controlled and monitored. Although the THF-d/17 D_2O solution does not scatter identically to heavy water, the similar chemical composition allows for a meaningful cross-check of the scattering magnitude, given a dedicated measurement of heavy water is performed. Such a dedicated total cross section measurement of heavy water was conducted during experiment 3-07-419 at PF1B and is presented was Figure 6.14. The excellent agreement with literature values provides confidence in the experimental technique and validates the scattering magnitude of the THF-d/17 D_2O solution.

As a next step, the consistency of the cross section results of the THF-d/17 D_2O solution across different experiments can be verified. Figure 6.32 displays the total cross section data from all conducted experiments. Differences in mass density due to varying temperatures were accounted for using the data provided in [241].

Table 6.10.: Densities of the constituents of deuterated and protonated THF-hydrates at 293 K.

Substance	Density [g/cm^3]
Heavy Water (D_2O)	1.11
Ordinary Water (H_2O)	0.997
THF-d	0.985
THF	0.889

The cross section values for the deuterated THF-d/17 D_2O solution were calculated by multiplying the values for the protonated solution THF/17 H_2O with a conversion factor f, using the weighted average of the density ratios of heavy water to regular water and THF-d to THF. With the densities given in Table 6.10 this factor can be calculated by

$$f = \frac{17\left(\frac{1.11}{0.997}\right) + \left(\frac{0.985}{0.889}\right)}{18} \approx 1.113\,. \tag{6.34}$$

The resulting mass densities are given in Table 6.11. The mass density at 293 K was obtained via interpolation between the available data points. From the mass density (ρ), the number density (N) used in Equation 6.3 can be calculated by

$$N = \frac{N_A}{M}\rho\,, \tag{6.35}$$

for a known atomic or molecular mass M, where N_A is Avogadro's constant.

Although the local maximum of the cross section appears slightly shifted at BOA compared to PF1B, the consistency of the overlapping data in Figure 6.32 suggests that any variations in the measured quantities between the two experiments are intrinsic to the sample rather than artifacts of differing experimental setups. This allows us to draw important conclusions regarding the measurements of the bulk sample.

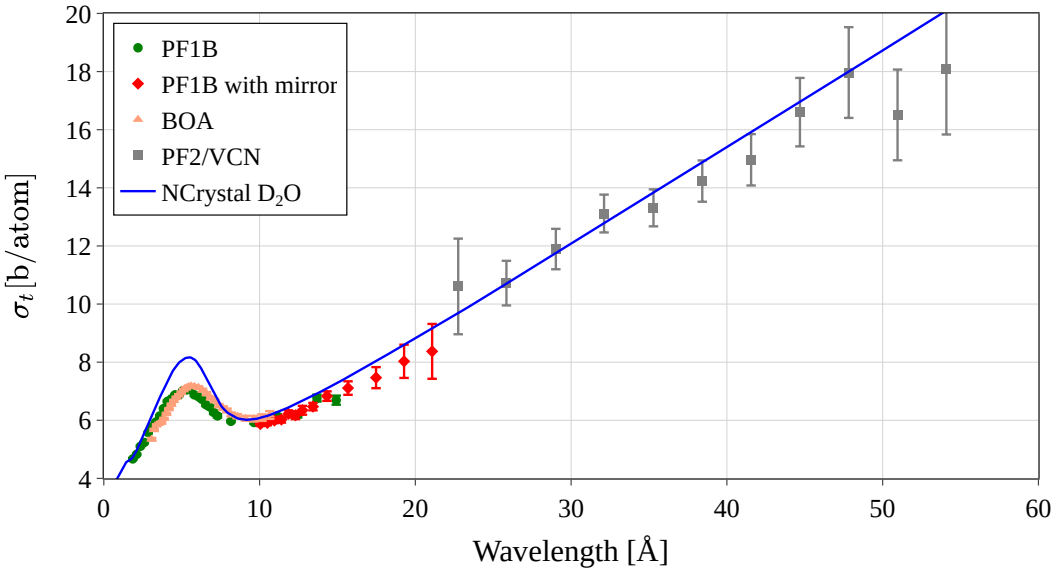

Figure 6.32.: Total cross section of the THF-d/17 D_2O solution experiments across the conducted experiment. The temperature at BOA was $T \approx 293\,\mathrm{K}$, while the temperature at the other experiments was $T \approx 298\,\mathrm{K}$. The densities of the solutions were adapted accordingly following an interpolation of the values given in Table 6.11.

Table 6.11.: Density of THF / 17H_2O and THF-d / 17D_2O solutions at different temperatures, based on data from [241], using a conversion factor of $f = 1.113$. The uncertainties in the temperature are $\pm 0.03\,\mathrm{K}$, and the uncertainties in the density are $\pm 8 \times 10^{-5}\,\mathrm{g/cm^3}$, as reported in [241].

Temperature [K]	THF/17H_2O [g/cm^3]	THF-d/17D_2O [g/cm^3]
277.65	0.996	1.109
278.15	0.996	1.109
288.15	0.991	1.103
298.15	0.986	1.097
308.15	0.980	1.090

6.4.2. THF-d Deuterates in Bulk

Recalling the three experiments at BOA and PF1B, the most notable difference between these three results is the discrepancy in the magnitude of the cross section between the measurements at BOA conducted at 20 K and those at PF1B conducted at 4 K. The absence of this trend in the liquid solution measurements suggests a physical cause inherent to the sample. This difference can most likely be attributed to varying elastic coherent scattering due to different crystallization processes. The purity of the sample, along with the fraction of hexagonal ice or other mixed phases, can significantly influence the proportion and magnitude of both Bragg scattering and small-angle-scattering (SANS). This likely results in much weaker Bragg scattering and SANS in the BOA measurements, which cannot compensate for the expected slightly higher inelastic fraction due to the elevated temperature. An important factor to consider is that the volume of the sample container used at BOA is about nine times larger than that used at PF1B. The volume-to-surface-area ratio, along with the amount of heat required to form the hydrate and the resulting time for hydrate formation, likely has a significant influence on the resulting crystal structure. Larger volumes may lead to differences in hydrate purity and mesoscopic structure,

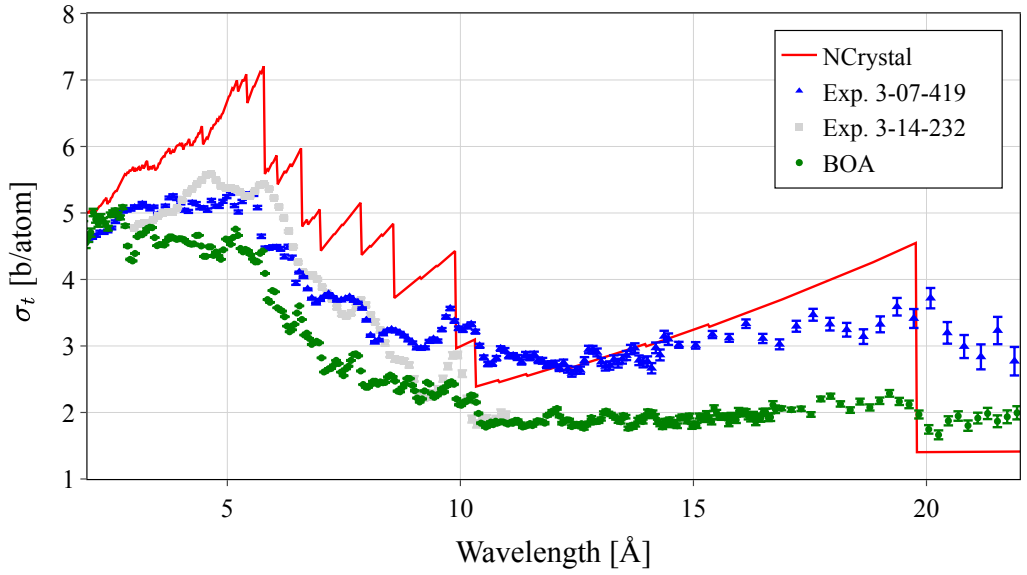

Figure 6.33.: Comparison of the total cross sections for the bulk sample. The transmission through 40 mm at BOA (green circles), the transmission through 15 mm in experiment 3-14-232 (grey squares), and the transmission through 15 mm in experiment 3-07-419 (blue triangles) differ significantly in magnitude as discussed in the text. This is most likely due to different crystallization conditions within different sample environments.

affecting the overall scattering behavior.

These differences in the sample would have considerable consequences for the application of the material as a moderator. As proposed by the author in [93], an *in-situ* annealing of the moderator, followed by reestablishing the hydrate structure within the moderator volume, could help preventing a "burp" of the moderator [242, 243, 244], due to radiolysis.[14] However, if the hydrate or resulting solid solution forms with different scattering behavior due to variations in crystallization processes, this approach would be significantly compromised. If *in-situ* annealing is necessary for the specific moderator application, it is essential to analyze the reproducibility of the hydrate formation, as well as the influence of the sample quantity and the cooling capacity, for the required mass of material in advance, as consistent crystallization is critical for the application as a neutron moderator.

While the data measured in the CN range with different containers at BOA and PF1B exhibit significant discrepancies, the measurements performed with smaller containers at PF1B and PF2/VCN show a consistent overlap. This consistency provides further indication that the variations observed in the larger-container measurements are likely due to differences in sample crystallization processes.

Given the consistency of the smaller-container data, we can confidently combine the bulk sample measurements taken at PF1B with those collected at PF2/VCN at a wavelength of $\lambda = 20\,\text{Å}$. The resulting combined data set is shown in Figure 6.34. The red dashed curve represents the sum of all expected contributions to the cross section, including the small-angle neutron scattering (SANS) contribution modeled using the parameters $C = 1.41 \pm 0.04$ and $R_g = (10.12 \pm 0.57)\,\text{Å}$, determined from the VCN transmission data as described in Section 6.3, within the Guinier model. The Bragg scattering in the bulk seems to be reduced with respect to

[14] Radiation damage, as well as radiolytic D_2, could pose significant challenges for designs that employ the moderator "in-pile". A future design study should consider the radiation hardness of clathrate hydrates.

the Bragg contribution expected for a powder sample, with the remaining contributions behaving as anticipated.

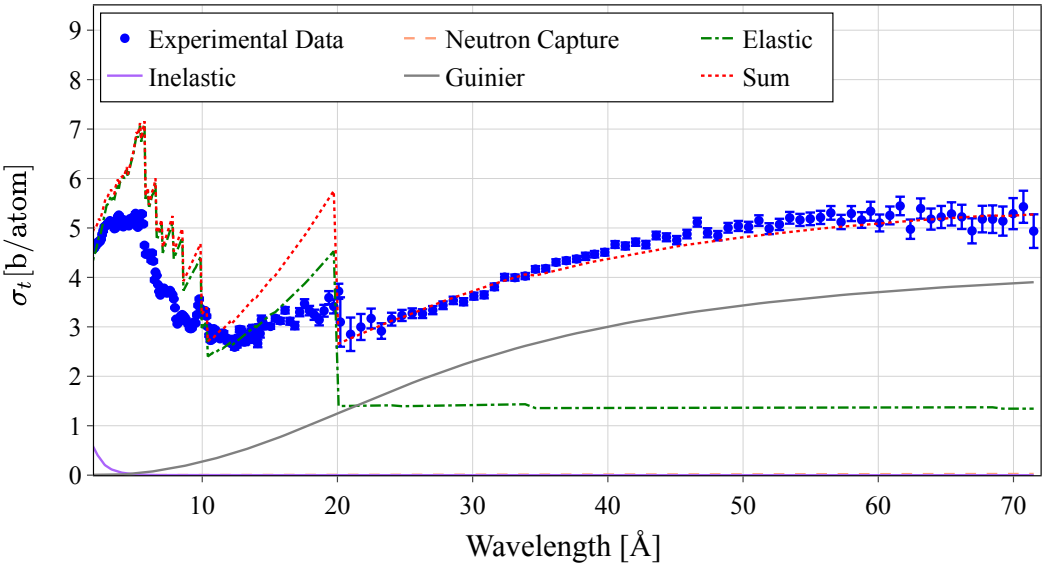

Figure 6.34.: Combined total cross sections of the bulk sample of THF-d deuterates at PF1B and PF2/VCN measured at 4 K (blue circles). The cross-over point is at $\lambda = 20$ Å. The red dashed curve represents the cross section calculated using NCrystal, extended with a SANS model based on the Guinier approximation, with parameters $C = 1.41 \pm 0.04$ and $R_g = (10.12 \pm 0.57)$ Å (see Section 6.3). The Bragg scattering in the bulk sample appears to be reduced compared to the level expected for a powder sample.

6.4.3. Powders of THF-d Deuterates

The cross section of a fine powder of THF-d-deuterates, prepared by quenching a stoichiometric solution of 17 D_2O/THF-d followed by ball milling as discussed in Chapter 4, is shown in Figure 6.12. This cross section was calculated using transmission data from the two setups of experiment 3-07-419. The result clearly exhibits Bragg edges at the expected positions and the expected magnitude for CS-II hydrates. However, above 10 Å the cross section is dominated by a contribution that increases with wavelength. As discussed previously, SANS is probably responsible for this effect.

Following the discussion in 6.3, a densely packed fine powder can be conceptualized as a two-phase system. In this model, particles of THF-d-deuterates, with an unknown but expectedly narrow size distribution, are homogeneously distributed in vacuum (neglecting the scattering density of residual gas). This creates a contrast in the scattering length density leading to small-angle-scattering. With this in mind, we can apply the expression for the Guinier removal cross section that was derived in Section 6.3 and attempt to fit all known contributions to the cross section with an additional Guinier term to the calculated cross section from CN transmission. The result is given in Figure 6.35. One can see that a Guinier model with the parameters of $C = 6.88 \pm 0.31$ and $R_g = (8.51 \pm 0.24)$ Å fits the data quite well. The resulting SANS in the Guinier model is indicated with the solid gray line.

Furthermore, a combination of these two models, labeled as "Guinier-Porod model", is described in [38]. This model is based on the work of [37] and has been implemented as a plug-in in NCrystal (openly available under [245]). The results for a hard sphere radius of 10 Å are

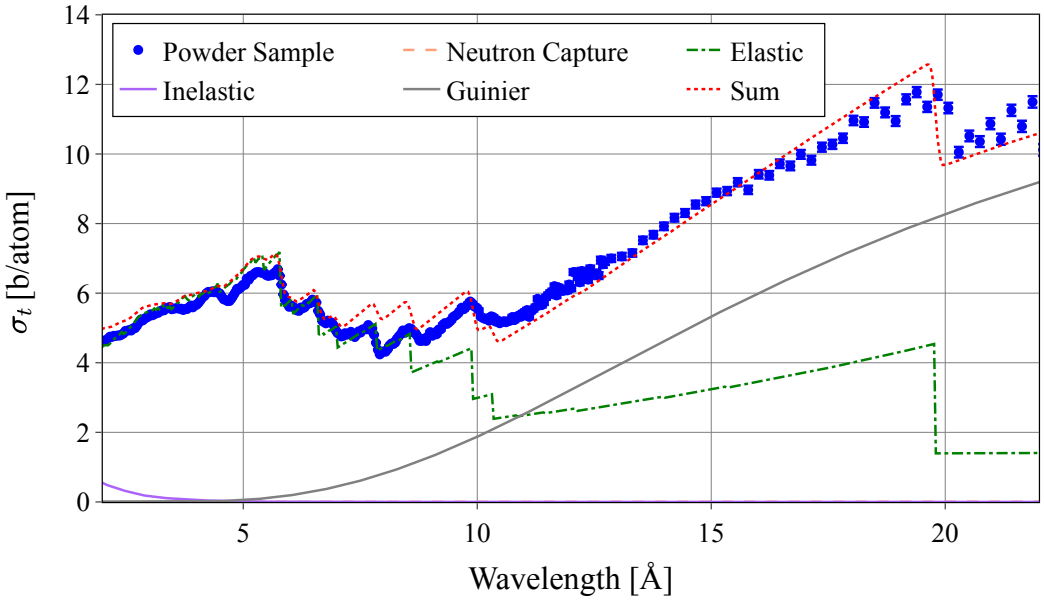

Figure 6.35.: Total cross section σ_t of a fine powder of THF-d-deuterates, prepared by quenching a stoichiometric solution of 17 D_2O·THF-d and subsequent ball milling as described in Chapter 4. The Bragg edges appear at the expected positions and at the expected magnitude for a CS-II hydrate. At higher wavelengths, a wavelength-dependent increase of σ_t is observed, indicating the presence of small-angle-scattering (SANS). The fit to the experimental data incorporates a Guinier term with parameters $C = 6.88 \pm 0.31$ and $R_g = (8.51 \pm 0.24)$ Å, represented by the grey solid line. The sum of all modelled contribution is indicated by the red dotted line.

presented in the lower panel of Figure 6.36.

Both the Guinier and hard sphere models effectively describe the small-angle neutron scattering (SANS) contribution to the measured data. An important caveat arises from the solid angle covered by the detector, which has a circular active area with a diameter of 10.8 cm. While the covered solid angle of the detector only introduces a small error under isotropic scattering conditions, it becomes more critical for the SANS contribution. The Guinier model used here addresses this issue by integrating from the minimal scattering angle not registered by the detector. However, this correction is not incorporated in the hard sphere model implemented in the NCrystal plug-in, leading to a poorer fit to the data below 10 Å.

6.4.4. Conclusions

The transmission experiments conducted at PF1B, BOA, and PF2/VCN cover a broad range of the thermal, cold, and very cold neutron spectra. Despite the inherent challenges in obtaining reliable total cross section measurements, especially in the CN and VCN regimes without a dedicated instrument, the consistent results observed in the THF-d/17 D_2O solution across different experiments demonstrate the reliability of this experimental approach and can serve as an internal standard. In contrast, significant variations in the bulk sample measurements, particularly between experiments at BOA and PF1B, underscore the substantial impact of sample container volume and crystallization conditions on neutron scattering behavior. This could be critical when relying on in situ annealing and re-crystallization in order to mitigate radiation damage or prevent the fast heating of the moderator, often referred to as "burp". The reduced

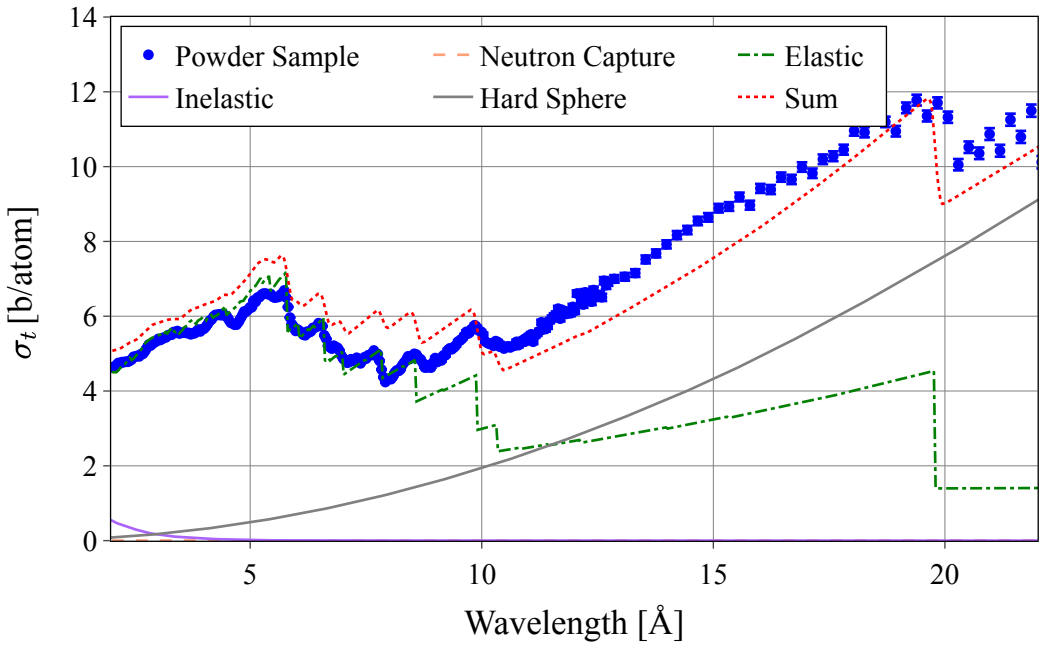

Figure 6.36.: Analysis of neutron scattering cross sections using a Guinier-Porod model as described in [38]. The lower panel illustrates the results of the Guinier-Porod model for a hard sphere radius of 10 Å, based on the Guinier-Porod model implemented as a NCrystal plug-in see [245].

Bragg scattering and the occurrence of SANS could be due to texture and imperfect formation of the hydrate during in-situ crystallization. In contrast, the powder sample exhibits Bragg scattering at expected strength. Above $\lambda \approx 10$ Å, the wavelength-dependent increase in the experimental cross section is modeled using either the Guinier or hard sphere model [38], with the latter accounting for inter-particle correlations.

Future investigations of this hydrate system should include dedicated SANS experiments on both the powder and bulk samples. For the powder such measurements would offer insights into the particle size distribution and enable accurate modeling of the SANS contribution to the total cross section. Additionally, the mesoscopic structure of bulk samples could be explored by annealing the powder and refreezing it *in situ* under controlled temperature cycling protocols. This could provide insights on the impact of the thermal history on crystalline size, shape, and hydrate purity within the sample. Monitoring formation time, temperature, and heat transfer dynamics would improve understanding of the scattering mechanisms contributing to the VCN cross section. Once understood, the SANS contribution could be modeled by adapting the existing NCrystal plug-in [245] or developing a new method, crucial for realistic moderator/reflector configurations.

A proposal for this experiment at the SAM instrument [246] at the Laboratoire Léon Brillouin (LLB) has been accepted; however, its realization lies beyond the timeline of this thesis. Alternatively, such a measurement could be conducted at D11, D22, or D33 at the ILL. A complementary experiment could be conducted at PF2/VCN by analyzing the small-angle neutron scattering signal on the areal detector, which was previously hindered by the flight tube used in the experiment discussed above. Such a combination of experiments would provide an interesting case study for a SANS investigation on a VCN beamline.

7. Conclusions and Future Perspectives

This thesis presented the first comprehensive experimental investigation into the neutron scattering properties, key neutron cross sections, and neutron transport behavior of deuterated clathrate hydrates, laying the groundwork for their application as a novel moderator material for Very Cold Neutrons (VCN). The experimental work was accompanied by computational studies and the development of thermal scattering libraries (TSL) on these compounds [41, 42], which are now openly available to the community [94]. The experimental and simulated results presented provide a detailed picture of the investigated hydrates hosting tetrahydrofuran (THF) and dioxygen (O_2) and enable further steps towards VCN source developments using clathrate hydrates as a moderator material.

Manufacturing Techniques and Diffraction

A method for producing protonated, deuterated, and mixed clathrate hydrates with THF, as well as a novel technique for manufacturing binary hydrates containing both THF and O_2, was presented. In a diffraction study at D20, we demonstrated that the stoichiometric solution of THF-d/17D_2O reliably forms the CS-II structure. Significant texture was observed in the bulk, which became evident when the sample was rotated between subsequent measurements. We also demonstrated through neutron diffraction that manufacturing the hydrate powder via ball milling preserves the CS-II structure. Subsequent pressurization with O_2 resulted in a cage occupancy of 80%. For the resulting binary hydrate, a lattice parameter of 17.122 Å at 2 K was measured, and the thermal expansivity, $\alpha(T)$, was determined for the first time between 2 K and 90 K.

Future work could explore the open question of the grain size distribution obtained through milling. This should, in principle be addressable with optical microscopy, provided that the samples can be maintained at low temperatures within an argon or nitrogen atmosphere. Alongside the optimization of pressurization parameters, a detailed study of grain size distribution could provide valuable insights into hydrate formation mechanisms and the influence of grain size on cage occupancy. Optimizing these parameters appears worthwhile, as the efficiency of the moderator is directly influenced by the abundance of O_2. Nuclear Magnetic Resonance (NMR) and Raman spectroscopy are complementary techniques to neutron diffraction that could effectively address the question of O_2 cage occupancy.

Inelastic Neutron Scattering

In the inelastic neutron scattering study at the time of flight spectrometers IN5 and Panther, we successfully measured the dynamical structure factor of fully and partly deuterated THF hydrates in absolute units. The experimental data provided crucial input for the development of novel thermal scattering libraries (TSL). Furthermore, we measured for the first time the magnetic down-scattering of neutrons of paramagnetic dioxygen confined in a binary clathrate hydrate. These data were used to verify the magnetic scattering model developed in [58] and [42] and demonstrate that binary clathrate hydrates hosting THF-d and O_2 are effective for magnetic cooling in a future moderator. While the temperature dependency of the magnitude

of the magnetic scattering signal seems to be well modeled, the observed peak broadening behavior raises further questions. Those will be addressed during an already granted beamtime at the backscattering spectrometer IN16B at the ILL [201]. A systematic measurement of a temperature curve extending beyond 20 K would allow a precise quantification of both the peak broadening and the potential shift of the peak center.

With the data taken on the vibrational spectroscopy instrument IN1-Lagrange, we were able to verify the simulation input of the fully and partly deuterated THF hydrates across their whole excitation spectrum. The librational band of THF hydrates exhibit similar characteristics to other CS-II hydrate structures. The dynamics of the THF molecule in confinement agrees remarkably well with the normal modes of single isolated molecule, while the differences to established data of crystalline and liquid THF are significant.

Transmission Experiments

The transmission experiments conducted at PF1B, BOA, and PF2/VCN serve as an important benchmark of the established TSL. The transmission data of the bulk sample reveal a significant influence of the sample container and crystallization conditions on the total cross section. The decrease in Bragg scattering across various measurements suggests the presence of texture and an impact on the purity of the hydrate phase. This effect could be critical when relying on in situ annealing and re-crystallisation, in order to mitigate possible radiation damage or radiolytic deuterium. In contrast, the powder sample displays the expected Bragg scattering behavior. However, at wavelengths greater than approximately 10 Å, the experimental cross section shows a clear wavelength-dependent increase. This rise can be attributed to a SANS contribution, which can be effectively modeled using either a Guinier approximation or hard sphere model, the latter described in [38].

Future investigations of these hydrate systems should include dedicated SANS experiments on both the powder and bulk samples, as discussed in Section 6.4.4. One such measurement is already approved at the SAM instrument [246] at the Laboratoire Léon Brillouin (LLB). Once this contribution is sufficiently understood, it should be part of the TSL for future design studies. The detailed descriptions of the transmission experiments could also provide valuable insights and important lessons for future total cross section measurements. Considering the substantial effort required to convert fundamental physics beamlines into "cross section instruments", it might be beneficial to invest in the design of instrumental elements, such as dedicated translation stages, sample environment and detectors, that could help to facilitate these conversions. Alternatively, depending on the required wavelength spectrum, some SANS and neutron imaging instruments could be used for time efficient total cross section measurements.

As a next step in developing a clathrate hydrate moderator, constructing a demonstrator capable of operating with either THF-d or binary THF-d – O_2 deuterate would be a practical approach. This demonstrator would require a cryogenic system capable of cooling large amounts of material to temperatures below 4 K. A significant engineering challenge would be the pressurization with O_2 and the subsequent cold transfer of the hydrate powder into the moderator volume, ensuring that no condensation occurs. After resolving these challenges, the demonstrator could undergo testing at various facilities, such as the PF1B beamline at the ILL, Big Karl at the Jülich Centre for Neutron Research (JCNS) [247], or the Cold Moderator Test Facility (CMTF) at the Budapest Neutron Center (BNC) [248]. In a time-of-flight setup complemented by a pin-hole imaging system, the spectrum of the moderator prototype could be quantified following the principles of a camera obscura, as described in [249].

8. Appendix

A. Hydrates in Environmental and Climate Sciences

Before discussing the properties that render hydrates as very promising VCN moderators, it is pertinent to highlight the most prominent and societally relevant aspect of gas hydrate research, in order to contextualize their scientific and environmental significance. The role that hydrates play in environmental and climate sciences is closely linked to the large deposits of natural gas (primarily methane CH_4), which are contained in clathrate hydrates. Current estimates of this methane content vary within an order of magnitude. More conservative estimates assume about $1 \times 10^{15}\,m^3$ to $5 \times 10^{15}\,m^3$ [250] [251], while others estimate up to $14 \times 10^{15}\,m^3$ [252].[1]

This is equivalent to $\sim$ 500 Gt to 2500 Gt or 7000 Gt of methane carbon respectively. To put these numbers into perspective, the global anthropogenic CO_2 emissions in 2023 were the highest ever recorded and totalled 37.4 Gt [253], resulting in $\sim$ 10 Gt of carbon. That means that even for conservative estimates, gas hydrates store a carbon emission equivalent of the of 50-250 years of the current anthropogenic emissions. Most of these hydrates are located in shallow ocean sediments, continental shelf slopes, and permafrost soils around the globe. Exploiting even the easily accessible parts of these natural gas reserves for combustion as fossil fuel is hardly in line with the required decarbonization and climate change mitigation measures suggested by the IPCC [254]. Moreover, a significant aspect in environmental and climate sciences concerning hydrates is the *clathrate gun hypothesis*.

It is important at this point to differentiate between methane and CO_2 emissions. While the atmospheric lifetime[2] of methane is approximately 12 years, which is shorter than the centuries-long atmospheric lifetime of CO_2, its potency as a greenhouse gas – i.e., its ability to absorb infrared radiation – is much higher than that of CO_2. This leads to the fact that for the same mass of emitted methane and CO_2 over a time of 20 years, methane would trap about 80 times more heat. While over a period of a 100 years, the atmospheric lifetime difference slowly closes the gap and methane is assumed to absorb about 28 times more heat [255]. It is therefore safe to state that carbon emissions in the form of methane have an higher impact on anthropogenic climate change than the equivalent amount of carbon in the form of CO_2.

The clathrate gun hypothesis is based on the fact that gas hydrates remain stable only under conditions of low temperature and/or high pressure. So, according to this theory, the combination of rising temperatures and the dissociation of gas hydrates could thus trigger substantial methane releases from present-day submarine gas hydrate deposits. Those, in turn, would cause further warming, fueling a feedback loop with catastrophic consequences for the global climate. While clathrate hydrates located in seabed sediments are less of a concern due to very high and stable hydrostatic pressures, this is not necessarily true for hydrate deposits closer to shore lines. Many of these shallower hydrates are located in the Arctic sea, where they were able to remain

[1] Methane clathrate usually form CS-I structures with 8 cavities per unit cell. When the clathrate is fully occupied the composition of the hydrate is 1 mol of methane for every 5.75 mol of water. The associated molar masses are 16.043 g and 18.015 g for methane and water respectively. Given that the methane hydrate has a density of about $0.9\,g\,cm^{-3}$ and methane gas has a density of $0.716\,kg\,m^{-3}$ (at 276.15 K), we can easily calculate that 1 l of methane hydrate contains about 0.85 l of water and 168.6 l of methane gas.

[2] The atmospheric lifetime describes the average time a molecule spends in the atmosphere before being removed by physical or chemical atmospheric processes.

stable because of low temperatures rather than high pressures. They are further stabilized with a permafrost "lid" that prevents natural gas from escaping the sediment. This phenomenon is known as self-preservation of gas hydratres [256].

A serious concern during the last decade was whether ocean waters could warm enough to compromise those self-perservation mechanisms. A supersaturation with methane of "80% of the bottom water" and about "50% of the surface water over the East Siberian Arctic Shelf" seemed to confirm these concerns at the beginning of the last decade [257]. However, the 2014 IPCC report points out, that the exact proportion of methane originating from decomposing organic carbon versus destabilizing hydrates remains uncertain. Furthermore, there is a lack of evidence to ascertain whether these emissions have been influenced by recent regional warming or if they have been present since the last deglaciation period [252]. It is important to not, that the dissociation of gas hydrates in specific terrains does not yet imply a net methane emission into the atmosphere. Indeed, it seems more likely that a large portion of the methane released in these processes is confined or interacts elsewhere in the sediment or water column, rather than being transported to the sea-air interface. A 2016 study [258] claims that there is no conclusive proof thathane released from gas hydrates enteenterssphere at a level detectabldetectable against emissions. The most recent IPCC report concludes that it is very unlikely that gas hydrates located in deeper terrestrial permafrost and submarine hydrates will cause a detectable departure from the emissions trajectory during this century [254].

Given these circumstances, naming this phenomenon *clathrate gun hypothesis* seems unfortunate as these sediments move and transform quite literally at a glacial pace. It seems undisputed however, that methane emissions from gas hydrates have a slow positive feedback on global warming on long time scales (over centuries and millennia). Due to sheer amount of green house gases confined in hydrates they remain an important factor.

B. Wavelength Dependent Attenuation of Neutrons in Air

In many neutron experiments, particularly those involving transmission with colder neutron spectra, neutron attenuation in air becomes a significant factor. Attenuation refers to neutrons that fail to reach the detector due to scattering or absorption by air constituents while passing through the experimental setup. Typically, air attenuation is similar whether the sample is present or absent, in the transmission path. However, variations in laboratory conditions, such as temperature, pressure, and humidity, can introduce additional uncertainties. Minimizing air attenuation can enhance counting statistics, reduce measurement time, and improve precision.

To calculate the attenuation of a neutron beam in air, it is essential to consider both scattering and absorption events involving the primary constituents of the laboratory atmosphere—namely nitrogen, oxygen, argon, and water vapor. The density and abundance of these constituents vary with changes in temperature, pressure, and humidity. The total energy-dependent, macroscopic cross section, denoted as $\Sigma_{\text{tot}}(E)$, along with the number densities of each constituent, enables the calculation of the macroscopic cross section, $\sigma_{\text{air}}(E) \cdot N(h, p, T)$, where $N(h, p, T)$ represents the number density of each air constituent as a function of relative humidity, pressure, and temperature. Neutron cross section data can be obtained from sources such as the Evaluated Nuclear Data File (ENDF) [54]. This framework allows for the determination of the total macroscopic cross section of air as a function of neutron energy E , humidity h , pressure p , and temperature T , which is expressed by the following equation [259]:

$$\Sigma_{\text{air}}(E, h, p, T) = N_{\text{N}} \cdot \sigma_{\text{N}}(E) + N_{\text{O}} \cdot \sigma_{\text{O}}(E) + N_{\text{Ar}} \cdot \sigma_{\text{Ar}}(E) + N_{\text{H2O}} \cdot \sigma_{\text{H2O}}(E) \tag{B.1}$$

Calculation of Water Content in Air

One method to calculate the saturation vapor pressure of water in air is by using the Tetens equation [260], given as:

$$p_{sv,\,T}(T) = 0.61078 \times \exp\left(\frac{17.27 \times T}{T + 237.3}\right) , \tag{B.2}$$

where T is the temperature in degrees Celsius. More contemporary models employ a modified version of the Tetens equation, as provided in [261]:

$$p_{sv}(T) = \exp\left(1.2348847 \times 10^{-5} \times T^2 - 0.019121316 \times T + 33.93711047 + \frac{-6343.1645}{T}\right), \tag{B.3}$$

which enhances the accuracy across a broader range of temperatures. Using this expression for the saturation vapor pressure, the water content in air as a function of pressure p, temperature T, and relative humidity h can be calculated as:

$$wc(h, p, T) = h \cdot \frac{p_{sv}(T)}{p} . \tag{B.4}$$

ISO Standard 8529 Cross Check

According to ISO Standard 8529, Part 2 [262], the significant contributions to air attenuation are due to scattering from oxygen and nitrogen. The air-attenuation factor for a temperature of 21 °C, a pressure of 100.4 kPa, and 50% relative humidity is given by [259]:

$$F_A(l, \Sigma(E)) = \exp(\Sigma(E) \cdot l) = \exp\left([3.88 \cdot \sigma_{\mathrm{N}}(E) + 1.04 \cdot \sigma_{\mathrm{O}}(E)] \cdot 10^{-5} \cdot l\right), \tag{B.5}$$

where l is the path length and $\Sigma(E)$ is the macroscopic cross section. Figure B.1 shows a comparison of this equation with the model presented above. The two approaches demonstrate overall good agreement.

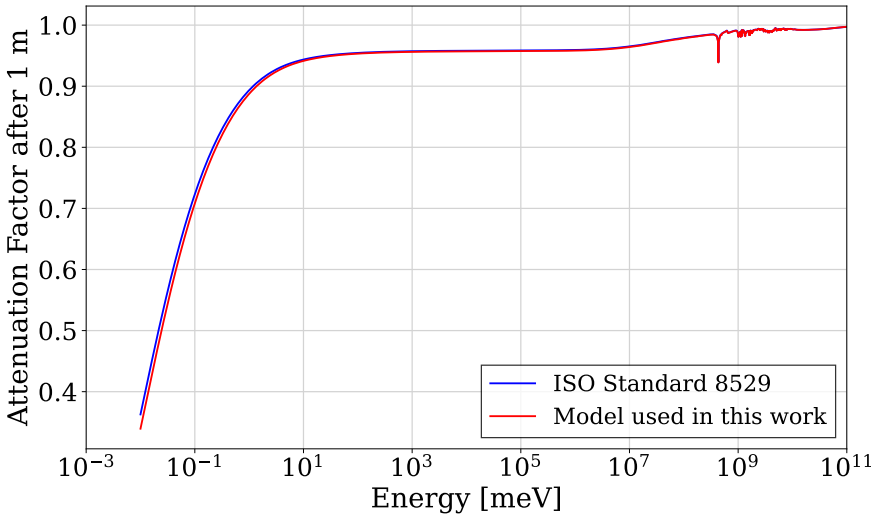

Figure B.1.: Comparison of the air-attenuation factor after 1 m, as calculated using ISO Standard 8529 (Equation B.5) and the model employed in this work using Equation B.1. The figure demonstrates the overall good agreement between the two approaches.

C. Accounting for Non-Negligible Chopper Opening Times Using Wiener Deconvolution

In neutron experiments in a time-of-flight setup that employ choppers, achieving a balance between neutron flux and resolution while avoiding frame overlaps is crucial. This balance involves optimizing the chopper's duty cycle – the fraction of time the chopper is open versus closed. Extending the chopper's opening time can increase neutron flux, but this comes at the cost of reduced wavelength resolution, as neutrons of the same wavelength arrive over a range of times, leading to feature broadening and degradation of the measured spectra. With a well-defined chopper opening function $T(t)$, Wiener deconvolution can be employed to recover the true spectra [263]. This technique is particularly effective for data corrupted by Gaussian noise and has been successfully applied in neutron transmission experiments to resolve overlapping pulses [216].

The spectrum measured at a detector in a time-of-flight setup, $y(t)$, can be represented as a convolution of the "true" spectrum $x(t)$ with the chopper opening function $T(t)$ [3], with the addition of some noise $n(t)$:

$$y(t) = x(t) * T(t) + n(t), . \tag{C.6}$$

A direct application of Wiener deconvolution is complicated by the presence of Poisson noise in $x(t)$, as the technique is designed for Gaussian-distributed signals. To address this, an Anscombe transformation can be applied, converting the Poisson-distributed variable into one with an approximately Gaussian distribution with unity variance [264]. This transformation allows for proper noise suppression before applying Wiener deconvolution, as described in [265]. Assuming that the noise suppression does not alter the chopper opening function, equation C.6 can be rewritten as:

$$\hat{y}(t) = x'(t) * T(t) + n'(t), \tag{C.7}$$

where $x\prime(t)$ represents the noise-suppressed true spectrum, and $n\prime(t)$ accounts for any remaining Gaussian noise. The Wiener deconvolution can then be applied to retrieve $x'(t)$:

$$\hat{x}(t) = \mathscr{F}^{-1}\left\{\frac{\mathscr{F}\{\hat{y}(t)\}\mathscr{F}\{T(t)\}}{|\mathscr{F}\{T(t)\}|^2 + c}\right\}, \tag{C.8}$$

where $\mathscr{F}$ denotes the Fourier transform, $\mathscr{F}^{-1}$ the inverse Fourier transform, and c is the Wiener coefficient, defined as [263]:

$$c = \frac{N'(f)}{X'(f)} = \frac{1}{\mathrm{SNR}}, \tag{C.9}$$

where $X'(f)$ is the mean spectral power density of the signal, $N'(f)$ is the mean spectral power density of the noise, and SNR is the signal-to-noise ratio. Without prior knowledge of $n'(t)$, the Wiener coefficient cannot be exactly determined, so a fixed Wiener coefficient was used, as established in previous work [216]. Although this approach may overestimate the contribution of high-frequency components, it prevents oscillatory artifacts caused by dominant single frequencies when using an inexact value of c. A value of $c = 0.01$ proved to be versatile, as it is low enough to allow the observation of closely spaced peaks without introducing artifacts.

[3] Generally, this can be any resolution function, but as described in Section 6.1, in slow neutron transmission experiments the resolution function is dominated by the chopper opening function.

D. Determination of the Chopper Offset

The data acquired during the VCN transmission experiment, are neutron events at a measured time-of-flight $\tilde{\tau}$. These times $\tilde{\tau}$ are measured with respect to a trigger signal which is given by a magnet mounted on the chopper disk that induces a current in a coil placed on the stator every time it passes. Since this magnet is not aligned perfectly with the center of the chopper window, there is a time offset $t_{\mathbf{offset}}$ between the measured time-of-flight $\tilde{\tau}$ and the actual time-of-flight τ, such that

$$\tau = \tilde{\tau} + t_{\text{offset}} \; . \tag{D.10}$$

This offset can be estimated by comparing two time-of-flight spectra $R_1(\tilde{\tau}_1)$ and $R_2(\tilde{\tau}_2)$ with two different flight paths D_1 and D_2, where $D_1 < D_2$. Since these two spectra correspond to the same wavelength spectrum $R(\lambda)$, the time offset can be determined by finding a $t_{\mathbf{offset}}$ that, when added to $\tilde{\tau}$, minimizes the discrepancy between the estimates of $R(\lambda)$. This way to estimate the timing offset was introduced in [266] for a UCN chopper. The method was adapted here. Since D_1 and D_2 are different an additional parameter α was introduced to account for the $\tilde{\tau}$ dependent attenuation of the beam. One can think of the parameter α as the macroscopic cross section of air attenuating the beam on the longer flight path. If we consider that both spectra $R_1(\tilde{\tau}_1)$ and $R_2(\tilde{\tau}_2)$ are attenuated according to their respective flight path such that:

$$R_i(\tau) = R_0(\tau) \exp\left(-\alpha \tau D_i\right), \tag{D.11}$$

we can relate $R_1(\tau)$ and $R_2(\tau)$ by

$$R_2(\tau) = R_1(\tau) \exp\left(-\alpha \tau (D_1 - D_2)\right). \tag{D.12}$$

After the subtraction of background we can add t_{offset} as well as an attenuation factor $\exp\left(-\alpha\tau(D_1 - D_2)\right)$, so that

$$R_1(\tau) = R_1(\tilde{\tau} + t_{\text{offset}}) \exp\left(-\alpha \tau (D_1 - D_2)\right) \; , \tag{D.13}$$

and

$$R_2(\tau) = R_2(\tilde{\tau} + t_{\text{offset}}) \; . \tag{D.14}$$

Using equation 6.11 we can now transform $R_1(\tau)$ and $R_2(\tau)$. After making sure $R_1(\lambda)$ and $R_2(\lambda)$ have the same binning one can calculate the quantity

$$\chi^2(t, \alpha) = \frac{(R_1(\lambda) - R_2(\lambda))^2}{\sqrt{\delta R_1^2 + \delta R_2^2}} \; . \tag{D.15}$$

That is, $\chi^2(t, \alpha)$ represents the total sum of squared deviations in each bin, taking into account the estimated uncertainties. This quantity can be minimized using standard numerical recipes for an initial guess of t_0 and α_0 to find the optimum values for t_{offset} and α in an iterative process. For the following results the L-BFGS-B-algorithm [267] implemented in scipy [268] was used. Figure D.3 shows the result of this iterative procedure for a range of $t = [-6, 6]$ms. The resulting timing offset t_{offset} of 1.45 ± 0.34 ms for a chopper speed of 900 rpm is indicated by the red dashed line. The parameter α resulted in $\alpha = 34.0 \pm 1$. The uncertainty was estimated by using the inverse Hessian matrix (H^{-1}). This is a square matrix of second-order partial derivatives of the objective function with respect to the optimization parameters ($H_{ij} = \frac{\partial f}{\partial x_i \partial x_j} = \frac{\partial \chi^2}{\partial t \partial \alpha}$) and can be obtained from the optimization.

We repeated that procedure for a chopper speed of 600 rpm, where the timing offset t_{offset} results in 2.14 ± 0.27 ms and $\alpha = 33.9 \pm 1$. The increasing timing offset for slower chopper speed indicates a geometrical displacement of the trigger signal. Figure D.2b shows a comparison of the time-of-flight spectra for two different flight paths $D_1 = 0.969$ m and $D_2 = 2.087$ m transformed to the wavelength domain with and without attenuation and timing offset. The spectra, particularly the maxima align reasonably well indicating reliable procedure. The resulting spectrum that is used to measure and compute the total cross section is shown in Figure 6.23.

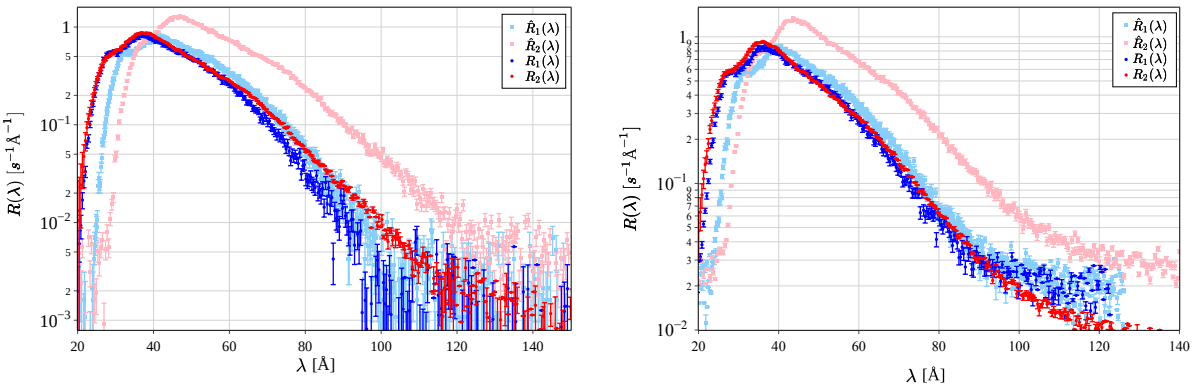

(a) Chopper speed 600 rpm.

(b) Chopper speed 900 rpm.

Figure D.2.: Comparison of the time-of-flight spectra for two different flight paths $D_1 = 0.969\,\mathrm{m}$ and $D_2 = 2.087\,\mathrm{m}$ transformed to the wavelength domain. $\hat{R}_1(\lambda)$ (light blue) and $\hat{R}_2(\lambda)$ (light pink) show the transformed spectra without a timing offset and attenuation. $R_1(\lambda)$ (blue) and $R_2(\lambda)$ (red) show the same datasets transformed with a timing offset and attenuation. See text for details.

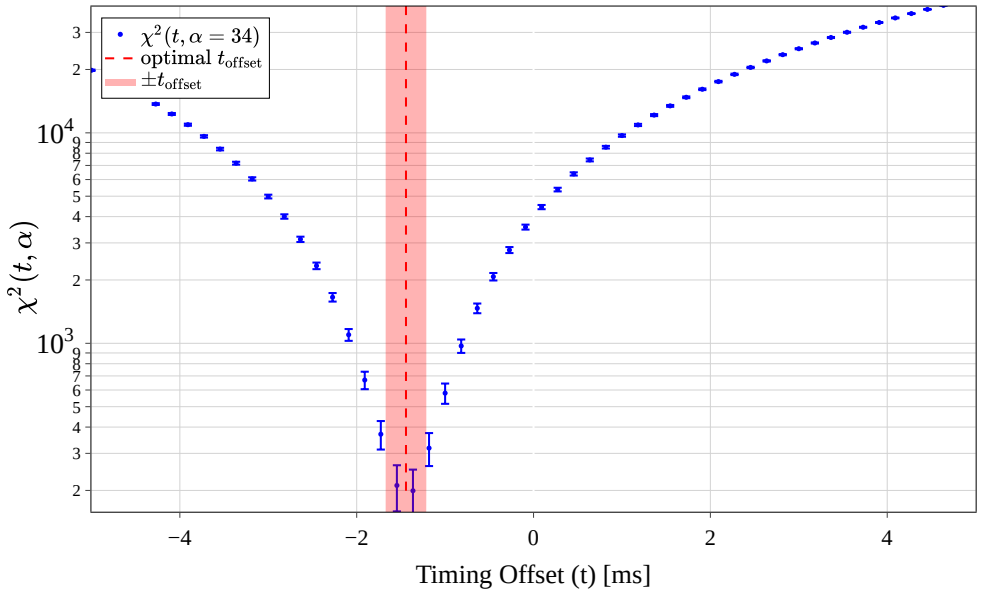

Figure D.3.: Calculated grid of trial offsets for a constant parameter $\alpha = 34$ at a chopper speed of 900 rpm. The minimum of the optimization at $t_{\mathrm{offset}} = 1.45\,\mathrm{ms}$ is indicated by the red dashed line, with the uncertainty of $\pm 0.34\,\mathrm{ms}$ shaded in light pink.

E. Derivation of the SANS Cross Section Using the Guinier Approximation

The differential cross section due to small-angle-scattering (SANS) in the Guinier approximation is given by

$$\frac{\mathrm{d}\sigma_{\mathrm{Guinier}}}{\mathrm{d}\Omega}(q) = C \exp\left(-\frac{q^2 R_{\mathrm{g}}^2}{3}\right). \tag{E.16}$$

The SANS cross section due to Guinier scattering can be calculated by integrating Equation E.16 over q and the solid angle [269]:

$$\sigma_{\mathrm{Guinier}}(\lambda) = \int_0^{2\pi} d\phi \int_0^{\pi} C \exp\left(-\frac{q^2 R_g^2}{3}\right) \sin(\theta)\, d\theta \tag{E.17}$$

$$= \frac{C\lambda^2}{2\pi} \int_0^{q_{\max}} q \exp\left(-\frac{1}{3} q^2 R_g^2\right) dq\,. \tag{E.18}$$

This integral can be solved analytically and results in:

$$\frac{3C\lambda^2}{4\pi R_g^2}\left[1 - \exp\left(-\frac{1}{3} q_{\max}^2 R_g^2\right)\right], \tag{E.19}$$

with $q_{\max} = \frac{4\pi}{\lambda}\sin(\theta_{\max/2})$, where $\theta_{\max} = 180^\circ$. As the transmission setups discussed in this thesis count neutrons scattered at small angles up to $\theta_{\min/2} \sim 2^\circ$, corresponding to $q_{\min} \sim \frac{4\pi}{\lambda}\sin(\theta_{\min})$, the experimental constraints adjust Equation E.18 to:

$$\sigma_{\mathrm{Guinier}}(\lambda) = \frac{C\lambda^2}{2\pi} \int_{q_{\min}}^{q_{\max}} q \exp\left(-\frac{1}{3} q^2 R_g^2\right) dq\,. \tag{E.20}$$

Solving this integral and using the relation $q = \frac{4\pi}{\lambda}\sin(\frac{\theta}{2})$ results in the expression used to fit the SANS contribution to the total cross section:

$$\sigma_{\mathrm{Guinier}}(\lambda) = \frac{3C\lambda^2}{4\pi R_g^2}\left[\exp\left(-\frac{4\pi^2 R_g^2}{3\lambda^2}\sin^2\left(\frac{\theta_{\min}}{2}\right)\right) - \exp\left(-\frac{4\pi^2 R_g^2}{3\lambda^2}\sin^2\left(\frac{\theta_{\max}}{2}\right)\right)\right]. \tag{E.21}$$

F. Chopper Characterization

Detailed knowledge of the chopper gating function, its timing offset, and the overall shape of its gating function is crucial for designing time-of-flight measurements and evaluating time-of-flight data. In this appendix, two convenient methods to characterize these quantities will be presented: (a) during an experiment and (b) in an independent characterization campaign.

F.1. Evaluation of the Chopper Gating Function with γ-Radiation of a Gd Coated Disk

The method presented here is an elegant way to measure both the timing offset of a disk chopper[4] and the width of its gating function. The prerequisite is having a neutron detector in the vicinity downstream of the disk chopper, which is sensitive to gamma radiation when the high voltage and threshold are modified.[5] For this experiment, a ^{3}He monitor detector was used. The neutron beam downstream of the chopper can be blocked by boronated rubber or another high-absorbing material.

In this setup, the detector will show an increased count rate when the chopper is in its closed position, as a short-lived component of the neutron capture-activated Gd decays and releases γ-radiation of relatively high energy (see [270]). As soon as the chopper opens, the γ-signal drops because there is no Gd to be activated in the beam. The signal rises again as soon as the window closes and the neutron beam hits the Gd again. This is illustrated in Figure F.4 for the chopper used in Experiment 3-14-323.

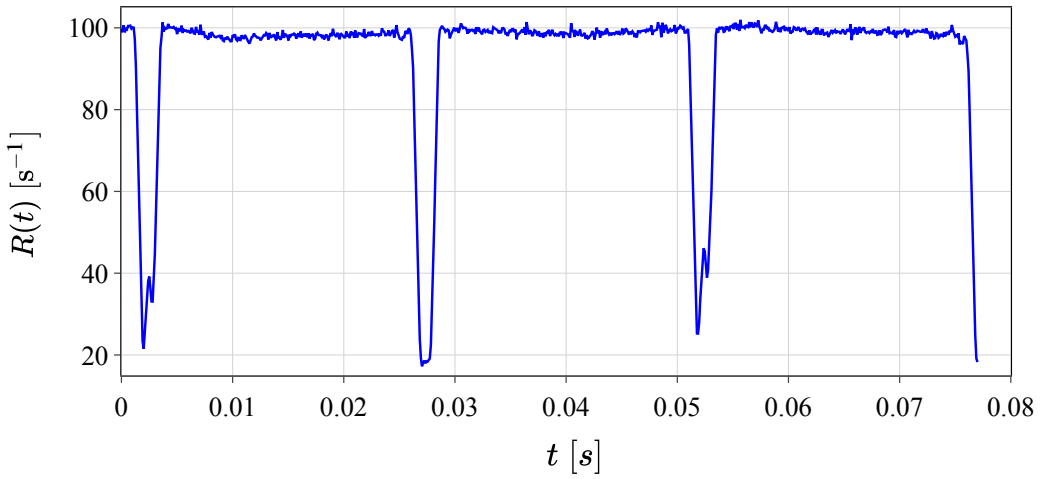

Figure F.4.: Gamma radiation signal recorded by a ^{3}He monitor detector downstream of the disk chopper, illustrating the timing offset and gating function width. The signal increases when the chopper is closed, due to neutron capture-activated Gd emitting gamma radiation, and decreases upon chopper opening. This behavior repeats as the chopper cycles. The detector located about 12 cm downstream of the chopper was operated at a high voltage of 964 V and a threshold of 100 mV.

Figure F.4 already highlights a critical issue with the chopper. It utilizes a single trigger mechanism for four openings, two of which were previously sealed with boron rubber. These

[4] This method has not been demonstrated for different chopping techniques. Based on the geometry, it might work similarly.

[5] It is recommended to only slightly increase the high voltage and lower the threshold until the detector noise starts to be visible.

sealed openings not only contribute to the observed gamma signal (first and third dip in Figure F.4) but also result in neutron leakage. Consequently, the chopper had to operate at half its nominal speed to utilize two spectra per time-of-flight frame effectively, thereby mitigating signal contamination from the sealed windows' neutron leakage.

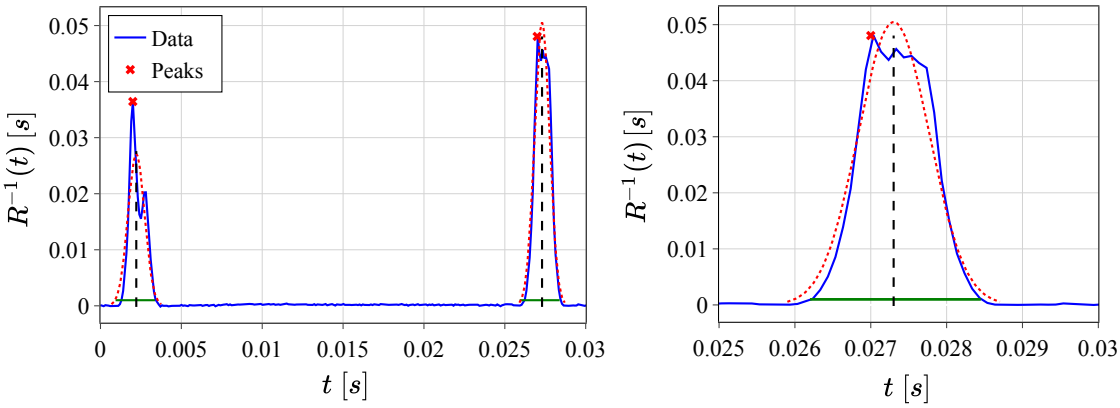

Figure F.5.: Inverted γ-signal from the ^{3}He monitor detector downstream of the chopper used in Experiment 3-14-323. The left plot shows half of the inverted signal with a Gaussian fit applied to the trapezoidal peaks. The right plot zooms in on the second peak, corresponding to the second opening of the chopper. The opening function of the first opening is identical. The fit allows the determination of the peak center and width, which are used to evaluate the timing offset and the width of the gating function.

Since the produced photons travel at the speed of light, they reach the detector almost instantaneously compared to the time scales considered here. Therefore, the offset can be determined by evaluating the time t between the start of the counting in channel 0 and the center of the first dip in the γ-signal, which occurs near the end of the time-of-flight frame (see Figure F.4). To analyze the peak shape, position, and width, it is beneficial to invert the signal. Figure F.5 displays the first half of the inverted signal with a Gaussian fit to the trapezoidal peaks, facilitating a simple determination of the peak center and width. While the last peak, corresponding to the first opening for the time-of-flight spectrum, is cut-off, the second identical opening can be analyzed to evaluate the width in t.

The timing offset (t_{offset}) in this particular case is the width between the rising edge of the last peak, which is still visible in the time-of-flight frame, and its center, which corresponds to the center of the opening function. The peak analysis of the second peak corresponding to the second opening of the chopper gives a width of (2.249 ± 0.040) ms. However, due to another design peculiarity, this does not correspond to the opening time for neutrons of (1.207 ± 0.031) ms determined from the chopper geometry and given in Table 6.1. This discrepancy arises because the neutron slit is defined by boronated rubber rather than the stadium shaped Gd-paint around it (see Figure F.6). Consequently, the timing offset is $t_{\text{offset1}} = (0.350 \pm 0.014)$ ms for the first opening and $t_{\text{offset2}} = (-27.301 \pm 0.043)$ ms for the second opening of the chopper.

F.2. Evaluation of the Chopper Gating Function with a Laser Optical Setup

A laser optical setup to characterize the chopper opening function and timing offset in an independent characterization is depicted in Figure F.7. The setup includes a 635 nm and 2.5 mW laser, paired with a set of lenses and a mirror to illuminate the chopper window. The final component is a lens with a focal length of 150 mm, which refocuses the beam onto a photodiode connected to an oscilloscope for measurement. Note that it is crucial to widen the laser beam

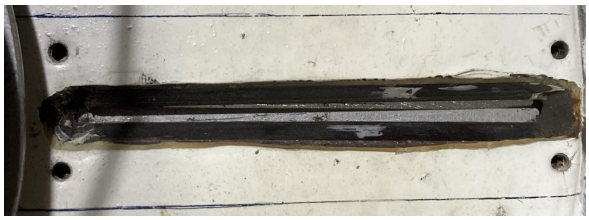

Figure F.6.: One of the open slits of the chopper used for experiment 3-14-323. The slit defining the opening time for neutron is constituted by the black boron rubber and has a width of 3.073 mm. The slit defining the shape of the γ-signal is the stadium shaped slit of Gd paint in white.

sufficiently during such a measurement so that the entire chopper window is illuminated. By connecting the chopper trigger to the same oscilloscope, the timing offset and shape of the transmission function can be evaluated by spinning the chopper at the desired angular frequency.

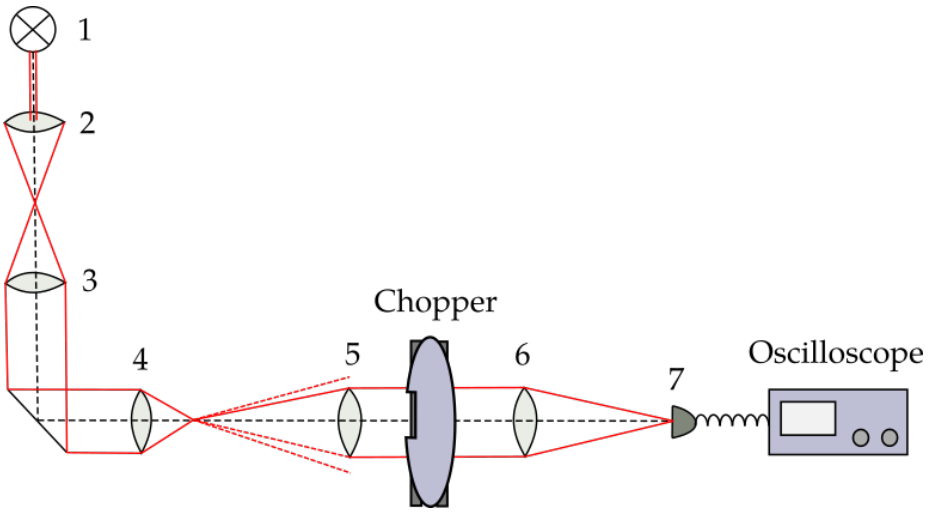

Figure F.7.: Laser setup used to characterize the gating function of the disk chopper at PF2/VCN (not to scale). A similar setup was used previously to measure the properties of different VCN and UCN choppers [271]. The setup consists of a 635 nm and 2.5 mW laser (1), a $f = 20$ mm lens (2), followed by a $f = 200$ mm lens (3) to widen the beam, a mirror, two more lenses $f = 20$ mm (4) and $f = 150$ mm (5) to illuminate the entire chopper window, and a final lens with $f = 150$ mm (6) to refocus the light on a photodiode (7) connected to an oscilloscope.

Figure F.8 shows the gating function of the laser (blue) with the chopper trigger (red) as measured on the oscilloscope in the setup depicted in Figure F.7 with a chopper frequency of 5.83 Hz. The timing offset is determined from the difference between the rising edge of the trigger and the center of the trapezoid of the chopper opening function. This results in an offset of $t_{\text{offset}} = (-3.05 \pm 0.09)$ ms. The chopper opening time is given by the width of the trapezoidal opening function and results in 8.7 ms.

An important caveat of this method is that the measured timing offset does not include possible delays in the neutron data acquisition. However, it provides valuable information about the gating function, which can be more complex than a simple trapezoid or triangle, particularly if the chopping technique employs something other than rotating discs.

The characterization of chopper gating functions and timing offsets is essential for accurate time-of-flight measurements. The methods described in this appendix—using γ-radiation from

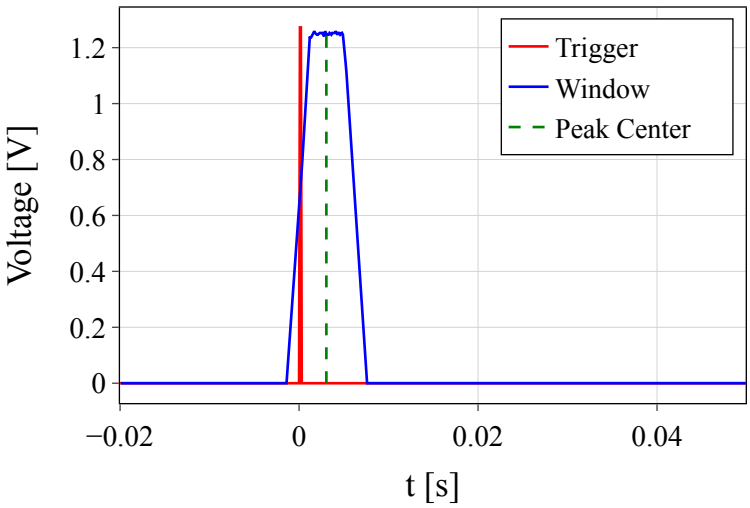

Figure F.8.: Chopper gating function measured with the laser setup depicted in Figure F.7. The laser signal is plotted in blue, and the trigger signal in red. The chopper spun at a frequency of 5.83 Hz. The timing offset (t_{offset}) is determined by the difference between the rising edge of the trigger and the center of the trapezoidal chopper opening function. The measured timing offset is $t_{\text{offset}} = (-3.05 \pm 0.09)$ ms, and the chopper opening time is (8.70 ± 0.05) ms.

a Gd-coated disk and a laser optical setup—provide reliable means to assess these parameters. Future experiments may benefit from these characterization methods, allowing for improvements in chopper design and time-of-flight parameters beforehand or characterization of unknown chopper parameters during an ongoing experiment.

G. Preparation of THF Hydrates

This appendix provides detailed instructions for preparing clathrate mixture samples containing protonated and deuterated versions of water (H_2O, D_2O) and tetrahydrofuran (THF, THF – d). The steps include the preparation of solutions, mixing ratios, and the necessary conditions to achieve the desired outcomes.

Materials and Equipment

- Protonated Water (H_2O)
- Deuterated Water (D_2O)
- Protonated Tetrahydrofuran (THF)
- Deuterated Tetrahydrofuran (THF – d)
- Balance (precision $\pm$ 1 mg)
- Volumetric flasks
- Magnetic Stirrer
- Temperature-controlled environment
- Fume hood for handling THF and THF – d
- Personal protective equipment (gloves, goggles, lab coat)

Preparation of the Stoichiometric Solution

We established in preliminary experiments that, during the typical duration of recipient opening required for precise pipetting (on the order of minutes), the evaporation of water can be neglected, whereas the evaporation of THF is significant and can be accurately monitored using a precision balance. It is noteworthy, that no change in weight was observed after closing the recipient with a screw-cap internally coated with Teflon. As a result, by initially adding slightly more THF than required for a stoichiometric mixture, it is possible to allow excess THF to evaporate until the exact stoichiometric amount is achieved.

The procedure to prepare the stoichiometric solution was as follows:

1. Place a Teflon-coated magnetic stirrer bar in an empty, clean glass recipient.[6] Determine the mass of the recipient with the stirrer bar and cap using a precision balance. Although this initial mass measurement is not critical since the balance will be tared afterward, it serves as a precautionary measure in case of balance malfunction, which did not occur during our preparations.
2. Pipette a mass A (typically between 0.5 g and 1 g) of water into the recipient. This mass A determines the required mass B of THF to achieve a stoichiometric mixture:

$$B = \frac{A}{\text{mass ratio}} \tag{G.22}$$

   with the corresponding mass ratios given in Table G.2. Slightly more than B mass of THF should be added to the water (see step 5 for further explanation).
3. Close the recipient with its cap to prevent evaporation and stir with the magnetic stirrer for 10 minutes.

[6] The volume depends on the amount of material to be prepared. Typically, 4 mL recipients were used.

4. Open the recipient and monitor the evaporation. At a typical laboratory temperature of 21 °C, the observed evaporation rate is approximately 3 mg per 5 minutes, in a 18 ml vial. The additional THF added in step 2 compensates for the expected evaporation. This rate can serve as a guideline, but actual evaporation should be monitored during each preparation.
5. Close the recipient when approximately 2 minutes (or an appropriate duration for accurate pipetting) remain to reach the stoichiometric mass ratio.
6. Transfer the desired mass to the sample holder. This step requires precision to avoid exceeding the target mass. Close the sample holder only after the specified time has elapsed. Any minor errors in pipetting do not affect the stoichiometry but result in a slightly larger or smaller sample mass, which can be accurately determined.

Volume and Mass Ratios

In order to calculate the mass ratio required in EquationG.22 for stoichiometry of 17 parts water to one part tetrahydrofuran one needs to calculate the mass ratios of water to THF in all different protonated and deuterated combination starting with the masses of the nuclear and molecular species:

- **Hydrogen (H):** 1.008 u
- **Deuterium (D):** 2.0141 u
- **Oxygen (O):** 15.999 u
- **Carbon (C):** 12.011 u

The resulting masses and densities of the molecular species are given in Table G.1 along with the densities at room temperature.

Table G.1.: Densities and masses of molecular species.

Molecule	**Molar Mass** (g/mol)	**Density** (g/mL) **at** 25 °C
H_2O	18.015	0.997
D_2O	20.027	1.107
THF	72.106	0.889
THF-d	80.156	0.985

Considering the stoichiometry of 17:1 of water to tetrahydrofuran, the mass and volume ratios for different combinations of THF, THF-d, H_2O, and D_2O are listed in Table G.2.

Table G.2.: Mass ratios, volume ratios, and mass calculations for different solutions of THF and water.

Sample	Mass Ratio	Volume Ratio
$17\,H_2O \cdot THF$	4.2472	3.7810
$17\,D_2O \cdot THF$	4.7217	3.7859
$17\,H_2O \cdot THF-d$	3.8207	3.7571
$17\,D_2O \cdot THF-d$	4.2475	3.7794

Safety Protocol

- THF and THF−d are highly flammable and possibly carcinogenic (classified as Group 2B by IARC). They should be handled under a fume hood to avoid inhalation of vapors.
- Personal protective equipment (gloves, goggles, lab coat) needs to be used when handling chemicals.
- Deuterated samples must be disposed of safely in special containers after usage in a neutron scattering experiment due to the production of tritium from neutron capture.
- Refer to the corresponding Safety Data Sheets (SDS) for detailed information on handling, storage, and emergency measures.

List of Abbreviations and Acronyms

BNC	Budapest Neutron Center
BOA	Beamline for neutron Optics and other Approaches
CDR	Conceptual Design Report
CH	Clathrate Hydrate
CMTF	Cold Moderator Test Facility
CN	Cold Neutrons
D20	High Intensity Two-Axis Diffractometer
DFT	Density Functional Theory
DOS	Density of States (vibrational)
EPP	Elastic Peak Position
ESS	European Spallation Source
FOM	Figure of Merit
HighNESS	High Intensity Neutron Source at the European Spallation Source
HWHM	Half-Width at Half Maximum
ILL	Institut Laue-Langevin
IN1-Lagrange	Indirect Geometry Spectrometer at ILL
IN16B	High-Resolution Backscattering Spectrometer at ILL
IN5	Direct Geometry Time-of-Flight Spectrometer at ILL
JCNS	Jülich Centre for Neutron Science
LD_2	Liquid Deuterium
LD-PE	Low Density Polyethylene
MC	Monte Carlo
MCNP	Monte Carlo N Particle
MD	Molecular Dynamics
NMR	Nuclear Magnetic Resonance
NNBAR	Neutron-Antineutron Oscillation Experiment

NSE	Neutron Spin Echo
PCC	Pearson Correlation Coefficient
PF1B	Cold Neutron Beamline at ILL
PF2	Ultracold Neutron Beamline at ILL
PHITS	Particle and Heavy Ion Transport code System
PSD	Position Sensitive Detector
PSI	Paul Scherrer Institut
ROI	Region of Interest
SD_2	Solid Deuterium
SAM	Small-Angle Modular Instrument
SANS	Small Angle Neutron Scattering
SDS	Safety Data Sheet
THF	Tetrahydrofuran
THF-d	Deuterated Tetrahydrofuran
ToF	Time-of-Flight
UCN	Ultra Cold Neutrons
VCN	Very Cold Neutrons
VDOS	Vibrational Density of States
WNRSE	Weighted Normalized Root Square Error
WSE	Weighted Squared Error

List of Figures

List of Tables

Bibliography

[1] J. Chadwick: *The existence of a neutron*, Proceedings of the Royal Society of London. Series A, Containing papers of a mathematical and physical character 136, no. 830, pp. 692–708, 1932, ISSN 0950-1207.

[2] J. Chadwick: *Possible existence of a neutron*, Nature (London) 129, no. 3252, pp. 312–312, 1932, ISSN 0028-0836.

[3] E. Rutherford: *Bakerian lecture: Nuclear constitution of atoms*, Proceedings of the Royal Society of London. Series A, Containing papers of a mathematical and physical character 97, no. 686, pp. 374–400, 1920, ISSN 0950-1207.

[4] E. Fermi: *Tentativo di una teoria dei raggi β*, Nuovo cimento 11, no. 1, pp. 1–19, 1934, ISSN 0029-6341.

[5] E. Fermi: *Versuch einer Theorie der β-Strahlen I*, Zeitschrift für Physik 88, pp. 161–177, 1934.

[6] D. Dubbers and M. G. Schmidt: *The neutron and its role in cosmology and particle physics*, Reviews of Modern Physics 83, no. 4, pp. 1111–1171, 2011, doi:10.1103/revmodphys.83.1111.

[7] J. Baumann, R. Gähler, J. Kalus and W. Mampe: *Experimental limit for the charge of the free neutron*, Physical Review D 37, no. 11, pp. 3107–3112, 1988, doi:10.1103/PhysRevD.37.3107.

[8] F. M. Piegsa: *Novel concept for a neutron electric charge measurement using a Talbot-Lau interferometer at a pulsed source*, Physical Review C 98, no. 4, p. 045503, 2018, doi:10.1103/PhysRevC.98.045503.

[9] R. L. Workman et al.: *Review of particle physics*, PTEP 2022, p. 083C01, 2022, doi:10.1093/ptep/ptac097.

[10] M. Åberg, N. Ahlfors, R. Ainsworth, C. Alba-Simionesco, S. Alimov, N. Aliouane, B. Alling et al.: *ESS Technical Design Report*, Tech. rep., European Spallation Source, 2013.

[11] F. Mezei: *Very cold neutrons in condensed matter research*, Journal of Neutron Research 24, no. 2, pp. 205–210, 2022, ISSN 14772655, 10238166, doi:10.3233/JNR-220012.

[12] V. Santoro, O. A. E. Kheir, D. Acharya, M. Akhyani, K. H. Andersen, J. Barrow, P. Bentley et al.: *HighNESS conceptual design report*, 2023.

[13] F. M. Piegsa: *New concept for a neutron electric dipole moment search using a pulsed beam*, Physical Review C 88, no. 4, p. 045502, 2013, doi:10.1103/PhysRevC.88.045502.

[14] H. Abele et al.: *Particle physics at the European Spallation Source*, Physics Reports 1023, pp. 1–84, 2023, doi:10.1016/j.physrep.2023.06.001.

[15] F. M. Piegsa and G. Pignol: *Limits on the axial coupling constant of new light bosons*, Physical Review Letters 108, no. 18, p. 181801, 2012, ISSN 0031-9007, 1079-7114, doi: 10.1103/PhysRevLett.108.181801.

[16] J. S. Nico, M. S. Dewey, D. M. Gilliam, F. E. Wietfeldt, X. Fei, W. M. Snow, G. L. Greene et al.: *Measurement of the neutron lifetime by counting trapped protons in a cold neutron beam*, Physical Review C 71, no. 5, p. 055502, 2005, doi:10.1103/PhysRevC.71.055502.

[17] A. T. Yue, M. S. Dewey, D. M. Gilliam, G. L. Greene, A. B. Laptev, J. S. Nico, W. M. Snow and F. E. Wietfeldt: *Improved determination of the neutron lifetime*, Physical Review Lett. 111, no. 22, p. 222501, 2013, doi:10.1103/PhysRevLett.111.222501.

[18] S. Paul: *The puzzle of neutron lifetime*, Nuclear Instruments and Methods in Physics Research Section A: Accelerators, Spectrometers, Detectors and Associated Equipment 611, no. 2-3, pp. 157–166, 2009, doi:10.1016/j.nima.2009.07.095.

[19] A. Addazi and e. al.: *New high-sensitivity searches for neutrons converting into antineutrons and/or sterile neutrons at the HIBEAM/NNBAR experiment at the European Spallation Source*, Journal of Physics G: Nuclear and Particle Physics 48, no. 7, p. 070501, 2021, doi:10.1088/1361-6471/abf429.

[20] F. Backman and e. al.: *The development of the NNBAR experiment*, Journal of Instrumentation 17, no. 10, p. P10046, 2022, doi:10.1088/1748-0221/17/10/P10046.

[21] V. Nesvizhevsky: *Why very cold neutrons could be useful for neutron-antineutron oscillation searches*, Journal of Neutron Research 2022, doi:10.3233/JNR-220003.

[22] K. Eder, M. Gruber, A. Zeilinger, R. Gähler, W. Mampe and W. Drexel: *The new very-cold-neutron optics facility at ILL*, Nuclear Instruments and Methods in Physics Research Section A: Accelerators, Spectrometers, Detectors and Associated Equipment 284, no. 1, pp. 171–175, 1989, ISSN 0168-9002, doi:10.1016/0168-9002(89)90273-8.

[23] H. Rauch and S. A. Werner: *Neutron Interferometry : Lessons in Experimental Quantum Mechanics, Wave-Particle Duality, and Entanglement*, Oxford University Press, Oxford, 2 ed., 2015, ISBN 978-0-19-178081-3.

[24] R. Colella, A. W. Overhauser and S. A. Werner: *Observation of gravitationally induced quantum interference*, Physical Review Letters 34, no. 23, pp. 1472–1474, 1975, doi:10.1103/PhysRevLett.34.1472.

[25] G. van der Zouw, M. Weber, J. Felber, R. Gähler, P. Geltenbort and A. Zeilinger: *Aharonov–Bohm and gravity experiments with the very-cold-neutron interferometer*, Nuclear Instruments and Methods in Physics Research Section A 440, no. 3, pp. 568–574, 2000, ISSN 0168-9002, doi:10.1016/S0168-9002(99)01038-4.

[26] J. Klepp, C. Pruner, Y. Tomita, C. Plonka-Spehr, P. Geltenbort, S. Ivanov, G. Manzin et al.: *Diffraction of slow neutrons by holographic SiO_2 nanoparticle-polymer composite gratings*, Physical Review A 84, no. 1, p. 013621, 2011, doi:10.1103/PhysRevA.84.013621.

[27] A. G. Klein and A. Zeilinger: *Wave optics with cold neutrons*, Journal de Physique Colloques 45, no. C3, pp. C3–239–C3–242, 1984, ISSN 0449-1947.

[28] R. Golub and J. Pendlebury: *Super-thermal sources of ultra-cold neutrons*, Physics Letters A 53, no. 2, pp. 133–135, 1975, ISSN 0375-9601, doi:10.1016/0375-9601(75)90500-9.

[29] S. Degenkolb, P. Fierlinger and O. Zimmer: *Approaches to high-density storage experiments with in-situ production and detection of ultracold neutrons*, Journal of Neutron Research 24, no. 2, pp. 123–143, 2023, ISSN 14772655, 10238166, doi:10.3233/JNR-220044.

[30] J.-L. Béchade, M. H. Mathon and Y. de Carlan: *Neutron analyses for nuclear materials: Texture, residual stresses and small angle scattering*, EPJ Web of Conferences 104, 2015, doi:10.1051/epjconf/201510401008.

[31] J. M. Carpenter and B. J. Micklich: *Proceedings of the workshop on applications of a very cold neutron source*, in *Proceedings of the Workshop on Applications of a Very Cold Neutron Source*, 2005.

[32] T. Jenke, H. Filter and T. Brenner: *PF2: Ultracold neutron facility*, accessed: 2024-06-17.

[33] V. Santoro, K. H. Andersen, M. Bernasconi, M. Bertelsen, Y. Bessler, D. Campi, V. Czamler et al.: *Development of a high intensity neutron source at the european spallation source: The highness project*, 2022.

[34] L. Zanini, E. Dian, D. DiJulio, B. Folsom, E. Klinkby, Z. Kokai, J. Marquez Damian et al.: *Very cold and ultra cold neutron sources for ESS*, Journal of Neutron Research 24, no. 2, pp. 77–93, 2022, doi:10.3233/JNR-220040.

[35] V. Santoro, K. H. Andersen, P. Bentley, M. Bernasconi, M. Bertelsen, Y. Bessler, A. Bianchi et al.: *The HighNESS project at the european spallation source: Current status and future perspectives*, Nuclear Science and Engineering 198, no. 1, pp. 31–63, 2024, doi:10.1080/00295639.2023.2204184.

[36] European Spallation Source: *European spallation source (ESS) official website*, 2024, accessed: 2024-09-02.

[37] V. V. Nesvishevsky, G. Pignol and K. V. Protasov: *Nanoparticles as a possible moderator for an ultracold neutron source*, International Journal of Nanoscience 06, no. 06, pp. 485–499, 2007, doi:10.1142/S0219581X07005073.

[38] R. Nicola, M. D. Jose I., K. Thomas, L. Bent, K. Esbe, E. Quentin and S. Valentina: *Benchmarking of the NCrystal SANS plugin for nanodiamonds*, Nuclear Science and Engineering 198, no. 1, pp. 92–100, 2024, doi:10.1080/00295639.2023.2196926.

[39] J. Granada, D. DiJulio, J. Marquez Damian and G. Muhrer: *A new scattering kernel for superfluid helium at low temperatures*, Nuclear Instruments and Methods in Physics Research Section A: Accelerators, Spectrometers, Detectors and Associated Equipment 1053, p. 168284, 2023, ISSN 0168-9002, doi:10.1016/j.nima.2023.168284.

[40] D. D. DiJulio, J. I. Marquez Damian, T. Kittelmann, S. Xu, J. R. Granada and G. Muhrer: *Advances in nuclear data development for moderator and reflector design at the European Spallation Source*, in *EPJ Web of Conferences*, vol. 298, p. 04002, EDP Sciences, 2024, doi:10.1051/epjconf/202429804002.

[41] S. Xu, S. I. Laporte, D. D. DiJulio, J. I. Marquez Damian, T. Kittelmann, M. Bernasconi, D. Campi, G. Gorini and V. Santoro: *Theoretical calculations of neutron scattering cross sections for tetrahydrofuran-containing clathrate hydrates at low temperature*, EPJ Web of Conferences 286, 2023, doi:10.1051/epjconf/202328606003.

[42] S. Xu, D. D. DiJulio, J. I. M. Damian, T. Kittelmann, M. Bernasconi, D. Campi, O. A. E. Kheir et al.: *Physical model of neutron scattering by clathrate hydrate and C_{60} hosting paramagnetic oxygen molecules*, Journal of Physics: Condensed Matter 36, no. 38, 2024, doi:10.1088/1361-648X/ad5947.

[43] A. T. Boothroyd: *Principles of Neutron Scattering from Condensed Matter*, Oxford University Press, Oxford, first edition ed., 2020, ISBN 978-0-19-886231-4.

[44] W. Demtröder: *Experimentalphysik 3*, Springer-Lehrbuch, Springer Berlin Heidelberg, Berlin, Heidelberg, 2010, ISBN 978-3-642-03910-2 978-3-642-03911-9, doi:10.1007/978-3-642-03911-9.

[45] K. H. Beckurts and K. Wirtz: *Neutron Physics*, Springer Berlin Heidelberg, Berlin, Heidelberg, 1964, ISBN 978-3-642-87616-5 978-3-642-87614-1, doi:10.1007/978-3-642-87614-1.

[46] R. Granada: *Fundamentals of Neutron Interactions with Matter*, 2012, lecture notes.

[47] V. F. Turchin: *Thermal Neutron Scattering*, Sivan Press, Jerusalem, translated from russian ed., 1965.

[48] V. F. Sears: *Neutron Optics: An Introduction to the Theory of Neutron Optical Phenomena and Their Applications*, Oxford University Press, New York, 1989.

[49] M. Peshkin and G. R. Ringo: *On the Repulsion of Slow Neutrons by Attractive Potentials*, American Journal of Physics 39, no. 3, pp. 324–327, 1971, ISSN 0002-9505, 1943-2909, doi:10.1119/1.1986132.

[50] V. F. Sears: *Neutron scattering lengths and cross sections*, Neutron News 3, no. 3, pp. 29–37, 1992.

[51] A. Munter: *Neutron scattering lengths and cross sections*, `https://www.ncnr.nist.gov/resources/n-lengths/`, accessed: 2024-07-28.

[52] G. Squires: *Thermal Neutron Scattering*, Cambridge University Press., 1978.

[53] E. Fermi: *Sul moto dei neutroni nelle sostanze idrogenate*, La Ricerca Scientifica 7, no. 2, pp. 13–52, 1936, english translation: On the motion of neutrons in hydrogenous substances.

[54] International Atomic Energy Agency: *Evaluated nuclear data file (ENDF)*, 2022, database Version of 2022-04-22.

[55] V. Sears: *Slow-neutron multiple scattering*, Advances in Physics 24, no. 1, pp. 1–45, 1975, doi:10.1080/00018737500101361.

[56] N. W. Ashcroft and N. D. Mermin: *Solid State Physics*, Cengage Learning, Boston, MA, 2021, ISBN 978-0357670811.

[57] X.-X. Cai and T. Kittelmann: *NCrystal: A library for thermal neutron transport*, Computer Physics Communications 246, p. 106851, 2020, ISSN 0010-4655, doi:10.1016/j.cpc.2019.07.015.

[58] O. Zimmer: *Neutron conversion and cascaded cooling in paramagnetic systems for a high-flux source of very cold neutrons*, Physical Review C 93, no. 3, p. 035503, 2016, doi:10.1103/PhysRevC.93.035503.

[59] J. J. Duderstadt and L. J. Hamilton: *Nuclear Reactor Physics*, Wiley, New York, 1976, ISBN 0-471-22363-8.

[60] W. M. Stacey: *Nuclear Reactor Physics*, Wiley-VCH, Weinheim, 2., completely revised and enlarged ed. ed., 2007, ISBN 978-3-527-40679-1.

[61] M. Narita and K. Narita: *Average number of collisions necessary for slowing down of neutrons*, Journal of Nuclear Science and Technology 26, no. 9, pp. 819–825, 1989, doi:10.1080/18811248.1989.9734392.

[62] L. Boltzmann: *Lectures on Gas Theory*, University of California Press, Berkeley, CA, USA, 1964.

[63] A. Steyerl: *A "neutron turbine" as an efficient source of ultracold neutrons*, Nuclear Instruments and Methods 125, no. 3, pp. 461–469, 1975, ISSN 0029-554X, doi:10.1016/0029-554X(75)90265-7.

[64] A. Steyerl, H. Nagel, F.-X. Schreiber, K.-A. Steinhauser, R. Gähler, W. Gläser, P. Ageron et al.: *A new source of cold and ultracold neutrons*, Physics Letters A 116, no. 7, pp. 347–352, 1986, ISSN 0375-9601, doi:10.1016/0375-9601(86)90587-6.

[65] P. A. Schmidt-Wellenburg: *Production of Ultracold Neutrons in Superfluid Helium under Pressure*, Ph.D. thesis, Technische Universität München, Fakultät für Physik, Physik Department E18, 2009, accessed: 2024-08-18.

[66] T. Dombeck, J. Lynn, S. Werner, T. Brun, J. Carpenter, V. Krohn and R. Ringo: *Production of ultra-cold neutrons using Doppler-shifted Bragg scattering and an intense pulsed neutron spallation source*, Nuclear Instruments and Methods 165, no. 2, pp. 139–155, 1979, ISSN 0029-554X, doi:10.1016/0029-554X(79)90264-7.

[67] T. Brun, J. Carpenter, V. Krohn, G. Ringo, J. Cronin, T. Dombeck, J. Lynn and S. Werner: *Measurement of ultracold neutrons produced by using Doppler-shifted Bragg reflection at a pulsed-neutron source*, Physics Letters A 75, no. 3, pp. 223–224, 1980, ISSN 0375-9601, doi:10.1016/0375-9601(80)90120-6.

[68] K. K. H. Leung: *Development of a New Superfluid Helium Ultra-Cold Neutron Source and a New Magnetic Trap for Neutron Lifetime Measurements*, Ph.D. thesis, Technische Universität München, Fakultät für Physik, Munich, Germany, 2016.

[69] A. Steyerl: *Ultracold Neutrons*, World Scientific, Singapore, 2020, ISBN 9789811212703.

[70] R. Golub, D. Richardson and S. K. Lamoreaux: *Ultra-Cold Neutrons*, Hilger, Bristol [u.a.], 1991, ISBN 0-7503-0115-5.

[71] M. Boehm, W. Henggeler, P. Allenspach and A. Furrer: *Phase space transformation on ultra cold neutrons*, Journal of Neutron Research 13, pp. 241–250, 2005, doi:10.1080/10238160512331329974, 4.

[72] W. Henggeler: *The phase-space transformer instrument (PASTIS)*, in *Condensed Matter Research with Neutrons and Muons Laboratory for Neutron Scattering*, Paul Scherer Institut, 2003.

[73] R. Golub and K. Böning: *New type of low temperature source of Ultra-cold neutrons and production of continous beams of UCN*, Zeitschrift für Physik B Condensed Matter 51, no. 2, pp. 95–98, 1983, ISSN 1431-584X, doi:10.1007/BF01308763.

[74] B. Lauss: *Ultracold neutron production at the second spallation target of the paul scherrer institute*, Physics Procedia 51, pp. 98–101, 2014, ISSN 1875-3892, doi:10.1016/j.phpro.2013.12.022, eSS Science Symposium on Neutron Particle Physics at Long Pulse Spallation Sources, NPPatLPS 2013.

[75] E. Gutsmiedl, F. Böhle, A. Frei, A. Maier, S. Paul, A. Orecchini and H. Schober: *Production of ultra-cold neutrons in solid α-oxygen*, Europhysics Letters 96, no. 6, p. 62001, 2011, doi:10.1209/0295-5075/96/62001.

[76] C. Y. Liu and A. R. Young: *Ultra-cold neutron production in anti-ferromagnetic oxygen solid*, `https://doi.org/10.48550/arXiv.nucl-th/0406004`, 2004.

[77] D. J. Salvat, E. Gutsmiedl, C.-Y. Liu, P. Geltenbort, A. Orecchini, S. Paul and H. Schober: *Investigating solid α-15N2 as a new source of ultra-cold neutrons*, Europhysics Letters 103, no. 1, p. 12001, 2013, doi:10.1209/0295-5075/103/12001.

[78] N. Metropolis: *The Beginning of the Monte Carlo Method*, Los Alamos Science Special Issue, Vol. 15, pp. 125-130 1987.

[79] R. Eckhardt: *Stan Ulam, John von Neumann, and the Monte Carlo Method*, Monte Carlo 1987.

[80] J. Spanier, E. M. Gelbard and G. Bell: *Monte carlo principles and neutron transport problems*, Physics today 23, no. 9, pp. 56–57, 1970, ISSN 0031-9228.

[81] J. I. Marquez-Damian: *Introduction to OpenMC*, 2023, accessed: 2024-09-18.

[82] P. L'Ecuyer: *Tables of linear congruential generators of different sizes and good lattice structure*, Mathematics of computation 68, no. 225, pp. 249–260, 1999, ISSN 0025-5718.

[83] OpenMC Development Team: *OpenMC documentation*, `https://docs.openmc.org/en/stable/`, 2023, accessed: 2023-09-03.

[84] Team, McStas Development: *McStas - A neutron ray-trace simulation package*, `https://www.mcstas.org/`, accessed: 2024-04-11.

[85] P. K. Willendrup and K. Lefmann: *McStas (i): Introduction, use, and basic principles for ray-tracing simulations*, 2020.

[86] X.-X. Cai, T. Kittelmann et al.: *Rejection-based sampling of inelastic neutron scattering*, Journal of Computational Physics 380, pp. 400–407, 2019, doi:10.1016/j.jcp.2018.11.043.

[87] T. Kittelmann and X.-X. Cai: *Elastic neutron scattering models for NCrystal*, Computer Physics Communications 267, p. 108082, 2021, ISSN 0010-4655, doi:https://doi.org/10.1016/j.cpc.2021.108082.

[88] P. Willendrup, E. Farhi and K. Lefmann: *McStas 1.7 - A new version of the flexible monte carlo neutron scattering package*, Physica B: Condensed Matter 350, pp. E735 – E737, 2004, doi:10.1016/j.physb.2004.03.193.

[89] P. K. Romano, N. E. Horelik, B. R. Herman, A. G. Nelson, B. Forget and K. Smith: *OpenMC: A state-of-the-art Monte Carlo code for research and development*, Annals of Nuclear Energy 82, pp. 90–97, 2015, ISSN 0306-4549, doi:10.1016/j.anucene.2014.07.048, joint International Conference on Supercomputing in Nuclear Applications and Monte Carlo 2013.

[90] J. T. Goorley, M. R. James et al.: *Initial MCNP6 Release Overview - MCNP6 Version 1.0*, Tech. Rep. LA-UR-13-22934, 1086758, Los Alamos National Laboratory, 2013, doi:10.2172/1086758.

[91] T. Sato, Y. Iwamoto, S. Hashimoto, T. Ogawa, T. Furuta, S.-I. Abe, T. Kai et al.: *Features of particle and heavy ion transport code system (PHITS) version 3.02*, Journal of Nuclear Science and Technology 55, no. 6, pp. 684–690, 2018, doi:10.1080/00223131.2017.1419890.

[92] T. Kittelmann: *NCMAT format*, `https://github.com/mctools/ncrystal/wiki/NCMAT-format`, 2020, online.

[93] V. Czamler, T. C. Hansen, M. M. Koza, R. Wagner and O. Zimmer: *Deuterated clathrate hydrates as a novel moderator material for very cold neutrons. Project aperçu and first results*, EPJ Web of Conferences 286, p. 05004, 2023, doi:10.1051/epjconf/202328605004.

[94] HighNESS Project: *HighNESS project GitHub repository*, `https://github.com/highness-eu`, 2024, accessed: 2024-07-28.

[95] E. D. Sloan and C. A. Koh: *Clathrate Hydrates of Natural Gases.*, CRC Press, Taylor & Francis, Berkeley, California, 3. ed., 2008, ISBN 978-0-8493-9078.

[96] H. Davy: *The bakerian lecture: On some of the combinations of oxymuriatic gas and oxygene, and on the chemical relations of these principles, to inflammable bodies*, Philosophical Transactions of the Royal Society of London 101, pp. 1–35, 1811, ISSN 02610523.

[97] M. Faraday: *LXXXVI. On fluid chlorine*, The Philosophical magazine (London, UK : 1798) 62, no. 308, pp. 413–416, 1823, ISSN 1941-5796.

[98] H. M. Powell: *15. The structure of molecular compounds. Part IV. Clathrate compounds*, Journal of the Chemical Society 0, pp. 61–73, 1948, doi:10.1039/JR9480000061.

[99] P. Englezos: *Clathrate hydrates*, Industrial & Engineering Chemistry Research 32, no. 7, pp. 1251–1274, 1993, ISSN 0888-5885, doi:10.1021/ie00019a001.

[100] D. Broseta, L. Ruffine and A. Desmedt (editors): *Gas Hydrates 1: Fundamentals, Characterization and Modeling*, John Wiley & Sons, Inc., Hoboken, NJ, USA, 1. ed., 2017, ISBN 978-1-119-33268-8, doi:10.1002/9781119332688.

[101] M. v. Stackelberg: *Feste Gashydrate*, Naturwissenschaften 36, no. 11, pp. 327–333, 1949, ISSN 1432-1904, doi:10.1007/BF00596788.

[102] W. F. Claussen: *A second water structure for inert gas hydrates*, The Journal of Chemical Physics 19, no. 11, pp. 1425–1426, 1951, ISSN 0021-9606, doi:10.1063/1.1748079.

[103] W. F. Claussen: *Suggested structures of water in inert gas hydrates*, The Journal of Chemical Physics 19, no. 2, pp. 259–260, 1951, ISSN 0021-9606, doi:10.1063/1.1748187.

[104] W. F. Claussen: *Erratum: Suggested structures of water in inert gas hydrates*, The Journal of Chemical Physics 19, no. 5, pp. 662–662, 1951, ISSN 0021-9606, doi:10.1063/1.1748327.

[105] L. Pauling and R. E. Marsh: *The structure of chlorine hydrate*, Proceedings of the National Academy of Sciences 38, no. 2, pp. 112–118, 1952, doi:10.1073/pnas.38.2.112.

[106] H. R. Müller and M. v. Stackelberg: *Zur Struktur der Gashydrate*, Naturwissenschaften 39, no. 1, pp. 20–21, 1952, ISSN 1432-1904, doi:10.1007/BF00591919.

[107] Plato: *Platons Dialoge Timaios und Kritias*, Philosophische bibliothek ; 179, Meiner, Leipzig, 2., durchges. Aufl. ed., 1922.

[108] J. Kepler: *Mysterium cosmographicum. The secrect of the universe.*, Abaris Books, New York, 1981.

[109] G. A. Jeffrey: *Hydrate inclusion compounds*, Journal of inclusion phenomena 1, no. 3, pp. 211–222, 1984, ISSN 1573-1111, doi:10.1007/BF00656757.

[110] A. Desmedt: *Structural and dynamic properties of THF clathrate hydrates: Neutron scattering and molecular dynamics studies*, Collection SFN 10, pp. 545–562, 2010, doi:10.1051/sfn/2010013.

[111] E. Arunan, G. R. Desiraju, R. A. Klein, J. Sadlej, S. Scheiner, I. Alkorta, D. C. Clary et al.: *Definition of the hydrogen bond (IUPAC Recommendations 2011)*, Pure and Applied Chemistry 83, no. 8, pp. 1637–1641, 2011, doi:doi:10.1351/PAC-REC-10-01-02.

[112] A. Einstein: *Die Plancksche Theorie der Strahlung und die Theorie der Spezifischen Wärme*, Annalen der Physik 22, p. 180, 1907.

[113] P. Debye: *On the theory of specific heats*, Annalen der Physik 39, pp. 789–839, 1912.

[114] U. Ranieri, M. M. Koza, W. F. Kuhs, R. Gaal, S. Klotz, A. Falenty, D. Wallacher, J. Ollivier, P. Gillet and L. E. Bove: *Quantum dynamics of H2 and D2 confined in hydrate structures as a function of pressure and temperature*, The Journal of Physical Chemistry C 123, no. 3, pp. 1888–1903, 2019, ISSN 1932-7447, doi:10.1021/acs.jpcc.8b11606.

[115] U. Ranieri, L. del Rosso, L. E. Bove, M. Celli, D. Colognesi, R. Gaal, T. C. Hansen, M. M. Koza and L. Ulivi: *Large-cage occupation and quantum dynamics of hydrogen molecules in sII clathrate hydrates*, The Journal of Chemical Physics 160, no. 16, p. 164706, 2024, ISSN 0021-9606, doi:10.1063/5.0200867.

[116] B. Chazallon, H. Itoh, M. Koza, W. F. Kuhs and H. Schober: *Anharmonicity and guest–host coupling in clathrate hydrates*, Physical Chemistry Chemical Physics 4, no. 19, pp. 4809–4816, 2002, doi:10.1039/B202464K.

[117] H. Schober, H. Itoh, A. Klapproth, V. Chihaia and W. Kuhs: *Guest-host coupling and anharmonicity in clathrate hydrates*, The European Physical Journal E, Soft matter (Print) 12, no. 1, pp. 41–49, 2003, ISSN 1292-8941.

[118] M. M. Koza and H. Schober: *Vibrational dynamics and guest–host coupling in clathrate hydrates*, in *Neutron Applications in Earth, Energy and Environmental Sciences*, pp. 351–389, Springer US, Boston, MA, 2009, ISBN 978-0-387-09416-8, doi:10.1007/978-0-387-09416-8_12, edited by Liang, Liyuan and Rinaldi, Romano and Schober, Helmut.

[119] O. Andersson, M. Saiduzzaman, P. H. Barros Brant Carvalho and U. Haussermann: *Amorphous-like thermal conductivity and high mechanical stability of cyclopentane clathrate hydrate*, Journal of Chemical Physics pp. –, 2024, doi:10.1039/D4CP01656D.

[120] A. I. Krivchikov, B. Ya. Gorodilov, O. A. Korolyuk, V. G. Manzhelii, O. O. Romantsova, H. Conrad, W. Press, J. S. Tse and D. D. Klug: *Thermal conductivity of Xe clathrate hydrate at low temperatures*, Physical Review B 73, no. 6, p. 064203, 2006, doi:10.1103/PhysRevB.73.064203.

[121] I. I. Gurevich: *Low-Energy Neutron Physics*, North-Holland, Amsterdam, 1968.

[122] V. Namiot: *Phononless cooling of neutrons to extremly low temperatures*, Dokl. Akad. Nauk SSSR 211, no. 1, 1973.

[123] H. Semat: *Introduction to Atomic and Nuclear Physics*, Chapman and Hall, London, 5. ed. ed., 1972, ISBN 0-412-11940-4.

[124] E. Tiesinga, P. J. Mohr, D. B. Newell and B. N. Taylor: *The 2022 CODATA recommended values of the fundamental physical constants*, Web Version 9.0. Database developed by J. Baker, M. Douma, and S. Kotochigova, 2024.

[125] W. H. Kleiner: *Magnetic scattering of slow neutrons from O_2 gas*, Physical Review 97, no. 2, pp. 411–418, 1955, doi:10.1103/PhysRev.97.411.

[126] Yu.A. Freiman and H. Jodl: *Solid oxygen*, Physics Reports 401, no. 1, pp. 1–228, 2004, ISSN 0370-1573, doi:10.1016/j.physrep.2004.06.002.

[127] B. Renker, G. Roth, H. Schober, P. Nagel, R. Lortz, C. Meingast, D. Ernst, M. T. Fernandez-Diaz and M. Koza: *Intercalation of molecular gases into C_{60}*, Physical Review B 64, no. 20, p. 205417, 2001, doi:10.1103/PhysRevB.64.205417.

[128] E. B. Gordon, V. V. Khmelenko, A. A. Pelemenev et al.: *Production of dry van der Waals clusters of helium and oxygen*, Chemical Physics 170, pp. 411–423, 1993, doi:10.1016/0301-0104(93)85122-O.

[129] Y.-H. Ahn, B. Lee and K. Shin: *Structural identification of binary tetrahydrofuran + O2 and 3-hydroxytetrahydrofuran + O2 clathrate hydrates by Rietveld analysis with direct space method*, Crystals 8, no. 328, 2018, ISSN 2073-4352, doi:10.3390/cryst8080328.

[130] H. Yang, S. Fan, X. Lang and Y. Wang: *Phase equilibria of mixed gas hydrates of oxygen + tetrahydrofuran, nitrogen + tetrahydrofuran, and air + tetrahydrofuran*, Journal of Chemical & Engineering Data 56, no. 11, pp. 4152–4156, 2011, doi:10.1021/je200676k.

[131] W. Kuhs, B. Chazallon, P. Radaelli et al.: *Cage occupancy and compressibility of deuterated N2-clathrate hydrate by neutron diffraction*, Journal of Inclusion Phenomena and Molecular Recognition in Chemistry 29, pp. 65–77, 1997, doi:10.1023/A:1007960217691.

[132] T. C. Hansen, A. Falenty and W. F. Kuhs: *Lattice constants and expansivities of gas hydrates from 10 K up to the stability limit*, The Journal of Chemical Physics 144, no. 5, p. 054301, 2016, ISSN 0021-9606, 1089-7690, doi:10.1063/1.4940729.

[133] W. F. Kuhs, A. Klapproth, F. Gotthardt, K. Techmer and T. Heinrichs: *The formation of meso- and macroporous gas hydrates*, Geophysical Research Letters 27, no. 18, pp. 2929–2932, 2000, ISSN 00948276, doi:10.1029/2000GL006112.

[134] A. Rosu-Finsen, M. B. Davies, A. Amon, H. Wu, A. Sella, A. Michaelides and C. G. Salzmann: *Medium-density amorphous ice*, Science 379, no. 6631, pp. 474–478, 2023, doi:10.1126/science.abq2105.

[135] S. Chabab, A. Valtz, S. Ahamada and C. Coquelet: *Hydrate stability of carbon dioxide + oxygen binary mixture (CO2 + O2) in pure water: Measurements and modeling*, Journal of Chemical and Engineering Data 66, pp. 767–779, 2021, doi:10.1021/acs.jced.0c00865.

[136] A. H. Mohammadi, B. Tohidi and R. W. Burgass: *Equilibrium data and thermodynamic modeling of nitrogen, oxygen, and air clathrate hydrates*, Journal of Chemical and Engineering Data 48, no. 3, pp. 612–616, 2003, ISSN 0021-9568, doi:10.1021/je025608x.

[137] J. Rodríguez-Carvajal: *Recent advances in magnetic structure determination by neutron powder diffraction*, Physica B: Condensed Matter 192, no. 1, pp. 55–69, 1993, ISSN 0921-4526, doi:10.1016/0921-4526(93)90108-I.

[138] J. Rodriguez-Carvajal: *Recent developments of the program FULLPROF, commission on powder diffraction*, IUCr Newsl. 26, 2001.

[139] H. M. Rietveld: *A profile refinement method for nuclear and magnetic structures*, Journal of Applied Crystallography 2, no. 2, pp. 65–71, 1969, doi:10.1107/S0021889869006558.

[140] R. Young: *The Rietveld Method*, International Union of Crystallography. Monographs on Crystallography 5, Oxford Univ. Press, Oxford [u.a.], 1993, ISBN 0-19-855577-6.

[141] R. J. Hill and C. J. Howard: *Quantitative phase analysis from neutron powder diffraction data using the Rietveld method*, Journal of Applied Crystallography 20, no. 6, pp. 467–474, 1987, ISSN 1600-5767.

[142] J. Rodriguez-Carvajal: *An introduction into the program fullprof 2000 (version july 2001)*, `https://www.psi.ch/sites/default/files/import/sinq/dmc/ManualsEN/fullprof.pdf`, 2001.

[143] R. Gross and A. Marx: *6 thermische Eigenschaften des Kristallgitters*, in *Festkörperphysik*, pp. 215–260, De Gruyter Oldenbourg, Berlin, Boston, 2022, ISBN 978-3-11-078239-4, doi:doi:10.1515/9783110782394-006.

[144] C. Kittel and P. McEuen: *Introduction to Solid State Physics*, Wiley, New York, NY, 8th ed., 2005.

[145] J. Tse: *Thermal expansion of the clathrate hydrates of ethylene oxide and tetrahydrofuran*, Journal de Physique Colloques 48, no. C1, pp. C1–543–C1–549, 1987, doi:10.1051/jphyscol:1987174.

[146] K. C. Hester, Z. Huo, A. L. Ballard, C. A. Koh, K. T. Miller and E. D. Sloan: *Thermal expansivity for sI and sII clathrate hydrates*, The Journal of Physical Chemistry B 111, no. 30, pp. 8830–8835, 2007, ISSN 1520-6106, doi:10.1021/jp0715880.

[147] D. W. Davidson, Y. P. Handa, C. I. Ratcliffe, J. A. Ripmeester, J. S. Tse, J. R. Dahn, F. Lee and L. D. Calvert: *Crystallographic studies of clathrate hydrates. Part I*, Molecular Crystals and Liquid Crystals 141, no. 1-2, pp. 141–149, 1986, doi:10.1080/00268948608080205.

[148] P. Virtanen, R. Gommers, T. E. Oliphant, M. Haberland, T. Reddy, D. Cournapeau, E. Burovski et al.: *SciPy 1.0: Fundamental algorithms for scientific computing in python*, Nature Methods 17, pp. 261–272, 2020, doi:10.1038/s41592-019-0686-2.

[149] W. I. F. David: *Powder diffraction: Least-squares and beyond*, Journal of research of the National Institute of Standards and Technology 109, no. 1, pp. 107–123, 2004, ISSN 1044-677X.

[150] National Center for Biotechnology Information: *PubChem compound summary for CID 8028, tetrahydrofuran*, accessed: 2024-3-4.

[151] National Center for Biotechnology Information: *PubChem compound summary for CID 977, oxygen*, accessed: 2024-3-4.

[152] A. Le Bail: *Whole powder pattern decomposition methods and applications: A retrospection*, Powder Diffraction 20, no. 4, pp. 316–326, 2005, doi:10.1154/1.2135315.

[153] C. Y. Jones, S. L. Marshall, B. C. Chakoumakos, C. J. Rawn and Y. Ishii: *Structure and thermal expansivity of tetrahydrofuran deuterate determined by neutron powder diffraction*, The Journal of Physical Chemistry B 107, no. 25, pp. 6026–6031, 2003, ISSN 1520-6106, doi:10.1021/jp020513n.

[154] H. Jiang and K. D. Jordan: *Comparison of the properties of xenon, methane, and carbon dioxide hydrates from equilibrium and nonequilibrium molecular dynamics simulations*, The Journal of Physical Chemistry C 114, no. 12, pp. 5555–5564, 2010, ISSN 1932-7447, doi:10.1021/jp9063406.

[155] V. R. Belosludov, T. M. Inerbaev, O. S. Subbotin, R. V. Belosludov, J.-i. Kudoh and Y. Kawazoe: *Thermal expansion and lattice distortion of clathrate hydrates of cubic structures I and II*, Journal of Supramolecular Chemistry 2, no. 4, pp. 453–458, 2002, ISSN 1472-7862, doi:10.1016/S1472-7862(03)00072-8, special Issue to Honor the Memory of Professor Yuri Dyadin.

[156] A. Falenty, T. C. Hansen and W. F. Kuhs: *Formation and properties of ice XVI obtained by emptying a type sII clathrate hydrate*, Nature 516, no. 7530, pp. 231–233, 2014, ISSN 1476-4687, doi:10.1038/nature14014.

[157] Y. Park, Y. N. Choi, S.-H. Yeon and H. Lee: *Thermal expansivity of tetrahydrofuran clathrate hydrate with diatomic guest molecules*, The Journal of Physical Chemistry B 112, no. 23, pp. 6897–6899, 2008, ISSN 1520-6106, doi:10.1021/jp8020112.

[158] D. J. Safarik, T. Klimczuk, A. Llobet, D. D. Byler, J. C. Lashley, J. R. O'Brien and N. R. Dilley: *Localized anharmonic rattling of Al atoms in $VAl_{10.1}$*, Physical Review B 85, no. 1, p. 014103, 2012, doi:10.1103/PhysRevB.85.014103.

[159] A. D. Caplin, G. Grüner and J. B. Dunlop: *$Al_{10}V$: An Einstein solid*, Physical Review Letters 30, no. 22, pp. 1138–1140, 1973, doi:10.1103/PhysRevLett.30.1138.

[160] J. Ollivier, M. Zbiri and J. Halbwachs: *Instrument Layout: Disk chopper time-of-flight spectrometer IN5*, https://www.ill.eu/users/instruments/instruments-list/in5.

[161] B. Fåk, S. Rols, G. Manzin and O. Meulien: *Panther — the new thermal neutron time-of-flight spectrometer at the ILL*, EPJ Web Conf. 272, p. 02001, 2022, doi:10.1051/epjconf/202227202001.

[162] B. Fak, M. M. Koza and O. Meulien: *Instrument Layout: Thermal neutron time-of-flight spectrometer PANTHER*.

[163] C. Bousige: *Structure et dynamique de systèmes unidimensionnels modèles: les nanopeapods de carbone*, Autre [cond-mat.other], Université Paris Sud - Paris XI, 2012, nNT: 2012PA112303.

[164] M. Jiménez-Ruiz, A. Ivanov and S. Fuard: *LAGRANGE - the new neutron vibrational spectrometer at the ILL*, Journal of Physics: Conference Series 549, p. 012004, 2014, doi:10.1088/1742-6596/549/1/012004.

[165] M. Jimenez Ruiz and A. Bertoni: *Instrument layout: IN1-LAGRANGE – large area graphite analyser for genuine excitations*, https://www.ill.eu/users/instruments/instruments-list/in1-lagrange/description/instrument-layout.

[166] D. Schmitt and B. Ouladdiaf: *Absorption correction for annular cylindrical samples in powder neutron diffraction*, Journal of Applied Crystallography 31, no. 4, pp. 620–624, 1998, doi:10.1107/S0021889898002672.

[167] K. D. Rouse, M. J. Cooper, E. J. York and A. Chakera: *Absorption corrections for neutron diffraction*, Acta Crystallographica Section A: Crystal Physics, Diffraction, Theoretical and General Crystallography 26, no. 6, pp. 682–691, 1970, doi: 10.1107/S0567739470001687.

[168] H. H. Paalman and C. J. Pings: *Numerical evaluation of X-ray absorption factors for cylindrical samples and annular sample cells*, Journal of Applied Physics 33, no. 8, pp. 2635–2639, 1962, ISSN 0021-8979, doi:10.1063/1.1729034.

[169] J. Wuttke: *Improved sample holder for multidetector neutron spectrometers*, Physica B: Condensed Matter 266, no. 1, pp. 112–114, 1999, ISSN 0921-4526, doi:10.1016/S0921-4526(98)01503-8.

[170] Mantid Project: *Manipulation and analysis toolkit for instrument data. Mantid project*, `http://dx.doi.org/10.5286/SOFTWARE/MANTID`, 2013.

[171] O. Arnold, J. Bilheux, J. Borreguero, A. Buts, S. Campbell, L. Chapon, M. Doucet et al.: *Mantid—Data analysis and visualization package for neutron scattering and μ SR experiments*, Nuclear Instruments and Methods in Physics Research A 764, pp. 156–166, 2014, ISSN 0168-9002, doi:10.1016/j.nima.2014.07.029.

[172] Mantid Project: *DirectILLSelfShielding algorithm*, `https://docs.mantidproject.org/nightly/algorithms/DirectILLSelfShielding-v1.html`, 2023, accessed: 2024-07-23.

[173] Mantid Project: *MonteCarloAbsorption algorithm*, 2023, accessed: 2024-07-23.

[174] W. C. Hamilton: *Significance tests on the crystallographic R factor*, Acta Crystallographica 10, p. 629, 1957, doi:10.1107/S0365110X57002212.

[175] C. G. Darwin: *The theory of X-ray reflexion*, Philosophical Magazine 43, p. 800, 1922, doi:10.1080/10448639208218770.

[176] T. M. Sabine: *The flow of radiation in a real crystal*, in A. J. C. Wilson and E. Prince (editors), *International Tables for Crystallography, Vol. C*, p. 609–616, Kluwer Publishers, 2004, doi:10.1107/978095536020600006.

[177] Mantid Project: *Mantid documentation. Algorithm contents*, `https://docs.mantidproject.org/nightly/algorithms/index.html`, 2023, accessed: 2024-08-06.

[178] J. Mayers and R. Cywinski: *A Monte Carlo evaluation of analytical multiple scattering corrections for unpolarised neutron scattering and polarisation analysis data*, Nuclear Instruments and Methods in Physics Research Section A: Accelerators, Spectrometers, Detectors and Associated Equipment 241, no. 2, pp. 519–531, 1985, ISSN 0168-9002, doi: 10.1016/0168-9002(85)90607-2.

[179] NIST Center for Neutron Research: *How thick should my sample be?*, 2007, accessed: 2024-07-24.

[180] O. Zimmer, Y. Calzavara, T. C. Hansen, M. Jamalipour, E. Klinkby, M. M. Koza, W. F. Kuhs, T. Neulinger, A. Wildes and L. Zanini: *Absolute inelastic neutron scattering cross sections of clathrate hydrate compounds for new very-cold-neutron moderators*, 2020, doi:10.5291/ILL-DATA.1-10-42.

[181] O. Zimmer, Y. Calzavara, V. Czamler, T. C. Hansen, M. Jamalipour, E. Klinkby, M. M. Koza et al.: *Absolute inelastic neutron scattering cross sections of clathrate hydrate compounds for new very-cold-neutron moderators*, 2021, doi: 10.5291/ILL-DATA.1-10-49.

[182] Goodfellow: *Vanadium*, https://www.goodfellow.com/usa/material/metals/vanadium, accessed: 2024-07-30.

[183] J. R. Copley and J. C. Cook: *LAMP: The large array manipulation program*, Neutron News 3, no. 3, pp. 29–34, 1992.

[184] R. McGreevy: *Neutron data analysis and visualization with LAMP*, Journal of Neutron Research 6, no. 1-3, pp. 7–19, 1997.

[185] Mantid Project: *DirectILLCollectData v1*, https://docs.mantidproject.org/nightly/algorithms/DirectILLCollectData-v1.html, 2024, accessed: 2024-07-28.

[186] Mantid Project: *DirectILLIntegrateVanadium v1*, https://docs.mantidproject.org/nightly/algorithms/DirectILLIntegrateVanadium-v1.html, 2024, accessed: 2024-07-31.

[187] Mantid Project: *DirectILLReduction v1*, https://docs.mantidproject.org/nightly/algorithms/DirectILLReduction-v1.html, 2024, accessed: 2024-07-28.

[188] Mantid Project: *SofQWNormalisedPolygon v1*, https://docs.mantidproject.org/nightly/algorithms/SofQWNormalisedPolygon-v1.html, 2024, accessed: 2024-08-02.

[189] E. F. Skelton and J. L. Katz: *Examination of the thermal variation of the mean square atomic displacements in zinc and evaluation of the associated debye temperature*, Physical Review 171, no. 3, pp. 801–808, 1968, doi:10.1103/PhysRev.171.801.

[190] H. Conrad, W. F. Kuhs, K. Nünighoff, C. Pohl, M. Prager and W. Schweika: *Inelastic scattering and spectral measurements of advanced cold moderator media*, Physica B: Condensed Matter 350, no. 1, Supplement, pp. E647–E650, 2004, ISSN 0921-4526, doi:10.1016/j.physb.2004.03.173.

[191] M. Celli, D. Colognesi, L. Ulivi, M. Zoppi and A. J. Ramirez-Cuesta: *Phonon density of states in different clathrate hydrates measured by inelastic neutron scattering*, Journal of Physics: Conference Series 340, no. 1, p. 012051, 2012, doi:10.1088/1742-6596/340/1/012051.

[192] Mantid Project: *LineProfile v1*, https://docs.mantidproject.org/nightly/algorithms/LineProfile-v1.html, 2024, accessed: 2024-08-06.

[193] G. James, D. Witten, T. Hastie and R. Tibshirani: *An Introduction to Statistical Learning: With Applications in R*, Springer Texts in Statistics, Springer, New York, NY, 2013, ISBN 978-1-4614-7137-0.

[194] N. R. Draper and H. Smith: *Applied Regression Analysis*, Wiley-Interscience, New York, NY, 3rd ed., 1998, ISBN 978-0-471-17082-2.

[195] W. H. Press, S. A. Teukolsky, W. T. Vetterling and B. P. Flannery: *Numerical Recipes: The Art of Scientific Computing*, Cambridge University Press, Cambridge, UK, 3rd ed., 2007, ISBN 978-0-521-88068-8.

[196] G. Cowan: *Statistical Data Analysis*, Oxford Science Publications, Clarendon Pr., Oxford [u.a.], 1998, ISBN 978-0-19-850156-5.

[197] V. Czamler, M. Appel, C. Beck, A. Desmedt, T. C. Hansen, M. Jimenez Ruiz, M. M. Koza et al.: *Neutron scattering study of the binary clathrate hydrate 17D2O:C4D8O:2O2 for application as novel very-cold-neutron moderator*, 2023, doi:10.5291/ILL-DATA.1-10-57.

[198] M. Tinkham and M. W. P. Strandberg: *Theory of the fine structure of the molecular oxygen ground state*, Physical Review 97, no. 4, pp. 937–951, 1955, doi:10.1103/PhysRev.97.937.

[199] E. van der Horst: *Phase Transitions Reflected in HF-EPR Spectra*, Ph.D. thesis, Radboud University, 2006.

[200] N. Bjerre: *Coupling of librations with acoustic phonons in crystals*, Journal of Chemical Physics 76, pp. 3347–3351, 1982, doi:10.1063/1.442425.

[201] M. Appel and T. Seydel: *IN16B - Backscattering Spectrometer*, https://www.ill.eu/users/instruments/instruments-list/in16b/how-it-works/simulated-experiment, 2024, accessed: 2024-08-24.

[202] M. J. Abraham, D. van der Spoel, E. Lindahl and B. Hess: *GROMACS: High performance molecular simulations through multi-level parallelism from laptops to supercomputers*, SoftwareX 1–2, pp. 19–25, 2015, doi:10.1016/j.softx.2015.06.001.

[203] Mantid Project: *ComputeIncoherentDOS-v1 algorithm*, `https://docs.mantidproject.org/v3.11.0/algorithms/ComputeIncoherentDOS-v1.html`, 2016, accessed: 2024-08-29.

[204] J.-C. Li: *INS data for ice ih*, Journal of Chemical Physics 105, pp. 6733–6755, 1996, instrument: TOSCA-1, http://wwwisis2.isis.rl.ac.uk/INSdatabase/Results.asp?IceIh.

[205] J.-C. Li: *INS data for ice ic*, Physical Chemistry Chemical Physics 105, pp. 6733–6755, 1996, instrument: TXFA, http://wwwisis2.isis.rl.ac.uk/INSdatabase/Results.asp?IceIc.

[206] M. E. Casco, S. Grätz, E. Zhang, M. Jiménez-Ruiz and L. Borchardt: *Inelastic neutron scattering of methane hydrate confined in hydrophilic and hydrophobic porous model carbons*, The Journal of Physical Chemistry C 128, pp. 10281–10289, 2024, doi:10.1021/acs.jpcc.4c01082.

[207] J.-C. Li: *INS data for ice ih deuterated*, Journal of Chemical Physics 105, pp. 6733–6755, 1996, instrument: TOSCA-1, http://wwwisis2.isis.rl.ac.uk/INSdatabase/Results.asp?IceIhDeuterated.

[208] M. Jiménez-Ruiz, D. S. Gahle, T. Lemishko, S. Valencia, G. Sastre and F. Rey: *Evidence of hydronium formation in water–chabazite zeolite using inelastic neutron scattering experiments and ab initio molecular dynamics simulations*, The Journal of Physical Chemistry C 124, no. 9, pp. 5151–5160, 2020, doi:10.1021/acs.jpcc.9b11815.

[209] BIOVIA: *Materials studio 2024 sp1 hf1*, `https://www.3ds.com/products-services/biovia/products/materials-studio/`, 2024, BIOVIA, Dassault Systèmes, San Diego, CA. Accessed: 2024-08-24.

[210] Mantid Project: *Abins v1*, `https://docs.mantidproject.org/v3.9.1/algorithms/Abins-v1.html`, 2024, accessed: 2024-08-28.

[211] B. Cadioli, E. Gallinella, C. Coulombeau, H. Jobic and G. Berthier: *Geometric structure and vibrational spectrum of tetrahydrofuran*, The Journal of Physical Chemistry 97, no. 30, pp. 7844–7856, 1993, doi:10.1021/j100132a010.

[212] D. E. Hare and C. M. Sorensen: *Interoscillator coupling effects on the OH stretching band of liquid water*, The Journal of Chemical Physics 96, no. 1, pp. 13–22, 1992, ISSN 0021-9606, doi:10.1063/1.462852.

[213] J. Schicks, J. Erzinger and M. Ziemann: *Raman spectra of gas hydrates—differences and analogies to ice 1h and (gas saturated) water*, Spectrochimica Acta Part A: Molecular and Biomolecular Spectroscopy 61, no. 10, pp. 2399–2403, 2005, ISSN 1386-1425, doi: 10.1016/j.saa.2005.02.019.

[214] E. Friedell: *Kulturgeschichte des Altertums: Leben und Legende der vorchristlichen Seele*, Helikon-Verl, Zürich, 1936.

[215] H. Pauly: *Velocity Measurement and Selection*, in H. Pauly (editor), *Atom, Molecule, and Cluster Beams II: Cluster Beams, Fast and Slow Beams, Accessory Equipment and Applications*, Springer Series on Atomic, Optical, and Plasma Physics, pp. 137–196, Springer, Berlin, Heidelberg, 2000, ISBN 978-3-662-05902-9, doi:10.1007/978-3-662-05902-9_3.

[216] M. Busi, J. Čapek, E. Polatidis, J. Hovind, P. Boillat, A. S. Tremsin, W. Kockelmann and M. Strobl: *Frame overlap Bragg edge imaging*, Scientific Reports 10, no. 1, p. 14867, 2020, ISSN 2045-2322, doi:10.1038/s41598-020-71705-4.

[217] V. Sears: *Optimum counting times in experiments governed by poisson statistics*, Nuclear Instruments and Methods in Physics Research Section B: Beam Interactions with Materials and Atoms 12, no. 3, pp. 430–433, 1985, ISSN 0168-583X, doi:10.1016/0168-583X(85)90044-8.

[218] National Institute of Standards and Technology (NIST): *Neutron scattering lengths and cross sections*, 1992.

[219] V. Czamler, J. Allen, H. Filter, T. Jenke, F. Lafont, T. Neulinger, L. Tolson, R. Wagner and O. Zimmer: *Neutron transmission through clathrate hydrate samples for new very-cold-neutron moderators*, 2023, doi:10.5291/ILL-DATA.3-14-431.

[220] V. Czamler, D. Di Julio, M. Hartl, J. I. Marquez Damian, V. Nesvizhevsky, L. Tolson, R. Wagner, S. Xu and O. Zimmer: *Neutron total cross-section measurements of cold reflector and moderator materials*, 2024, doi:10.5291/ILL-DATA.3-07-419.

[221] T. Soldner, V. Nesvizhvsky and D. Berruyer: *PF1B: Polarised cold neutron beam facility*, accessed: 2024-05-23.

[222] V. Nesvizhevsky, K. Henry, L. Dauga, B. Clavier, S. Le Floch, E. Lychagin, A. Muzychka et al.: *Poly(dicarbon monofluoride) (C2F)n bridges the neutron reflectivity gap*, Carbon 227, p. 119249, 2024, ISSN 0008-6223, doi:10.1016/j.carbon.2024.119249.

[223] D. Roulier, V. Nesvizhevsky, B. Clément, G. Freche, G. Pignol, D. Rebreyend, F. Vezzu, S. Baessler and A. Strelkov: *Design and test of a compact and high-resolution time-of-flight measurement device for cold neutron beams*, Physical Review Accellerators and Beams 22, no. 3, p. 032801, 2019, doi:10.1103/PhysRevAccelBeams.22.032801.

[224] P. Mutti, F. Cecillon, A. Elaazzouzi, Y. L. Goc, J. Locatelli, H. Ortiz and J. Ratel: *NOMAD – more than a simple sequencer*, in *Proceedings of ICALEPCS2011*, Institut Laue-Langevin, Grenoble, France, 2011.

[225] H. Abele, D. Dubbers, H. Häse, M. Klein, A. Knöpfler, M. Kreuz, T. Lauer et al.: *Characterization of a ballistic supermirror neutron guide*, Nuclear Instruments and Methods in Physics Research Section A: Accelerators, Spectrometers, Detectors and Associated Equipment 562, no. 1, pp. 407–417, 2006, ISSN 0168-9002, doi:10.1016/j.nima.2006.03.020.

[226] R. Ramadhan: *Development and Application of Bragg Edge Neutron Transmission*, Ph.D. thesis, Coventry University, 2019.

[227] A. S. Tremsin, J. B. McPhate, W. A. Kockelmann, J. V. Vallerga, O. H. W. Siegmund and W. B. Feller: *Energy-resolving neutron transmission radiography at the isis pulsed spallation source with a high-resolution neutron counting detector*, IEEE Transactions on Nuclear Science 56, no. 5, pp. 2931–2937, 2009, doi:10.1109/TNS.2009.2029690.

[228] J. I. Marquez-Damian, J. R. Granada, D. V. Baxter, S. R. Parnell and D. C. Evans: *Measurement of the total cross section of heavy water in the 0.1 meV - 1 eV energy range at 20 and 50° C*, Nuovo Cimento C 38, p. 178, 2015.

[229] F. Kropff, J. R. Latorre, J. R. Granada and C. C. Madero: *Total neutron cross-section of D_2O at 20 degrees-C between 0.0005 and 10 eV*, 1973.

[230] U. Filges and M. Busi: *Description – BOA beamline*, `https://www.psi.ch/en/sinq/boa/description`, accessed: 2024-07-12.

[231] S. W. Peterson and H. A. Levy: *A single-crystal neutron diffraction study of heavy ice*, Acta Crystallographica 10, pp. 70–76, 1957, doi:10.1107/S0365110X5700016X.

[232] I. Laue-Langevin: *ILL Yellowbook - 2008*, 2008, annual Report.

[233] H. M. Filter: *Interference Experiment with Slow Neutrons: A Feasibility Study of Lloyd's Mirror at the Institut Laue-Langevin*, Ph.D. thesis, TU Wien, Wien, 2018.

[234] G. Manzin: *Bidim80 and Bidim26 for UCN*, 2011, iLL internal document.

[235] T. Oda, M. Hino, M. Kitaguchi, H. Filter, P. Geltenbort and Y. Kawabata: *Towards a high-resolution TOF-MIEZE spectrometer with very cold neutrons*, Nuclear Instruments and Methods in Physics Research Section A: Accelerators, Spectrometers, Detectors and Associated Equipment 860, pp. 35–41, 2017, ISSN 0168-9002, doi:10.1016/j.nima.2017.03.014.

[236] D. Roulier: *Production et Détection de Neutrons Ultra-Froids Pour Le Spectromètre GRANIT*, Ph.D. thesis, Université Grenoble Alpes, Grenoble, France, 2015.

[237] T. Bry: *Extraction of Ultra Cold Neutrons from a Solid Deuterium Source*, Ph.D. thesis, ETH Zürich, Villigen, Switzerland, 2007.

[238] S. Döge: *Scattering of Ultracold Neutrons in Condensed Deuterium and on Material Surfaces*, Ph.D. thesis, Technische Universität München, Munich, Germany, 2020.

[239] A. Guinier and G. Fournet: *Small-Angle Scattering of x-Rays*, Structure of Matter Series, John Wiley & Sons, Inc., New York, 1955.

[240] S. Developers: *SciPy optimize: Curve_fit*, `https://docs.scipy.org/doc/scipy-1.13.1/reference/generated/scipy.optimize.curve_fit.html`, 2023, accessed: 2024-08-21.

[241] G. I. Egorov and D. M. Makarov: *Densities and thermal expansions of (water + tetrahydrofuran) mixtures within the temperature range from (274.15 to 333.15) K at atmospheric pressure*, Journal of Molecular Liquids 310, p. 113105, 2020, ISSN 0167-7322, doi:10.1016/j.molliq.2020.113105.

[242] D. Evans: *Irradiation effects in liquid methane used as a neutron moderator*, Cryogenics 35, no. 11, pp. 763–766, 1995, ISSN 0011-2275, doi:10.1016/0011-2275(95)90909-Y, nonmetallic Materials and Composites at Low Temperature-VII.

[243] E. Kulagin, S. Kulikov, V. Melikhov and E. Shabalin: *Radiation effects in cold moderator materials: Experimental study of accumulation and release of chemical energy*, Nuclear Instruments and Methods in Physics Research B 215, no. 1-2, pp. 181–186, 2004, ISSN 0168583X, doi:10.1016/j.nimb.2003.08.026.

[244] M. H. Parajon, E. Abad and F. Bermejo: *A review of the cold neutron moderator materials: Neutronic performance and radiation effects*, Physics Procedia 60, pp. 74–82, 2014, ISSN 1875-3892, doi:10.1016/j.phpro.2014.11.012.

[245] HighNESS: *Ncplugin-SANSND*, `https://github.com/highness-eu/ncplugin-SANSND`, 2024, accessed: 2024-07-15.

[246] A. Brulet, L. Clarke and L. Didier: *SAM - small angle modular spectrometer*, 2024, accessed: 2024-07-17.

[247] P. Zakalek, J. Baggemann, E. Mauerhofer, U. Rücker, J. Li, J. Voigt, K. Lieutenant et al.: *Big karl experimental area*, in *The Japanese RIKEN Center for Advanced Photonics (RAP) and the Jülich Centre for Neutron Science (JCNS) Fourth Joint Workshop on Compact Accelerator-Driven Neutron Sources (CANS) Special Webinar*, Forschungszentrum Jülich, Germany, 2020, 4th Joint RIKEN/HBS Workshop, 22-24 June 2020.

[248] A. Szakál: *Out-of-pile moderator test facility at the Budapest Neutron Centre*, in *International Conference on Neutron Scattering (ICNS 2022)*, Buenos Aires, Argentina, 2022, presented at the International Conference on Neutron Scattering (ICNS 2022).

[249] J. Füzi: *Direct measurement of cold neutron moderator spectra*, Nuclear Instruments and Methods in Physics Research Section A: Accelerators, Spectrometers, Detectors and Associated Equipment 586, pp. 41–45, 2008, doi:10.1016/j.nima.2007.11.055.

[250] R. Boswell and T. S. Collett: *Current perspectives on gas hydrate resources*, Energy Environ. Sci. 4, no. 4, pp. 1206–1215, 2011, doi:10.1039/C0EE00203H.

[251] A. V. Milkov: *Global estimates of hydrate-bound gas in marine sediments: How much is really out there?*, Earth-Science Reviews 66, no. 3, pp. 183–197, 2004, ISSN 0012-8252, doi:10.1016/j.earscirev.2003.11.002.

[252] I. P. on Climate Change: *Climate Change 2013 : The Physical Science Basis ; Working Group I Contribution to the Fifth Assessment Report of the Intergovernmental Panel on Climate Change*, Cambridge Univ. Press, New York, NY, 1. publ. ed., 2014, ISBN 978-1-107-05799-9.

[253] IEA: *CO2 emissions in 2023*, `https://www.iea.org/reports/co2-emissions-in-2023`, 2024, accessed: 2024-07-09.

[254] I. P. on Climate Change: *Climate Change 2022 : Mitigation of Climate Change : Working Group III Contribution to the Sixth Assessment Report of the Intergovernmental Panel on Climate Change*, Elements in Psychology and Culture, Cambridge University Press, / Intergovernmental Panel on Climate Change. Working Group III, author, Cambridge :, 1st ed. ed., 2023, ISBN 1-00-915792-2.

[255] IEA: *Methane tracker 2021*, https://www.iea.org/reports/methane-tracker-2021, 2021, accessed: 2024-07-09.

[256] V. Istomin, V. Yakushev, N. Makhonina, K. V.G. and E. Chuvilin: *Self-preservation phenomenon of gas hydrates*, Gas industry of Russia Digest 4, pp. 16–27, 2006.

[257] N. Shakhova, I. Semiletov, A. Salyuk, V. Yusupov, D. Kosmach and Ö. Gustafsson: *Extensive methane venting to the atmosphere from sediments of the east siberian arctic shelf*, Science 327, no. 5970, pp. 1246–1250, 2010, doi:10.1126/science.1182221.

[258] C. D. Ruppel and J. D. Kessler: *The interaction of climate change and methane hydrates*, Review of Geophysics 55, pp. 126–168, 2017, doi:10.1002/2016RG000534.

[259] D. Thomas: *Air Attenuation Corrections for Neutron Calibrations*, NPL Report IR 58, National Physical Laboratory, 2021, accessed: 2024-08-18.

[260] O. Tetens: *Original papers on the Tetens equation*, Meteorologische Zeitschrift 1930.

[261] J. G. Davis: *An improved equation for the calculation of saturation vapour pressure*, Journal of Applied Meteorology and Climatology 45, no. 2, pp. 0123–0129, 2008, doi: 10.1175/2007JAMC1674.1.

[262] International Organization for Standardization: *Reference neutron radiations – Part 2: Calibration fundamentals of radiation protection devices related to the basic quantities characterizing the radiation field*, https://www.iso.org/standard/25667.html, 2000, ISO 8529-2:2000.

[263] N. Wiener: *Extrapolation, Interpolation and Smoothing of Stationary Time Series: With Engineering Applications*, MIT, Cambridge, Mass, 1964.

[264] F. J. Anscombe: *The Transformation of Poisson, Binomial and Negative-Binomial Data*, Biometrika 35, no. 3-4, pp. 246–254, 1948, doi:10.1093/biomet/35.3-4.246.

[265] L. Tolson: *Fully deuterated tetrahydrofuran clathrate hydrates as a very cold neutron moderator: Measurements of the total neutron cross section*, Master's project, 2024.

[266] T. Neulinger, H. Filter and O. Zimmer: *Vertical time-of-flight spectroscopy of ultracold neutrons*, Nuclear Instruments and Methods in Physics Research Section A: Accelerators, Spectrometers, Detectors and Associated Equipment 1059, p. 168947, 2024, ISSN 0168-9002, doi:10.1016/j.nima.2023.168947.

[267] SciPy Community: *Minimization using the BFGS algorithm*, https://docs.scipy.org/doc/scipy/reference/optimize.minimize-bfgs.html, 2024, accessed: 2024-08-21.

[268] Team, SciPy Development: *Scipy.stats.pearsonr*, https://docs.scipy.org/doc/scipy-1.2.3/reference/generated/scipy.stats.pearsonr.html, 2020, accessed: 2023-09-03.

[269] K. B. Grammer and F. X. Gallmeier: *The small-angle neutron scattering extension in mcnpx and the sans cross section for nanodiamonds*, Nuclear Instruments and Methods in Physics Research Section A 953, p. 163226, 2020, doi:10.1016/j.nima.2019.163226.

[270] T. Tanaka, K. Hagiwara, E. Gazzola, A. Ali, I. Ou, T. Sudo, P. Kumar Das et al.: *Gamma-ray spectra from thermal neutron capture on gadolinium-155 and natural gadolinium*, Progress of Theoretical and Experimental Physics 2020, no. 4, p. 043D02, 2020, ISSN 2050-3911, doi:10.1093/ptep/ptaa015.

[271] T. Jenke: *Characterisation of the chopper opening function of a UCN chopper*, 2022, private communication.